Investigating human brain function and human brain organization using functional Magnetic Resonance Imaging at 4.7 T

by

Stanislau Hrybouski

A thesis submitted in partial fulfillment of the requirements for

Doctor of Philosophy

Neuroscience

University of Alberta

Abstract

Understanding the brain-cognition association has been a major goal of neuroscientists for more than 50 years. The discovery of functional magnetic resonance imaging (fMRI) blood-oxygen-level-dependent (BOLD) contrast by Ogawa and colleagues (1990, 1992) has fundamentally transformed the field of human neuroscience, allowing researchers to non-invasively measure function of the human brain. Since that initial discovery, imaging methodology has improved substantially, and new approaches for studying brain function are continuously developed. A recent shift towards high-field (> 3 T) scanners enabled researchers to probe brain structure and function with unmatched anatomical precision. However, the advantages of high-field fMRI datasets can be challenging to realize in practice, since greater spatial resolution comes at a cost: reduced contrast-to-noise ratio, increased vulnerability to head motion artifacts, and geometric distortions caused by longer readout times. High-field fMRI data are also more sensitive to cardiac and respiratory signals of no-interest, which can weaken or bias most statistical inferences, especially in resting-state functional connectivity work. Consequently, the primary objective of this thesis was to develop methodology that is capable of taking the full advantage of high-field fMRI to study brain function and brain organization. We accomplished this aim by combining precise anatomical localization on ultra-high-resolution structural MRI in native space, with an extensive set of fMRI denoising techniques as well as task-specific statistical models of each structure's hemodynamic response. To test our approach for studying brain function using high field high-resolution fMRI we investigated functional aspects of small medial temporal lobe (MTL) structures, which are notoriously difficult to study because of lower vascular density, susceptibility artifacts, and signal contamination from larger drainage veins.

The first two experiments of this thesis examine functional properties of the amygdala subnuclei and hippocampal subfields. To activate the amygdala subnuclei we employed negative

emotional stimuli that have been shown to elicit amygdala response in other fMRI studies, and the hippocampus was engaged by a computerized adaptation of a standardized clinical memory battery, that is capable of testing neurobiological processes responsible for item, spatial, and associative memory. In the third experiment, we combined a 4.7 T acquisition with a data-driven network parcellation to study age differences in the brain's functional architecture. We investigated network topography, network amplitude, and inter-network communication for the entire connectome. Inter-network functional connectivity was estimated using a novel sparse graphical estimation procedure that aims to uncover true graph structure with edges representing direct connections only. Simulation work by Allen and colleagues (2012) suggests that fMRI data with greater BOLD contrast-to-noise ratio (e.g., > 4 T) should produce network parcellation that in less biased and more sensitive to differences when performing statistical comparisons between groups.

In the MTL experiments, emotional stimuli elicited differential engagement of the amygdala subnuclei demonstrating the necessity of studying these small grey matter nuclei separately from each other. Similarly, our memory paradigm revealed a complex pattern of intra-hippocampal specialization within both the anterior and posterior hippocampal subfields in memory encoding and memory retrieval. Finally, our investigation into age effects on the brain's functional architecture revealed widespread BOLD signal reduction among old adults, affecting every major brain system. Connectivity analyses, however, showed a high degree of age-invariance in the brain's functional architecture with some subtle differences among age group. At 4.7 T, we were able to obtain a finer network splitting than is commonly reported in neuroimaging literature, highlighting the advantages of high-field acquisitions for studying the brain's connectome using data-driven network detection techniques. Together, these results revealed clear advantages of high-field fMRI for studying the brain's structure-function relationships and for investigating its network properties.

Preface

This thesis is an original work by Stanislau Hrybouski. All of the research projects in it were approved by the University of Alberta's Health Research Ethics Board.

I.

Chapter 3 has been published in a 2016 issue of *NeuroImage*: **Hrybouski, S.**, Aghamohammadi-Sereshki, A., Madan, C. R., Shafer, A. T., Baron, C. A., Seres, P., Beaulieu, C., Olsen, F., & Malykhin, N. V. (2016). Amygdala subnuclei response and connectivity during emotional processing. *NeuroImage*, *133*, 98–110.

Research in chapter 3 is a product of extensive collaboration among all of the listed authors. Stanislau Hrybouski, Antrea Shafer, Christopher Madan, and Nikolai Malykhin conceived the experiment. The fMRI paradigm was developed by Andrea Shafer. Pulse sequence was provided by Corey Baron and Christian Beaulieu. Data collection was performed by Stanisau Hrybouski, Peter Seres, and Fraser Olsen. Protocol for segmenting the amygdala subnuclei on T_2-weighted structural MRI was developed Arash Aghamohammadi-Sereshki and Nikolai Malykhin. FMRI analyses were performed by Stanislau Hrybouski and Christopher Madan. Stanislau Hrybouski and Nikolai Malykhin prepared the initial draft of the manuscript, and all authors contributed to its editing during the revision process. Nikolai Malykhin was the supervisory author of this project.

II.

Chapter 4 has been published in a 2019 issue of *NeuroImage*: [*]**Hrybouski, S.**, [*]MacGillivray, M., Huang, Y., Madan, C. R., Carter, R., Seres, P., & Malykhin, N. V. (2019). Involvement of hippocampal subfields and anterior-posterior subregions in encoding and retrieval of item, spatial, and associative memories: Longitudinal versus transverse axis. *NeuroImage*, *191*, 568–586.

[*] shared first authorship

Research in chapter 4 is a product of extensive collaboration among all of the listed authors. Stanislau Hrybouski, Melanie MacGillivray, and Nikolai Malykhin conceived the experiment. Stanislau Hrybouski was responsible for programming the fMRI task. Rawle Carter, Melanie

MacGillivray, and Peter Seres were responsible for volunteer recruitment and data collection. Yushan Huang segmented the hippocampal subfields and subregions. FMRI analysis pipeline was developed by Stanislau Hrybouski with contributions from Christopher Madan. Stanislau Hrybouski and Melanie MacGillivray performed fMRI data preprocessing. Statistical analyses were performed by Stanislau Hrybouski. Stanislau Hrybouski, Nikolai Malykhin, and Melanie MacGillivray wrote the initial draft of the manuscript. Nikolai Malykhin was the supervisory author of this project.

III.

Chapter 5 is a pre-publication draft of a research manuscript: **Hrybouski, S.**, Cribben, I., McGonigle, J., Olsen, F., Carter, R., Seres, P., Madan, C. R., & Malykhin, N. V. (in preparation). Investigating effecs of healthy cognitive aging on brain functional connectivity using 4.7 T resting-state functional Magnetic Resonance Imaging.

Research in chapter 5 is a product of collaboration among all of the listed authors. Stanislau Hrybouski and Nikolai Malykhin conceived the experiment. Fraser Olsen and Rawle Carter were responsible for volunteer recruitment and screening. Fraser Olsen and Peter Seres were responsible for data collection. Stanislau Hrybouski performed most of data analysis with John McGonigle providing scripts for ANTS-based image registration and Ivor Cribben developed and implemented sparse graph estimation methodology. Stanislau Hrybouski wrote this experimental chapter. Nikolai Malykhin was the supervisory author of this project and contributed to study design, data analysis, and editing of the manuscript draft.

Acknowledgements

Funding for this work was provided by the Canadian Institutes of Health Research (CIHR) and National Science and Engineering Research Council (NSERC). I would also like to extend a special thanks to all of our wonderful volunteers without whom none of the research in this thesis would have been possible.

Many individuals contributed to my scientific training. I thank CIHR, NSERC, and the University of Alberta for salary support, and National Institutes of Health (NIH) for providing me an opportunity to attend one of the best training programs in North America for aspiring neuroimagers, the NeuroImaging Training Program (NITP). Fraser Olsen and Rawle Carter deserve special acknowledgement for performing the bulk of participant recruitment and screening. Corey A. Baron and Christian Beaulieu provided us with a customized 4.7 T Echo Planar Imaging (EPI) sequence and reconstruction code, which enabled us to perform high-resolution fMRI experiments. Alan Willman and Marc Lebel developed a T_2-weighted Fast Spin Echo (FSE) sequence that was used for anatomical segmentation in our high-resolution work. Christopher Madan and Andrea Shafer helped me with paradigm design in task-based research, while John McGonigle and Ivor Cribben helped me with image registration and connectivity analyses.

Special thanks should be extended to my supervisory committee members, Drs. Jeremy Caplan and Esther Fujiwara, my labmates and colleagues, especially Arash Aghamohammadi-Sereshki and Christopher Madan, for helping me through difficult stages of the PhD research and providing technical and personal support during the most difficult stages. I also thank my supervisor, Dr. Nikolai Malykhin for all the mentorship and feedback throughout the PhD programme, and for teachning me to appreciate neuroanatomy in studies of brain function.

Lastly, I would like to acknowledge the kind support and love of my family during both difficult and exciting phases of this journey. Without them, I would not have been where I am today, and my success belongs to them as well.

Table of Contents

List of Tables

List of Figures

List of Symbols & Abbreviations

2D: two dimensional

3D: three dimensional

AB: accessory basal nucleus of the amygdala

AC-PC: anterior commisure – posterior commisure alignment

ANOVA: analysis of variance

AR: autoregressive

ASL: Arterial Spin Labeling

Au: auditory network

B: basal nucleus of the amygdala

B_0: main magnetic field

BA: basal group of the amygdala nuclei in Chapter 3; Brodmann Area in Chapter 5

BCa CI: bias corrected and accelerated bootstrap confidence interval

BLA: basolateral amygdala

AG: amygdala

BOLD: blood oxygenation level-dependent

CA: *Cornu Ammonis* subfields of the hippocampus

CBF: cerebral blood flow

CBV: cerebral blood volume

CDR: Clinical Dementia Rating

Ce: central nucleus of the amygdala

CeM: centromedial group of the amygdala nuclei

CNR: contrast-to-noise ratio

$CMRO_2$: rate of cerebral metabolic oxygen utilization

Co: cortical amygdala

CO_2: carbon dioxide

CSF: cerebrospinal fluid

CV: cross-validation

CVR: cerebrovascular reactivity

DA: dorsal attention network

DG: dentage gyrus subfield of the hippocampus

DMN: default mode network

DM1-5: default mode network's sub-system 1-5

DSC: Dice similarity coefficient

EC: executive control network

EPI: Echo Planar Imaging pulse sequence

GICA: group-level Independent Component Analysis

GIG-ICA: group-information-guided subject-level Independent Component Analysis

GLM: General Linear Model

GM: cerebral grey matter

GRAPPA: generalized autocalibrating partially parallel acquisition

HC: hippocampus

HH: hippocampal head

HIS: Hachinski Ischemic Scale

HB: hippocampal body

HT: hippocampal tail

HR: heart rate

HRf: hemodynamic response function

FC: functional connectivity

FDR: False Discovery Rate

FWE: Familywise Error Rate

FIR: finite impulse response model

fMRI: functional Magnetic Resonance Imaging

fNIRS: funtional Near-Infrared Spectroscopy

FOV: field of view

FP: fractional polynomial

FSE: Fast Spin-Echo pulse sequence

FWHM: full width at half maximum

I_q: ICASSO intra-cluster and extra-cluster similarity index, representing an ICA component's stability

IAPS: International Affective Picture System

IC: Independent Component

ICA: Independent Component Analysis

ICC: intraclass correlation coefficient

ISI: inter-stimulus interval

LA: lateral nucleus of the amygdala

M: medial nucleus of the amygdala

MCI: mild cognitive impairment

MOCA: Montreal Cognitive Assessment

MPRAGE: Magnetization Prepared Rapid Gradient-Echo pulse sequence

MR: Magnetic Resonance

MRI: Magnetic Resonance Imaging

MTL: medial temporal lobe

NEPSY-II: Developmental Neuropsychological Assessment, 2nd edition

NIRS: Near-Infrared Spectroscopy

NO: nitric oxide

O_2: oxygen

PCA: Principal Component Analysis

PET: Positron Emission Tomography

RSFA: resting-state fluctuation amplitude

RMSD: root-mean-squared-deviation

RS-fMRI: resting-state functional Magnetic Resonance Imaging

RSN: resting-state network

RVT: respiratory volume per time

SCAD: smoothly clipped absolute deviation regularization

SD: standard deviation

SM: somatomotor network

SNR: signal-to-noise ratio

SVM: support-vector-machine classifier

Sub: subiculum subfield of the hippocampus

T_1: longitudinal relaxation time

T_2: transverse relaxation time

T_2^*: effective transverse relaxation time in the presence of B_0 inhomogeneity

TE: echo time

TI: inversion time

TR: repetition time

tSNR: temporal signal-to-noise ratio

Vis: visual network

WM: cerebral white matter

WMS-IV: Wechsler Memory Scale 4th edition

UWD: Urbach-Wiethe disease

Chapter 1: Background Literature

1.1 Measuring Brain Activity Using Functional MRI

The human brain can be conceptualized as a collection of functionally distinct neuronal communities (Bullmore & Sporns, 2009; Fröhlich, 2016; Wig, 2017). At various time points, certain sub-networks are recruited to deal with salient information or to perform cognitive tasks. Understanding the precise neurobiological basis of human cognition and behavior has been a major goal of neuroscientists for over a century. Prior to the advent of modern imaging techniques, functional brain mapping was largely restricted to neurological populations, patients with surgical brain lesions, and experimental animal work.

In the late 20th century, the field of human neuroscience was dramatically transformed by a new generation of functional imaging tools, enabling researchers for the first time, to study brain function with a high degree of anatomical specificity (Fröhlich, 2016; Heeger & Ress, 2002; Logothetis & Wandell, 2004). Crucial to this transformation was the advent of functional Magnetic Resonance Imaging (fMRI) methodology (Gagnon et al., 2015; Logothetis, 2008; Logothetis et al., 2001; Ogawa et al., 1990; Uludağ & Blinder, 2018). Since its inception in 1990, fMRI has rapidly become a method of choice when studying human brain function *in vivo*. Compared to other non-invasive imaging techniques, fMRI provides superior spatial resolution (Fröhlich, 2016; Kim & Ogawa, 2012; Logothetis, 2008).

Functional MRI can be used to study both brain-cognition links and properties of the brain's architecture as a connectome (Buckner et al., 2013; Fröhlich, 2016; Logothetis, 2008; Wig, 2017). Studies belonging to the former category typically employ highly controlled tasks (although naturalistic stimuli have also be used; e.g., Nishimoto & Gallant, 2011) to drive hypothesis-based changes in neuronal firing, while studies belonging to the latter category employ data-driven methods to compare functional architecture between study groups or cognitive states. The two approaches provide complementary information about the brain and how its function might be altered in various neurological or psychiatric disorders. Despite differences in their primary objectives and analytical tools, all fMRI experiments use the *vascular hemodynamic response* as a proxy for neuronal activity.

1.2 Biophysics of BOLD fMRI

The human brain comprises 2% of the body's mass but is responsible for 20% of the body's energy use (Rolfe & Brown, 1997). The brain's energy consumption is used to maintain membrane gradients and for neurotransmitter trafficking/recycling (Attwell et al., 2010; Attwell & Laughlin, 2001). Synaptic and post-synaptic activity increases regional metabolic demands (i.e., O_2 and glucose), and to deal with this greater demand for metabolic resources, the brain has evolved neurovascular-coupling mechanisms to deliver additional metabolic resources to active areas. Activated brain regions experience a transient increase in cerebral metabolic oxygen utilization ($CMRO_2$). Regional cerebral vasculature responds to rising metabolic demands by dilating local blood vessels and increasing local cerebral blood flow (CBF) (Cohen et al., 2004; Kim, 2018; Kim & Ogawa, 2012; Uludağ & Blinder, 2018; Uludağ et al., 2009; Wright & Wise, 2018). Because the vascular response overcompensates O_2 utilization, venous deoxyhaemoglobin ratio rises, which in turn weakens susceptibility effects on T_2^*-sensitive MRI (Buckner et al., 2013; Fröhlich, 2016; Gagnon et al., 2015; Kim, 2018; Kim & Ogawa, 2012; Logothetis, 2008).

Biophysical processes, linking the underlying neuronal activity with the blood oxygenation level-dependent (BOLD) fMRI, are complex and only partially understood (Attwell et al., 2010; Hillman, 2014; Kim, 2018). The human brain comprises 2% of the body's mass but is responsible for 20% of the body's energy use (Rolfe & Brown, 1997). The brain's energy consumption is used to maintain membrane gradients and for neurotransmitter trafficking/recycling (Attwell et al., 2010; Attwell & Laughlin, 2001). Synaptic and postsynaptic activity increases regional metabolic demands (i.e., O_2 and glucose), and to deal with this greater demand for metabolic resources the brain has evolved neurovascular-coupling mechanisms to deliver additional metabolic resources to active areas. Vessel dilation is likely initiated via glutamate-initiated nitric oxide (NO) release by postsynaptic neurons, although other molecules, including blood [CO_2], may play additional roles (Attwell et al., 2010). The post-stimulus increase in CBF, and consequently, energy supply in response to sustained neuronal activity is 4+ times larger than increased metabolic demands by activated neurons (Lin et al., 2010). It is this differential in supply vs. demand on metabolic resources that is measured by BOLD fMRI (Attwell et al., 2010; Fröhlich, 2016; Gagnon et al., 2015; Hillman, 2014; Kim, 2018; Kim & Ogawa, 2012; Logothetis, 2008; Uludağ & Blinder, 2018).

1.3 BOLD Response Characteristics

The classical BOLD response to a short burst (< 1 s) of neuronal activity is characterized by an initial post-stimulus dip, followed by a steep rise and activity peaking 5-6 s after neural activity began, followed by a steep decline with a moderate undershoot and a gradual return to the pre-stimulus baseline. The initial post-stimulus BOLD dip is likely due to the mismatch between $CMRO_2$ and CBF changes (Kim & Ogawa, 2012). However, because measuring such subtle changes in the fMRI time series requires both high spatial and high temporal resolution, the initial dip is rarely modeled with standard 1.5-3.0 s temporal resolution. A slow return of $CMRO_2$ to pre-activity levels is the most likely cause of post-stimulus undershoots, although cerebral blood volume (CBV) and CBF contributions have been reported as well (Kim & Ogawa, 2012). Similar to the initial dips, post-peak undershoots are rarely investigated because most event-related designs do not employ sufficiently long inter-stimulus intervals (ranging between 15 and 30 s) that are necessary for accurate comparisons of the undershoot properties. Instead, most task-based fMRI experiments employ short inter-stimulus intervals with variable length, allowing for a greater number of stimuli in an experiment and boosting the statistical power of main comparisons (Amaro & Barker, 2006; Heeger & Ress, 2002).

Most fMRI experiments study peak BOLD amplitude, representing the greatest differential between CBF and $CMRO_2$ effects in response to a stimulus when comparing brain activity among groups or trial types (Fig. 1.1). Two other features of task-evoked BOLD are sometimes also examined: response latency and response duration (Handwerker et al., 2004; Henson et al., 2002; Lindquist et al., 2009; Lindquist & Wager, 2007; West et al., 2019). The first can be described as the time it takes for the BOLD activity to reach its post-stimulus peak and the second is oftentimes measured as the BOLD response's width at half maximum (Fig. 1.1). Because of analytical complexity, many event-related studies of brain function assume identical BOLD response shape in all task conditions and brain regions and simply convolve the expected duration of the underlying neuronal activity with a standard gamma or double-gamma response function (Heeger & Ress, 2002; Lindquist et al., 2009; Pernet et al., 2014). In addition to anatomical invariance, this approach also assumes (1) simple summation of the recorded BOLD signal from temporally adjacent events, (2) constant as opposed to adaptable or transient neuronal response in activated brain regions, and (3) a linear relationship between blood flow and neuronal activity (Heeger & Ress, 2002). Evidence

for linear summation has been mixed with some studies supporting linear additive properties and others failing to demonstrate such effects (Hillman, 2014; Hirano et al., 2011; Martin et al., 2006; Yeşilyurt et al., 2008; Zhang et al., 2009), and other assumptions are not always met (Ekstrom, 2010; Heeger & Ress, 2002; Hillman, 2014; Nauer et al., 2015). An alternative, although a more complex, approach is to estimate task-specific hemodynamic response function for brain areas of interest, allowing for more accurate BOLD response modeling, and an ability to compare multiple BOLD response characteristics among different populations or task conditions. Timing and duration properties can provide additional information about the underlying neuronal activity (Calhoun et al., 2004; Formisano & Goebel, 2003; Henson et al., 2002; Lindquist et al., 2009; Logothetis & Wandell, 2004; Pernet, 2014; West et al., 2019). Furthermore, region-specific and task-specific BOLD models allow for greater statistical sensitivity, an advantage when working with high-field high-resolution data since fMRI contrast-to-noise ratio tends to decrease with increasing spatial resolution (De Martino et al., 2018; Kim, 2018; Kim & Ogawa, 2012; Uludağ & Blinder, 2018).

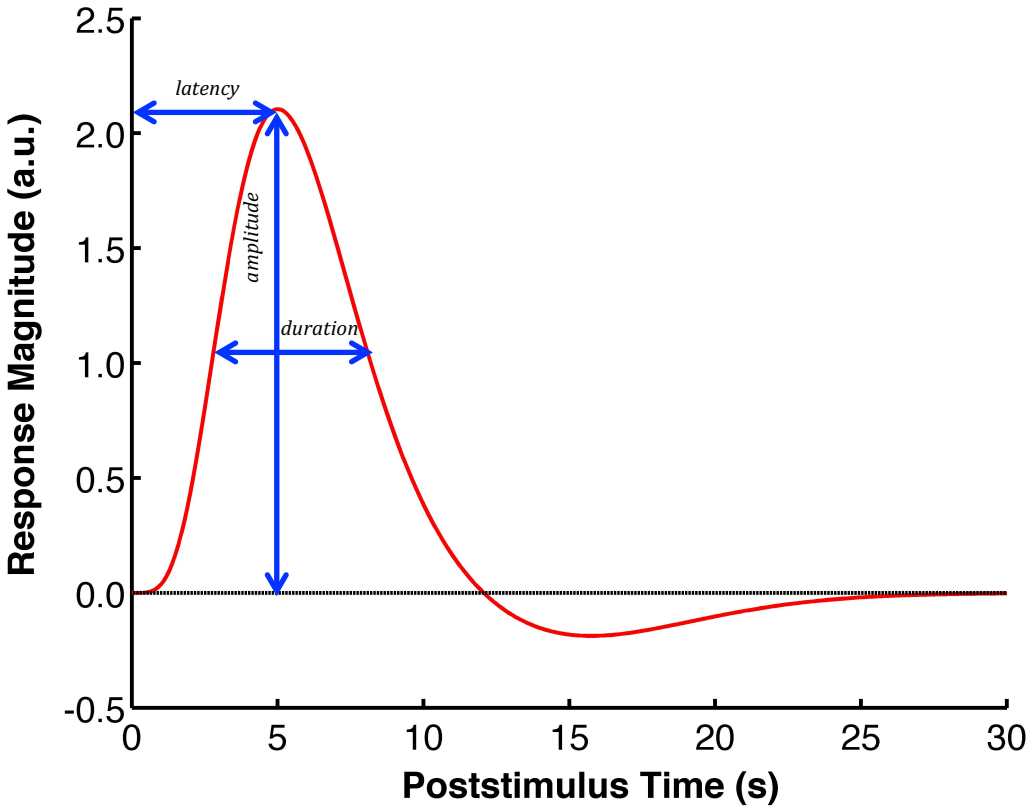

Fig. 1.1. Simulated double-gamma BOLD function is shown in red (a.u., arbitrary units). Estimates of response height, time-to-peak, and full-width at half-max are depicted in blue.

1.4 Functional MRI at High Field

The goal of the current set of projects was to leverage the power of 4.7 T fMRI to advance our understanding of the relationship between small medial temporal lobe structures in human cognition and to provide a detailed depiction of system-level changes in brain's functional organization caused by aging processes. If spatial resolution remains unchanged, moving from a lower (e.g., 1.5 T) to a higher (above 4 T) magnetic field strength results in increased MRI signal sensitivity (De Martino et al., 2018; Kim, 2018; Kim & Ogawa, 2012; Uludağ & Blinder, 2018; Vaughan et al., 2001), producing BOLD effects of greater magnitude (Sladky et al., 2013), and improving the statistical power of BOLD comparisons if physiological noise does not dominate the fMRI time series (Hutton et al., 2011; Triantafyllou et al., 2005; van der Zwaag et al., 2009). Functional MRI data acquired at high fields are more sensitive to BOLD contrast originating within grey matter microvasculature, as opposed to BOLD from larger drainage veins (De Martino et al., 2018; Gagnon et al., 2015; Shmuel et al., 2007; Uludağ & Blinder, 2018), improving activity localization. Increased sensitivity to the BOLD signal that originates from small intra-cortical blood vessels in combination with improved SNR enables high-field scanners to achieve spatial resolution with voxel volume smaller than 8 mm^3 (Fig. 1.2), substantially reducing partial volume effects and signal contamination from neighbouring structures (De Martino et al., 2018; Pohmann et al., 2016; Shmuel et al., 2007; Ugurbil, 2016). The improved contrast-to-noise ratio (CNR) at high fields can also be used to obtain more accurate community mapping in functional connectivity studies since many algorithms produce more accurate network and sub-network estimates from data with greater temporal SNR (Allen et al., 2012; Ugurbil, 2016).

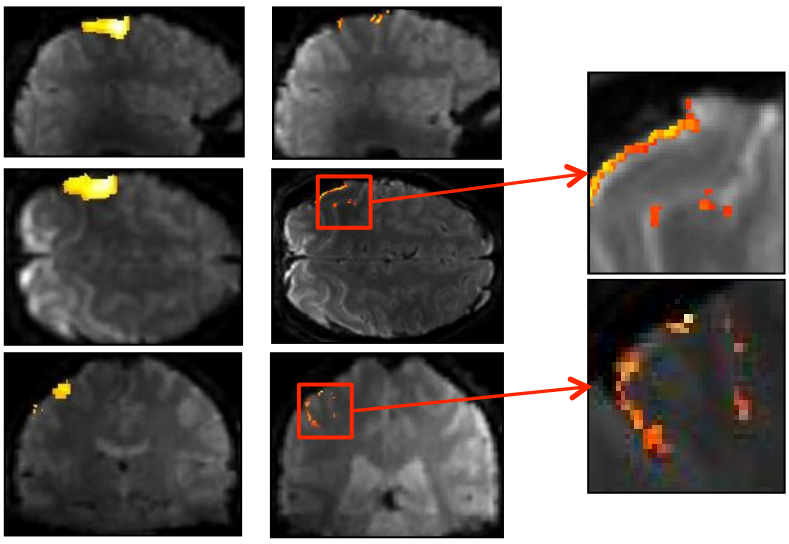

Fig. 1.2. Statistical parametric maps for a 4.7 T block-design finger tapping experiment [alternating 30 s tap/rest blocks]. Left panel: standard resolution acquisition [3 × 3 × 3 mm^3] smoothed* with a 6-mm FWHM Gaussian kernel. Right panel: high-resolution acquisition [1.5 × 1.5 × 1.5 mm^3] from the same participant with no spatial smoothing of any kind.

*Standard-resolution images were smoothed for consistency with analysis pipelines commonly used in other human fMRI studies.

Unfortunately, high-field acquisitions are not only more sensitive to BOLD activations but are also more sensitive to non-neurovascular physiological signals, reducing many of the advantages of high-field datasets if such physiological noise sources are not minimized. As a consequence of reduced partial volume effects, physiological confounds are less pronounced in high-resolution (8-mm^3 or less) images (Hutton et al., 2011; Triantafyllou et al., 2005; van der Zwaag et al., 2009), and one way to reduce the severity of physiological noise is to acquire fMRI data with greater spatial resolution (Hutton et al., 2011; Triantafyllou et al., 2005; van der Zwaag et al., 2009). Unfortunately, longer readout times in high-resolution acquisitions result in greater geometric distortions that may be difficult to correct (Hutton et al., 2011), reducing the anatomical accuracy of activity localizations using anatomical labels derived from structural MRI.

Another approach is to optimize statistical modeling by employing a more accurate hemodynamic response model together with post-acquisition cleanup of the physiological noise. In fMRI datasets, the dominant sources of physiological noise are cardiac pulsatility, heart rate variability, cerebrospinal fluid (CSF) flow, respiration-induced magnetic field changes, and fluctuations in CO_2 (a potent vasodilator; Cohen et al., 2004) concentration resulting from differences in breath depth and/or breath rate (Birn et al., 2006; Chang et al., 2009; Glover et al., 2000; Hutton et al., 2011). Consequently, in order to take a full advantage of high-field fMRI acquisitions it is critical to reduce the effects of non-BOLD physiological signals on the data, especially at standard resolutions (i.e., 16-mm^3 or more). Cardiac and breathing-related information can be removed by regressors that are derived from synchronized cardiac and respiratory waveforms (Birn et al., 2008; Chang et al., 2009; Glover et al., 2000). A subject's cardiac waveforms are commonly recorded by a pulse photoplethysmograph, while breathing-related waveforms can be obtained by strapping a pneumatic belt around his or her abdomen. Substantial post-processing is then performed to convert these recordings to GLM-style (GLM, General Linear Model; Worsley & Friston, 1995) regressors capable of removing aliased physiological noise (Birn et al., 2008; Chang et al., 2009; Glover et al., 2000; see section, 5.2 for a more detailed methodological description on how to remove physiological noise using cardiac and respiratory waveforms).

In addition to the supplemental cardiac and respiratory waveforms, some physiological noise sources can be removed from the fMRI data using post-processing techniques. One approach is to estimate the dominant sources of the time series variability in the CSF and cerebral white matter

(WM) and use this information for physiological noise cleanup (Behzadi et al., 2007; see sections 3.2 and 4.2 for details). Another, and perhaps better, data-driven approach for the physiological noise removal is to perform a subject-level independent component analysis (ICA) decomposition that can remove not only physiological but many other noise sources, including head motion, from the fMRI data (Griffanti et al., 2017). With accurate BOLD modeling, such data cleaning procedures enable researchers to take full advantage of high-field MRI systems in task-based and resting-state work. In the ensuing set of experiments, we combined ultra-high-resolution structural MRI with high-resolution functional MRI (3.375 mm^3 voxels) to understand how small structures of the medial temporal, namely the amygdala subnuclei and hippocampal subfields, lobe contribute to processing of emotionally salient information and declarative memory. Understanding the functional properties of such small structures necessitates high-resolution acquisitions, an ideal application for high field MRI systems due to their improved BOLD contrast sensitivity.

1.5 Amygdala Subnuclei

The amygdala (AG) is an almond-shaped medial temporal lobe structure involved in the neural circuits of fear/reward learning, as well as aggressive, sexual, maternal, and feeding behaviors (Janak & Tye, 2015; LeDoux, 2012; LeDoux & Schiller, 2009). The AG interacts extensively with numerous cortical and subcortical regions and can modulate human attention and perception (Adolphs et al., 2005; Pitkänen et al., 2000; Sah et al., 2003). Of particular interest to our experiments is the AG's role in the processing of emotionally relevant stimuli and the creation of emotionally salient memories (Dolcos et al., 2004; Kensinger, 2009; LeDoux & Schiller, 2009; Murty et al., 2010; Sergerie et al., 2008; Shafer et al., 2012; Shafer & Dolcos, 2012).

To gain a better understanding of the AG's role in human cognition, it is vital to acknowledge that the AG is not a homogenous structure and instead represents a grey matter complex of a at least thirteen nuclei (Brabec et al., 2010; Janak & Tye, 2015; LeDoux, 2012; Sah et al., 2003; Whalen et al., 2009). These are generally grouped into two major subdivisions: basolateral and centrocorticomedial (Johnston, 1923; LeDoux & Schiller, 2009). The lateral (LA), basal (B), and accessory basal (AB) nuclei constitute the basolateral (BLA) complex, while the cortical (Co), medial (M), and central (Ce) nuclei belong to the centrocorticomedial group (Fig. 1.3a).

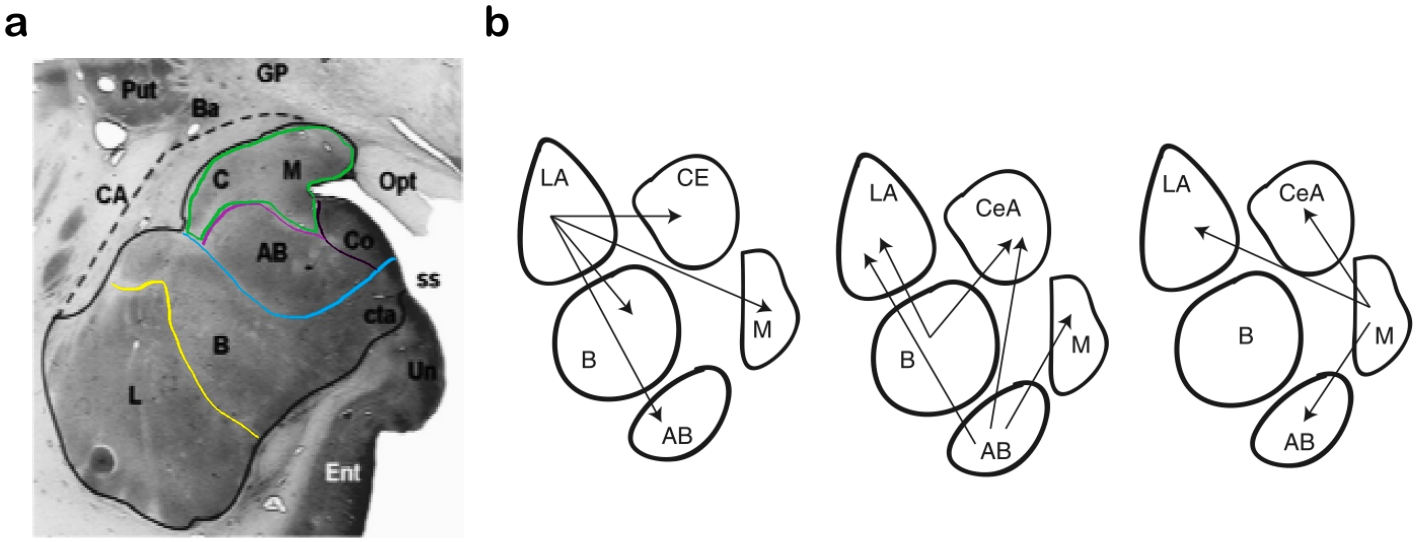

Fig. 1.3. (a) Human amygdala subnuclei (L, lateral; B, basal; AB, accessory basal; C, central; M, medial; Co, cortial). Adapted from Brabec et al. (2010). (b) Schematic of intra-amygdala information flow in non-human primates. Adapted from Sah et al. (2003).

In rodents, the LA nucleus receives inputs from multiple sensory systems acts as the sensory interface of the AG complex (Phelps & LeDoux, 2005). The BA nucleus receives most of its inputs from two sources, the LA nucleus of the AG, and the orbitofrontal cortex, while its outputs mainly project to the Ce AG and striatum, where they provide context-dependent modulation of emotional processing (Freese & Amaral, 2009) and contribute to the regulation of instrumental behaviors (LeDoux & Schiller, 2009). Although direct inputs into the CeM group from the LA nucleus exist (Pitkänen et al. 1997), those are few in comparison to the indirect pathway through the B and AB nuclei (Duvarci & Paré, 2014; Freese & Amaral, 2009). The Ce nucleus, in turn, acts as the primary output of the AG circuitry (see Fig 1.3b for a schematic overview of intra-AG connectivity), projecting to the lateral and paraventricular hypothalamus, ventral tegmental area, locus coeruleus, and basal forebrain (Davis & Whalen, 2001; Kalin et al., 2004). It is because of these connections that AG circuitry can influence heart rate, blood pressure, corticosteroid release, skin conductance, arousal, and vigilance (Davis & Whalen, 2001), while Ce projections to the periaqueductal grey and cranial nerve nuclei are behind well-established freezing and escape behaviors in classical fear conditioning experiments (Davis & Whalen, 2001; LeDoux, 2012; Macedo et al., 2007; Phelps & LeDoux, 2005). The Co nucleus is oftentimes viewed as a secondary olfactory structure (Doty,

2012), involved in olfactory memory, feeding-associated behaviors, and pheromone-driven sexual response (Yilmazer-Hanke, 2012).

Functional properties of the AG subnuclei are rarely studied in humans because standard fMRI acquisitions and analysis pipelines do not attain sufficient spatial resolution for reliable separation of the AG subnuclei from each other. According to post-mortem histological measurements, the centromedial (CeM) AG is smaller than 150 mm^3 (Brabec et al., 2010; Garcia-Amado & Prensa, 2012), translating to less than 9 voxels on fMRI with standard 16–64 mm^3 voxels. The resolution limitations are even more pronounced after applying spatial normalization since manipulating individual subjects' MRIs into template space can introduce substantial distortions and inaccuracies during the deformation process (Yassa & Stark, 2009), errors which are oftentimes corrected by applying large spatial smoothing (6-10 mm FWHM) kernels. Unfortunately, smoothing further reduces the effective spatial resolution of the data, making it even more difficult to study the AG subnuclei function. Because of the aforementioned limitations, several authors have classified AG activations into coarse subdivisions, including dorsal vs. ventral AG (Kim et al., 2004; Morris et al., 2001; Whalen et al., 1998; Whalen et al., 2001), medial vs. lateral AG (Kim et al., 2003; Zald & Pardo, 2002), and anterior vs. posterior AG (Gottfried et al., 2002; Morris et al., 2002; Wang et al., 2008).

The potential value of studying the AG subnuclei function separately from each other is suggested by behavioural studies on patients suffering from a rare genetic condition called Urbach-Wiethe disease (UWD), which can lead to a progressive calcification of the AG complex in otherwise cognitively and neurologically healthy adults. Patients with focal lesions of the BLA AG display reduced fear conditioning (Klumpers et al., 2014), fear hypervigilance (Terburg et al., 2012), and extreme generosity (van Honk et al., 2013). Such behavioral/cognition effects are contrasted by observations in a UWD patient with bilateral calcification of the entire AG (Adolphs et al., 1994, 1995). This patient is incapable of recognizing fear in facial expressions, a pattern that is seemingly at odds with reports of hypervigilance in patients with BLA-specific calcifications.

Although a few research groups acquired high-resolution (2-mm isotropic or smaller voxels) fMRI data to study the AG subnuclei activity in fear conditioning (Bach et al., 2011; Boll et al., 2013), processing of emotional facial expressions (Boll et al., 2011; Gamer et al., 2010), appetitive conditioning (Prévost et al., 2013), instrumental learning (Prévost et al., 2012), reward-seeking (Prévost et al., 2011, 2013), and punishment avoidance (Prévost et al., 2011), little is known about

human AG subnuclei function in other contexts. Furthermore, no human imaging studies examined intra-AG functional connectivity patterns to determine whether intra-AG connectivity in humans is consistent with non-human studies. The basolateral AG is significantly larger in humans than in rodents, even though most knowledge of the AG circuitry arises from rodent studies. In rodents, the BLA complex represents 28% of the total AG volume, while that number rises to 69% in humans (Chareyron et al., 2011). The implications of this evolutionary BLA enlargement on AG function are poorly understood.

In summary, novel approaches for studying the AG are required to understand this structure's role in cognition. Consequently, the first aim of my thesis was to leverage the full power of high-resolution structural and functional imaging at 4.7 T to understand how human AG processes negative vs. neutral visual stimuli. Because of the AG involvement in depression, anxiety, schizophrenia, and autism (LeDoux, 2007; Otte et al., 2016), developing techniques for studying the AG subnuclei function *in vivo* is valuable not only for understanding AG function in healthy individuals but also for learning how various AG subnuclei relate to psychiatric disorders.

1.6 Hippocampal Subfields and Subregions

The hippocampus (HC) is a seahorse-shaped medial temporal structure located immediately posterior to the AG (Fig. 1.4). Indeed *hippocampus* is a Latin word for seahorse. The structure has been a major source of scientific interest since the middle of the 20th century, beginning with the seminal publication by Scoville & Milner (1957), who reported severe memory deficits in patient HM following bilateral medial temporal lobectomy. Since then, many human and animal studies confirmed the HC role in episodic memory (for reviews, see Cohen et al., 1999; Lisman et al., 2017; Moscovitch et al., 2005, 2016; Squire et al., 2015). In human neuroimaging studies, HC activity was reported during both explicit and incidental learning (Azab et al., 2014; Bakker et al., 2008; Cohen et al., 1999; Lacy et al., 2011; Ranganath et al., 2004) with a wide variety of stimuli, covering a broad set of cognitive and perceptual domains: words, objects, tones, scenes, faces, and spatial routes and landmarks (for an overview, see Cohen et al., 1999; Lisman et al., 2017).

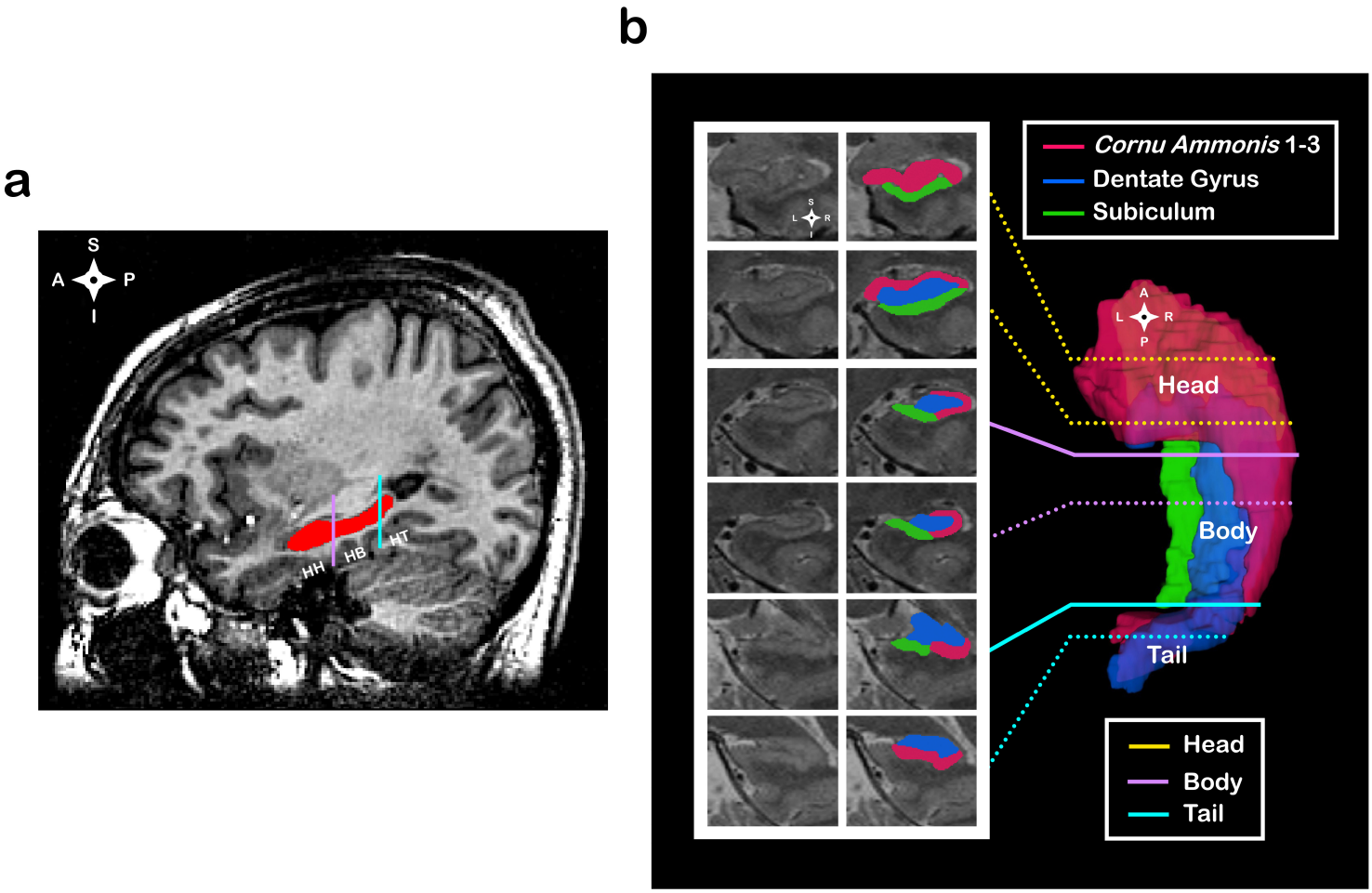

Fig. 1.4. (a) Human hippocampus is segmented in red on a T_1-weighted anatomical scan. Abbreviations: HH, hippocampal head; HB, hippocampal body; HT, hippocampal tail. The magenta line demarcates the most anterior slice of the hippocampal body; cyan line demarcates the most anterior slice of the hippocampal tail. (b) Segmented hippocampal subfields on an ultra-high-resolution T_2 MRI scan. A 3D model of the hippocampal formation and each of its subfields and subregions is shown on the right. Solid lines represent head/body and body/tail transition areas as in panel (a).

In their attempts to develop a more accurate understanding of the HC function, researchers are beginning to appreciate the complexities of its internal anatomy. From front to back, the HC can be subdivided into three anatomically defined anterior-posterior segments or subregions: head, body, and tail (Fig. 1.4) (Duvernoy, 2005; Malykhin et al., 2007; Rajah et al., 2010). A number of studies demonstrated that the posterior (body together with tail) HC is particularly active during spatial memory tasks, while the anterior (mostly head) HC is activated by memory tasks with an emotional component (Bannerman et al., 2004; Dolcos et al., 2004; Kensinger & Corkin, 2004; Kensinger, 2009; Strange et al., 2014; Poppenk & Moscovitch, 2011). It has also been suggested

that the anterior HC is linked to coarse gist-like memory, while the posterior HC is critical for detailed episodic memory (Bonne et al., 2008; Hayes et al., 2011; Poppenk & Moscovitch, 2011; Poppenk et al., 2008, 2013), while others showed that the anterior HC is specialized for memory encoding, and the posterior HC is preferentially engaged during memory retrieval (Kim, 2015; Lepage et al., 1998; Schacter & Wagner, 1999; Spaniol et al., 2009; de Vanssay-Maigne et al., 2011; Woollett & Maguire, 2012; Woollett et al., 2009). Although many fMRI studies split the HC into anterior and posterior segmenting, binary long-axis grouping might lead to oversimplified models of the HC function (Small, 2002; Strange et al., 2014): some recent structural and functional imaging studies indicate that each of the HC anterior-posterior subregions has distinct implications for memory (Chen et al., 2010; DeMaster et al., 2014; Evensmoen et al., 2013; Spalletta et al., 2016; Travis et al., 2014; de Vanssay-Maigne et al., 2011). Consequently, separating the HC body from the HC tail may provide additional information about how each of those long-axis subregions contributes to memory.

In addition to the anterior-posterior differences in HC function, recent advances in fMRI methodology made it possible to study functional features of the HC transverse axis, namely the *Cornu Ammonis* 1-3 (CA1-3), dentate gyrus (DG), and subiculum (Sub) subfields (Fig. 1.4b) (Aly & Turk-Browne, 2016; Azab et al., 2014; Bakker et al., 2008; Berron et al., 2016; Bonnici et al., 2012; Copara et al., 2014; Duncan et al., 2012; Eldridge et al., 2005; Lacy et al., 2011; Reagh et al., 2014; Stokes et al., 2015; Suthana et al., 2009, 2011, 2015; Tompary et al., 2016; Yassa & Stark, 2011; Zeineh et al., 2003). Most models of the HC role in memory emphasize sequential encoding by the trisynaptic circuit: from the entorhinal cortex to the DG, then via the CA3 to the CA1, with final outputs to the Sub, entorhinal cortex (EC) and parahippocampal areas; however, new memories can also be encoded in the CA1 subfield through direct projections from the EC to the CA1, and CA2 subfields (Jones & McHugh, 2011).

Both animal and computational literature (Hasselmo et al., 1995; Lisman & Grace, 2005; Meeter et al., 2004; Norman & O'Reilly, 2003; Vinogradova, 2001) suggest that the HC is a dynamic task-sensitive system, continuously switching between integration and discrimination states. Substantial efforts have been made at experimental validation of such models in human participants, mainly using pattern separation (encoding of novel memories) and pattern completion (retrieval of previously encoded stimuli from partial cues) tasks (Bakker et al., 2008; Duncan et al., 2012; Lacy et al., 2011; Yassa & Stark, 2011). Patient studies and high-resolution fMRI

experiments support the DG (or DG/CA3) role in pattern separation and CA1 in pattern completion (Azab et al., 2014; Baker et al., 2016; Bakker et al., 2008; Berron et al., 2016; Duncan et al., 2012; Lacy et al., 2011). The main limitation of most pattern separation/completion studies is their reliance on incidental learning tasks that use varying amounts of stimulus similarity to bias the HC circuitry towards one state or another.

Although some studies examined the HC subfields' role in memory using explicit memory tasks (e.g., Chen et al., 2011; Eldridge et al., 2005; Suthana et al., 2009, 2011, 2015; Zeineh et al., 2003), because of technical limitations at lower magnetic fields, many of those studies did not segment subfields within the entirety of the HC head (Chen et al., 2011; Eldridge et al., 2005; Nauer et al., 2015; Suthana et al., 2009, 2011; Zeineh et al., 2003) or tail (Chen et al., 2011; Eldridge et al., 2005; Zeineh et al., 2003), producing activity measurements heavily dominated by the signal from the HC body. Consequently, how various subfields within each long-axis segment contribute to episodic memory is largely unexplored.

Furthermore, there is a lack of consensus in the HC literature as to whether the HC is dedicated to the processing of spatial vs. non-spatial information in episodic memory (Eichenbaum, 2017; Eichenbaum & Cohen, 2014; Kumaran & Maguire, 2005; Lisman et al., 2017; Nadel et al., 2012), and whether the HC is involved in item-memory, not just relation-memory (Davachi et al., 2003; Gold et al., 2006; Konkel et al., 2008). For example, Kumaran & Maguire (2005) reported that the HC BOLD activity was correlated with spatial-relational, but not social-relational memory. The authors also reported that neither spatial nor relational processing on its own was sufficient to activate the HC, and combining the two factors was vital for the HC engagement. Another research group (Ryan et al., 2010) differentiated spatial from non-spatial relations during memory retrieval. Retrieving spatial relations engaged the HC to a greater degree than retrieving non-spatial relations, while no voxels showed the opposite pattern (non-spatial > spatial). In contrast, a study by Konkel et al. (2008) demonstrated that amnesic patients, with HC-specific damage, were impaired not only on all tests of relational memory, including spatial, associative, and sequential but also on tests of item memory, although the performance on the former was more affected than the performance on the latter (Konkel et al., 2008).

How different subfields within various long-axis segments contribute to memory formation and memory retrieval is largely unexplored. In a previous structural MRI study (Travis et al., 2014), we showed that performance on the 'Designs' subtest of the Wechsler Memory Scale (WMS-IV;

Pearson Education Inc., 2009) was correlated with volumes of the posterior CA1-3 and DG subfields. This particular subtest was designed to test the behavioral performance for item, spatial, and item-location associative memories. However, volumetric measurements are indirect links to brain function and thus cannot fully explain how processes underlying formation and retrieval of item, spatial, and associative memories (assessed by this task) relate to neuronal activity within various HC segments. For that, more direct measurements of metabolic demand are required. Consequently, the main goal of my second experiment was to determine whether the anterior and posterior HC subfields show differences in activation properties during the formation and retrieval of item, spatial, and associative memories. Similar to studying the AG subnuclei, high-resolution imaging is vital for answering this research question. Because the CA1-3 subfield within the HC body is 1.0 to 1.5 mm thick on most coronal slices (Malykhin et al., 2010), $1.5 \times 1.5 \times 1.5$ mm^3 or smaller voxels are required (as opposed to standard $2.5 \times 2.5 \times 2.5$ or $3.0 \times 3.0 \times 3.0$ mm^3 voxels) to probe task-evoked signal changes in the CA1-3 subfield without contamination concerns from the other subfields.

1.7 Resting-State fMRI

Lin et al. (2010) estimated that task-induced changes in neuronal spiking represent less than 15% of the brain's total energy consumption. Consequently, most of the brain's metabolic demands are a consequence of the intrinsic or so-called resting-state activity (Buckner et al., 2013; Lin et al., 2010; Raichle et al., 2001). Somewhere between 60% and 80% of energy consumption by the human brain supports communication between neurons, implicating substantial background functional activity that exists regardless of whether one is engaged in a cognitive task or not (Raichle & Mintun, 2006). Presumably, this intrinsic activity is integral to normal brain function and represents vital neurobiological processing as well as internally oriented thoughts (Andrews-Hanna et al., 2014; Christoff et al., 2016; Raichle & Snyder, 2007; Raichle, 2015). Even though functional links between the brain's baseline metabolic activity and cognition are not fully understood, resting-state fMRI data can be used to study functional features of various brain systems without a need for an explicit task (Buckner et al., 2013).

The brain's functional connectome can be inferred from spontaneous low-frequency (< 0.1 Hz) BOLD signal fluctuations, recorded during a resting-state fMRI scan in which a subject

passively rests inside an MRI scanner with eyes either open or closed (Buckner et al., 2013; Craddock et al., 2013; Smith et al., 2011; Wig, 2017; Wig et al., 2014). Subsequently, data-driven analytic techniques (e.g., clustering, independent component analysis, boundary mapping) are used to reconstruct the brain's functional architecture (Beckmann, et al., 2005; Calhoun et al., 2001; Power et al., 2011; Smith et al., 2011; Wig et al., 2014; Yeo et al., 2011).

Most functional connectivity (FC) studies report 7 to 20 resting-state networks (RSNs) with network topography belonging to the visual, somatosensory, motor, or cognitive (i.e., spontaneous thought, memory, attention) regions of the brain (Allen et al., 2011; Andrews-Hanna, 2012; Christoff et al., 2016; Gordon et al., 2017; Laumann et al., 2015; Petersen & Posner, 2012; Power et al., 2011; Raichle & Snyder, 2007; Smith et al., 2009; Wig, 2017; Yeo et al., 2011, 2014; Zonneveld et al., 2019). It is thought that resting-state networks (RSNs) detected by FC-MRI (Fig. 1.5) capture fundamental units of brain organization, which are recruited in various combinations to perform cognitive and sensorimotor functions (Buckner et al., 2013). Since stronger MRI field strength leads to improved BOLD response sensitivity (De Martino et al., 2018; Pohmann et al., 2016; Ugurbil, 2016), simulations studies suggest greater accuracy/detail of network features on high-field data (Allen et al., 2012).

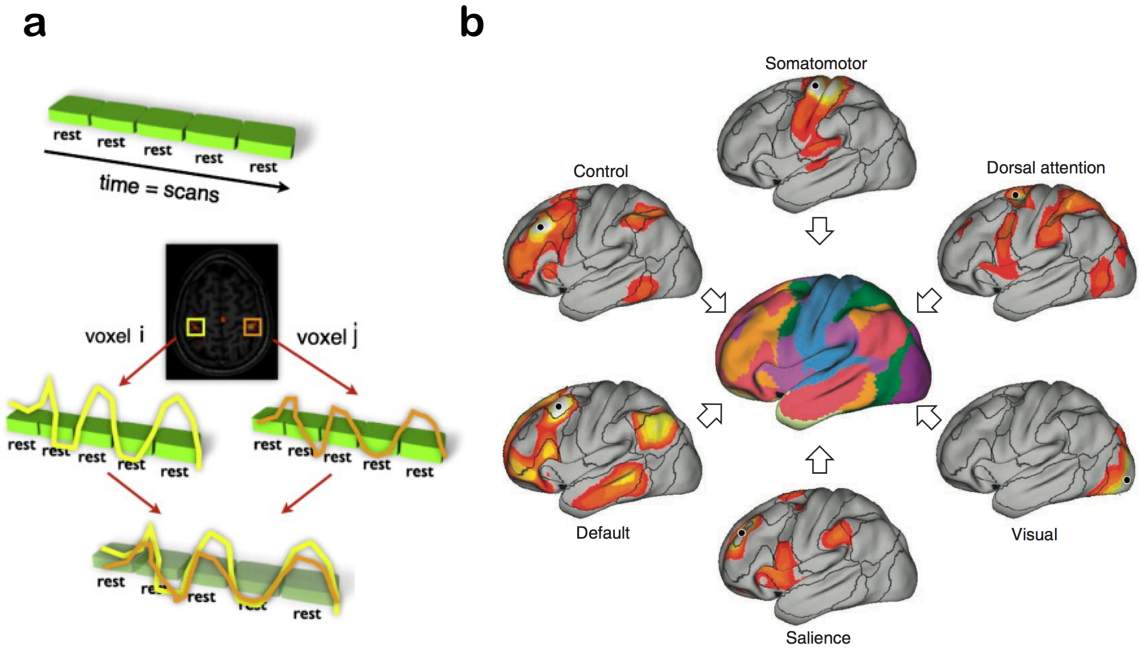

Fig. 1.5. (a) Functional connectivity studies investigate the BOLD time series synchronicity, largely using resting-state scans (figure adapted from van den Heuvel & Hulshoff Pol, 2010). (b) 7 commonly identified resting-state networks (figure adapted from Buckner, 2013). Peripheral maps represent patterns obtained using Pearson correlation coefficients: colored areas represent regions of the brain statistically associated with a seed (represented by a black circle) region. The central map depicts the brain's community structure obtained using a winner-takes-all clustering algorithm (Yeo et al., 2011).

1.8 Aging Brain

It is well established that human cognitive capacity declines in advanced age (Buckner, 2004; Grady, 2008, 2012; Fabiani, 2012; Hedden & Gabrieli, 2004; Reuter-Lorenz & Cappell, 2008; Schneider-Garces et al., 2010; Spreng et al., 2010). Fluid intelligence, working memory, selective attention, and processing speed progressively decline throughout the lifespan, starting in early adulthood (Salthouse, 2012; Hanna-Pladdy & Gajewski, 2012; Fabiani, 2012). Even face-based recognition of such basic emotions as happiness, fear, surprise, and sadness is compromised in older individuals (Suzuki & Akiyama, 2012). Yet language proficiency and crystallized intelligence, which primarily rely on lifelong cultural awareness and knowledge, remain fairly intact and, in some cases, even improve with aging (Hafkemeijer et al., 2012). It is thought that by studying alterations in brain function, it will be possible to understand age effects on human cognition (Buckner, 2004; Grady, 2008, 2012; Li et al., 2015; Reuter-Lorenz & Cappell, 2008; Sala-Llonch et al., 2015; Sperling, 2007; Spreng et al., 2010; Sugiura, 2016; Wig, 2017).

The brain undergoes numerous structural alterations as a part of the healthy aging process (Raz & Rodrigue, 2006). Studies in rats and monkeys report that old animals have 30-40% fewer dendritic spines compared to their younger counterparts (Duan et al., 2003; Page et al., 2002), while human post-mortem and *in vivo* imaging studies report that aging is associated with thinning of the cerebral cortex, a substantial increase in the CSF volume, and gradual sulcal expansion (Michielse et al., 2010; Lebel et al., 2012; Raz & Rodrigue, 2006). Most structural imaging studies showed that multimodal association cortices show the greatest cortical thinning, with frontal lobes being particularly vulnerable to age-related atrophy (Allen et al., 2005; Raz et al., 2005, 2010; Raz & Rodrigue, 2006; Resnick et al., 2003). Despite these large-scale effects, there is little, if any, neuronal loss occurring in older adults' cerebral cortex (Peters et al., 1998; Morrison & Hof, 2007). Instead, both human and animal post-mortem studies suggest a loss of neuropil, including a loss of synapses and dendritic spines, as the cause of the apparent cortical thinning with age (for a detailed review see, Morrison & Baxter, 2012). Unlike frontal regions, the medial temporal structures display no volumetric differences between age groups until late middle adulthood (Aghamohammadi-Sereshki et al., 2019; Malykhin et al., 2017; Raz et al., 2010). This is in contrast to the dramatic HC atrophy in patients with Alzheimer's disease (Buckner 2004; Jeon et al., 2012). From such studies, it is clear that age effects on the cortical and subcortical grey matter are not

uniform and that the rate of tissue atrophy is may increase with age. However, the full effects of these volumetric trends on cognitive capacity might be masked by neurobiological compensatory mechanisms (Fabiani, 2012; Reuter-Lorenz & Cappell, 2008), and only studies of brain function can detect those effects (Buckner et al., 2013; Grady, 2008, 2012; Fabiani, 2012; Reuter-Lorenz & Cappell, 2008).

Most of the early fMRI studies on the relationship between brain function and age were task-based (Cabeza et al., 2002, 2004; Grady et al., 1994; D'Esposito et al., 1999; Fabiani et al., 2014; Gutchess et al., 2005; Hesselmann et al., 2001; Hutchinson et al., 2002; Levine et al., 2000; Logan et al., 2002; Madden et al., 1996; Park et al., 2003, 2004; West et al., 2019). Early studies, which investigated the relationship between resting-state functional connectivity and age, focused on intra-network communication within the default mode system (e.g., Andrews-Hanna et al., 2007; Damoiseaux et al., 2008; Grady et al., 2012; Hampson et al., 2012; Koch et al., 2010; Onoda et al., 2012; Persson et al., 2014; Sambataro et al., 2010). Those studies revealed an age-related loss of functional integration between the medial frontal and the posterior cingulate/retrosplenial cortices (but see, Persson et al., 2014). More recent FC-MRI studies showed that in addition to the default mode network, age-related reduction in intra-network connectivity is also present in brain networks that are involved in attention, cognitive control, sensory processing, and motor function (Allen et al., 2011; Betzel et al., 2014; Grady et al., 2016; Ng et al., 2016; Song et al., 2014; Spreng et al., 2016; Zonneveld et al., 2019). Research that employed graph theory to quantify age effects on FC showed that network community structure becomes less efficient and less segregated with age (Cao et al., 2014; Chan et al., 2014; Chong et al., 2019; Geerligs et al., 2015; Spreng et al., 2016), and it is thought that long-range FC is particularly vulnerable to aging (Tomasi & Volkow, 2012).

Despite this progress, the number of studies that investigated age-related functional reorganization at the brain-wide level is still relatively small, and most defined their network sources based on probabilistic anatomical atlases or functional parcellations from unrepresentative samples of young adults (Betzel et al., 2014; Chan et al., 2014; Chong et al., 2019; Fjell et al., 2015; Geerligs et al., 2015; Meunier et al., 2009; Song et al., 2014; Wang et al., 2010). Employing ROIs from a predefined atlas may fail to capture individual variability in the functional organization since individual network architecture can deviate, sometimes substantially, from an average map (Gordon et al., 2017; Laumann et al., 2015; Mueller et al., 2013). Furthermore, most prior studies of age effects on FC used correlational methods to quantify age differences (Andrews-Hanna et al., 2007;

Betzel et al., 2014; Geerligs et al., 2015; Grady et al., 2016; Han et al., 2018; Meier et al., 2012; Rubinov & Sporns, 2010; Zonneveld et al., 2019). However, correlation is an ambiguous tool for quantifying network structure, since, in addition to BOLD signal coherence over time (a true measure of functional coupling), two other factors are responsible for correlations in all RS-fMRI data: network amplitude and magnitude of background noise (Duff et al., 2018).

Consequently, the main focus of my third experiment was to investigate the relationship between age effects on every major RSN measure: network topography, network activation amplitude, and inter-network communication. Taken together, these measures can link previous task-based aging studies with resting-state work, providing a comprehensive overview of brain aging. Relative to 3 T fMRI, relying on 4.7 T acquisition enables more detailed network parcellations, primarily due to higher BOLD CNR.

Chapter 2: Obectives & Hypotheses

Objectives

1. Develop approaches for studying brain function on a 4.7 T MRI system. Apply those techniques to investigate the functional properties of the AG subnuclei *in vivo*.
2. Develop an fMRI task and analysis methodology for studying functional specialization of the anterior and posterior HC subfields using 4.7 T MRI.
3. Develop approaches for studying the brain's functional architecture using 4.7 T scans. Apply those methods for studying age effects on brain organization.

Experiments

For *Experiment 1*, addressing *Ojective 1*, we made the following hypotheses:

- We hypothesized that the nuclei of the dorsal AG would be more sensitive to aversive visual stimuli than to neutral visual stimuli because the CeM AG acts as the major control center of physiological and behavioural responses to information with emotional content.
- We also hypothesized that CeM ↔ LA functional connectivity will be weaker than CeM ↔ BA or LA ↔ BA functional connectivity, consistent with non-human work on intra-AG connectivity.

For *Experiment 2*, addressing *Objective 2*, we made the following hypotheses:

- We hypothesized preferential engagement of the anterior/posterior HC during memory encoding/retrieval, respectively.
- We expected to observe increasing activity along the longitudinal axis of the hippocampus from anterior to posterior during spatial memory performance, consistent with previous studies (Maguire et al., 2000, 2003; Woollett et al., 2009; Woollett & Maguire, 2011).
- Based on our previous observation that volumes of the posterior DG and CA1-3 subfields of the HC were particularly strongly correlated to visual-spatial memory in the Designs subtest of the WMS-IV (Travis et al., 2014), we predicted greater functional engagement of the CA1-3 and DG, compared to the Sub, in an fMRI adaptation of the Designs task.

For *Experiment 3*, addressing *Objective 3*, we hypothesized the following:

- Given previous reports of age-related reduction in fMRI signal amplitude during task-based neuroimaging studies, we expected to see a widespread reduction of BOLD amplitude throughout life.
- Because gradient-based network parcellation schemes revealed age-invariance in brain network structure (Han et al., 2018), we expected to see small age differences in a functional organization, potentially restricted to the default mode network, which was shown to have weaker integration in old age (Andrews-Hanna et al., 2007).
- Given structural aging patterns, which consistently show greater volumetric atrophy in frontal and parietal association cortices than in sensorimotor areas (Resnick et a., 2003; Raz et al., 2005, 2010), we predicted that brain networks localized to frontal and parietal association areas would be more vulnerable to aging than sensorimotor regions of the cortex.

Experiments

Chapter 3: Amygdala Subnuclei Response and Connectivity During Emotional Processing.

3.1. Introduction

The amygdala (AG) is a fundamental structure involved in the neural circuits of fear and reward learning, as well as aggressive, sexual, maternal, and feeding behaviors (Janak & Tye, 2015; LeDoux, 2012; LeDoux & Schiller, 2009). Through extensive interactions with cortical and various subcortical areas, the AG also modulates attention and perception (Adolphs et al., 2005; Pitkänen et al., 2000; Sah et al., 2003). Of particular interest is the AG's involvement in processing of emotionally relevant stimuli and encoding of emotionally salient memories (Dolcos et al., 2004; Kensinger, 2009; LeDoux and Schiller, 2009; Murty et al., 2010; Sergerie et al., 2008; Shafer et al., 2012; Shafer and Dolcos, 2012).

To gain a better understanding of the functional role of the AG, it is important to acknowledge that the AG is not a homogenous structure and thus it is crucial to differentiate response properties of the AG subnuclei (LeDoux, 2000, 2012; Sah et al., 2003). Human and animal studies have demonstrated that the AG is a gray matter complex, composed of at least thirteen distinct nuclei (Brabec et al., 2010; Janak & Tye, 2015; LeDoux, 2012; Sah et al., 2003; Whalen et al., 2009). These are generally grouped into two major subdivisions: basolateral and centrocorticomedial (Johnston, 1923; LeDoux & Schiller, 2009). The lateral (LA), basal (B), and accessory basal (AB) nuclei constitute the basolateral (BLA) complex, while the cortical (Co), medial (M), and central (Ce) nuclei belong to the centrocorticomedial group.

For over fifty years, the AG has been thought to be fundamental to processing of emotions (Weiskrantz, 1956), with much of the non-human research utilizing Pavlovian conditioning procedures, a form of emotional learning in which a biologically irrelevant stimulus starts to elicit defensive behaviors, and physiological responses when associated with an aversive or threatening event (Davis & Whalen, 2001; LeDoux, 2000, 2012; Phelps & LeDoux, 2005). Animal fear conditioning experiments demonstrated that the nuclei of the AG play unique roles in this form of learning (LeDoux, 2012; Macedo et al., 2007; Phelps & LeDoux, 2005).

Human fMRI and patient studies proved that the human AG is also involved in fear conditioning (Bach et al., 2011; Büchel et al., 1998; Klumpers et al., 2014; LaBar et al., 1998;

Phelps et al., 2004). Furthermore, recent studies of patients with Urbach-Wiethe disease (UWD) support the notion of functional specialization of the AG subnuclei. For instance, focal lesions of the BLA AG result in reduced fear conditioning (Klumpers et al., 2014), unregulated fear hypervigilance (Terburg et al., 2012), and extreme generosity (van Honk et al., 2013). This is in contrast to studies of a UWD patient with bilateral loss of the entire AG, who is incapable of recognizing fear in facial expressions (Adolphs et al., 1994, 1995). Despite these advances in our understanding of the human AG, it is still poorly understood how various AG subnuclei contribute to processing of emotional information in a broader context.

To understand functional significance of the AG subnuclei, it is crucial to understand how neurons within the AG subnuclei interact with each other. In rodent literature, there is a substantial debate between two potential mechanisms of intra-AG communication: validity of the classical serial model is questioned by the proponents of the parallel processing model. The serial model proposes that intra-AG information-processing stream occurs predominantly from the LA nucleus to the BA/AB nuclei, and from the BA/AB nuclei to the Ce nucleus (Duvarci & Paré, 2014; Freese & Amaral, 2009; Pitkänen et al., 1997). However, numerous animal reward learning studies revealed competing functions of the CeM and the BLA AG (for review see, Balleine & Killcross, 2006). Although some attempts have been made to investigate the AG connectivity in humans using fMRI (Grant et al., 2015; Roy et al., 2009), these studies were limited by low spatial resolution in echo planar imaging. Consequently, little is known about how the human AG subnuclei interact with each other.

Although most fMRI acquisition sequences do not provide sufficient spatial resolution to identify individual subnuclei of the AG, several authors have coarsely segregated AG activations into dorsal vs. ventral (Kim et al., 2004; Morris et al., 2001; Whalen et al., 1998; Whalen et al., 2001), medial vs. lateral (Kim et al., 2003; Zald & Pardo, 2002), and anterior vs. posterior (Gottfried et al., 2002; Morris et al., 2002; Wang et al., 2008) subdivisions. More recent human fMRI studies, with coronal plane resolution of 4-mm^2 or less, and a total voxel volume of 8-mm^3 or less, attempted to localize intra-AG activations more precisely (see Table 3.1). Most of these studies employed image-processing pipelines, which relied on normalizing participants' MR images to a common template space (i.e., MNI or Talairach). Unfortunately, recent evidence indicates that such procedures detect not only hemodynamic changes within the AG, but are also substantially influenced by activations in more distal brain regions (see Boubela et al., 2015). Furthermore, there

are substantial variations in methodology used to localize intra-AG activations. Generally, two main references have been used: Mai et al. (1997)/Mai et al. (2008) anatomical atlas (Bach et al., 2011; Boll et al., 2011, 2013; Gamer et al., 2010; Prévost et al., 2011, 2012, 2013) or Amunts et al. (2005) probabilistic atlas of the human AG subnuclei (Ball et al., 2007, 2009; Frühholz and Grandjean, 2013; Grant et al., 2015; Roy et al., 2009; Styalidis et al., 2014).

Because of substantial methodological differences between human and animal studies of the AG, there is a notable discrepancy between our knowledge of the AG subnuclei's functions in humans and animals. To bridge this gap, we defined human emotion as a psychological response driven by neurophysiological survival and reinforcement circuits (see LeDoux, 2012, 2014, for comprehensive reviews), and relied on the framework established by the core-affect model (Russell, 1980, 2003) to elicit AG responses. The core affect theory proposes that, at a fundamental level, emotional information is interpreted as a blend of two independent dimensions — pleasantness and intensity (Bradley & Lang, 1994; Russell, 1980, 2003). These dimensions are consistent across cultures, and can be used to describe an individual's affective response to verbal and non-verbal stimuli, facial expressions, sounds, body postures, and odors (e.g., Bradley & Lang, 1994; Lang et al., 1998; Russell, 1980, 2003). In combination with other factors, such as context, cultural experience, and genetic makeup, arousal and valence dimensions contribute to the human experience of feelings (Barret, 2006; Russell, 2003).

The primary goal of this study was to investigate sensitivity of the human AG subnuclei to high arousing negative emotion. Our secondary goal was to understand how the human AG subnuclei might function at the network level. To answer these questions we acquired high-resolution structural and functional MRI data at a high field, and manually subdivided each participant's AG into 3 subnuclei groups. To improve accuracy and validity of our BOLD response measurements, we used a two-parameter hemodynamic response function in the fMRI analysis procedure, which allowed not only the response amplitude, but also the response timing (delay to peak) to explain the effects of emotional processing on the AG subnuclei groups. To answer our secondary research question, we examined intra-AG functional connectivity by assessing relationships between the subnuclei group time courses.

Table 3.1
Recent high-resolution fMRI studies of the amygdala subnuclei (AG, amygdala; CeM, centromedial group; BLA, basolateral group; LB, laterobasal group).

Study	Resolution (mm^3)	Stimuli	Other Methodological Details	Summary of Results	ROI vs. Localization
Bach et al. (2011)	1.5×1.5×1.5	electric shocks	N/A	BLA group and centrocortical AG have similar sensitivity profiles in fear conditioning	ROI [d]
Boll et al. (2011)	1.5×1.5×1.5	angry and fearful faces	Manipulated context as self vs. other as cause of facial expression	AB nucleus responded to facial expression in general, regardless of the stimulus context; context-dependent threat evaluation was localized to the corticomedial AG	Cluster [a]
Boll et al. (2013)	1.5×1.5×1.5	electric shocks	Employed Pavlovian conditioning procedure with cue reversal	Corticomedial activity was positively correlated with outcome uncertainty; BLA activity was correlated with outcome certainty	Cluster [b]
Gamer et al. (2010)	2.0×2.0×2.0	happy, neutral, and fearful faces	Administering oxytocin or placebo	Oxytocin reduced sensitivity of dorsal and lateral AG to fearful faces, while enhancing sensitivity to happy faces	Cluster [a]
Frühholz and Grandjean (2013)	1.5×1.5×2.4	nonwords spoken in angry or neutral tone	N/A	Superficial complex and the LB complex were sensitive to emotional tone; activity was modulated by attentional focus and proximal temporal context	Cluster [c]
Prévost et al. (2011)	1.58×1.63×2.5	monetary outcomes	Manipulated context as reward, punishment, or neutral in a choice task	BLA showed greater activation for successful attainment of reward; CeM showed greater activation for successful avoidance of punishments	Cluster within anatomically defined ROIs [b]
Prévost et al. (2012)	1.8×1.8×1.8	food images and rewards	General vs. specific Pavlovian-to-instrumental transfer (PIT)	Activity in CeM correlated with general PIT across participants; BLA correlated with specific PIT	Cluster within anatomically defined ROIs [b]
Prévost et al. (2013)	1.58×1.63×2.5	Pleasant, neutral, and unpleasant liquids	Appetitive vs. aversive Pavlovian learning	Investigated model-based learning in the amygdala: expected value signals in BLA correlated with in appetitive learning, while expected value signals in CeM activity correlated with aversive learning; precision signals in CeM correlated with precision signals in both types of learning	Cluster within anatomically defined ROIs [b]

[a] Mai et al. (1997) atlas [b] Mai et al. (2008) atlas [c] Amunts et al. (2005) atlas [d] Data driven (structural connectivity-based)

3.2. Materials and Methods

Participants

A total of 28 right-handed healthy volunteers were recruited through online, newspaper, and poster advertisements. Healthy volunteers had no lifetime psychiatric disorders and no reported psychosis or mood disorders in first-degree relatives, as assessed by the Anxiety Disorders Interview Schedule-IV (Brown et al., 2001; Di Nardo et al., 1994), which provides detailed assessment of several anxiety disorders, affective disorders, and substance use disorders. The project's participants had no history of medical, neurological disorders, and had no prior exposure to the stimuli used in the fMRI paradigm. Medical exclusion criteria were defined as those active and inactive medical conditions that may interfere with normal cognitive function: cerebrovascular pathology, all tumors or congenital malformations of the nervous system, diabetes, multiple sclerosis, Parkinson's disease, epilepsy, dementia, organic psychosis (other than dementia), schizophrenia, and stroke. Drugs that directly affect cognition, including alcohol, anti-cholinergic medications, benzodiazepines, antipsychotics, and antidepressants were also exclusionary. Written, informed consent was obtained from each participant. Imaging data from three participants was excluded from analyses due to excessive head motion, reducing the sample size to 25 individuals (12 females) with mean age of 27.6 years (19–46, SD = 6.2). This study was approved by the University of Alberta Health Research Ethics Board.

Stimuli

Pictures were selected from the International Affective Picture System (IAPS; Lang et al., 2008) database based on normative ratings for valence and arousal and were supplemented with in-house pictures used in prior studies (Singhal et al., 2012; Wang et al., 2005, 2008). All pictures contained a central biological presence (predominantly a head/face). The chosen pictures were grouped into four categories (15 pictures/category) based on IAPS normative scores and ratings scores from a preliminary rating study (N = 8). Mean valence/arousal scores (9-point scale, as described below) from the volunteers who participated in the fMRI experiment were as follows: Neutral (Neu: 5.8/1.6), Low Emotional (Low Emo: 3.6/3.3), Medium Emotional (Med Emo: 2.3/5.8), and High Emotional (High Emo: 2.3/6.1). A repeated-measure ANOVA showed that valence ratings for each category were significantly different from each adjacent category except for Med and High Emo (i.e., Neu > Low Emo > Med Emo = High Emo, [$F(3,72) = 132.97$, $p <$

.001, η^2 = .85]). A repeated-measure ANOVA of arousal ratings showed that each category was significantly different from each adjacent category such that, Neu < Low Emo < Medium Emo < High Emo [$F(3,72) = 150.59$, $p < .001$, $\eta^2 = .86$]. Pair-wise comparisons were Holm–Bonferroni-corrected.

Experimental design

Pictures were partitioned across five experimental runs such that three pictures per category were presented in each run. To prevent fatigue, participants received a break between experimental runs. Each picture was presented only once for 2 s and was followed by a response screen for 2 s. The inter-trial interval was randomized on a negative exponential distribution with a median of 8 s, ranging from 6 to 14 s. To attenuate habituation, pictures were presented to participants in a semi-random sequence, such that no more than two pictures of the same category were shown sequentially. As valence and arousal were correlated in our paradigm, participants were instructed to categorize their emotional reactions to each picture on a 4-point scale by pressing one of 4 MR-compatible buttons (1 = 'non-emotional', 4 = 'very emotional'). After the scanning session, participants rated the pictures viewed in the scanner on valence and arousal using the 9-point Self-Assessment Manikin scale (Bradley & Lang, 1994).

Data acquisition

All images were acquired on a 4.7 T Varian Inova MRI scanner at the Peter Allen MR Research Centre (University of Alberta, Edmonton, AB). 370 functional volumes were collected axially (in parallel to the AC–PC line) over 5 runs using a custom-written T_2^*-sensitive Gradient Echo Planar Imaging (EPI) pulse sequence [repetition time (TR): 2000 ms; echo time (TE): 19 ms; flip angle: 90°; field of view (FOV): 168 × 210 mm^2; voxel size: 1.5 × 1.5 × 1.4 mm^3; interslice gap: 0.1 mm; 35 slices; GRAPPA parallel imaging with acceleration factor 2 (Griswold et al., 2002)]. For the AG segmentation and subdivision, high-resolution coronal structural images were acquired perpendicular to the AC–PC orientation using a custom-written T_2-weighted 2D Fast Spin Echo (FSE) sequence [TR: 1100 ms; TE: 39 ms; FOV: 200 × 200 mm^2; voxel size: 0.52 × 0.68 × 1.00 mm^3; 90 slices]. To improve image registration accuracy between the anatomical scans and the functional data, axial high-resolution 2D FSE images were also acquired with coverage closely matching the functional data [TR: 7000 ms; TE: 38 ms; FOV: 210 × 200 mm^2; voxel size: 0.52 × 0.68 × 1.0 mm^3; 45 slices]. A whole brain T_1-weighted 3D Magnetization Prepared Rapid Gradient-

Echo (MPRAGE) sequence [TR: 8.5 ms; TE: 4.5 ms; inversion time: 300 ms; flip angle: 10°; FOV: 256 × 200 × 180 mm^3; voxel size: 1 × 1 × 1 mm^3] was used to acquire anatomical images for automatic tissue segmentation. Fig. 3.1 demonstrates orientation and brain tissue coverage for structural and functional data.

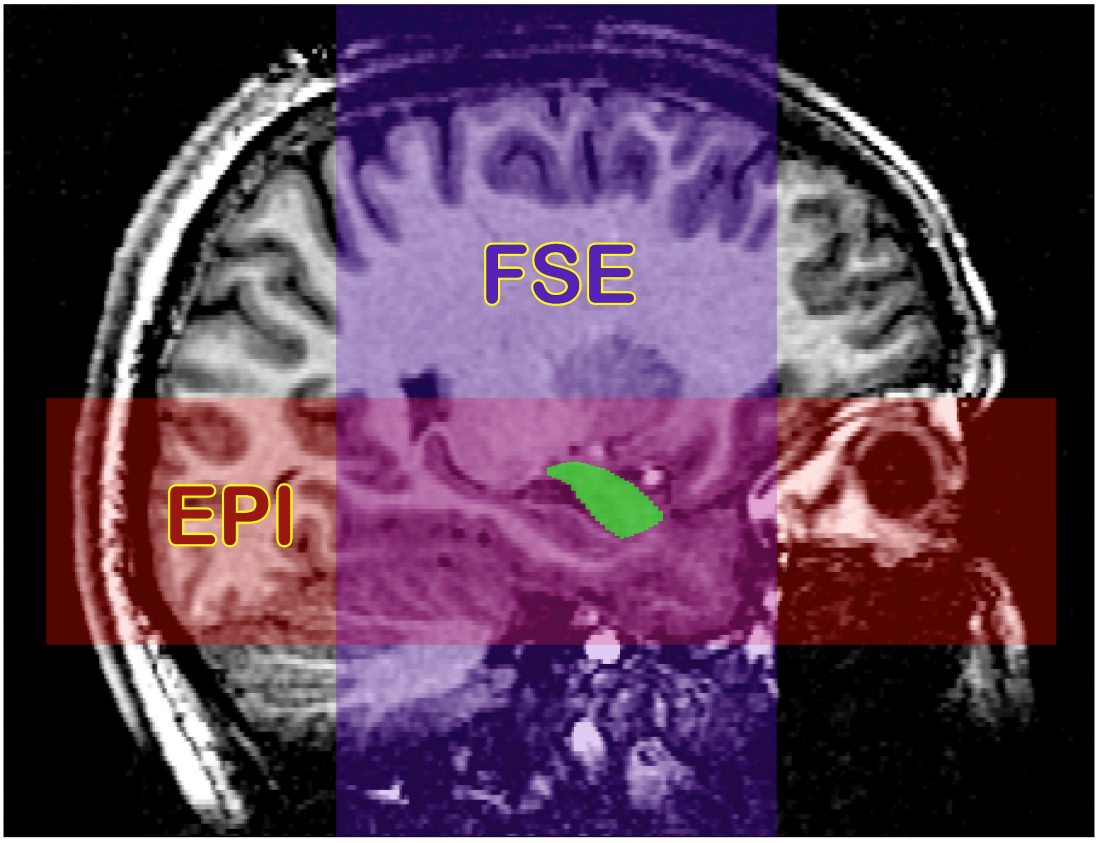

Fig. 3.1. Brain tissue covered by high-resolution anatomical and high-resolution functional scans. Single participant's full-brain T_1-weighted anatomical scan is shown in the background. Violet overlay represents coverage of ultra-high-resolution anatomical 2D FSE scan, which was used for manual amygdala segmentation. Red overlay represents areas captured by high-resolution fMRI EPI acquisition. Segmented amygdala is shown in green.

Amygdala segmentation and subdivision

In agreement with some previous studies (Entis et al., 2012; Prévost et al., 2011), we found that the Amunts et al. (2005) AG map extends beyond the limits of the AG into the MTL white matter suggesting a mismatch between the anatomical location of the AG in our sample, and its location according to the Amunts et al. (2005) atlas. Because of this limitation, and because source localization using probabilistic maps necessitates manipulation of MRI data into standard space, a

process that can produce inaccuracies due to the deformations required (Yassa & Stark, 2009), we used Mai et al. (2008) atlas to manually segment the AG and its subnuclei groups in native space.All AG ROIs were traced with a mouse-driven cursor using the interactive freely available software program Freeview v. 4 (MGH, Boston, MA). The AG was traced on each participant's high-resolution structural scan by the developer of the protocol (NM), who has extensive experience with the method for which a comprehensive description has been previously published (Malykhin et al., 2007). Next, a single rater (AAS) subdivided each AG into three subnuclei groups: (1) the centromedial (CeM) group, consisting of the Ce and the M nuclei; (2) the basal (BA) group, consisting of the B, the AB, and the Co nuclei; and (3) the LA nucleus (Fig. 3.2a–h). Though our intention was to measure BOLD signal from all of the principle AG subnuclei, due to technical limitations of the fMRI acquisition we were able to delineate and measure BOLD signal only from three major subnuclei groups. Many previous studies combined the B, the AB, and the LA nuclei into a single functional unit, the BLA complex; however, Boll et al. (2011) provided evidence that in humans these nuclei might respond differently in certain tasks. Furthermore, animal experiments demonstrated that the LA nucleus and the B/AB nuclei display distinct neurophysiological and connectivity properties (Duvarci & Paré, 2014; Janak and Tye, 2015). For these reasons, we studied the nuclei of the BA group separately from the LA nucleus.

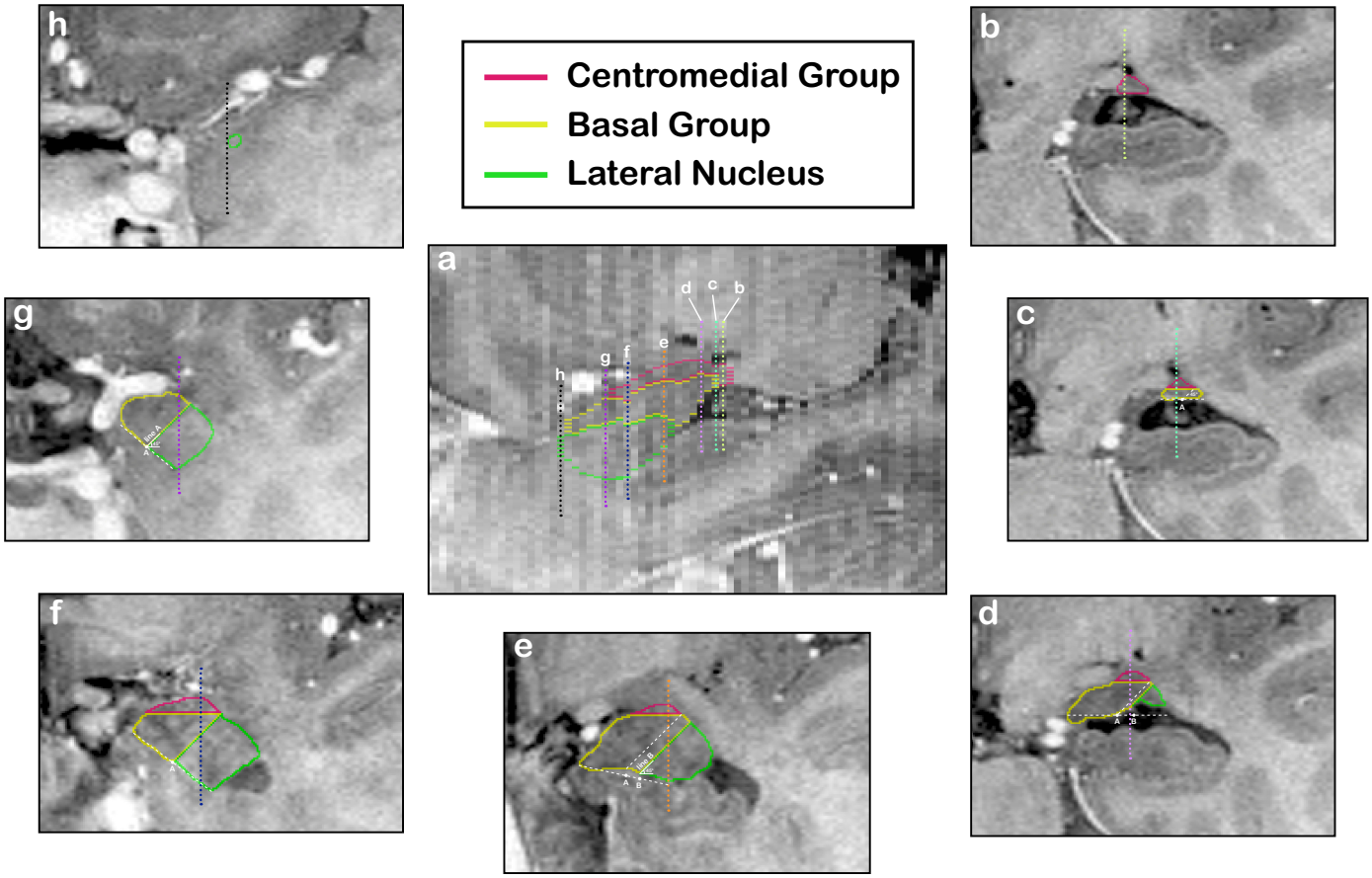

Fig. 3.2. Segmentation of the amygdala into its subnuclei groups is shown on high-resolution T2-weighted structural FSE images with inverted contrast. (a). Sagittal view of the amygdala with references to coronal slices. (b–h). Coronal slices with segmentation protocol for the amygdala subnuclei groups. Panels are organized clockwise to follow the tracing protocol, and flow from the most posterior section of the amygdala (panel b) to the most anterior slice of the amygdala (panel h). Point A, point B, and white dashed lines were used as major landmarks, when delineating the subnuclei groups' boundaries (see text for details).

Since macroscopic delineation of the AG subnuclei requires histological staining, we divided the human AG into subregions corresponding to approximations of the CeM, BA, and LA subnuclei groups. First, we outlined global AG boundaries on sagittal, axial, and coronal planes as was previously described by Malykhin et al. (2007). Our measurements started from the most posterior slice of the AG (Fig. 3.2b), continued through slices where both the AG and the hippocampus were present, and ended at the level of the lateral sulcus closure. Once the total AG boundaries were outlined, only the coronal plane was used to subdivide the AG into subnuclei groups using a single internal landmark line, defined on each coronal slice where the AG is present. This landmark line allowed us to separate the AG into subnuclei groups, approximately matching the intra-AG anatomy described in the Mai et al. (2008) atlas, and a postmortem histological study by Brabec et al. (2010).

First, we delineated the CeM group. Next, the LA nucleus was defined. Subsequently, the remaining AG tissue was assigned to the BA group. Our approach relied on one principle landmark line. Initially, this line is horizontal, and was drawn by connecting the most medial border of the AG with the most lateral border of the AG (Fig. 3.2c,d). As soon as the AG expanded in the inferior-lateral direction, the landmark line was drawn by connecting the most inferior medial border of the AG with the most medial inferior border of the AG (Fig. 3.2e–g). On each slice of the AG, we placed point A exactly in the middle of the landmark line (see Fig. 3.2c–g). On slices, where the hippocampus is present the landmark line was also split into the lateral 1/3 and the medial 2/3 by point B, (see Fig. 3.2d,e). These two points were then used to define two secondary lines. The first line, subsequently called ‘line A,’ began on the AG border, directly above point A, and was drawn at a 45° angle (from the horizontal plane) towards the lateral border of the AG (Fig. 3.2c–g). The second line, subsequently called ‘line B,’ began on the AG border, directly above point B, and was also drawn at a 45° angle (from the horizontal plane) towards the lateral border of the AG (Fig. 3.2d,e).

Measurements of the CeM group started at the first coronal slice, when the AG appears as a small gray matter structure superior to the uncal recess (Malykhin et al., 2007; Fig. 3.2b). The CeM group occupies the entirety of the AG tissue until the AG extends (completely or partially) towards the ambient gyrus (Fig. 3.2b). In subsequent slices, the CeM group occupies only the superior portion of the AG, separated from the BA group by a horizontal line, drawn from the intersection of line A with the lateral border of the AG towards the medial border of the AG (Fig. 3.2c–f). This rule

was used to define the inferior border of the CeM group on all slices anterior to the AG extension towards the ambient gyrus. In general, the last slice of the CeM group was 3 mm (3 slices) anterior to the most anterior slice of the hippocampus (Mai et al., 2008; Fig. 3.2a,g).

The LA nucleus usually starts 2 mm (2 slices) anterior to the AG extension towards the ambient gyrus (Mai et al., 2008; Fig. 3.2d). Since the LA nucleus occupies the inferior-lateral portion of the AG (Fig. 3.2d–g), our goal was to establish its superior-medial border, which separates the LA nucleus from the BA group. Prior to the disappearance of the hippocampus, this was accomplished using line B (Fig. 3.2d,e). When the hippocampus is no longer present, the LA nucleus extends medially and line A was used to define the superior-medial boundary of the LA nucleus.

Once the CeM group and the LA nucleus were demarcated, the remaining AG tissue was assigned to the BA group (Fig. 3.2f). In the most anterior slices, where the CeM group is not present, the AG consists of the BA group and the LA nucleus only (Mai et al., 2008; Fig. 3.2a,g). In the last (i.e. most anterior) slice, all of the AG tissue was assigned to the LA nucleus (Fig. 3.2h). ITK-SNAP (v. 3.2.0; Yushkevich et al., 2006) was used to construct 3D models of these subnuclei groups (Fig. 3.3).

The AG subnuclei group ROIs were resampled to fMRI resolution and manually inspected for overlap with major blood vessels and susceptibility artifacts. ROI voxels corresponding to blood vessels and signal dropouts were excluded from statistical analyses. Average final left/right ROI volumes (and SDs), not corrected for intracranial volumes, and measured in mm^3, were 155.5 (62.9)/125.4 (32.6) for the CeM group; 812.2 (168.2)/806.5 (151.7) for the BA group; 625.3 (134.9)/573.4 (118.8) for the LA nucleus; and 1593.0 (269.0)/1505.3 (243.6) for the total AG. These total AG volumes are consistent with post-mortem histological studies (Brabec et al., 2010), and previously reported in vivo volumetric measurements using structural MRI (Malykhin et al., 2007). Reliability for the total AG and its subnuclei measurements was assessed by retracing the AG from 5 participants (10 AG total) after a one-week delay. Inter/intra-rater reliability intra-class correlations coefficients (ICCs) for the AG subnuclei were 0.90/0.85 for the CeM group, 0.90/0.94 for the LA nucleus, 0.98/0.96 for the BA group, and 0.97/0.95 for the total AG.

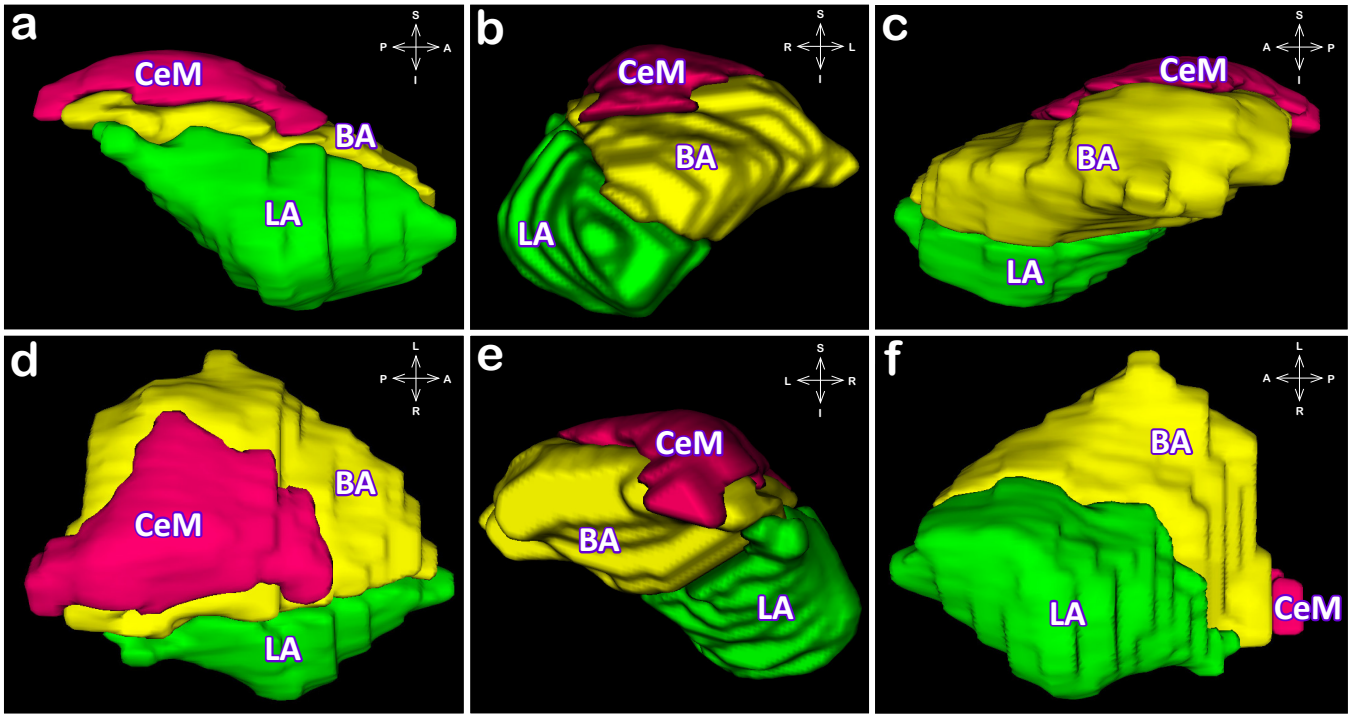

Fig. 3.3. Three-dimensional reconstruction of the amygdala subnuclei groups from a healthy volunteer. (a). Lateral view; (b). anterior view; (c). medial view; (d). superior view; (e). posterior view; (f). inferior view. Abbreviations: CeM, centromedial group; BA, basal group; LA, lateral nucleus.

Image preprocessing

Most of the image processing was performed in SPM8 (Wellcome Trust Centre for Neuroimaging, UCL, UK). Prior to registration, MPRAGE images underwent correction for intensity non-uniformity using N3 (McGill University, Montreal, QC). Due to differences in coverage between three anatomical scans, anatomical images were cropped using ImageJ (NIH, Bethesda, MD) to isolate areas of overlapping coverage. Subsequently, overlapping portions of anatomical images were registered to each other using automated rigid-body transformations.

Next, the first functional volume was registered to the axial FSE image using a combination of manual and automatic registration tools. Functional data was then realigned to the first volume and corrected for slice acquisition delay. Artifact Detection Tool (ART; http://www.nitrc.org/projects/artifact_detect/) was used to identify signal spikes and to account for spin-history-related head-movement artifacts in the fMRI time series. The head-movement threshold was set at 0.5 mm/TR, and signal intensity threshold was set at 3 SDs from the global signal mean. Volumes that exceeded these thresholds were excluded (5 volumes/run, on average). No spatial smoothing was applied to the functional data.

White matter (WM) and cerebrospinal fluid (CSF) masks were thresholded at 0.90 tissue probability and resampled to functional volume coverage and resolution. Voxels classified as WM and CSF were used as signal sources of no interest. As our goal was to account for as much physiological noise as possible without substantially sacrificing statistical power, we extracted the first five principal eigenvariates from the raw WM signal and the first five principle eigenvariates from the raw CSF signal using REX toolbox (http://www.nitrc.org/projects/rex/). Effects of motion were co-varied out of WM and CSF time courses, and the filtered WM and CSF signal eigenvariates were used as regressors of no-interest together with 6 head motion parameters in the General Linear Model (GLM) analysis. In all GLM procedures low frequency signal drifts were removed with a high-pass filter (128 s), and AR1 correction for serial autocorrelation was applied.

To ensure that BOLD sensitivity was consistent across all AG ROIs, we computed temporal signal-to-noise ratio (tSNR) for each AG subnuclei group, averaged across all voxels in each ROI. Left/right tSNR (and SD) for the CeM group were 14.9 (2.1)/16.4 (2.4); 13.7 (2.0)/15.2 (2.1) for the BA group; and 13.6 (1.8)/15.2 (1.7) for the LA nucleus. Thus, the signal profiles were similar for all of the AG subnuclei groups.

General linear model and estimation of response amplitude and delay-to-peak

The profile of the hemodynamic response function in the AG need not be the same as the standard double-gamma function often used to model cortical responses (Devonshire et al., 2012; Handwerker et al., 2004; Pernet, 2014). Extracting the raw percentage of signal change over points in time after stimulus onset without reference to a standard hemodynamic template often leads to more accurate BOLD signal measurements, as is done with a Finite Impulse Response (FIR) model. Unfortunately, this approach also reduces statistical power and can lead to overfitting of the data. Here, we used an approach that minimizes the hemodynamic response function (HRf) bias, without substantial loss of statistical power by determining the appropriate parameters for an optimized double-gamma function suitable for our AG data.

First, the HRf was deconvolved using a FIR model as implemented in MarsBar (v. 0.43; http://marsbar.sourceforge.net) toolbox. Events for all picture categories were pooled together and the mean HRf was estimated for each hemisphere's AG, separately for each participant. The fitted HRf timecourses were then averaged across all participants and hemispheres. Next, we fit a double-gamma function (as implemented in the *spm_hrf* function within SPM) to the mean fitted time

course using the SIMPLEX algorithm (Nelder & Mead, 1965). Five parameters (delay to response, delay of undershoot, dispersion of response, dispersion of undershoot, and ratio of response to undershoot) were optimized over 15,000 iterations to minimize the root-mean-squared-deviation (RMSD) between the double-gamma function and the FIR-fitted HRf time course (Fig. 3.4). The optimized double-gamma model, along with its first-order derivative, was used to estimate the BOLD response for each stimulus condition. MarsBar was used to extract HRf and time derivative betas for each event type from each ROI. In total, each condition was represented by 15 trials/HRfs.

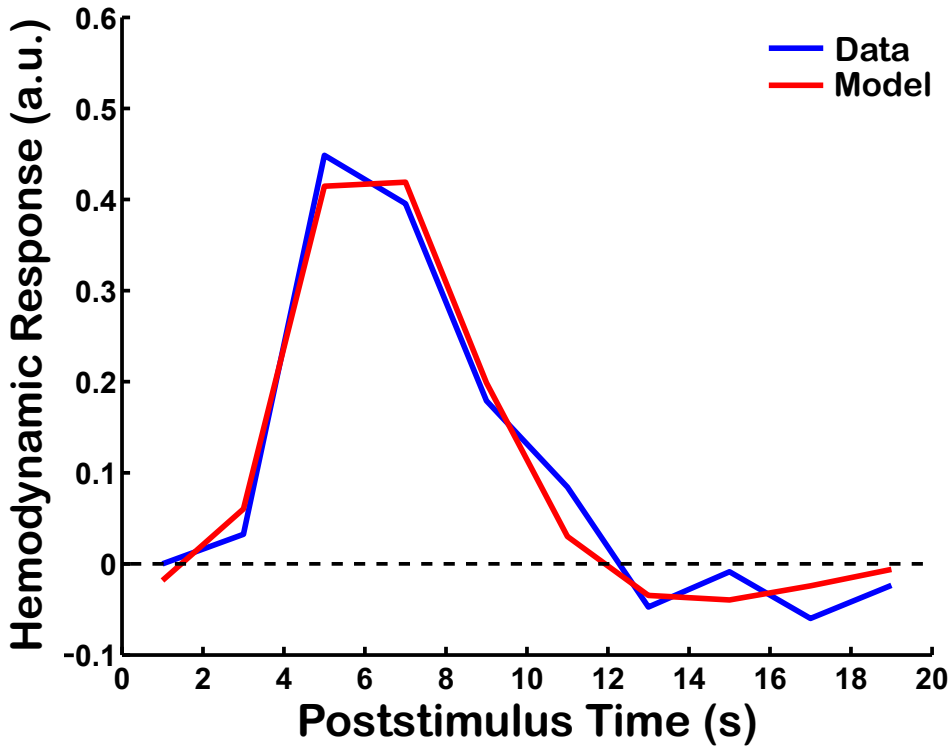

Fig. 3.4. BOLD response in bilateral amygdala, averaged across participants and stimulus categories is shown in blue. A double-gamma function that was optimized to fit the amygdala BOLD response is shown in red (a.u., arbitrary units). Fitted parameters were 6.909 for delay of response, 9.525 for delay of undershoot, 0.9657 for dispersion of response, 3.740 for dispersion of undershoot, and 1.310 for ratio of response to undershoot.

The BOLD response amplitude at peak was estimated using a protocol proposed by Calhoun et al. (2004), which incorporates not only the HRf parameter beta, but also the derivative beta, when estimating the BOLD response amplitude. However, when the derivative component dominates the hemodynamic response estimate, this approach can produce ambiguous amplitude estimates. In such instances, whether the final model represents activation or deactivation can become unclear. Here we developed a method that utilizes group-level parameter estimates to resolve these ambiguous cases (see *Appendix* in section 3.6 for details). Final response amplitude estimates were rescaled to percent signal change units using MarsBar toolbox. BOLD response delay-to-peak was defined as post-stimulus time, where activation or deactivation is the strongest.

To ensure that neither the BOLD response amplitude, nor the delay-to-peak information used in the analyses below is redundant, we conducted correlation analyses on the response amplitude and the delay-to-peak contrasts for total AG and each subnuclei group. None of the correlations reached statistical significance at a liberal $p < .10$ threshold: (1) total AG [$r = -.29$], (2) CeM group [$r = -.14$]; (3) BA group [$r = -.38$]; (4) LA group [$r = -.24$]. This suggests that our amplitude and delay-to-peak data accounted for unique aspects of hemodynamic response.

Imaging analysis

Behavioral data analysis was performed on the in-scanner rating task using a repeated-measure ANOVA. This analysis showed a main effect of picture category [$F(2,72) = 224.79$, $p < .001$, $\eta^2 = .90$] such that participants rated the Neu pictures as least emotional ($M = 1.16$, SE = 0.07) and the High Emo pictures as most emotional ($M = 3.11$, SE = 0.1). Holm–Bonferroni-corrected pair-wise comparisons demonstrated that each picture type was significantly different from its adjacent picture type (i.e., Neu < Low Emo < Med Emo < High Emo). However, due to the lack of statistical separation in IAPS-based valence ratings between Med and High Emo pictures (as reported above) and because seven of our participants assigned less than 10 pictures as highly emotional, we collapsed the Med and High Emo picture categories into a single negative emotional category for fMRI analyses. This allowed for an increased number of trials in which participants were likely to have perceived the pictures as being “highly” or “moderately” emotional. Since our research interest was limited to detecting differences in sensitivity of the AG subnuclei groups to negative emotion, we did not analyze BOLD response estimates from the Low Emo category. To ensure that visual complexity of the High/Med Emo stimuli was similar to visual complexity of the

Neu stimuli, we compared spatial frequencies of these two stimuli groups using Image Statistics Toolbox for MATLAB (Bainbridge & Oliva, 2015; Torralba & Oliva, 2003). Spatial frequency analysis revealed that visual complexity of the stimuli in the combined High/Med Emo category was equal to visual complexity of the stimuli in the Neu category. SPSS (v. 21; IBM Inc., Armonk, NY) was used to perform random-effects analyses on the response amplitude and the delay-to-peak difference scores between the collapsed High/Med Emo category and Neu category (in the results section called simply negative minus neutral contrast). No correction for sphericity assumption violations was required, as our data did not violate these assumptions in any of the response amplitude or delay-to-peak tests. Post-hoc comparisons (6 for response amplitude, and 6 for response latency) employed Holm–Bonferroni correction to control for Type I error inflation. Only family-wise error (FWE) corrected *p*-values are reported.

Classification analysis

To determine whether BOLD response amplitude and BOLD response delay-to-peak data from the AG subnuclei groups can be used to predict emotionality of visual stimuli, we used a sequential minimal optimization algorithm, from the MATLAB Statistics Toolbox (The MathWorks Inc., Natick, MA) to train binary linear support-vector-machine (SVM) classifiers on standardized BOLD response amplitude and delay-to-peak parameters (25 for Neu stimuli, 25 High/Med Emo stimuli) from anatomically defined ROIs. A box constraint penalty parameter search was carried out on a base-10 logarithmic scale ($C = 10^{-4.0}, 10^{-3.9}, ..., 10^{2.4}, 10^{2.5}$) using an internal 9-fold cross-validation loop to find the optimal penalty parameter without excessively over-fitting the model. Classifier performance was assessed using an external 10-fold cross-validation loop. To minimize classifier variability due to random partitioning of the data into train/test folds, the classifier was trained and assessed 200 times for each ROI. The average classification accuracy was computed for all ROIs and rounded to the nearest integer. Rather than make any assumptions about the null distributions of our classifiers, we chose to empirically estimate these null distributions using permutation tests. During this procedure the stimulus category label [‘neutral’, ‘negative’] was randomly shuffled 1500–5000 times (depending on the level of precision demanded by each hypothesis test), and the classification procedure was repeated each time. Subsequently, statistical tests were conducted to test against the null hypothesis that stimulus category labels have no meaning and observed classification accuracy could have resulted from random sampling only. To

account for null distribution differences between classifiers trained on data from different ROIs, we report classification accuracies above or below the median of the corresponding null distributions. Only Holm–Bonferroni-corrected *p*-values are reported for classifier performance comparisons (4 tests for ROI comparison; 3 tests for CeM comparison).

Intra-amygdala functional connectivity

For intra-AG functional connectivity analysis, EPI timecourses were preprocessed using CONN toolbox (v. 13.o; Whitfield-Gabrieli & Nieto-Castanon, 2012). After correcting for head motion, 5 principle eigenvariates from WM and 5 from CSF voxels were co-varied out of the realigned time courses. This procedure removes spurious autocorrelations from the data that are a byproduct of physiological noise. Subsequently, we regressed out task-induced signal changes evoked by each stimulus category. To model stimulus-evoked signal changes, we used a two-parameter model of hemodynamic response, represented by the optimized double-gamma function (as previously estimated using the SIMPLEX algorithm) and its first-order derivative. Next, time points with excessive head motion and signal spikes (as previously identified by ART) were identified and removed from the data. Resulting time courses were band-pass filtered (Low = 0.09 Hz, High = 0.008 Hz). Because serial autocorrelation (i.e. BOLD data in sequential TRs is correlated) violates assumptions of the least-squares algorithm, and results in biased correlation coefficients (Arbabshirani et al., 2014), we carried out a partial autocorrelation analysis to identify the most appropriate autoregressive (AR) model. This analysis revealed that, in most cases, lag 5 was the last lag to produce a significant autocorrelation. Thus, the AR5 model sufficiently corrected for serial autocorrelations and was used for the reported results. For each pairing of the three subnuclei groups we performed a partial correlation analysis, controlling for the other ROI (e.g., correlation between the CeM group and the BA group, controlling for the LA nucleus), on the time courses. These correlation coefficients were then converted to Fisher's *Z*-scores (Fisher, 1921). Each participant's *Z*-transformed correlation values were averaged across all runs, and were carried over for the random-effects analysis, which was performed in SPSS. Where appropriate, Huynh–Feldt correction for sphericity violation was applied.

To ensure that direct comparison of connectivity measures was not biased by unequal variability in signal over time in each ROI, we computed the standard deviation (SD) of the time

courses that went into the final connectivity analysis, and compared them to each other by performing a two-factor [Hemisphere: Left, Right; ROI: CeM, BA, LA] repeated-measures ANOVA on SD measures from each ROI. The main effect of hemisphere was not significant [$F(1,24) = 1.013$, $p = .324$, $\eta^2 = .006$], and neither was the two-way interaction [$F(2,48) = 1.402$, $p = .256$, $\eta^2 = .005$], suggesting that SDs of fMRI time courses were similar for the two hemispheres. However, the main effect of ROI was significant [$F(2,48) = 125.581$, $p < .001$, $\eta^2 = .63$]. To investigate the main effect of ROI further, we performed pairwise comparisons on SD data, averaged across hemispheres. Holm–Bonferroni correction for multiple hypothesis testing was applied. The signal from the CeM group had greater variation than the signal from the BA group [$t(24) = 13.357$, $p < .0001$, Cohen's $d = 2.67$], and greater variation than the signal from the LA nucleus [$t(24) = 13.751$, $p < .0001$, $d = 2.75$]. However, the time course variability from the BA group was similar to the time course variability from the LA nucleus [$t(24) = 0.455$, $p = .653$, $d = 0.09$]. Because signal profiles for the CeM ↔ BA, and the CeM ↔ LA con- nectivity measures were similar to each other, while the BA ↔ LA con- nectivity was estimated from less noisy sources, we only compared the CeM ↔ BA and the CeM ↔ LA connectivity measures to each other. For simplicity of interpretation, group *Z*-score values were inverse-transformed into corresponding correlation coefficients. Post-hoc comparisons of intra-AG connectivity also employed Holm–Bonferroni correction for multiple comparisons (4 tests). Only FWE-corrected findings are reported.

3.3. Results

Total amygdala

First, we performed a paired-samples *t*-test to determine whether the left and the right total AG differed in their sensitivity to negative emotional stimuli. We observed no laterality effects [amplitude: $t_{(24)} = 1.45$, $p = .16$, Cohen's $d = 0.29$; delay to peak: $t_{(24)} = 1.16$, $p = .26$, $d = 0.23$]. Therefore, data for each emotional condition of interest (i.e., negative and neutral) was averaged across the hemispheres. To examine differences in the total AG's response to negative versus neutral items, paired-samples *t*-tests were performed on the amplitude and the delay-to-peak data. Consistent with prior findings (Ball et al., 2009; Sergerie et al., 2008), analysis of the amplitude data showed increased sensitivity in bilateral AG to the negative stimuli [$t_{(24)} = 4.804$, $p < .0001$,

$d = 0.96$, $M_{diff} = 0.16\%$ signal change] (Figs. 3.5a, 3.6a). However, analysis of delay to peak showed only a trend with later time to peak in response to negative emotion [$t_{(24)} = 1.89$, $p = .071$, $d = 0.23$, $M_{diff} = 0.36$ s] (Figs. 3.5a, 3.6b).

Amygdala subnuclei groups

Amplitude of response

To determine whether the AG subnuclei groups differentially respond to negative emotional stimuli we calculated difference scores by subtracting amplitude values in response to neutral stimuli from those in response to negative emotional stimuli. The resulting values indicated the degree of emotional sensitivity. A repeated-measures ANOVA with two factors [Hemisphere (left, right); Subnuclei Group (CeM, BA, LA)] revealed a significant main effect of Subnuclei Group [$F_{(2,48)} = 4.40$, $p = .018$, $\eta^2 = .061$], demonstrating that the AG subnuclei groups responded differently to the negative stimuli. Because neither the main effect of hemisphere was significant [$F_{(2,48)} = 1.63$, $p = .21$, $\eta^2 = .014$], nor the two-way interaction [$F_{(2,48)} = 0.90$, $p = .41$, $\eta^2 = .014$], we concluded that the effect of the negative emotional stimuli on the AG subnuclei groups was consistent across hemispheres. Therefore, we performed simple effects analyses on the difference scores averaged across the two hemispheres.

To determine how the AG subnuclei groups differed in their sensitivity to emotion we first examined the difference scores for each subnuclei group separately. The CeM group responded significantly to the negative emotional stimuli [$t_{(24)} = 4.09$, $p = .003$, $d = 0.82$, $M_{diff} = 0.28\%$ signal change] (Figs. 3.5b, 3.6a), as did the BA group [$t_{(24)} = 3.24$, $p = .017$, $d = 0.64$, $M_{diff} = 0.14\%$ signal change] (Figs. 3.5c, 3.6a). The LA nucleus, however, did not differentially respond to the emotional stimuli [$t_{(24)} = 1.81$, $p = .17$, $d = 0.36$] (Figs. 3.5d, 3.6a). Comparing the AG subnuclei to each other showed that the CeM group was more sensitive to the negative stimuli than the LA nucleus [$t_{(24)} = 2.82$, $p = .038$, $d = 0.56$, $M_{diff} = 0.21\%$ signal change]. However, neither the CeM group nor the LA nucleus differed significantly from the BA group [$t_{(24)} = 1.84$, $p = .23$, $d = 0.37$; $t_{(24)} = 1.02$, $p = .32$, $d = 0.20$, respectively].

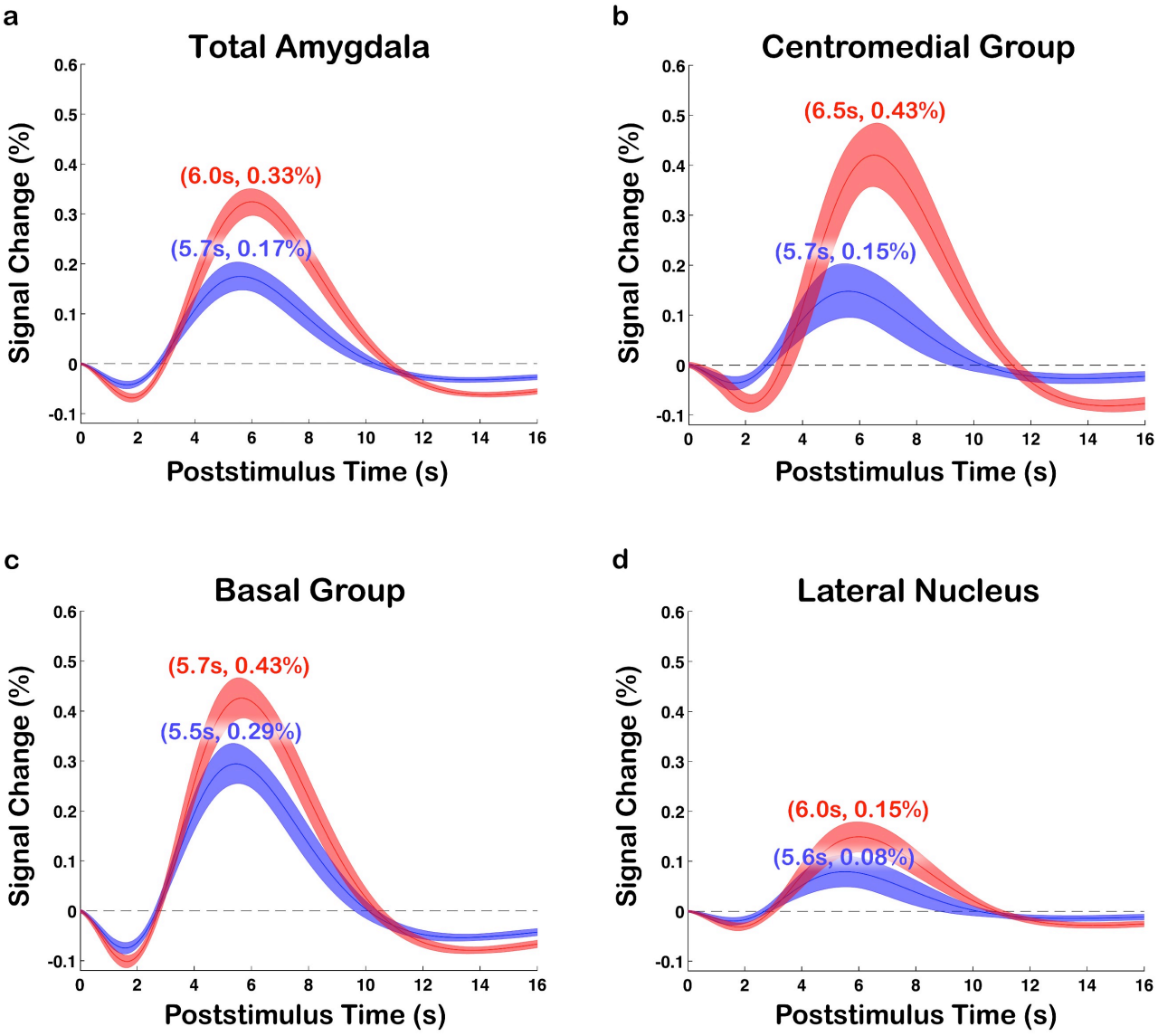

Fig. 3.5. Reconstructed hemodynamic response function for negative (red) and neutral (blue) stimuli in the total amygdala and its subnuclei groups, averaged across hemispheres. Shaded areas represent the standard error of the mean, corrected for inter-individual differences. BOLD response amplitude and delay to peak are shown in brackets for each stimulus category.

Delay to peak BOLD response

To determine whether the AG subnuclei groups display latency differences in hemodynamic response due to negative stimulus processing we calculated latency difference scores by subtracting delay-to-peak values in response to neutral stimuli from those in response to negative stimuli. A repeated-measures ANOVA with two factors [Hemisphere (left, right); Subnuclei Group (CeM, BA, LA)] was performed on these difference scores. The main effect of subnuclei group showed a trend towards significance [$F_{(2,48)} = 2.53$, $p = .090$, $\eta^2 = .039$] suggesting that subnuclei might differ in their peak latency in response to emotional relative to neutral stimuli. Neither the main effect of hemisphere [$F_{(1,24)} = 2.59$, $p = .12$, $\eta^2 = .010$] nor the two-way interaction [$F_{(2,48)} = 0.06$, $p = .98$, $\eta^2 < .001$] was significant, demonstrating that latency differences between emotional and neutral stimuli were consistent across hemispheres. Consequently, the delay-to-peak data was averaged across the two hemispheres.

To determine which AG subnuclei group, if any, was driving the marginal main effect of the Subnuclei Group in the above analysis we examined the latency difference scores for each AG subnuclei group separately. The CeM group showed significantly later BOLD response peak for the negative emotional stimuli compared to the neutral stimuli [$t_{(24)} = 3.245$, $p = .021$, $d = 0.65$, $M_{diff} = 0.83$ s] (Figs. 3.5b, 3.6b). The LA nucleus and the BA group, however, did not show significant emotion-related differences in BOLD response latency [$t_{(24)} = 2.087$, $p = .19$, $d = 0.42$, $M_{diff} = 0.46$ s; $t_{(24)} = 1.005$, $p = .32$, $d = 0.20$, $M_{diff} = 0.19$ s, respectively] (Figs. 3.5c–d, 3.6b). Although, the CeM group had the largest difference in BOLD response latency due to negative stimulus processing, this difference was only marginally larger than the difference found in the BA group [$t_{(24)} = 2.51$, $p = .097$, $d = 0.50$, $M_{diff} = 0.64$ s], and no different from the latency difference in the LA nucleus [$t_{(24)} = 1.10$, $p = .84$, $d = 0.22$]. The difference in the delay to peak to emotional relative to neutral stimuli did not differ between the LA nucleus and the BA group [$t_{(24)} = 1.04$, $p = 0.61$, $d = 0.21$]. These results suggest that sensitivity to negative emotional stimuli, as measured by the delay-to-peak contrast, is likely different between the AG subnuclei groups.

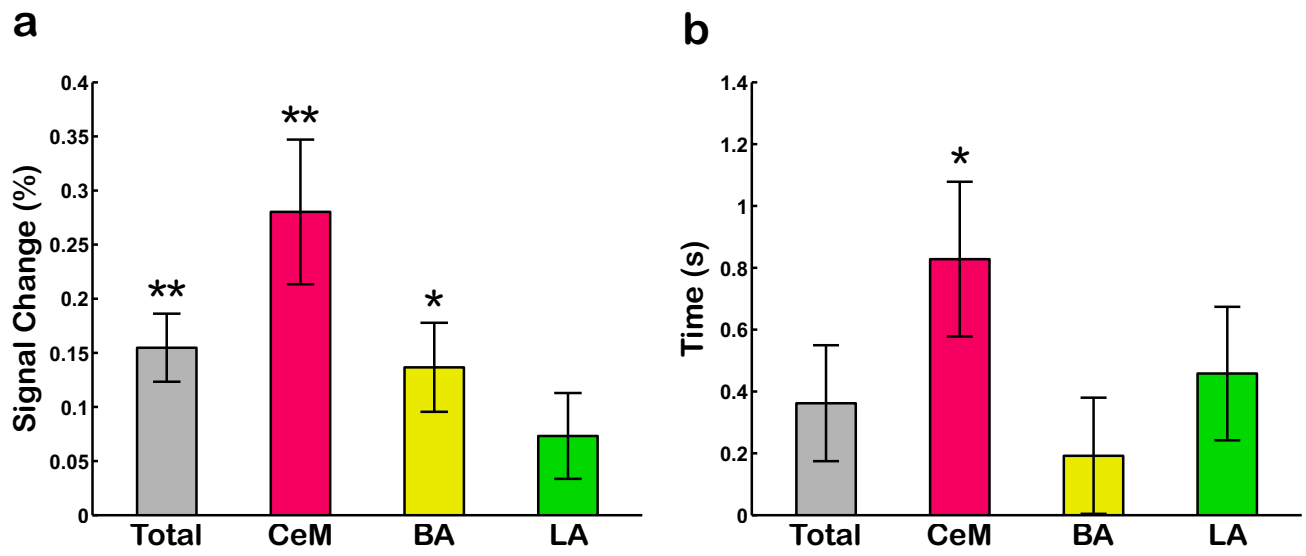

Fig. 3.6. Amplitude (a) and Latency (b) negative minus neutral contrasts for the total amygdala and each of its subnuclei groups (CeM, centromedial group; BA, basal group; LA, lateral nucleus).
*FWE $p < 0.05$; **FWE $p < 0.01$.

Prediction of image emotional content based on BOLD response parameters

To determine whether BOLD response parameters (response amplitude and delay to peak) from any of the AG subnuclei groups are better at predicting the emotional content of a stimulus than BOLD response parameters from the total AG we trained 4 linear Support Vector Machine (SVM) classifiers, one for the total AG and one for each AG subnuclei group, on 4 features from each participant [average left/right hemisphere amplitude of response, average left/right hemisphere delay to peak]. The classifier trained on the data from the total AG performed statistically no better than chance [59% accuracy (14% above median), $p < 0.1$]. The classifiers trained on the data from the BA group and the data from the LA nucleus were even less accurate at predicting the emotional content of the stimuli [52% accuracy (6% and 8% above median, respectively), $p < 0.1$]. The only classifier that succeeded at predicting the emotional category of a stimulus better than chance was the classifier trained on BOLD response parameters from the CeM group [71% accuracy (24% above median), $p < 0.01$]. This demonstrated that BOLD measures from the CeM group are better at predicting the emotional content of a stimulus than BOLD measures from the total AG or any other AG subregion (Fig. 3.7a). To ensure that neither the CeM BOLD response amplitude nor the CeM BOLD response delay to peak was redundant to the overall classification model, we trained two separate CeM classifiers, one only on the amplitude data, and the other only on the delay-to-peak

data. While both of these classifiers performed better than chance [Amplitude accuracy = 62% (16% above median), $p < 0.05$; Latency accuracy = 70% (19% above median), $p < 0.05$], the CeM model trained on both parameters at the same time performed best (Fig. 3.7a,b). Holm–Bonferroni-corrected pair-wise comparisons of classifier performances demonstrated that each classifier achieved classification accuracy that was significantly different from the other classifiers (all ps < .001).

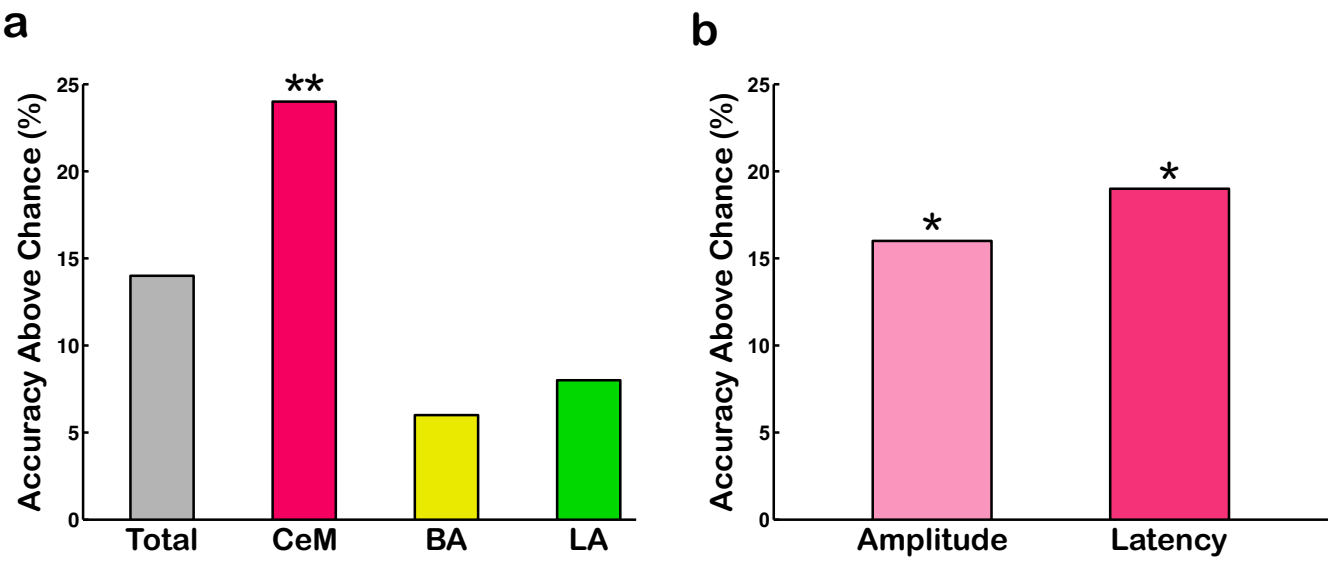

Fig. 3.7. (a) Classification accuracy above median of linear SVM classifiers trained on response amplitude and delay-to-peak data from the total amygdala and each of its subnuclei groups (CeM, centromedial group; BA, basal group; LA, lateral nucleus). (b). Classification accuracy above median achieved by linear SVM classifiers trained separately either on the CeM BOLD response amplitude or the CeM BOLD response latency. *FWE $p < 0.05$; **FWE $p < 0.01$.

Intra-amygdala connectivity

To examine potential pathways of information flow within the AG, we performed a functional connectivity analysis between the AG subnuclei groups. A repeated-measures ANOVA was performed on Fisher Z-transformed partial correlations between the AG subnuclei groups (called edges) with Hemisphere [left, right] and Edge [CeM ↔ BA, CeM ↔ LA, BA ↔ LA] as factors. We observed a significant main effect of Edge [$F_{(2,48)} = 17.69$, p < .00001, $\eta^2 = .235$], demonstrating that three edges representing intra-AG connectivity differed in the strength of their correlation. The main effect of hemisphere was not significant [$F_{(1,24)} = 3.38$, $p = .079$, $\eta^2 = .012$],

and neither was the two way interaction [$F_{(2,48)} = 0.535$, $p = .54$, $\eta^2 = .008$], demonstrating that the pattern of intra-AG connectivity was consistent across hemispheres.

Based on partial correlation analysis, statistically significant connectivity existed between all of the AG subnuclei groups (all ps $< .01$), suggesting that all subnuclei groups are functionally related to each other (Fig. 3.8). Furthermore, the CeM group was more connected to the nuclei of the BA group than to the LA nucleus [$t_{(24)} = 2.53$, $p = .018$, $d = 0.51$, $M_{z\_diff} = 0.07$].

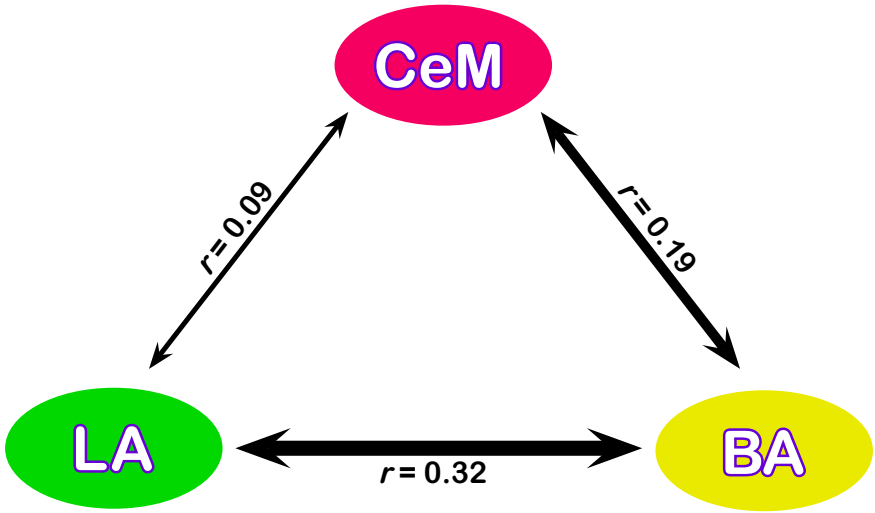

Fig. 3.8. Human intra-amygdala functional connectivity is represented by partial correlation coefficients (CeM, centromedial group; BA, basal group; LA, lateral nucleus). All subnuclei groups were connected to each other. For connectivity comparisons see the main text.

3.4. Discussion

Using high-resolution fMRI we demonstrated for the first time that anatomically-defined subnuclei groups of the human AG respond differently to negative emotional stimuli, and that strength of functional connectivity between various AG subregions is not identical. Although most prior functional neuroimaging studies analyzed the AG as a single homogeneous structure, our findings provide strong evidence in support of functional specialization within the human AG. As measured by BOLD response amplitude, the CeM group was most sensitive to the negative emotional stimuli, followed by the BA group, while the LA nucleus was largely insensitive to negative emotions. The CeM AG also demonstrated clear latency differences in its hemodynamic

response to the negative emotional stimuli, while the BA group and the LA nucleus did not. Critically, only the activity in the CeM group was able to predict the emotional content of the stimuli based on BOLD response parameters in a classification analysis. Investigation of intra-AG functional connectivity demonstrated that all three AG subnuclei groups were functionally related to each other. Furthermore, the CeM group showed greater connectivity with the nuclei of the BA group than with the LA nucleus.

Although, some previous studies attempted to elucidate functions of the AG subnuclei in negative stimulus processing, they were substantially limited by spatial resolution (e.g. Styalidis et al., 2014; Yoder et al., 2015). This limitation is most pronounced for the nuclei of the dorsal AG. Histological experiments revealed that the CeM AG is smaller than 150 mm^3 (Brabec et al., 2010; Garcia-Amado & Prensa, 2012). Consequently, the CeM AG is only 2–9 voxels large on fMRI images with 16–64 mm^3 voxels. Here, we optimized all our acquisitions to guarantee sufficient spatial resolution to study the effects of negative stimulus processing not only on the AG subnuclei groups from the ventral AG, but also from the dorsal AG.

The overall efficacy of our experimental paradigm at eliciting AG activation and our analysis approach at detecting it was validated by our whole AG results, which demonstrated increased sensitivity to negative emotional stimuli in the bilateral AG. These results are in agreement with the extant fMRI literature (Sergerie et al., 2008), case studies of patients with the AG lesions (Adolphs et al., 1994, 1995; Broks et al., 1998), and non-human fear conditioning experiments (Davis, 1992; Kapp et al., 1994), providing further support to the body of literature on AG's involvement in processing of high arousing negative emotions. In agreement with similar fMRI studies as reported in a large meta-analysis of fMRI literature on the human AG by Sergerie et al. (2008), we observed no laterality effects in any measure of hemodynamic response in the total AG or any of its subnuclei.

Differential engagement of the amygdala subnuclei groups in response to negative emotional stimuli

The main finding from the current study showed preferential sensitivity of the CeM AG to highly arousing negative emotional stimuli. The CeM group was sensitive to negative emotion in all of the analyses we performed. Its BOLD response to negative pictures was greater and peaked later, when compared to BOLD response to neutral pictures.

While we did not initially have any predictions about differences in delay-to-peak latency as a function of emotion, there are several lines of evidence that may help explain this finding. It is reasonable to expect that non-task-related differences across ROIs in the timing of the BOLD response may be due to vasculature, neuronal, or neurovascular coupling effects that are similar for one area of tissue but not another (Kim & Ogawa, 2012; Logothetis & Wandell, 2004). However, task-related differences in BOLD latency within the same ROI are likely reflective of differences in the underlying neuronal activity (Formisano & Goebel, 2003; Pernet et al., 2004). In this regard, the delay to peak for emotional relative to neutral stimuli in the CeM AG is likely due to emotion-specific changes in neuronal activity. Animal work has shown that increasing stimulation frequency of somatosensory neurons produces higher and later hemodynamic response peaks (Martin et al., 2006). Similarly, our CeM amplitude and latency findings might simply represent greater stimulation of the CeM neurons as a consequence of negative stimulus processing. It is also possible that emotion-related firing rates within the human AG are of different durations. Consequently, our CeM latency findings might represent longer lasting activation of the CeM group driven by negative stimulus processing. Although we did not directly test differences in the duration (i.e., dispersion) of the BOLD response, this explanation is supported by recent animal literature which demonstrated subnuclei-specific variations in neuronal firing durations during fear conditioning experiments (Duvarci & Paré, 2014). Additionally, the motivational processes evoked by the AG subnuclei may also be of relevance, e.g., if the AG activity corresponds to not only a response due to negative emotion, but also approach- vs. avoidance-related processes, which involve interactions with the prefrontal cortex and insula (Cardinal et al., 2002; Harmon-Jones et al., 2013; Madan, 2013). As our study was not designed to assess emotion-driven causes of hemodynamic latency differences, future research is needed determine the exact cause of these findings.

To gain greater insight into biological significance of our results, we must turn to animal experiments. Non-human fear-conditioning experiments have shown that the Ce nucleus of the AG is the primary regulator of behavioral and autonomic responses. Through its connections with the lateral and paraventricular hypothalamus, Ce AG modulates heart rate, blood pressure, corticosteroid release, and skin conductance (Davis & Whalen, 2001). Ce projections to the ventral tegmental area, locus coeruleus, and basal forebrain modulate arousal, vigilance, and attention, while its projections to the periaqueductal gray and cranial nerve nuclei control freezing and escape

behaviors (Davis & Whalen, 2001). Recent primate work on functional role of the Ce AG arrived at similar conclusions (Kalin et al., 2004).

Similarly, images of negative valence and high arousal have been found to elicit increased skin conductance response, decreased heart rate, and increased attention in humans (Lang et al., 1998). Therefore, based on extant knowledge of processes underlying fear conditioning, and commonalities between different organisms' physiological responses to unpleasant stimuli, we think that the CeM activation reported in the current study, is related to its involvement in regulation of autonomic, endocrine, and behavioral responses induced by negative stimulus processing.

Our parametric response amplitude results also demonstrated some sensitivity of the BA group nuclei to negative emotion. Animal work has shown that the BA nucleus receives most of its inputs from two sources, the LA nucleus of the AG, and the orbitofrontal cortex, while its outputs mainly project to the Ce AG and the striatum, where they provide context-dependent modulation of emotional processing (Freese & Amaral, 2009), and contribute to regulation of instrumental behaviors (LeDoux & Schiller, 2009).

Previous high-resolution fMRI studies on the AG subnuclei investigated the AG subnuclei function in fear conditioning (Bach et al., 2011; Boll et al., 2013), processing of emotional facial expressions (Boll et al., 2011; Gamer et al., 2010), appetitive conditioning (Prévost et al., 2013), instrumental learning (Prévost et al., 2012), reward seeking (Prévost et al., 2011, 2013), and punishment avoidance (Prévost et al., 2011). Although our paradigm employing complex visual stimuli covering broad emotional spectrum is quite different from the stimuli used in previous high-resolution fMRI experiments of the AG, our findings are in general agreement with findings from other high-resolution fMRI experiments on the AG, suggesting that the CeM AG is particularly involved in processing of aversive and threatening stimuli or situations. For instance, Boll et al. (2011) demonstrated that activity in the corticomedial amygdala was positively correlated with outcome uncertainty; Prévost et al. (2013) demonstrated that the CeM AG activity correlated with expected value in aversive learning; furthermore, patients with focal lesions to the BLA AG, but no damage to the CeM AG, display hypervigilance (Terburg et al., 2012). Future studies will also need to investigate the role of the AG subnuclei in processing of positive emotions, as well as other functions that engage the AG, e.g. sexual behaviors, feeding, and risk-taking (LeDoux & Schiller, 2009; van Honk et al., 2013).

Intra-amygdala connectivity

In general, our connectivity results are in agreement with previous animal work. In rodents the LA nucleus acts as the sensory interface of the AG, and receives inputs from primary sensory systems (Phelps & LeDoux, 2005). However, activation of the Ce output neurons is necessary for physiological and behavioral changes that increase chances of effectively coping with a biologically relevant stimulus. Although, direct inputs into the CeM group from the LA nucleus exist (Pitkänen et al., 1997), those are few in comparison to the indirect pathway through the B and the AB nuclei (Duvarci & Paré, 2014; Freese & Amaral, 2009). Similarly, our results showed greater connectivity of the CeM AG with the nuclei of the BA group than the LA nucleus. Although this study was not designed to directly compare the two predominant models of emotional processing by the AG subnuclei (Balleine & Killcross, 2006; LeDoux, 2007), our findings provide some support for both. Our activation results suggest that the CeM AG functions independently of the BA group and the LA nucleus, when processing aversive visual stimuli. Our connectivity findings, on the other hand, support the traditional serial model. Additional work, employing a different paradigm and different data analysis approaches, is required to further elucidate the specific mechanisms of emotional processing by the subnuclei of the human AG.

Even though our connectivity results are in agreement with animal literature, they are not consistent with another human functional connectivity study (Roy et al., 2009), which reported negative correlation patterns within the right AG, and observed no connectivity between the subnuclei of the left AG. These differences in connectivity measurements may have occurred because Roy et al. (2009) relied on Amunts et al. (2005) probabilistic atlas to define the AG subnuclei ROIs in MNI space, while we used Mai et al. (2008) atlas to manually segment the AG ROIs in native space.

Although, our connectivity findings were very robust and reliable, they should still be interpreted with caution because our correlation coefficients are fairly small. It is currently unknown whether such low correlation coefficients are a byproduct of lower SNR produced by high-resolution acquisition or whether they represent weak intra-AG communication. Nonetheless, our findings conclusively demonstrated that the CeM AG interacts differently with the other two subnuclei groups.

Hemodynamic properties of the amygdala subnuclei groups

The current study demonstrated that time and amplitude domains of BOLD response are not necessarily correlated and can provide unique information about the hemodynamic response of a region. Many prior fMRI studies of the AG relied on the canonical hemodynamic response function to model BOLD response (e.g. Ball et al., 2007; Boll et al., 2011; Davis et al., 2010; Gamer et al., 2010; Frühholz & Grandjean, 2013; Prévost et al., 2011). When constructing activation contrasts, this approach assumes that BOLD response across various conditions varies only in its amplitude. Friston et al. (1998) proposed the use of the temporal derivative to account for the delay-induced variations in hemodynamic response. Later, Calhoun et al. (2004) demonstrated that incorporating the derivative and non-derivative terms into response amplitude contrasts produces more accurate estimates of BOLD amplitude differences between various conditions. Furthermore, as was demonstrated by Henson et al. (2002), BOLD response timing effects may be condition-dependent. In our results, we demonstrated that hemodynamic response amplitude and latency parameters are, at times, independent of each other. Our parametric results showed that for some ROIs, there was difference in BOLD response amplitude between the two conditions (BA group), while other ROIs displayed differences in time and amplitude domains (CeM group). We also showed that multivariate methods might benefit from including both of these BOLD response parameters when training a model. For instance, our best CeM classification model was trained on both response amplitude and delay to peak.

The current study also demonstrated that employing univariate hypothesis testing in conjunction with multivariate classification provides additional insight into properties of the fMRI data. In our univariate findings, both the CeM and the BA group were sensitive to negative emotion. However, when we used the same BOLD response parameters in a multivariate classification analysis, we discovered that only BOLD response from the CeM group could predict above chance which stimulus category these parameters represent. This suggests that while mean responsiveness to negative stimuli was higher in both subnuclei groups, BOLD response parameters for neutral and negative stimuli were clearly separable in the CeM group, but not in the BA group, suggesting that the nuclei of the CeM group process those stimuli differently than the nuclei of the BA group.

Limitations and future directions

In the current study we relied on ROI analysis to study the AG subnuclei. While ROI techniques provide great anatomical accuracy and precision, they are largely insensitive to dispersed activation patterns. This important caveat likely accounts for the seeming discrepancy between the vital role that the LA nucleus plays in non-human conditioning experiments (Phelps & LeDoux, 2005) and our fMRI-based LA activation findings. There is evidence in animal literature that only 20% of cells in the LA nucleus show plasticity-dependent modulation of sensitivity in response to threat (Duvarci & Paré, 2014). If there are distributed emotion-sensitive neural populations in the human LA nucleus, future studies employing pattern recognition techniques might be able to identify them. Another caveat of our analysis procedure is reliance on mathematical interpolation to measure BOLD response timing. Our raw fMRI data was acquired with a 2-s TR, but we report sub-second differences in BOLD response delay to peak. Although future studies employing multi-band sequences with shorter TR are required to verify our latency findings, we do not consider our mathematical interpolation to be a major concern because we relied on previously researched properties of the hemodynamic response in our parameter estimation procedures (Devonshire et al., 2012; Kim and Ogawa, 2012; Logothetis et al., 2001; Logothetis & Wandell, 2004; Martin et al., 2006; Pernet, 2014).

Furthermore, future fMRI studies of the AG subnuclei need to investigate the effects of emotional valence and gender. Although there is substantial evidence that positive emotions engage the AG (Ball et al., 2009; Sergerie et al., 2008), it is currently unclear how the AG subnuclei investigated here would respond to positive versus negative emotional stimuli. The need to investigate the responsiveness of the AG subnuclei to positive stimuli is supported by recent animal work, which suggests that positive and negative stimuli are processed by different pathways within the AG (Namburi et al., 2015). There is also some debate concerning the influence of gender on the AG function (Sergerie et al., 2008). Even though this study was not designed to address this question, in preliminary analyses, we included gender as a between subjects factor, but did not observe a main effect of gender, nor any interactions including it (all *p*s > .1).

Because fMRI signal variability is a function of ROI volume, direct comparison of connectivity strength between structures that substantially differ in volumes is not straightforward. For this reason, it is currently unclear how the BA ↔ LA fMRI connectivity, as defined by the strength of the correlation coefficient, compares to the CeM ↔ BA connectivity, and to the CeM ↔

LA connectivity. To address this issue, future fMRI studies will need to employ segmentation, and statistical methodology that can minimize such effects.

3.5. Conclusions

In the current study, we used anatomical landmarks to extract BOLD signal from distinct AG subnuclei groups, and directly compared their activations in response to negative emotional stimuli. Our results showed that the CeM AG is particularly responsive to negative emotions. We also demonstrated that human intra-AG functional connectivity is consistent with animal literature. Future high-field high-resolution fMRI studies of emotional processing will allow researchers to further understand the structure–function relationship of the human AG and its subnuclei, as well as the roles that the AG subnuclei play in neuropsychiatric disorders.

Acknowledgments

We thank Matt R. Brown, Tyler M. Rolheiser, and Alexander Lebedev for their suggestions in improving our data analysis methodology. This project was supported by the Canadian Institutes of Health Research (CIHR) operating grant (MOP 111049) to N.V.M S.H. was supported by Sir Fredrick Banting and Dr. Charles Best CIHR Doctoral scholarship. C.R.M. was supported by the National Science and Engineering Research Council (NSERC) Doctoral Scholarship. C.A.B. was supported by NSERC Vanier Doctoral scholarship. C.B. was supported by the Alberta Inno- vates Health Solutions (AIHS) Scientist Award.

3.6. Appendix

Computation of Response Amplitude and Delay to Peak Values

In simplified form, a stimulus-induced BOLD signal can be estimated using Ordinary Least Squares (OLS) algorithm as a weighted sum of a double-gamma function, x_t, and its first-order derivative, $\frac{\partial x_t}{\partial t}$, from the acquired data, y_t:

$$y_t = \hat{\beta}_0 + \hat{\beta}_1 x_t + \hat{\beta}_2 \frac{\partial x_t}{\partial t} + \varepsilon_t \quad (1)$$

where ε_t is the residual error term, $\hat{\beta}_0$ is the intercept term, and *t* stands for poststimulus time. If conditions of generality and orthogonality for the normalized HRf and its temporal derivative are met (as outlined in Calhoun et al., 2004), the estimated amplitude of BOLD response at its peak is:

$$\alpha = \pm\sqrt{\hat{\beta}_1^2 + \hat{\beta}_2^2} \quad (2)$$

where α represents response amplitude at the HRf peak. In most instances

$$\text{sign}(\alpha) = \text{sign}\left(\hat{\beta}_1\right) \quad (3)$$

These instances are characterized by two criteria:

$$\text{sign}\left(\hat{\beta}_2\right) = \text{sign}\left(\hat{\beta}_1\right) \text{ and/or } \left|\hat{\beta}_2\right| < \left|\hat{\beta}_1\right| \quad (4)$$

However, in cases when

$$\text{sign}\left(\hat{\beta}_2\right) \neq \text{sign}\left(\hat{\beta}_1\right) \text{ and } \left|\hat{\beta}_2\right| > \left|\hat{\beta}_1\right| \quad (5)$$

$\text{sign}(\alpha)$ is ambiguous. To resolve such ambiguous cases we developed a data-driven approach based on group-level estimates of $\hat{\beta}_1$ and $\hat{\beta}_2$. First, we computed group-level estimates of $\hat{\beta}_1$ and $\hat{\beta}_2$ for each stimulus category:

$$\mu_{\hat{\beta}_1} = \frac{1}{N}\sum_{1}^{N}\hat{\beta}_1, \ \mu_{\hat{\beta}_2} = \frac{1}{N}\sum_{1}^{N}\hat{\beta}_2 \quad (6)$$

where *N* is the number of participants in the study. Consequently, group-level HRf function, z_t, can be represented in equation form as:

$$z_t = \mu_{\hat{\beta}_1} x_t + \mu_{\hat{\beta}_2} \frac{\partial x_t}{\partial t} \quad (7)$$

Group-level estimate of response magnitude is a modification of equation (2):

$$\left|\alpha_{\text{group}}\right| = \sqrt{\mu_{\hat{\beta}_1}^2 + \mu_{\hat{\beta}_2}^2} \tag{8}$$

The direction of group-level HRf signal change (i.e. positive for activation, and negative for deactivation) can determined by computing the definite integral of z_t for t = 2–15 second post-stimulus interval:

$$\text{sign}\left(\alpha_{\text{group}}\right) = \text{sign}\left(\int_2^{15} z_t dt\right) \tag{9}$$

Equations 7 and 8 can be combined to represent the estimated group-level response amplitude for each stimulus category:

$$\alpha_{\text{group}} = \text{sign}\left(\int_2^{15} z_t dt\right)\sqrt{\mu_{\hat{\beta}_1}^2 + \mu_{\hat{\beta}_2}^2} \tag{10}$$

The group-level response amplitude was computed for each stimulus category (i.e. neutral, low emotional, and highly emotional) using equation 10. These were then used to construct 3 group-level response amplitude ratios:

$$r1 = \frac{\alpha_{\text{high}}}{\alpha_{\text{low}}},\ r2 = \frac{\alpha_{\text{high}}}{\alpha_{\text{neutral}}},\ r3 = \frac{\alpha_{\text{low}}}{\alpha_{\text{neutral}}} \tag{11}$$

Group-level delay to peak for each stimulus category was computed as follows:

$$t_{\alpha_{\text{group}}} = \begin{cases} \arg\max_t z_t, \text{if } \alpha_{\text{group}} > 0 \\ \arg\min_t z_t, \text{if } \alpha_{\text{group}} < 0 \end{cases} \tag{12}$$

Similar to amplitude group-level ratios, we computed delay-to-peak group-level ratios:

$$r4 = \frac{t_{\alpha_{\text{high}}}}{t_{\alpha_{\text{low}}}},\ r5 = \frac{t_{\alpha_{\text{high}}}}{t_{\alpha_{\text{neutral}}}},\ r6 = \frac{t_{\alpha_{\text{low}}}}{t_{\alpha_{\text{neutral}}}} \tag{13}$$

Next, we computed all unambiguous subject-level α values using equation (2) based on criteria in (4). For the ambiguous α instances, the entire potential solution space was generated as positive and negative α. Sign of ambiguous α cases at subject level was resolved using exhaustive enumeration algorithm that minimized the difference between group-level ratio estimates from mean beta values (Equations 11, 13) and group-level estimates computed from subject-level α values. The algorithm assigned equal penalty values for amplitude and delay-to-peak errors when computing RMSD. To ensure that the algorithm performed as intended, we manually inspected the ambiguous instances

where sign of response amplitude of the canonical model differed from the sign of the amplitude of the canonical with the temporal derivative model. Once the sign of the ambiguous subject-level alpha instances was resolved, we were able to compute subject-level latency by finding the time-point of either maximum activation or maximum deactivation:

$$t_\alpha = \begin{cases} \underset{t}{\operatorname{argmax}}\, y_t, \text{if } \alpha > 0 \\ \underset{t}{\operatorname{argmin}}\, y_t, \text{if } \alpha < 0 \end{cases} \tag{14}$$

List of Pictures from the IAPS Database that Were Used as Stimuli

High Emo	**Med Emo**	**Low Emo**
1050	3071	2110
1525	3110	2120
2811	3168	3280
3000	3170	6244
3060	3266	6312
3063	6315	6314
3068	6825	6821
3069	6838	6830
3150	9042	6834
3500	9050	9041
6212	9253	
6550	9429	
6560		
8480		
9410		

Chapter 4: Involvement of Hippocampal Subfields and Anterior-Posterior Subregions in Encoding and Retrieval of Item, Spatial, and Associative Memories: Longitudinal vs. Transverse Axis.

4.1. Introduction

For over fifty years the hippocampus (HC) has been a major source of scientific interest because of its role in establishing and supporting episodic memories (Eichenbaum, 2001; Scoville & Milner, 1957; Squire & Dede, 2015; Squire & Wixted, 2011). Extensive research into HC function in both animals and humans confirmed the HC role in numerous components of episodic memory, including content, spatial, and temporal information (for reviews, see Cohen et al., 1999; Lisman et al., 2017; Moscovitch et al., 2005, 2016; Squire et al., 2015).

In humans, the HC activity was reported during both explicit and incidental learning (Azab et al., 2014; Bakker et al., 2008; Cohen et al., 1999; Lacy et al., 2011; Ranganath et al., 2004) with a wide variety of stimuli, covering a broad set of cognitive and perceptual domains: words, objects, tones, scenes, faces, and spatial routes and landmarks (for an overview, see Cohen et al., 1999; Lisman et al., 2017). From these studies, various hypotheses of HC function emerged: novelty detection, cognitive mapping, pattern separation/completion, and relational memory (Cohen et al., 1999; Cohen & Eichenbaum, 1993; Lisman et al., 2017; Yassa & Stark, 2011).

To gain a more accurate understanding of the HC function, it is important to acknowledge its complex internal anatomy. The HC can be subdivided along the anterior-posterior axis into three major sections (sometimes called subregions): head, body, and tail (Duvernoy, 2005; Malykhin et al., 2007; Rajah et al., 2010). Although functional differences between the anterior (i.e., head) and posterior (i.e., body together with tail) HC have been discovered, the exact nature of these differences is still unknown (Poppenk et al., 2013; Small, 2002; Strange et al., 2014). For instance, a number of studies demonstrated that the posterior HC is active during spatial memory tasks, while the anterior HC is engaged if a memory task contains emotional information (Bannerman et al., 2004; Dolcos et al., 2004; Kensinger & Corkin, 2004; Kensinger, 2009; Strange et al., 2014; Poppenk & Moscovitch, 2011). It has also been suggested that the anterior HC is related to coarse

gist-like memory, while the posterior HC is particularly involved in detailed episodic memory (Bonne et al., 2008; Hayes et al., 2011; Poppenk & Moscovitch, 2011; Poppenk et al., 2008, 2013). Yet other work has shown that the anterior HC is specialized for memory encoding, while the posterior HC is critical for memory retrieval (Kim, 2015; Lepage et al., 1998; Schacter & Wagner, 1999; Spaniol et al., 2009; de Vanssay-Maigne et al., 2011; Woollett & Maguire, 2012; Woollett et al., 2009). However, encoding and retrieval processes were oftentimes studied separately, using memory paradigms unrelated to standardized neuropsychological batteries commonly used for memory assessment in clinical populations. Furthermore, most studies of the HC long-axis specialization did not separate the HC body from the HC tail, and as a consequence, it is currently unclear whether these two subregions perform similar functions (Poppenk et al., 2013; Small, 2002).

Anatomical connectivity studies suggest that splitting the HC into just two (i.e., anterior and posterior) sections might lead to oversimplified models of its function (Small, 2002; Strange et al., 2014). Due to differences in sensory input, it has been proposed that the anterior-posterior axis is organized along a gradient (Poppenk et al., 2013), with the intermediate HC serving as a key interface point between spatial encoding and behavioral control systems (Strange et al., 2014). Based on anatomical connectivity profiles of different HC segments, Small (2002) proposed three functionally distinct segments within the HC: anterior, middle, and posterior. Consistent with this notion, a series of volumetric and functional experiments revealed that the HC head, body, and tail might play unique roles in memory (Chen et al., 2010; DeMaster et al., 2014; Evensmoen et al., 2013; Spalletta et al., 2016; Travis et al., 2014; de Vanssay-Maigne et al., 2011), while a growing body of clinical MRI literature suggests that different pathological processes sometimes affect the HC head, sometimes the HC body, and sometimes the HC tail (Bouchard et al., 2008; Elliott et al., 2016; Frisoni et al., 2008; Huang et al., 2013; Lindberg et al., 2012; Maller et al., 2007, 2012; Malykhin et al., 2017; Spalletta et al., 2016; Vassilopoulou et al., 2013).

Aside from studying functional differences along the HC anterior-posterior axis, recent advances in functional Magnetic Resonance Imaging (fMRI) enabled researchers to study functional implications of its cross-sectional subfields (transverse axis): Cornu Ammonis 1-3 (CA1-3), dentate gyrus (DG), and subiculum (Sub) (Aly & Turk-Browne, 2016; Azab et al., 2014; Bakker et al., 2008; Berron et al., 2016; Bonnici et al., 2012; Copara et al., 2014; Duncan et al., 2012; Eldridge et al., 2005; Lacy et al., 2011; Reagh et al., 2014; Stokes et al., 2015; Suthana et al.,

2009, 2011, 2015; Tompary et al., 2016; Yassa & Stark, 2011; Zeineh et al., 2003). Because of technical limitations, many of these studies did not segment subfields within the entirety of the HC head (Chen et al., 2011; Copara et al., 2014; Eldridge et al., 2005; Nauer et al., 2015; Stokes et al., 2015; Suthana et al., 2009, 2011; Zeineh et al., 2003) or tail (Berron et al., 2016; Chen et al., 2011; Eldridge et al., 2005; Zeineh et al., 2003), producing activity estimates heavily dominated by the signal from the HC body. Furthermore, while many studies report sub-millimetre in-plane resolution for their subfield segmentations, these were oftentimes collected with relatively thick (i.e, >1.5 mm) slices (Copara et al., 2014; Eldridge et al., 2005; Suthana et al., 2009, 2011; 2015; Stokes et al., 2015; Zeineh et al., 2003). In general, sufficient contrast for subfield segmentation in the most anterior and posterior segments of the HC formation is obtained with slice thickness of 1 mm or less (Bonnici et al., 2012; Malykhin et al., 2010, 2017; Winterburn et al. 2013; Wisse et al., 2012); however, several studies (e.g., La Joie et al., 2010; Yushkevich et al., 2015b) managed to segment subfields within the HC head and tail on T2-weighted MRI data with 2-mm thick slices. Finally, most of the aforementioned subfield studies relied on either some form of voxel-wise hypothesis testing (which can be vulnerable to Type-II error due to strict correction for multiple comparisons, further compounded by small sample sizes of 10–20 participants in most fMRI studies of the HC subfields) or performed region of interest (ROI) analyses on subfields, collapsed across the entire long-axis coverage, potentially oversimplifying the HC anatomy and its relationship to memory. It is currently unclear whether it is the longitudinal or the transverse axis or the interaction between the two that best explains the HC role in episodic memory.

In addition, there is a lack of consensus in the HC literature as to whether the HC formation is dedicated to processing of spatial vs. non-spatial components of episodic memory (Eichenbaum, 2017; Eichenbaum & Cohen, 2014; Kumaran & Maguire, 2005; Lisman et al., 2017; Nadel et al., 2012), and whether the HC is involved in item, not just relational memory (Davachi et al., 2003; Gold et al., 2006; Konkel et al., 2008). In our previous structural MRI study (Travis et al., 2014), we showed that performance on the 'Designs' subtest of the Wechsler Memory Scale (WMS-IV; Pearson Education Inc., 2009) was correlated with volumes of the posterior CA1-3 and DG subfields. This particular subtest was designed to test performance on item, spatial, and item-location associative memories. Despite widespread clinical use of the WMS-IV since its inception in 2009, little research has been done on the 'Designs' subtest other than the initial validation study (Martin & Schroeder, 2014). Although our earlier structural work (Travis et al., 2014) provides

some insight into how the WMS-IV 'Designs' subtest relates to the HC neuroanatomy, volumetric measurements are crude proxies for brain function and cannot truly explain how processes underlying formation and retrieval of item, spatial, and associative memories (assessed by this task) relate to metabolic activity in various segments of the HC structure. Consequently, the main goal of this study was to investigate how activity in various HC subfields and long-axis subregions relates to both encoding and retrieval processes for item, spatial, and associative memories in a 'Designs'-like paradigm, within a single fMRI experiment. To answer these questions, we administered a computerized adaptation of the WMS-IV 'Designs' subtest and used high-resolution fMRI methods in conjunction with manual delineation of the HC subfields within the entire HC formation on ultra-high-resolution structural MRI.

Since multiple theories of HC function (for an overview, see Poppenk et al., 2013) suggest that the posterior HC should be more active during retrieval of detailed memories, we expected to see greater involvement of the posterior HC in retrieval processes. Second, we expected preferential engagement of the posterior HC subfields on spatial memory trials, while item and associative memory trials would not show longitudinal differences in HC activity. Furthermore, we hypothesized that longitudinal differences are not a sharp dichotomy and are best represented by a linear head to tail gradient (Kim, 2015; Poppenk et al., 2013; Small, 2002; Strange et al., 2014). Lastly, based on our previous volumetric study (Travis et al., 2014) we predicted that the posterior DG and CA1-3 subfields play a critical role in the 'Designs' subtest. To additionally improve accuracy and validity of our HC blood oxygen-level dependent (BOLD) response measurements, we used a multi-parameter hemodynamic response deconvolution procedure, aimed at minimizing assumptions about neural and vascular responses during different phases of our memory task.

4.2. Materials and Methods

Participants

Twenty-five healthy individuals (12 males, 13 females, mean age = 25.4 years, range 20–33, mainly graduate and undergraduate students attending the University of Alberta) were recruited through online and poster advertisements. All participants were right-handed with no reported personal history of psychiatric or neurological illness, and drug or alcohol abuse as assessed by a structured interview (Anxiety Disorders Interview Schedule-IV; Brown et al., 2001). The exclusion

criteria were (1) active and inactive medical conditions that may interfere with normal cognitive function and (2) use of medication and non-prescribed substances that could affect brain function. Written, informed consent was obtained from each participant. The study protocol was approved by the University of Alberta Health Research Ethics Board.

Memory task

Our memory task was based on the "Designs" subtest of the Wechsler Memory Scale (WMS-IV; Pearson Education Inc., 2009). The 'Designs' subtest is a highly flexible tool for assessing item, spatial, and item-location binding simultaneously. During the "Designs" test, an examiner shows the examinee a 4 × 4 grid containing 4–8 abstract symbols for 10 s. Episodic memory is tested after a brief (≈5 s) break in two different ways: the examinee (1) re-creates the grid by choosing the abstract symbols they remember and placing them in the corresponding locations, and (2) by performing spatial pattern recognition.

However, when administering the WMS-IV, each examinee is presented with only 4 grids, a number of trials that is insufficient for event-related fMRI. To increase the number of potential grids for our fMRI paradigm, we presented symbols not only from the "Designs," but also from the "Symbol Span" subtest. Abstract symbols from the 'Designs' and 'Symbol Span' subtests were scanned from a paper version of the WMS-IV and resampled to a 700 × 500 pixel resolution. Next, a single rater (MM) generated 11 categories broadly summarizing symbols' patterns and categorized each symbol accordingly (e.g., arrow-like, XX-shaped). Symbol classification was performed to ensure that all symbols within each fMRI trial were sufficiently distinct: only one symbol from a given category could appear on the same grid during encoding or retrieval.

Experimental design

Similar to the "Designs" subtest of the WMS-IV, each trial in our paradigm consisted of one encoding and one retrieval phase. Between the encoding and retrieval trials, an odd/even judgment task (one judgment every 1.25 s) was performed in place of passive fixation. Performing odd/even judgments between the two task phases not only limits rote rehearsal but also produces more accurate estimates of memory-related BOLD activation, especially for the HC formation (Stark & Squire, 2001). All odd/even inter-stimulus-intervals (ISIs), which separated the encoding and retrieval phases from each other, were randomized on a negative exponential distribution with a

median of 12.5 s and lasted between 7.5 and 20.0 s.

During the encoding phase, participants studied 4 × 4 horizontal grids, each containing four abstract symbols randomly placed in 4 out of 16 possible cells. Each trial began with one of three cues: ‘S’ for Symbol, ‘L’ for location, and ‘B’ for both. The ‘S’ cue instructed participants to prioritize symbol learning, regardless of their positions inside the grid (see Fig. 4.1a). The ‘L’ cue instructed the participants to remember which cells in the grid contained a symbol, regardless of which symbols were present in those cells. The ‘B’ cue instructed the participants to learn symbol-location associations. Recent work by Aly & Turk-Browne (2016) demonstrated that HC activity is modulated by attention and that this modulation is stable across various stimuli as long as attention is maintained on a particular type of information within a stimulus. Our design leveraged this finding: during encoding we manipulated attention, as opposed to the stimuli themselves, guaranteeing that any encoding-related activity differences within the HC, when comparing item, location, and associative memories to each other, would be unrelated to visual properties of the stimuli themselves.

Participants' memories were tested in accordance with the previous cue on 2 (out of 4) randomly chosen items. If ‘S’ was the encoding cue, participants completed symbol recognition: they saw four symbols on a screen for 5 s, only one of which was present in the previously studied grid (Fig. 4.1b). To decouple memory retrieval from motor planning, response cues (randomly placed numbers corresponding to MR-compatible button presses) were presented only for the last 3 s of each recognition test. If ‘L’ served as the encoding cue, participants completed a location recognition task, during which they saw a blank 4 × 4 grid for 2 s. Subsequently, numbers 1 to 4 (corresponding to MR button presses) appeared in 4 cells. Only one of those cells contained a symbol in the previously studied grid (Fig. 4.1c). Finally, if ‘B’ was the encoding cue, participants performed one of two versions of a cued recall task (Fig. 4.1d and e). In the first version, grid locations were used as cues, and participants were instructed to identify which symbol was shown in a cued location during the previous encoding phase (Fig. 4.1d). In the second version, symbols were used as cues, and participants were asked to identify in which location on the grid a cued symbol was initially placed (Fig. 4.1e).

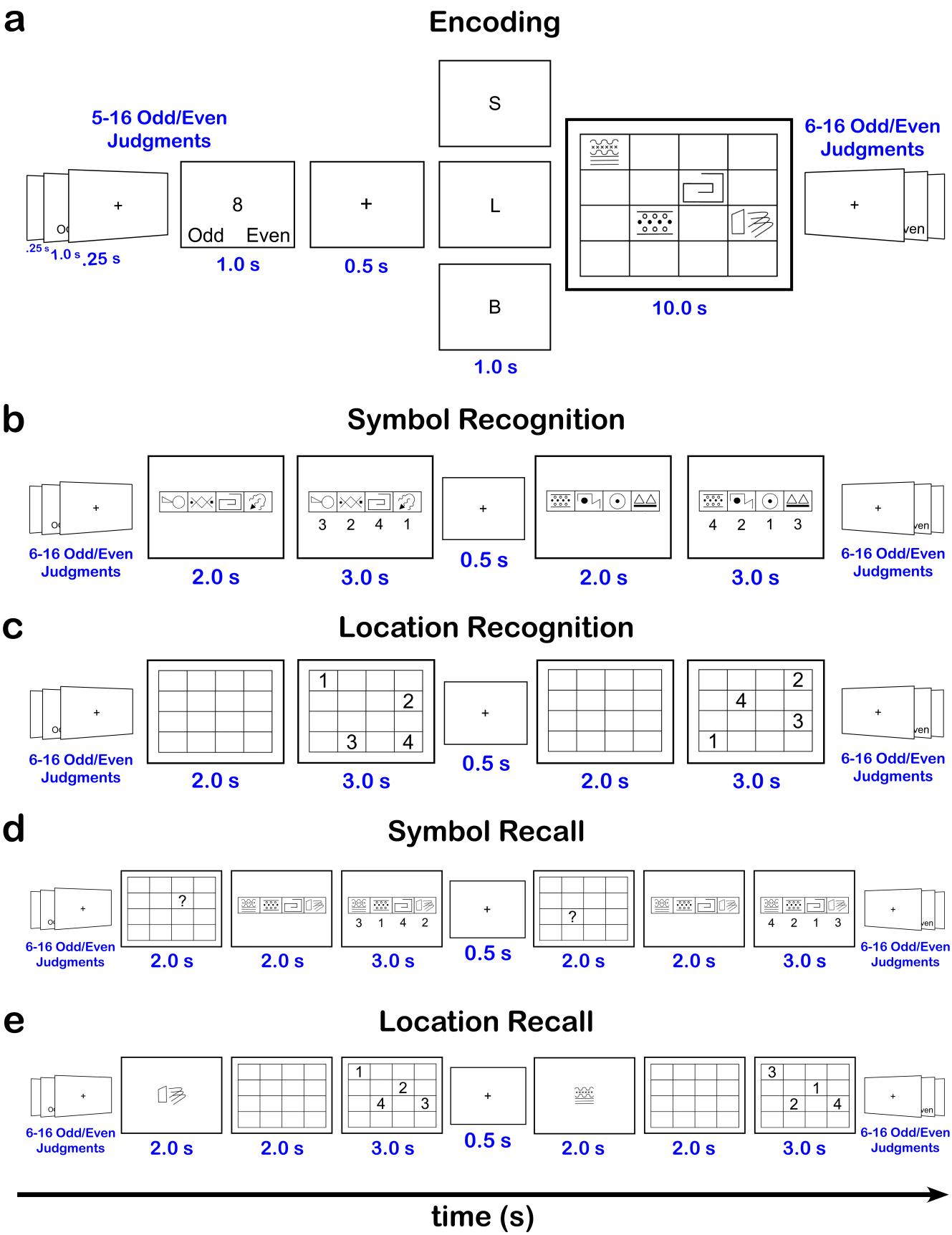

Fig. 4.1. Computerized adaptation of the WMS-IV 'Designs' subtest that was used to study memory encoding (a) and memory retrieval (b–e) processes. Depending on encoding cue, memory was tested using one of the retrieval designs (b–e). An odd/even judgment task was used as a cognitive baseline and separated trials from each other. See main text for detailed task description.

To ensure that participants were familiar with the task and the button-press response system, they completed in-scanner button-press training, odd/even judgment training, and one practice run with immediate accuracy feedback while the scanner was undergoing calibration procedures. In total, there were 12 task runs, each lasting 155 s, with three trials in each run: one set of symbol, location, and both in randomized order. All encoding trials lasted 10 s, regardless of the encoding cue. The retrieval sessions for the symbol and location conditions lasted 10.5 s, and 14.5 s for the association condition. In addition, for the association condition, 6 trials tested memory by providing symbols as cues, and 6 trials tested memory by providing grid locations as cues, in a random order for each participant. To establish the fMRI baseline and to capture the hemodynamic response for the final memory trial, each run began with 6.25 s, and ended with 11.25 s, of the odd/even judgment task. Our task was programmed in Python-based software PsychoPy (Peirce, 2007, 2009), and was displayed inside the scanner through an MR-compatible 1080p 32" LCD panel (Cambridge Research Systems Ltd., Rochester, UK).

Experimental design

All images were acquired on a 4.7 T Varian Inova MRI scanner at the Peter S. Allen MR Research Centre (University of Alberta, Edmonton, AB) using a single-transmit volume head coil (XL Resonance) with a 4-channel receiver coil (Pulseteq). 744 functional volumes were collected axially (in parallel to the AC–PC line) over 12 runs using a custom-written T_2^*-sensitive Gradient Echo Planar Imaging (EPI) pulse sequence [repetition time (TR): 2500 ms; echo time (TE): 19 ms; flip angle: 75°; field of view (FOV): 168 × 210 mm^2; voxel size: 1.5 × 1.5 × 1.4 mm^3; inter-slice gap: 0.1 mm; 35 slices acquired sequentially; GRAPPA parallel imaging with in-plane acceleration factor 2 (Griswold et al., 2002)]. For the HC subfield and subregion segmentation, high-resolution coronal structural images were acquired perpendicular to the AC–PC orientation using a custom-written T_2-weighted 2D Fast Spin Echo (FSE) sequence [TR: 11000 ms; TE: 39 ms; FOV: 200 × 200 mm^2; voxel size: 0.52 × 0.68 × 1.0 mm^3; 90 slices]. To improve image registration accuracy between anatomical and functional scans, axial high-resolution 2D FSE images were acquired with brain coverage approximate to that of the fMRI data [TR: 7000 ms; TE: 38 ms; FOV: 210 × 200 mm^2; voxel size: 0.52 × 0.68 × 1.0mm^3; 45 slices]. A whole brain T_1-weighted 3D Magnetization Prepared Rapid Gradient-Echo (MPRAGE) sequence [TR: 8.5 ms; TE: 4.5 ms; inversion time: 300 ms; flip angle: 10°; FOV: 256 × 200 × 180 mm^3; voxel size: 1 × 1 × 1 mm^3] was used to acquire

anatomical images for automated tissue segmentation. Finally, to correct for inhomogeneity-related EPI distortions, we used a multi-echo 3D gradient echo sequence [TR: 577.8 ms; TE: 3.56, 6.71 ms; flip angle: 50°; FOV: 192 × 168 mm^2; voxel size: 1.5 × 1.5 × 1.5 mm^3; 35 slices] to calculate B_0 fieldmap for each participant. The entire image acquisition was spread over two separate sessions, at most two weeks apart. Coronal FSE images and whole-brain MPRAGE images were acquired during the first (1 h) visit, while the fMRI data, along with the Axial FSE, and the fieldmaps were collected during the second (1.5 h) visit. During our fMRI acquisitions, we also collected cardiac and respiration waveforms using an MP150 system with a pulse photoplethysmograph placed on the left ring finger and a pneumatic belt strapped around the upper abdomen, respectively (Biopac Systems Inc., Montreal, QC). Fig. 4.2 demonstrates orientation and brain tissue coverage of our structural and functional scans.

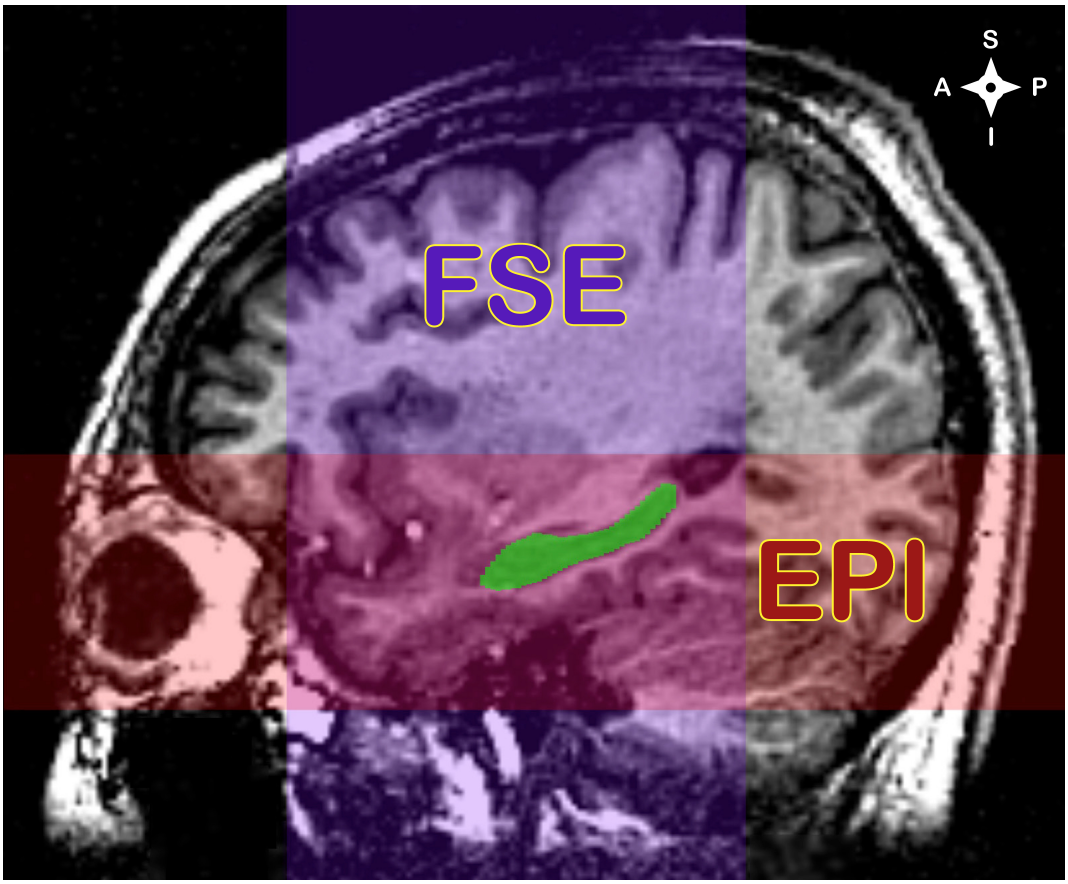

Fig. 4.2. Brain tissue covered by high-resolution anatomical and high-resolution functional scans. A single participant's full-brain T_1-weighted anatomical scan is shown in the background. The violet overlay represents coverage of the ultra-high-resolution anatomical 2D FSE scan, which was used to manually segment the hippocampal subfields and subregions. The red overlay represents areas captured by the high-resolution fMRI EPI acquisition. A segmented hippocampus is shown in green.

Hippocampal segmentation

All HC ROIs were manually traced on the T_2-weighted coronal FSE images with a mouse-driven cursor using freely available FreeView v. 4.0 software (MGH, Boston, MA). ITK-SNAP (v. 3.6.0; Yushkevich et al., 2006) was used to build 3D models of the HC ROIs for visualization purposes (see Fig. 4.3). Our subfield segmentation technique (Malykhin et al., 2010) was developed with the guidance from the Duvernoy (2005) atlas of the human HC and is based on structural connectivity, as opposed to cytoarchitectonic properties.

Here, we divided the HC into three subfield areas corresponding to our best approximation of the CA areas 1–3 (CA1-3), DG&CA4 (henceforth referred to as DG), and Sub within the HC head, body, and tail (Malykhin et al., 2007, 2010). In our parcellation method, the most posterior coronal slice of the HC head was the first slice where the uncal apex (uncus) was clearly present (Duvernoy, 2005). Consequently, the most anterior coronal slice of the HC body was the slice immediately posterior to uncus (Malykhin et al., 2007, 2010). The most anterior coronal slice of the HC tail was the first slice where the fornix was clearly seen in full profile or was separated from the wall of the ventricle, whichever came first (Malykhin et al., 2007, 2010). Similar definitions of the long-axis subregions have been used by other studies with MRI acquisitions perpendicular to the AC-PC axis (Boccardi et al., 2015; Malykhin et al., 2007, 2010; Pruessner et al., 2000), as well as by studies with MRI acquisitions perpendicular to the HC longitudinal axis (Daugherty et al., 2015; La Joie et al., 2010). Because a substantial portion of the CA3 subfield is encapsulated within the DG/CA4 on coronal slices (Adler et al., 2014; Ding & Van Hoesen, 2015), it is virtually impossible to separate the CA3 from the DG ROIs based on image contrast alone (Reagh et al., 2014). As a result, the CA3 subfield in our segmentations was almost evenly split between the DG and CA1-3 ROIs (Malykhin et al., 2010), while the CA2 subfield was fully integrated into the CA1-3 ROI. Furthermore, our Sub volumes consisted predominantly of the Sub proper and excluded most of the presubiculum or parasubiculum.

All segmentations of the HC subregions (head, body & tail) and HC subfields (CA1-3, DG & Sub) were performed by a single highly experienced rater (YH), trained by the developer of the protocol (NM). Intra-rater and inter-rater reliabilities for the HC subfield/subregion volumes were assessed by retracing structural T2-weighted MRI images from 5 subjects (i.e., 10 HC total) at a one-week interval. Inter/intra-rater reliability intraclass correlation coefficients (ICCs) for the long-axis subregions were as follows: 0.95/0.92 for the HC head, 0.83/0.93 for the HC body, and

0.95/0.88 for the HC tail. The corresponding inter/intra-rater Dice similarity coefficients (DSCs) were 0.89/0.90 for the HC head, 0.86/0.87 for the HC body, and 0.80/0.82 for the HC tail. For the cross-sectional subfields, the inter/intra-rater reliability ICCs were as follows: 0.92/0.92 for the CA1-3, 0.86/0.84 for the DG, and 0.87/0.95 for the Sub. Matching inter/intra-rater DSCs were 0.73/0.75 for the CA1-3, 0.81/0.81 for the DG, and 0.74/0.74 for the Sub. For the total HC, inter/intra-rater ICCs were 0.95/0.97, and inter/intra-rater DSCs were 0.89/0.90. All ICCs were statistically significant at $\alpha = 0.001$.

Following manual segmentation on structural MRI, the HC labels were down-sampled (using nearest neighbor interpolation) to match the resolution of fMRI acquisition. Next, a single rater (YH) manually adjusted all ROIs to ensure accurate overlap between the original labels and the downsampled ones and to remove all ROI voxels severely impacted by susceptibility artifacts. Since individual subfield volumes (particularly Sub) within the HC tail are very small when resampled to the fMRI resolution (see Table 4.1 for ROI volumes), we merged subfields from the HC body with those from the HC tail. This reduced volumetric discrepancies between subfield ROIs and improved the temporal signal-to-noise ratio (tSNR) in smaller subfields (see Table 4.2 for tSNR details). However, to verify that activity in the HC body was indeed similar to that in the HC tail, we also analyzed activity in each long-axis subregion separately. Fig. 4.3 demonstrates our segmentation methodology on structural and functional data.

Table 4.1
Number of voxels for each of the hippocampal subregion and/or subfield ROIs. Values are in raw fMRI voxel counts (1.5-mm isotropic), averaged across participants.

Subregion/Subfield (voxel count ± SD)	*Cornu Ammonis* 1-3		Dentate Gyrus		Subiculum		Total HC Subregions	
	Left	Right	Left	Right	Left	Right	Left	Right
HC Head	317.8 ± 72.0	359.8 ± 85.1	94.7 ± 16.4	102.9 ± 11.3	131.6 ± 30.5	135.6 ± 33.5	544.1 ± 99.2	598.2 ± 112.8
HC Body	110.0 ± 23.7	122.6 ± 15.8	147.8 ± 23.7	148.6 ± 20.1	105.0 ± 20.1	109.1 ± 20.3	362.8 ± 48.4	380.2 ± 41.3
HC Tail	63.8 ± 12.0	63.3 ± 17.3	106.2 ± 29.0	110.8 ± 30.2	13.0 ± 6.4	14.5 ± 7.2	183.0 ± 41.0	188.6 ± 41.1
HC Body + Tail	173.9 ± 29.5	185.9 ± 24.0	254.0 ± 42.4	259.4 ± 42.8	118.1 ± 22.6	123.4 ± 22.2	545.8 ± 72.5	568.8 ± 66.4
Total HC Subfields	491.7 ± 74.5	545.6 ± 84.2	348.7 ± 46.2	362.3 ± 45.7	249.7 ± 41.8	259.2 ± 46.7	1090.0 ± 108.6	1155.6 ± 113.3

Table 4.2

Effective temporal signal-to-noise (tSNR) ratios for each hippocampal ROI. All tSNR values were computed on preprocessed data (motion correction, despiking, and removal of non-BOLD cardiac- and pulmonary-related waveforms). The upper half of the table shows ROI-level tSNR, computed from voxel-averaged time series across the entire ROI. The bottom half of the table shows voxelwise tSNR. Here, tSNR was computed for each hippocampal voxel and the resulting tSNR values were averaged across voxels, which belong to a given subfield or subregion.

Subregion/Subfield	*Cornu Ammonis* 1-3		Dentate Gyrus		Subiculum		Total HC Subregions	
	Left	Right	Left	Right	Left	Right	Left	Right
ROI tSNR ± SD								
HC Head	285.5 ± 42.0	344.6 ± 37.4	176.7 ± 37.6	215.6 ± 35.2	201.9 ± 26.4	229.1 ± 39.3	324.8 ± 41.6	385.6 ± 42.3
HC Body	202.5 ± 44.4	278.0 ± 49.8	218.4 ± 41.0	261.9 ± 40.1	215.6 ± 40.5	259.9 ± 39.7	300.2 ± 50.3	371.1 ± 48.9
HC Tail	213.4 ± 45.1	261.5 ± 46.3	252.7 ± 50.5	284.8 ± 48.0	115.2 ± 29.6	136.9 ± 34.2	305.5 ± 53.4	348.8 ± 48.6
HC Body + Tail	272.1 ± 55.2	352.2 ± 52.3	296.0 ± 47.7	342.4 ± 47.7	232.2 ± 41.7	276.6 ± 39.8	374.7 ± 56.2	443.4 ± 47.2
Total HC Subfields	360.4 ± 52.4	450.2 ± 48.2	319.4 ± 46.7	370.7 ± 45.8	290.2 ± 29.6	342.2 ± 40.2	423.7 ± 58.3	516.4 ± 50.6
Voxel tSNR ± SD								
HC Head	36.0 ± 6.7	38.9 ± 7.7	35.1 ± 7.7	41.1 ± 8.3	33.3 ± 6.0	35.9 ± 6.9	35.2 ± 6.6	38.6 ± 7.6
HC Body	33.2 ± 7.3	44.2 ± 7.6	36.2 ± 7.6	44.8 ± 7.5	35.9 ± 7.0	42.4 ± 6.4	35.2 ± 7.2	43.9 ± 7.2
HC Tail	45.9 ± 7.6	52.3 ± 6.6	47.0 ± 7.3	52.2 ± 7.0	44.6 ± 6.8	49.2 ± 6.7	46.4 ± 7.3	52.1 ± 6.8
HC Body + Tail	37.9 ± 7.4	47.0 ± 7.0	40.7 ± 7.4	48.0 ± 7.0	36.9 ± 6.9	42.9 ± 6.2	39.0 ± 7.3	46.6 ± 6.8
Total HC Subfields	36.6 ± 6.7	41.7 ± 7.6	39.2 ± 7.3	46.0 ± 7.2	35.0 ± 6.2	39.4 ± 6.5	37.1 ± 6.8	42.4 ± 7.5

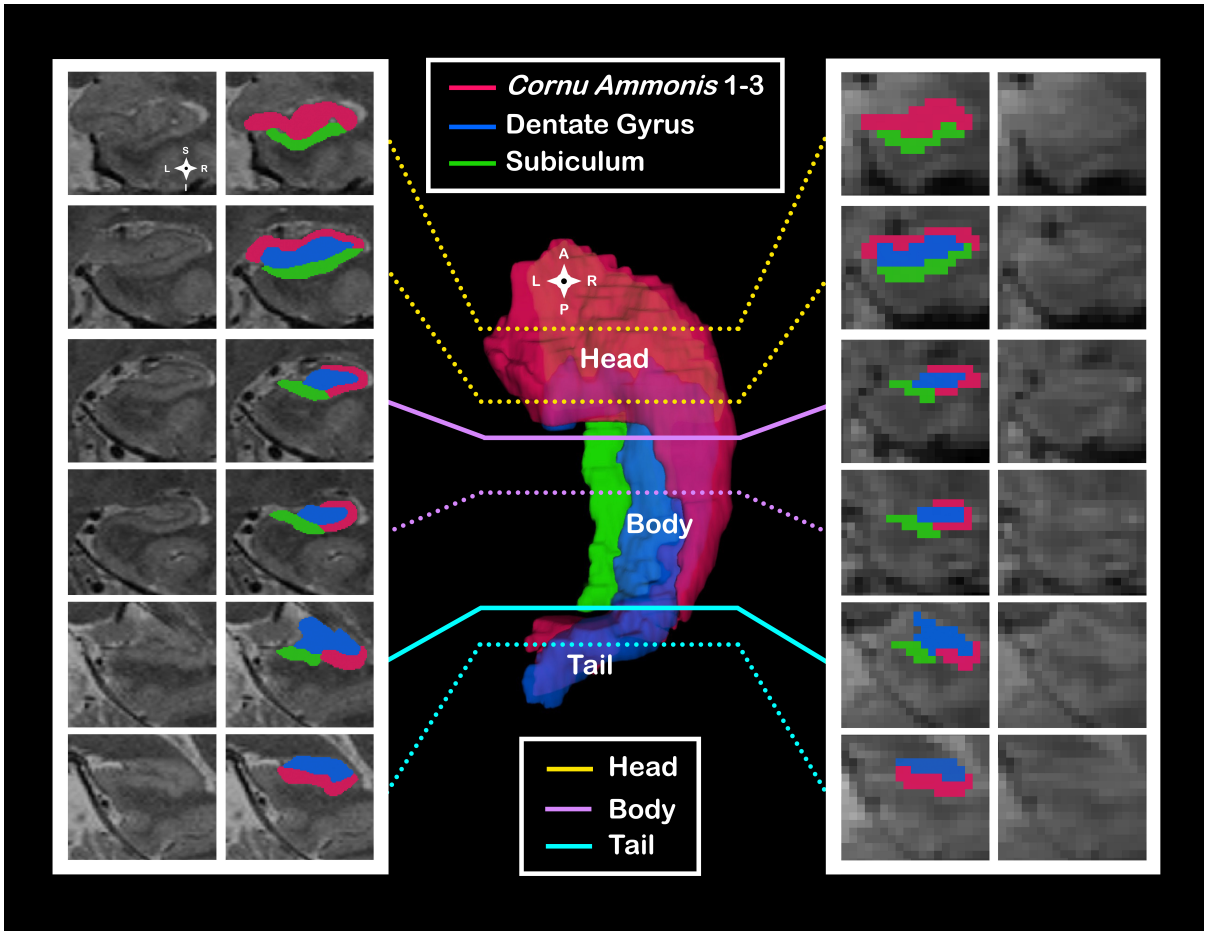

Fig. 4.3. Three-dimensional reconstruction of the hippocampal subfields and anterior-posterior subregions from a healthy volunteer. Panels to the left of the 3D model show subfields and subregions on a high-resolution T_2-weighted structural scan. Panels to the right of the 3D reconstruction show subfield and subregion masks after they were registered to the fMRI data and downsampled to match the fMRI resolution.

Image preprocessing

Most of the image processing was performed in SPM12 (Wellcome Trust Centre for Neuroimaging, UCL, UK). Prior to registration, MPRAGE images underwent correction for intensity non-uniformity using N3 program (Sled et al., 1998). Next, anatomical images were cropped using a custom-written MATLAB (The MathWorks Inc., Natick, MA) script in order to isolate areas of overlapping coverage. These overlapping portions of anatomical images were used to compute rigid-body transformation matrices to register all anatomical images to each other.

The unified '*realign & unwarp'* function in spm12 was used to correct geometric distortions in fMRI data caused by B_0 inhomogeneity and to realign all fMRI volumes to the first functional volume (Andersson et al., 2001). Next, an average EPI was computed and was registered to the axial FSE image using a combination of manual and automatic registration tools. To ensure optimal registration for the HC formation, white matter (WM)/gray matter (GM) boundaries were (manually traced on three coronal, three axial, and three sagittal slices proximal to the HC) used to fine-tune image alignment. Automated rigid-body registration tools were then used to register all the remaining fMRI volumes to the manually registered average EPI volume. To identify signal spikes and to account for spin-history-related head-movement artifacts in the fMRI time series, we used the Artifact Detection Toolbox (ART; http://www.nitrc.org/projects/artifact_detect/) for MATLAB. All fMRI volumes with framewise displacement > 0.5 mm/TR were marked for scrubbing, as were all fMRI volumes with noticeable signal spikes (i.e., scan-to-scan differences in signal intensity > 3 SDs above the run's mean). Because we employed sequential slice acquisition, the most superior and the most inferior slices with the HC tissue were acquired less than 1.25 s apart in most participants. Rather than risk artifacts caused by slice timing correction, we ensured that all HRf-related regressors during GLM parameter estimation were temporally aligned to the acquisition of the middle HC slice in each subject. Similarly, in order to preserve the spatial resolution, no spatial smoothing was applied to the fMRI data.

Physiological noise correction was performed using custom-written MATLAB implementation of the RETROICOR (Glover et al., 2000) and RVTHR techniques (Birn et al., 2006, 2008; Chang et al., 2009). From cardiac waveforms, we created 12 nuisance regressors to absorb signal changes due to blood flow pulsatility (RETROICOR 2^{nd}-order Fourier basis, temporally aligned to the acquisition of the most superior, the middle HC, and the most inferior slices of each fMRI volume) and one regressor to absorb signal changes due to heart rate variability

(Chang et al., 2009; Glover et al., 2000). Each participant's respiratory wave-forms were used to generate 4 respiratory regressors (RETROICOR 2nd-order Fourier basis temporally aligned to the acquisition of the middle HC slice, t_{TR}), accounting for respiration-induced magnetic field changes (Glover et al., 2000), as well as 3 time-lagged [t_{TR} – 8 s, t_{TR} – 2 s, t_{TR} + 4 s] regressors representing respiratory volume per time (RVT) convolved with the respiratory response function (Birn et al., 2008). Those three RVT-related regressors were used to absorb variability in the fMRI time series caused by fluctuations in CO_2 concentration resulting from variation in breath depth and/or breath rate (Birn et al., 2006, 2008). Next, we generated a partially filtered fMRI dataset, from which motion, cardiac sources, respiratory-related signals and low-frequency drifts (128 s high-pass filter) were removed. From this dataset, the first three eigenvariate WM time courses and the first three eigenvariate CSF time courses were extracted using preprocessing functions implemented in the CONN toolbox for MATLAB (v. 16.a; Whitfield-Gabrieli & Nieto-Castanon, 2012). In total, for each fMRI run, there were 32 nuisance regressors (20 RETROICOR&RVTHR, 6 WM&CSF, and 6 motion from realignment), plus one regressor for each fMRI volume marked for scrubbing based on movement and global signal intensity criteria described above. In all GLM procedures, low-frequency signal drifts were removed with a 128 s high-pass filter, and the first-order autoregressive (AR1) correction for serial autocorrelation was applied.

Estimation of hemodynamic response functions for encoding and retrieval

The profile of the hemodynamic response function (HRf) in subcortical brain regions need not be the same as the standard double-gamma function often used to model cortical responses (Devonshire et al., 2012; Ekstrom, 2010; Handwerker et al., 2004; Hrybouski et al., 2016; Pernet, 2014). Consequently, extracting raw signal change over points in time without reference to a standard hemodynamic template often leads to more accurate BOLD signal measurements. While it is well established that FIR-based approaches provide more accurate depictions of BOLD response (Glover, 1999; Lindquist et al., 2009) as they make no assumption about neural or vascular properties of a region (FIR basis set contains one free parameter for every time point in every trial type) FIR deconvolutions can produce noisy solutions in typical fMRI datasets (Goutte et al., 2000; Lindquist et al., 2009). Similar to our previous high-resolution fMRI work (Hrybouski et al., 2016), we incorporated methodology designed to minimize the HRf bias without substantial loss of statistical power by computing task- and region-specific double-gamma functions for our HC

activity analyses.

First, the HC HRf was deconvolved using the FIR technique (8 TR bins). Events for all stimuli categories ('S', 'L', and 'B') were pooled together, regardless of subsequent memory performance, and the mean HRf was estimated for each HC, separately for encoding and retrieval phases. These FIR results revealed that the informed basis set (i.e., canonical HRf with time and dispersion derivatives) would be sufficient to estimate the HC HRf in our task. Consequently, we used the informed basis set model to deconvolve the HRf for each event for each condition separately (encoding 'S', encoding 'L', encoding 'B', retrieval 'S', retrieval 'L', and retrieval 'B'). The HRf and derivative betas were used to reconstruct task-related signal change for each event. It is worth noting that this approach treats the derivative betas as BOLD response modulators rather than covariates (Calhoun et al., 2004; Henson et al., 2002; Hrybouski et al., 2016). Because the ISI between the retrieval tests was short (0.5 s), and did not vary from trial to trial, it was not feasible to deconvolve BOLD signal for individual retrieval tests. Instead, we restricted all activity analyses to trials for which participants obtained 2 out of 2 retrieval accuracy: 11.12 (SD = 0.97) trials for the symbol condition, 8.40 (SD 1 = 2.36) trials for the location condition, and 8.00 (SD = 2.06) trials for the association condition, on average. These numbers are substantially higher than what would be expected if subjects were randomly guessing on memory tests [sampling distribution for 2 out 2 retrieval accuracy under the null hypothesis was estimated using 1,000,000 Monte Carlo simulations; mean = 0.75, standard error = 0.17]. By limiting our analyses to trials on which successful learning took place, we eliminated memory-related variability in BOLD signal onset during retrieval and ensured that our HC activity estimates during the preceding encoding phase were linked to successful formation of novel memories. The latter is particularly important as prior fMRI studies demonstrated differential encoding activity for remembered vs. forgotten stimuli (Chua et al., 2007; Gold et al., 2006; Ranganath et al., 2004).

Subsequently, subject-specific encoding and retrieval HRf time courses were estimated for each left/right HC ROI (i.e., total HC, total head, total body, total tail, total CA1-3, total DG, total Sub, head CA1-3, head DG, etc.), separately for each memory condition (i.e., symbols, locations, both). Using this approach, we obtained 96 encoding and 96 retrieval HRfs from each subject. These HRfs were then rescaled to % signal change units and averaged across participants. Next, each of the 192 (96 encoding, 96 retrieval) subject-averaged HRf time courses was manually classified by a single observer (SH) as being (1) BOLD-like activations, (2) BOLD-like

deactivations, or (3) noise. The following rules, developed based on previously published neurovascular coupling literature (Glover, 1999; Goutte et al., 2000; Lindquist et al., 2009; Logothetis et al., 2001; Shmuel et al., 2006), were used to perform this HRf labeling:

1. The reconstructed response must be non-linear with an initial increase (or decrease for deactivation) in signal, followed by a peak (or trough for deactivation) with a subsequent return to the baseline. The informed basis set, which was used to estimate HRfs in this study, enforces the zero baseline prior to the stimulus onset and ≈16 s after the stimulus onset. HRfs showing consistent increases or decreases in activity were classified as noise.
2. At least one clear positive or negative peak is present. The time gap between the stimulus onset and the HRf peak (or trough) must be at least 3.5 s (≈2nd poststimulus TR in our study). Whether the HRf activity was sustained (i.e., a plateau) or peaked and quickly returned to the zero baseline was irrelevant for classification purposes.
3. For BOLD classification, the absolute (relative to the zero baseline) value of the largest peak/trough is greater than the absolute (relative to the zero baseline) value of signal amplitude at the first poststimulus TR; noise classification otherwise.
4. (a) If multiple peaks were present, (b) instances when all peaks & troughs were only positive or only negative were classified as BOLD activations or deactivations, respectively. (c) For ambiguous cases with two opposing peaks (i.e., one activation and one deactivation), only HRf cases when the absolute value (relative to the zero baseline) of the larger peak was twice as large as the absolute value (relative to the zero baseline) of the smaller peak were retained (i.e., noise otherwise, as a consequence of poor signal-to-noise ratio), and activation/deactivation labels were assigned in accordance with the sign of the greatest (i.e., dominant) peak/trough.
5. Classify BOLD-like (i.e., remaining) HRfs as activation or deactivation. For activation, the largest HRf peak must be above the HRf amplitude at the first poststimulus TR. For deactivation, the strongest BOLD deactivation must be below the HRf amplitude at the first poststimulus TR.

An algorithmic diagram providing step-by-step instructions on how to classify HRfs using these rules, along with accompanying examples, is available in Fig. 4.4.

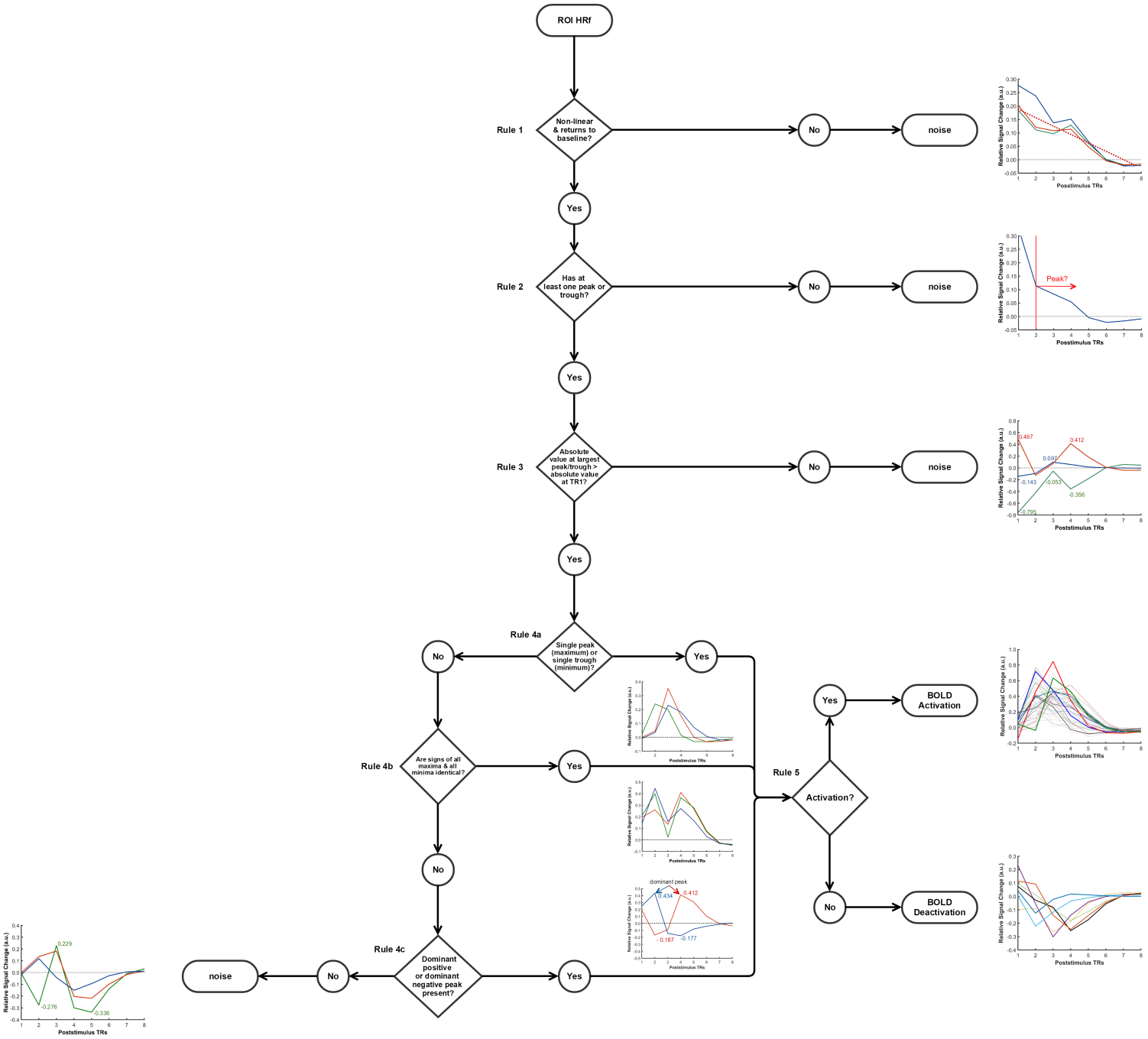

Fig. 4.4. Step-by-step algorithmic instructions on how to manually classify an ROI's HRf as activation, deactivation, or noise.

Intra-rater and inter-rater classification agreement was assessed by reclassifying 40 randomly chosen HRfs into positive BOLD, negative BOLD, or noise at a one-week interval. Intra-rater reclassification produced the same labels for all 40 HRfs, while inter-rater classification comparison resulted in 97.5% classification agreement between the two raters (SH and NM). Out of 192 HRfs, approximately 15% were categorized as noise, 5% as BOLD deactivation, and the remaining 80% as BOLD activation. All negative BOLD responses were inverted in order to ensure that not only activations but also deactivations were considered when estimating the optimal overall BOLD response model for the HC formation. Finally, the overall encoding and retrieval HRfs were computed by collapsing positive and inverted negative BOLD responses across all HC ROIs and memory conditions (i.e., symbol, location, both). Averaging across task conditions reduces the risk of overfitting the data, especially when comparing HC activity among different memory trials. Similarly, averaging BOLD response across the HC ROIs reduces the risk of overfitting a BOLD response model in any particular HC segment, a problem when comparing activity among various HC ROIs. Because of differences in task timing, we did not collapse HRfs across the encoding and retrieval phases, and as a result, each phase of our memory task had its own empirically-derived HRf. Manual labeling of HRfs in our analysis pipeline took approximately 2 h to complete.

Next, the SIMPLEX algorithm (Nelder & Mead, 1965) was used to fit double-gamma functions (as implemented in the *spm_hrf* function within SPM12) to the average encoding and average retrieval HRfs. During each fitting procedure, six parameters (delay to response, delay of undershoot, dispersion of response, dispersion of undershoot, ratio of response to undershoot, and onset) were optimized over 20,000 iterations to minimize the root-mean-squared-deviation (RMSD) between the double-gamma function and each of the two HRf time courses. These optimized double-gamma functions (see Fig. 4.5) were used to model the expected BOLD response for every encoding and retrieval event with 2 out of 2 retrieval accuracy. Our data processing steps are summarized in flow-chart form in Fig. 4.6.

Lastly, the MarsBar toolbox for SPM (v. 0.43; http://marsbar.sourceforge.net) was used to extract beta parameters for each event of interest and to rescale activity estimates to percent signal change units. MarsBar performs ROI-specific scaling, and all rescaled parameters represent signal change in relation to the baseline activity. Such scaling procedure is especially relevant to fMRI studies of the HC because, as Olman et al. (2009) showed, the anterior HC subfields are more vulnerable to susceptibility artifacts than their posterior counterparts. It is worth noting that in

addition to scaling, our acquisition parameters and preprocessing procedures were specifically designed to minimize susceptibility-related confounds when measuring the HC activity. Consequently, tSNR differences among various HC segments in our preprocessed fMRI data were less than 15% in most instances (see Table 4.2 for details).

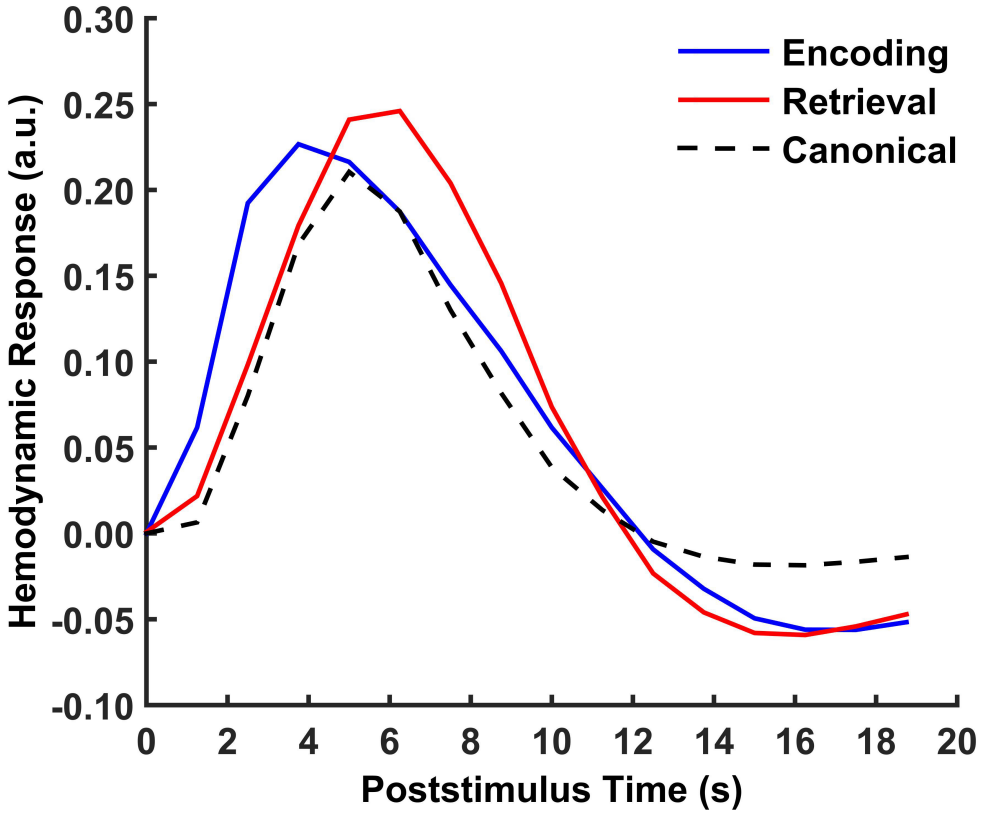

Fig. 4.5. Fitted BOLD response functions for encoding and retrieval phases of our task, averaged across participants. Encoding and retrieval double-gamma functions were optimized to fit the hippocampal BOLD response, estimated using Finite Impulse Response and Informed Basis Set models (a.u., arbitrary units). Fitted encoding/retrieval parameters were 6.01/11.98 for delay of response, 16.23/12.08 for delay of undershoot, 2.75/2.06 for dispersion of response, 1.35/2.06 for dispersion of undershoot, 2.19/1.01 for ratio of response to undershoot, and 0.69/-0.81 for onset.

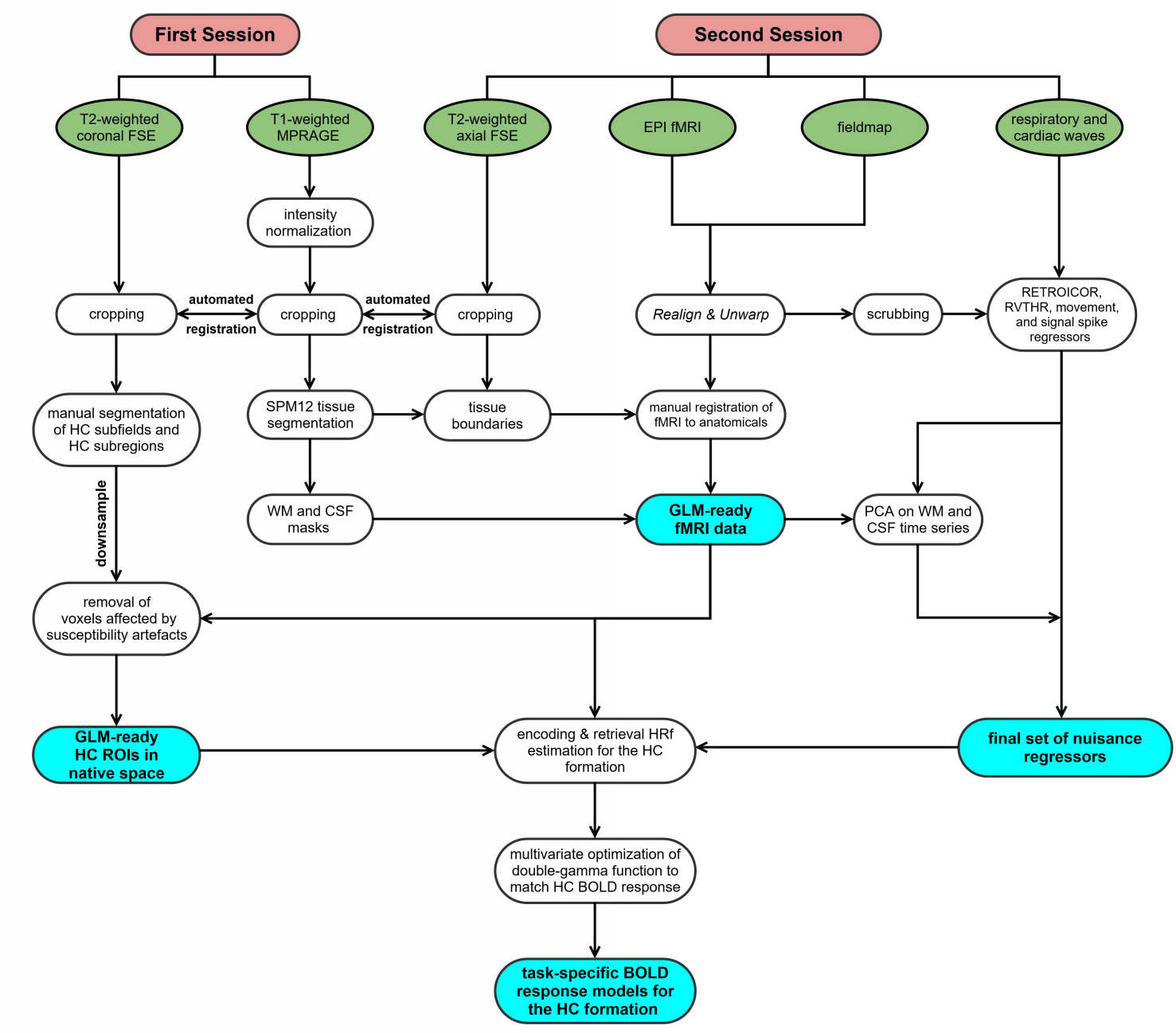

Fig. 4.6. Schematic of the analysis pipeline. Green boxes represent raw data, and blue boxes represent final inputs into hippocampal ROI activity analyses. See methods section for a detailed description of each step.

Statistics

All random-effects analyses were performed in SPSS (v. 22; IBM Inc., Armonk, NY). We statistically compared BOLD activity using four separate ANOVA designs: (1) a two-way repeated-measures ANOVA on total HC activity with participants as a random factor, and Hemisphere (left, right) and Condition (symbol, location, both) as fixed factors; (2) a three- way repeated-measures ANOVA on total subfields' activity estimates with participants as the random factor, and ROI (CA1-3, DG, Sub), Hemisphere (left, right), and Condition (symbol, location, both) as fixed factors; (3) a three-way repeated-measures ANOVA on total subregions' activity estimates with Total Subregions (head, body, tail) as the ROI factor, and otherwise the same design as in (2); (4) four- and three-way repeated measures ANOVAs, aimed at comparing activities in the anterior (head) and posterior (body + tail) subfields to each other, with Subregion (anterior, posterior), Subfield (CA1-3, DG, Sub), Hemisphere (left, right), and Condition (symbol, location, both) as fixed factors, and participants as the random factor. ANOVAs were first conducted on the HC activity during memory encoding, followed by analyses of memory retrieval, and finally on encoding vs. retrieval differences. One-sample *t*-tests were used to compare the HC signal during memory-related processing to the baseline activity (i.e., HC activity while performing the odd/even judgment task). Holm–Bonferroni correction for multiple hypothesis testing was used for all post-hoc comparisons (whether follow-up ANOVAs or *t*-tests) and for all tests vs. the odd/even baseline. Only FWE-corrected *p*-values are reported in the results section. All parametric results were subsequently verified using permutation tests (100,000 shuffles). Since statistical decisions from both approaches were identical, we report GLM-based inferences only.

4.3. Results

Behavior

Behavioral results showed that participants performed best during the symbol condition [M = 95.5%; 95% bias-corrected and accelerated (BCa) bootstrap confidence interval (CI) = (93.0%, 97.5%)]. Performance on the more difficult location and association trial types was 79.5% [95% BCa bootstrap CI = (74.2%, 84.8%)] and 78.3% [95% BCa bootstrap CI = (73.3%, 83.5%)], respectively. We used a one-way repeated-measure ANOVA to compare accuracies across conditions, which revealed a significant main effect of Condition [$F_{(2,48)}$ = 28.18, p < .001, η^2 = 0.540] where performance on the symbol condition was higher than on the location [$t_{(24)}$ =

6.05, $p < .001$, $d = 1.21$, $M_{diff} = 16.0\%$] and association [$t_{(24)} = 7.47$, $p < .001$, $d = 1.49$, $M_{diff} = 17.2\%$] conditions. There was no statistical difference in performance between the location and association conditions ($p = .67$).

Functional MRI: total hippocampus

During memory encoding, there were no differences in activity between conditions in either HC [two-way repeated-measures ANOVA; Condition, $F_{(2,48)} = 0.09$, $p = .91$, partial $\eta^2 = 0.004$; Condition × Hemisphere interaction, $F_{(2,48)} = 0.78$, $p = .47$, partial $\eta^2 = 0.031$]. After averaging across trial types, both HC showed increased activity (relative to the odd/even baseline) during memory encoding [Left: $t_{(24)} = 8.00$, $p < .001$; Right: $t_{(24)} = 4.30$, $p < .001$], although activity in the left HC was marginally greater than that in the right HC [$F_{(1,24)} = 3.88$, $p = .060$] (see Fig. 4.7a, Table 4.3 for details).

In contrast to the encoding trials, during memory retrieval, there were condition-related differences in HC activity [two-way repeated-measures ANOVA; Condition × Hemisphere interaction, $F_{(2,48)} = 9.26$, $p < .001$, partial $\eta^2 = 0.278$]. In the right HC, activity did not differ between conditions [$F_{(2,48)} = 2.64$, p = .092, $\eta^2 = 0.099$], and after averaging across all trial types, was marginally greater than during odd/even judgment making [$t_{(24)} = 1.98$, $p = .059$]. However within the left HC, we observed condition-related differences in activity [$F_{(2,48)} = 5.63$, $p = .013$, $\eta^2 = 0.190$], with location trials showing statistically significant deactivation [$t_{(24)} = -3.22$, $p = .011$], while activity during item and item-location association trials was not statistically different from the odd/even baseline (Table 4.3). Laterality effects were significant only for the Location condition [$F_{(1,24)} = 30.95$, $p < .001$] (Fig. 4.7b). This Condition × Hemisphere interaction was statistically significant in all long-axis segments of the HC formation, and in every subfield (all ps < .050), demonstrating consistent preference of the right HC for spatial memory retrieval.

Both HC were more active during memory encoding than during memory retrieval [left: $t_{(24)} = 6.52$, $p < .001$; right: $t_{(24)} = 2.19$, $p = .039$] (Table 4.3); however, encoding vs. retrieval differential in the HC activity was larger in the left hemisphere [$t_{(24)} = 2.58$, $p = .016$]. None of the condition-related effects for the encoding vs. retrieval contrast reached statistical significance [two-way repeated-measures ANOVA; Condition, $F_{(2,48)} = 0.85$, $p = .432$; Condition × Hemisphere interaction, $F_{(2,48)} = 2.17$, $p = .134$].

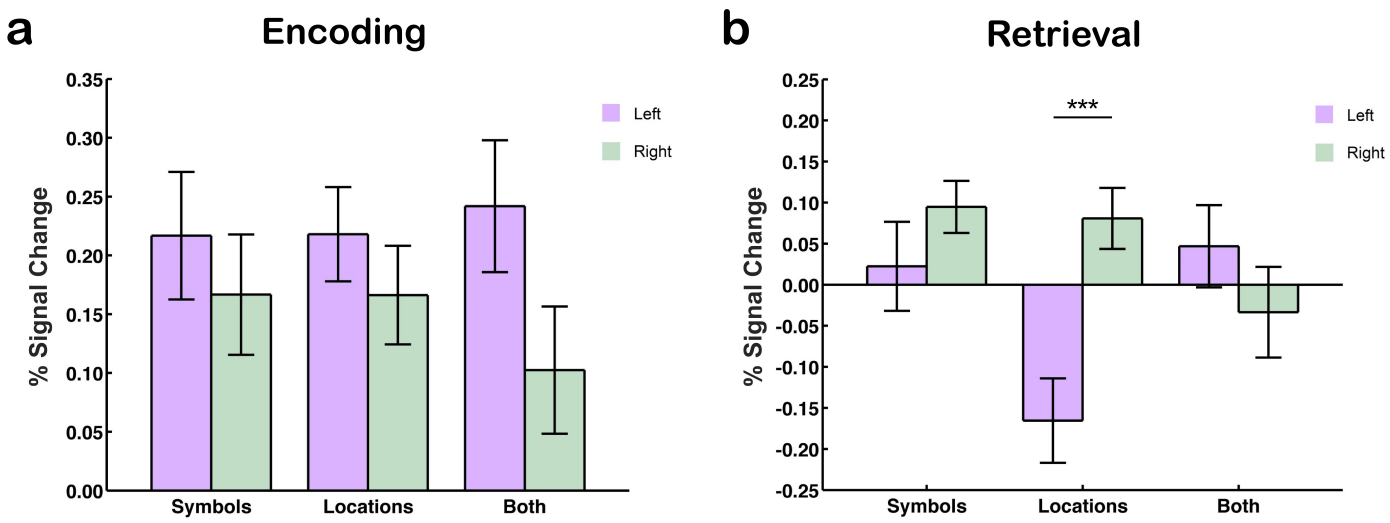

Fig. 4.7. Activity in the total hippocampus during the encoding (a) and retrieval (b) phases of our memory task, separated by trial type and hemisphere. Error bars represent the standard error of the mean. *** FWE $p < .001$.

Functional MRI: total hippocampal subfields

Each of the three-way repeated-measures ANOVAs on the total subfield data revealed a significant main effect of Subfield [encoding: $F_{(2,48)} = 15.98$, $p < 10^{-5}$, partial $\eta^2 = 0.400$; retrieval: $F_{(2,48)} = 13.54$, $p < .001$, partial $\eta^2 = 0.361$; encoding − retrieval: $F_{(2,48)} = 4.38$, $p = .018$, partial $\eta^2 = 0.154$], while all Subfield-related interactions were not statistically significant (all ps > .10). Consequently, we collapsed all encoding and all retrieval data across hemispheres and memory (item, spatial, associative) trial types.

Although all HC subfields were active during the encoding trials (see Fig. 4.8a, Table 4.3), encoding activity in the DG was larger than in the other two subfields [DG vs. CA1-3: $t_{(24)} = 4.51$, $p < .001$; DG vs. Sub: $t_{(24)} = 5.16$, $p < .001$]. Similar to encoding, the DG was more active than the CA1-3 or Sub during memory retrieval [DG vs. CA1-3: $t_{(24)} = 5.75$, $p < .001$; DG vs. Sub: $t_{(24)} = 2.91$, $p = .031$]. However, unlike during encoding, the DG was the only subfield to show an increase in BOLD activity during memory retrieval, when compared to the odd/even judgment task (see Fig. 4.8b, Table 4.3). Comparing encoding and retrieval phases to each other revealed that the CA1-3 and DG subfields were more active during memory formation than during memory retrieval [CA1-3: $t_{(24)} = 6.54$, $p < .001$; DG: $t_{(24)} = 4.34$, $p < .001$], while encoding and retrieval activities in the Sub did not differ from each other ($p = .112$).

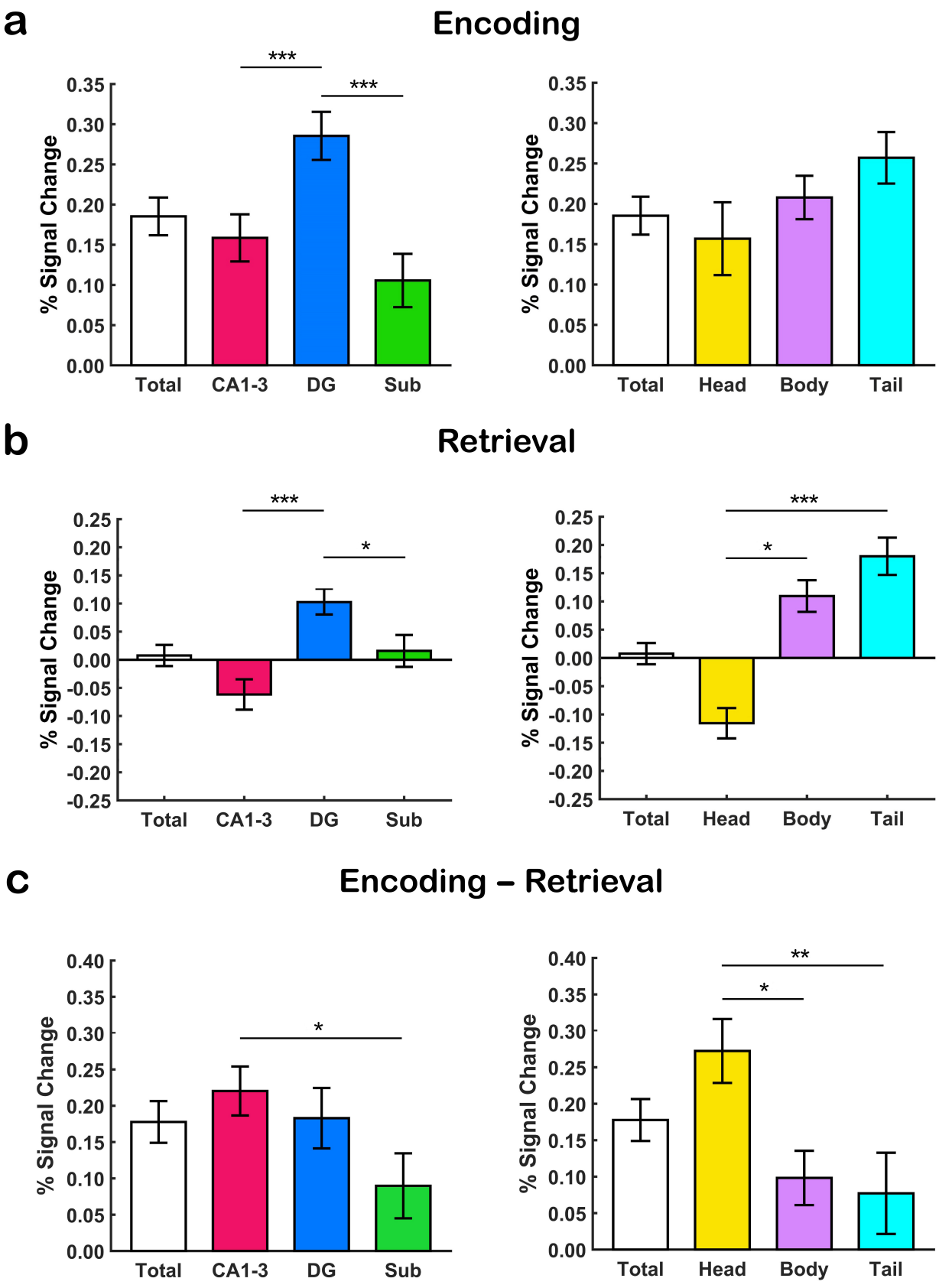

Fig. 4.8. Activity in the total hippocampal subfields and anterior-posterior subregions during the encoding (a) and retrieval (b) phases, collapsed across symbol, location, and association trial types and both hemispheres. The bottom row (c) shows the encoding vs. retrieval BOLD activity differential. Abbreviations: CA1-3, *Cornu Ammonis* 1-3; DG, dentate gyrus; Sub, subiculum. Error bars represent the standard error of the mean. See main text for statistical comparisons vs. baseline. * FWE $p < .05$; ** FWE $p < .01$; *** FWE $p < .001$.

Table 4.3
Summary of main results.

	encoding		retrieval		encoding – retrieval	
	relative to zero	**differences**	**relative to zero**	**differences**	**relative to zero**	**differences**
total hippocampus						
left	↑ 0.23% [d = 1.60] ***	left > right [d = 0.39] $^{\sim}$	↓ 0.18% [d = 0.64] * (location trials only)	right > left 0.25% [d = 1.11] *** on location trials only	0.26% [d = 1.20] ***	left > right [d = 0.52] *
right	↑ 0.15% [d = 0.86] ***		↑ 0.05% [d = 0.40] $^{\sim}$ (all trials)		0.10% [d = 0.44] *	
bilateral total subfields (transverse axis)						
CA1-3	↑ 0.16% [d = 1.08] ***	DG > CA1-3 [d = 0.90] ***	↓ 0.06% [d = 0.47] $^{\sim}$	DG > CA1-3 [d = 1.15] ***	0.22% [d = 1.31] ***	CA1-3 > Sub [d = 0.55] *
DG	↑ 0.29% [d = 1.91] ***	DG > Sub [d = 1.03] ***	↑ 0.10% [d = 0.93] ***	DG > Sub [d = 0.58] *	0.18% [d = 0.88] ***	DG > Sub [d = 0.55] $^{\sim}$
Sub	↑ 0.11% [d = 0.64] **		↑ 0.02% [d = 0.11], n.s.		0.09% [d = 0.40] $^{\sim}$	
bilateral subregions (longitudinal axis)						
head	↑ 0.16% [d = 0.70] **	head < body < tail linear gradient for location trials only (p = .025); no other differences	↓ 0.12% [d = 0.86] ***	head < body < tail linear gradient, regardless of memory type	0.27% [d = 1.24] ***	head > body [0.17%, d = 0.74] **
body	↑ 0.21% [d = 1.54] ***		↑ 0.11% [d = 0.78] ***		posterior (i.e. body + tail): 0.10% [d = 0.62] *	head > tail [0.20%, d = 0.54] *
tail	↑ 0.26% [d = 1.61] ***		↑ 0.18% [d = 1.09] ***			
bilateral anterior (i.e., head) subfields						
CA1-3	↑ 0.15% [d = 0.56] *	none	↓ 0.14% [d = 0.80] **	none	0.29% [d = 1.10] ***	none
DG	↑ 0.19% [d = 0.69] **		↓ 0.09% [d = 0.46] $^{\sim}$		0.28% [d = 0.96] ***	
Sub	↑ 0.15% [d = 0.56] *		↓ 0.06% [d = 0.32], n.s.		0.21% [d = 0.66] **	
bilateral posterior (i.e., body + tail) subfields						
CA1-3	↑ 0.20% [d = 1.49] ***	DG > CA1-3 [d = 0.53] *	↑ 0.06% [d = 0.39] $^{\sim}$	DG > CA1-3 [d = 0.76] **	0.14% [d = 0.75] **	DG > Sub [d = 0.58] *
DG	↑ 0.31% [d = 1.85] ***	DG > Sub [d = 1.13] ***	↑ 0.18% [d = 1.51] ***	DG > Sub [d = 0.54] *	0.13% [d = 0.57] *	CA1-3 > Sub [d = 0.52] *
Sub	↑ 0.09% [d = 0.59] **	CA1-3 > Sub [d = 0.51] *	↑ 0.09% [d = 0.56] *		0.00% [d = 0.01], n.s.	
bilateral posterior – bilateral anterior subfields						
CA1-3	0.05% [d = 0.16], n.s.	none	0.20% [d = 0.92] ***	DG > Sub [d = 0.55] *	– 0.15% [d = 0.48] $^{\sim}$	none
DG	0.12% [d = 0.35], n.s.		0.27% [d = 1.30] ***		– 0.15% [d = 0.47] $^{\sim}$	
Sub	– 0.06% [d = 0.18], n.s.		0.15% [d = 0.75] ***		– 0.21% [d = 0.59] *	

$^{\sim}$ FEW $p < .10$ * FWE $p < .05$ ** FWE $p < .01$ *** FWE $p < .001$

Functional MRI: total hippocampal subregions

Performing three-way repeated-measures ANOVAs on encoding, retrieval, and encoding vs. retrieval data for the total subregions did not reveal any significant Subregion × Condition, Subregion × Hemisphere, or Subregion × Condition × Hemisphere interactions (all ps > .10). Consequently, as was the case with the total subfields, encoding and retrieval activity estimates for the longitudinal subregions were collapsed across both hemispheres and all (i.e., item, spatial, and associative memory) trial types.

One sample t-tests showed that all three HC subregions were active during memory encoding [head: $t_{(24)} = 3.48$, $p = .002$; body: $t_{(24)} = 7.72$, $p < .001$; tail: $t_{(24)} = 8.04$, $p < .001$] (see Fig. 4.8a, Table 4.3). Although our omnibus ANOVA did not reveal any differences among the HC subregions during memory encoding [$F_{(2,48)} = 2.20$, $p = .122$], prior studies suggest presence of an anterior to posterior activity gradient during spatial learning (Colombo et al., 1998; Ryan et al.,

2010; Strange et al., 2014; Woollett & Maguire, 2012). To investigate whether our data supported presence of such a gradient, we performed a planned linear trend analysis, separately for each condition. Results from this analysis were statistically significant only for the location trials [$F_{(1,24)} = 5.68$, $p = .025$, partial $\eta^2 = 0.191$, Head < Body < Tail], confirming presence of the anterior to posterior gradient in HC activity during spatial learning.

In contrast to encoding, during memory retrieval the HC activity rose gradually as a function of anatomical location along the anterior-posterior axis, regardless of the type of memory being retrieved [linear contrast for Symbols: $F_{(1,24)} = 18.08$, $p < .001$; linear contrast for Locations: $F_{(1,24)} = 36.04$, $p < .001$; linear contrast for Both: $F_{(1,24)} = 7.37$, $p = .012$]. This pattern was driven by BOLD deactivation in the HC head [$t_{(24)} = -4.30$, $p < .001$], and activation in the HC body and tail [body: $t_{(24)} = 3.91$, $p = .001$; tail: $t_{(24)} = 5.45$, $p < .001$] (Fig. 4.8b, Table 4.3). Furthermore, direct comparisons of subregions' retrieval activity showed that both posterior subregions were more active than the HC head during the retrieval trials [body: $t_{(24)} = 7.85$, $p < 10^{-6}$; tail: $t_{(24)} = 6.12$, $p < 10^{-4}$], while retrieval activities in the body and tail did not differ statistically ($p = .124$).

Additionally, encoding vs. retrieval activity differentials were greater in the HC head than in the HC body or tail [head vs. body: $t_{(24)} = 3.69$, $p = .005$; head vs. tail: $t_{(24)} = 3.69$, $p = .026$; body vs. tail, $p = .737$]. Comparing encoding and retrieval activities to each other showed that both anterior (i.e., head) and posterior (body together with tail) segments of the HC formation were more active during the encoding phase than during the retrieval phase [anterior: $t_{(24)} = 6.21$, $p < .001$; posterior: $t_{(24)} = 3.09$, $p = .015$].

Functional MRI: anterior vs. posterior hippocampal subfields

Finally, we examined the encoding activity in subfields within the anterior (head) and posterior (body together with tail) HC. The posterior HC subfields responded differently during memory encoding [$F_{(2,48)} = 14.16$, $p < .001$, partial $\eta^2 = 0.371$], which was not the case in the anterior HC ($p = .697$). Furthermore, all subfields within the posterior HC showed different levels of activity [DG vs. CA1-3: $t_{(24)} = 2.63$, $p = .030$; DG vs. Sub: $t_{(24)} = 5.65$, $p < .001$; CA1-3 vs. Sub: $t_{(24)} = 2.56$, $p = .017$]. Activities in the anterior and posterior segments of each subfield did not differ statistically (all ps > .10), implying that the underlying activity patterns were similar in both the anterior and posterior HC, although differences in encoding activity were more pronounced in the posterior HC (Fig. 4.9a, Table 4.3). Finally, we compared each anterior/posterior subfield's

encoding activity (collapsed across hemispheres and memory instructions) to the baseline task. These tests showed that every subfield in both the anterior and posterior HC was active during the encoding phase (all ps < .050) (see Fig. 4.9a, Table 4.3). Consistent with previously described results, we did not observe any activity differences related to the trial type (i.e., symbol, location, and both) in any of the anterior or posterior subfields (all ps > .10).

During memory retrieval, all posterior subfields were more active than their anterior counterparts [CA1-3: $t_{(24)} = 4.62$, $p < .001$; DG: $t_{(24)} = 6.49$, $p < .001$; Sub: $t_{(24)} = 3.76$, $p = .003$]. In congruence with the encoding results, all subfields responded similarly in the anterior ($p = .222$), but not in the posterior HC [$F_{(2,24)} = 5.87$, $p = .010$, partial $\eta^2 = 0.197$] (Fig. 4.9b, Table 4.3). Within the posterior HC, retrieval-related activity was statistically larger in the DG than in the CA1-3 or Sub [$t_{(24)} = 3.82$, $p = .004$; $t_{(24)} = 2.72$, $p = .036$, respectively]; however, the CA1-3 retrieval activity did not differ from the Sub activity [$t_{(24)} = 0.76$, $p = .456$] (Fig. 4.9b, Table 4.3). Examining the posterior HC subfields separately revealed that all subfields were either activated or trended towards activation during memory retrieval [CA1-3: $t_{(24)} = 1.95$, $p = .062$; DG: $t_{(24)} = 7.55$, $p < .001$; Sub: $t_{(24)} = 2.80$, $p = .020$]. This is in contrast to the anterior HC, which, as we described earlier, showed a statistically significant negative BOLD response during memory retrieval (Fig. 4.9b, Table 4.3).

Comparing encoding and retrieval activities to each other (Fig. 4.9c, Table 4.3) showed that within the anterior HC, every subfield was more active during memory encoding than during memory retrieval [CA1-3: $t_{(24)} = 5.49$, $p < .001$; DG: $t_{(24)} = 4.82$, $p < .001$; Sub: $t_{(24)} = 3.30$, $p = .009$]. Within the posterior HC, encoding vs. retrieval contrasts were significant for the CA1-3 [$t_{(24)} = 3.77$, $p = .004$] and DG [$t_{(24)} = 2.86$, $p = .017$], but not for the Sub ($p = .969$). Finally, for every subfield, encoding vs. retrieval activity differences were larger in the anterior HC than in the posterior HC [CA1-3: $t_{(24)} = 2.38$, $p = .050$; DG: $t_{(24)} = 2.34$, $p = .028$; Sub: $t_{(24)} = 2.94$, $p = .022$], and these anterior-posterior differences in encoding vs. retrieval activity were similar in all subfields [$p = .668$] (Fig. 4.9c, Table 4.3).

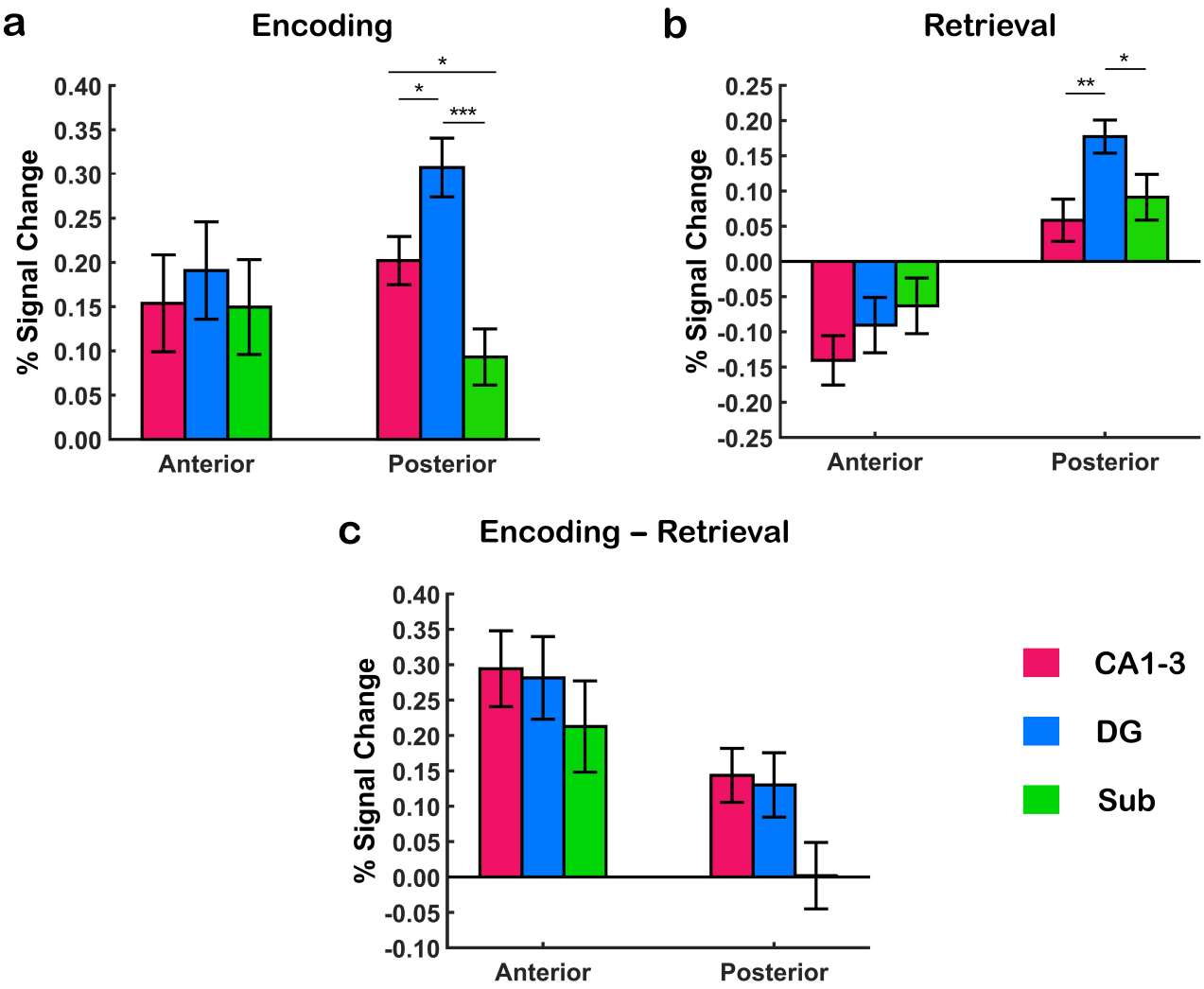

Fig. 4.9. Estimated BOLD activity in the anterior (i.e., head) and posterior (i.e., body + tail) hippocampal subfields during memory encoding (a) and retrieval (b), collapsed across symbol, location, and association trial types and both hemispheres. The bottom panel (c) shows the encoding vs. retrieval BOLD activity differential for the anterior and posterior sections of all hippocampal subfields (CA1-3, *Cornu Ammonis* 1-3; DG, dentate gyrus; Sub, subiculum). Error bars represent the standard error of the mean. Only comparisons among subfields within, but not across, the anterior and posterior HC segments are shown. See main text for statistical comparisons between the anterior and posterior segments of each subfield, and for statistical comparisons vs. baseline.
* FWE $p < .05$; ** FWE $p < .01$; *** FWE $p < .001$.

4.4. Discussion

To our knowledge, this is the first fMRI study to examine how anterior-posterior HC subregions and cross-sectional subfields are involved in the encoding and retrieval of item, spatial, and associative memories across the entire HC structure. Four major patterns emerged from our results. First, although all HC subregions and all subfields (in both the anterior and posterior HC) were active during memory encoding, during memory retrieval we observed an anterior-to-posterior gradient in HC activity that was independent of the type of memory being retrieved. This gradient was characterized by above-baseline activity in the posterior HC (HC body and tail) and below-baseline activity in the anterior HC (HC head). Second, we observed larger activity in the DG subfield than in the CA1-3 or Sub during both encoding and retrieval. Third, although our paradigm employed an explicit set of instructions aimed at priming attention to specific aspects of a stimulus, those instructions had minimal effects on the HC activity during memory encoding. Fourth, encoding vs. retrieval activity differences were larger in the anterior HC for all subfields, suggesting that the aforementioned anterior-posterior differences in HC function are likely subfield-independent. Finally, to our best knowledge, this is the first study to adapt the 'Designs' subtest from the WMS-IV to an fMRI paradigm, and our results provide insight into how the WMS-IV 'Designs' subtest relates to HC function.

Previous literature demonstrated that the HC formation plays a crucial role in item-location memory (Allen et al., 2014; Smith and Milner, 1981; Watson et al., 2013). However, whether different types of memory rely on the HC to a similar extent is still a matter of scientific debate. There is evidence from fMRI and patient studies showing that memory for relations can be distinguished from memory for spatial information (Eichenbaum, 2017; Eichenbaum & Cohen, 2014; Kumaran & Maguire, 2005; Lisman et al., 2017; Nadel et al., 2012), and from memory for items themselves (Caplan & Madan, 2016; Konkel et al., 2008; Madan et al., 2017). Here, we employed an fMRI paradigm, based on the 'Designs' subtest from the WMS-IV, to perform direct comparisons of the HC activity during encoding and retrieval of item, spatial, and associative memories.

Despite the widespread clinical use of the WMS-IV, little research has been done on the 'Designs' subtest (Martin & Schroeder, 2014), and especially on how it relates to brain function. Studies have shown that this task assesses visual attention and visual memory, and shares common factor loadings with tests of visual reproduction (Hoelzle et al., 2011; Holdnack et al., 2011). The

'Designs' subtest itself is a modification of the 'Memory for Designs' subtest found in the Developmental Neuropsychological Assessment, second edition (NEPSY-II), a neuropsychological battery commonly used in pediatric studies (Brooks et al., 2009, 2010). Those studies have shown that performance on 'Memory for Designs' shares little variance with other NEPSY-II tests of visual memory, such as 'Memory for Faces' and 'Memory for Names' (Brooks et al., 2010), suggesting that at least in children this task relies on a different set of cognitive processes than face recognition or formation of visual-auditory associations.

Although this is the first fMRI adaptation of the 'Designs' subtest, our paradigm has much in common with item-location memory tasks (Horecka et al., 2018; Kessels et al., 2002; Owen et al., 1996; Postma et al., 2008; Smith & Milner, 1981), except for one major difference: we used abstract images instead of pictures of everyday objects or faces. In general, abstract images are more suitable for studying item memory because participants are less able to use pre-existing semantic knowledge and associations to support the task-specific episodic memory, and thus, contaminate the test of item memory itself. Other researchers (e.g., Konkel et al., 2008) have also used highly abstract novel objects in their tests of item and relational memory for very similar reasons.

Despite the fact that most fMRI studies focused on one type of information at a time, several fMRI and neuropsychological studies attempted to compare the HC role in processing of spatial vs. non-spatial memories (Horecka et al., 2018; Konkel et al., 2008; Kumaran & Maguire, 2005; Ryan et al., 2010). For example, Kumaran & Maguire (2005) reported that BOLD activity in the HC formation was correlated with spatial-relational, but not social-relational memory. The authors also reported that neither the spatial nor the relational processing alone was sufficient to activate the HC, but that the combination of those two factors was crucial for the HC engagement. Another research group (Ryan et al., 2010) used a within-subject design to separate spatial and non-spatial relations from episodic and semantic memory during memory retrieval. In agreement with the cognitive map theory (O'Keefe & Nadel, 1978), spatial relations (collapsed across episodic-spatial, semantic-spatial-old and semantic-spatial-new) engaged the HC to a greater degree than non-spatial relations, while no voxels showed the opposite pattern (nonspatial > spatial). In contrast, a study by Konkel et al. (2008) demonstrated that amnesic patients, with HC-specific damage, were impaired not only on all tests of relational memory, including spatial, associative, and sequential, but also on tests of item memory, although the performance on the former was more affected than the performance on the

latter (Konkel et al., 2008). Our results also suggest the domain-agnostic nature of HC function, especially during memory encoding.

Even though we did not detect any condition-related differences within any of our HC ROIs, we observed global laterality effects for the retrieval of spatial memories. These results are in agreement with studies of MTL patients, which showed that memories for spatial relationships are particularly susceptible to right, but not left, HC damage (Kessels et al., 2002; van Asselen et al., 2008). Our work builds on those previous findings by demonstrating that left vs. right HC differences were present in all HC subfields, in both the anterior and posterior HC segments. However, our results showed that these hemispheric effects were present only during the retrieval phase, and only for spatial memory. This further extends our knowledge of encoding/retrieval differences in HC function, particularly as they related to spatial tasks.

In addition to comparing different memory components, our design enabled us to examine both longitudinal and cross-sectional properties of the HC architecture. Anatomical connectivity studies showed that splitting the HC into just two (i.e., anterior and posterior sections) sections might lead to oversimplified models of its function (Small, 2002; Strange et al., 2014). Such anterior/posterior subdivisions often do not correspond to anatomical properties of the HC; instead, the HC (or the entire MTL) is split into two or three long-axis segments of approximately equal length (Ranganath & Ritchey, 2012; Small, 2002). In contrast, when the HC was subdivided in accordance with anatomical properties, all three subregions (i.e., head, body, and tail) showed different patterns of connectivity (Ranganath & Ritchey, 2012), different subfield compositions (Malykhin et al., 2010, 2017), and unique roles in episodic memory (Chen et al., 2010; DeMaster et al., 2014; Evensmoen et al., 2013; Spalletta et al., 2016; Travis et al., 2014; de Vanssay-Maigne et al., 2011). Our results showed that the level of activity in the HC body was somewhere between that of the head and that of the tail, suggesting that anterior-posterior differences might be organized along a gradient rather than being a simple dichotomy. These observations are consistent with a recent meta-analysis by Kim (2015) as well as theoretical framework outlined by Poppenk et al. (2013): both emphasize that the anterior versus posterior functional specialization is a relative difference, not a sharp dichotomy.

It has been suggested that the anterior and posterior HC are specialized for encoding and retrieval, respectively (Kim, 2015; Lepage et al., 1998; Schacter & Wagner, 1999; Spaniol et al., 2009); however, experiments by Greicius et al. (2003) and Schacter et al. (1999) reported encoding-

related activity in both the anterior and posterior segments of the HC formation. One major limitation of most standard-resolution studies of HC function is a high degree of smoothness among activation clusters, which in the anterior HC can bleed into the amygdala nuclei, and in the posterior HC tend to overlap with the nearby MTL cortices. Since we did not smooth our data and used manual segmentation to define each anterior-posterior subregion in native space, we were able to isolate the HC formation from surrounding MTL structures. Our results agree with both of the aforementioned arguments because (1) all 3 HC subregions were active (relative to the odd/even baseline) during memory encoding, and (2) the encoding vs. retrieval activity differential was larger in the HC head than in the HC body or tail. However, it remains to be determined whether the HC subregions perform similar functions in memory encoding or whether they encode different aspects of a stimulus. The latter view is partially supported by our results from spatial trials, for which we observed an anterior to posterior gradient in BOLD activation. Similar anteroposterior differentials in HC activity for spatial memory have been reported in primates (Colombo et al., 1998), while human imaging studies reported (1) greater activity in the right posterior HC during tasks with a spatial memory component (Banks et al., 2012; Hoscheidt et al., 2010; Ryan et al., 2010), and (2) enlargement of the posterior HC in London taxi drivers with expert knowledge of the city (Maguire et al., 2000, 2003; Woollett et al., 2009; Woollett & Maguire, 2011). Interestingly, London taxi drivers eventually experience a loss of gray matter volume in the anterior HC, and as years on the road increase, become less proficient on memory tasks requiring formation of novel object-location associations (Woollett & Maguire, 2009, 2012). Presumably, this is a consequence of heavy reliance on memory retrieval processes during daily work-related activities. As demonstrated by our results, retrieval of all types of memories engages the posterior HC, while metabolic demands on the HC head during memory retrieval were less than those required to perform the baseline odd/even judgment task.

In recent years interest has shifted towards studying the functional role of HC subfields in episodic memory (e.g., Azab et al., 2014; Bakker et al., 2008; Chen et al., 2011; Copara et al., 2014; Das et al., 2011; Eldridge et al., 2005; Preston et al., 2010; Reagh et al., 2014; Suthana et al., 2011, 2015; Yassa et al., 2011; Zeineh et al., 2003) with much of this work aimed at elucidating neural correlates of pattern separation and pattern completion processes (Bakker et al., 2008; Duncan et al., 2012; Lacy et al., 2011; Yassa & Stark, 2011). Both animal and computational literature (Hasselmo et al., 1995; Lisman & Grace, 2005; Meeter et al., 2004; Norman & O'Reilly, 2003; Vinogradova,

2001) suggest that the HC is a dynamic system, continuously shifting between integration and discriminations states in response to task demands. Recent high-resolution fMRI (Azab et al., 2014; Bakker et al., 2008; Berron et al., 2016; Duncan et al., 2012; Lacy et al., 2011) and patient work (Baker et al., 2016) confirmed the DG (or DG/CA3) role in pattern separation. However, unlike our task, most pattern separation/completion studies employed incidental (as opposed to explicit) encoding paradigms and studied HC processes responsible for laying down separate memory traces from similar perceptual inputs. Interestingly, these studies indicate that the DG/CA3 subfield acts as universal pattern separator (Azab et al., 2014; Bakker et al., 2008; Copara et al., 2014; Lacy et al., 2011), meaning that its basic role of laying down distinct memory traces from overlapping information is similar for item, spatial, and temporal information. Although our task did not employ incidental learning and was not designed to study integration/discrimination states, we also observed similar activity for all types of learning in every subfield.

In addition to pattern separation/completion studies, the DG/CA3 subfield demonstrated involvement in memory tasks with a spatial component: it showed robust activity to specific spatial cues in overlapping navigational environments (Brown et al., 2014), sensitivity to changes in spatial–contextual input (Stokes et al., 2015), and was activated during retrieval of both spatial and temporal information (Copara et al., 2014). In contrast, Zeidman & Maguire (2016) implicated the anterior presubiculum and parasubiculum in tasks involving the construction and recall of scenes. However, Kyle et al. (2015) found that retrieving information regarding spatial or temporal proximity of elements within spatial or temporal context resulted in similar patterns of activity spanning multiple HC subfields.

From previous research on explicit associative memory a general pattern of subfield specialization emerges: preferential role of the DG/CA23 in encoding processes and subiculum in retrieval processes (Eldridge et al., 2005; Suthana et al., 2015; Zeineh et al., 2003). A similar pattern was also reported in a task employing spatial learning using navigation-like video clips (Suthana et al., 2011). However, no direct comparisons of the HC subfields' activity during different types of learning were carried out since paradigms studying spatial and associative memories were acquired on different subjects, using different baseline tasks, and sometimes even different MRI systems. Furthermore, because of technical limitations, some of those studies did not segment the most anterior and the most posterior segments of the HC structure (e.g., Chen et al., 2011; Eldridge et al., 2005; Suthana et al., 2011; Zeineh et al., 2003). Our results filled the gap in

this literature by: (1) showing that all three subfields were active during memory encoding, regardless of which memory domain was involved, and (2) further demonstrating that task-related signal changes in the CA1-3 and Sub were half the magnitude of those in the DG. Even during the retrieval phase, our results implicate greater involvement of the DG, as opposed to the CA1-3 or Sub. In contrast to the results reported by Eldridge et al. (2005), Suthana et al. (2015), and Zeineh et al. (2003), we did not observe total Sub activation during memory retrieval. Differences among studies of Sub function can be partially attributed to differences in subfield segmentation protocols used by different research groups (Malykhin et al., 2017; Yushkevich et al., 2015a). Studies, which reported increased Sub activity during memory retrieval, generally included the presubiculum and parasubiculum within their Sub ROIs, while our segmentation protocol was designed to isolate the Sub proper. Consequently, it is plausible that presubiculum and parasubiculum are more active than the Sub proper during memory retrieval. Lastly, our results showed that the encoding vs. retrieval activity differences were larger in the anterior HC in every subfield, suggesting that such anterior-posterior differences in HC function are subfield-independent. Further work is needed to explain why this is the case.

At the cellular level, encoding/retrieval differences in subfield function could be driven by their connectivity profiles. During encoding, most models emphasize sequential steps of information processing within the trisynaptic circuit: from the entorhinal cortex (EC) to the DG, then via the CA3 to the CA1, with final outputs to the Sub, EC and parahippocampal regions (Jones & McHugh, 2011). However, new memories can also be rapidly encoded in the CA1 subfield through direct projections from the EC to the CA1, and CA2 subfields (Jones & McHugh, 2011). In contrast, during memory retrieval information does not flow directly from the EC to the CA1-2, and instead passes through the DG or CA3 subfields first (Jones & McHugh, 2011). This emphasizes the importance of the DG and CA3 for both encoding and retrieval of episodic memories, whilst inputs to the CA1-2 vary between those two states. Despite the fact that both the CA1 and Sub serve as the major output regions of the HC (O'Mara, 2006), Sub involvement in encoding processes is less clear.

To our best knowledge, there is only one study to date (Reagh et al., 2014), which clearly demonstrated subfield-specific long-axis differences in HC function in relationship to memory. In that study, the anterior (mostly head) DG/CA3 region displayed repetition suppression effects, while the posterior (mostly body and tail) DG/CA3 showed activity enhancement for previously

studied highly familiar scenes, such as Mona Lisa, Eiffel Tower, and Taj Mahal. Although no explicit memory tests were carried out, it is plausible that neural correlates of individual stimuli were reinstated in the posterior DG/CA3. Recent work by Tompary et al. (2016) suggests that successful memory retrieval is driven by the reinstatement of encoding-related activity within the CA1 subfield, although the CA23DG region showed a similar trend. Whether the anterior or posterior segments of the HC subfields are the main drivers of pattern reinstatement is largely unknown. Based on our results, we think that the posterior DG is particularly important for memory reinstatement, although we were not able to test this hypothesis directly due to the insufficient number of forgotten trials. Together with the work done by Reagh et al. (2014), our results demonstrate the importance of considering both the anterior-posterior and the transverse axis properties of the HC architecture, when carrying out studies of HC function. In light of recent evidence that the anterior, but not posterior, Sub plays an important role in basic scene discrimination (Hodgetts et al., 2017), it is advisable to account for the longitudinal differences in subfield function even in tasks other than memory.

In addition to providing insight into how the HC anatomy relates to memory processes, our analysis methodology suggests that retrieval- and encoding-related changes in neural firing within the HC occur on a sub-TR scale. As seen in Fig. 4.5, encoding-related BOLD in the HC peaked 4–5 s after trial onset (on average), and retrieval-related BOLD response peaked 6–7 s after the trial onset (on average), indicating relatively short-lasting changes in the HC activity evoked by memory processes. This further highlights the importance of estimating hemodynamic response in each brain region individually, separately for each task. Assuming constant increase/decrease in neural firing rate for the entire trial duration (e.g., for 10 s during encoding in our design) is likely to result in inaccurate assumptions about neural and vascular properties in different brain regions. Recent work by Nauer et al. (2015) pointed out similar pitfalls in assuming sustained HC firing, which produced surprisingly poor models of the HC BOLD response.

Limitations and future directions

Except for hemispheric differences during the retrieval phase, we did not find any statistical differences between item, spatial, and associative memories. Consistent with our observations, a number of other studies, comparing different memory domains, also reported a lack of difference in HC activity for different types of memory (Azab et al., 2014; Ekstrom et al., 2011) and similar

subfield activity patterns were reported in a variety of memory tasks (Suthana et al., 2009, 2011; Eldridge et al., 2005; Zeineh et al., 2003). However, it should be noted that whenever a study with a modest sample size fails to find statistical differences, the issue of statistical power comes to mind (Button et al., 2013). Although our study employed a larger sample size than many recent fMRI studies of the HC subfields (e.g., Aly & Turk-Browne, 2016; Azab et al., 2014; Copara et al., 2014; Duncan et al., 2012; Reagh et al., 2014; Suthana et al., 2015; Stokes et al., 2015; Tompary et al., 2016; all with sample sizes in the range of 14–22 participants), it is plausible that a larger number of trials per condition and/or a larger number of subjects is required to detect relatively subtle differences in subfield activity, particularly when comparing HC activity during encoding/retrieval of different types of memory. Alternatively, multivoxel classification techniques might be able to detect differences in patterns of activity within subfields for different types of memory. However, this also requires a greater number of trials than were feasible in the current study. Furthermore, our study sample consisted primarily of younger adults (mostly undergraduate and graduate students, 20–33 years of age) and future studies will need to investigate the extent to which our findings are relevant to individuals from different populations. For instance, in our recent aging study (Malykhin et al., 2017) we demonstrated that subfields within the HC body are particularly vulnerable to age-related atrophy, while subfields within the HC head and tail showed minor if any, age-related effects. It is currently unclear whether those structural changes contribute to changes in BOLD activity within various HC subregions and subfields and if so, whether those functional changes can explain age effects on performance in visuospatial memory tasks.

On the technical side, some limitations related to our data and segmentation protocol must be pointed out. Although there were no differences in head motion between symbol, location, and both trial types, our participants were more likely to move during memory encoding than during memory retrieval, regardless of memory condition. During the encoding phase, on average 1.8 out of 12 trials per condition were affected, while 1.1 out of 12 trials per condition were affected during the retrieval phase. However, considering strict scrubbing thresholds and extensive denoising procedures that we employed during our preprocessing, it is unlikely that these differences in head motion played a consequential role in our encoding vs. retrieval tests.

Furthermore, because of methodological constraints, we were unable to study activity in the individual CA subfields. According to post-mortem work (Adler et al., 2014; Rössler et al., 2002; Simić et al., 1997), the CA23 segment takes up 6–10% of the total HC volume. Recent attempts at

segmenting the CA1, CA2, and CA3 on structural MRI reported similar proportions (Goubran et al., 2013; Iglesias et al., 2015; Winterburn et al., 2013; Wisse et al., 2012; Yushkevich et al., 2015b), and a recent 7 T study by Suthana et al. (2015) attempted to compare encoding and retrieval activities in each individual CA subfield. Those results showed that the CA3 subfield is particularly important for memory encoding. Given spatial resolution limitations of our fMRI data (1.5-mm isotropic voxels), the combined CA23 volume is expected to consist of two to three voxels on each coronal slice of the HC body, with the CA3 and CA2 subfields being one voxel large on most slices. Because of the inherent spatial blur in all fMRI datasets (approximately 2 mm FWHM within the HC formation for our fMRI images), partial volume effects, geometric distortions caused by the B_0 inhomogeneities, and imperfections in motion correction by realignment techniques, the anatomical validity of one- or two-voxel activity localization would be tenuous at best. Furthermore, since the DG/CA3, CA3/CA2, CA2/CA1, and CA1/Sub tissue boundaries are not visible on *in vivo* ultra-high-resolution T_2-weighted structural MRI even at 7 T (Berron et al., 2016; Suthana et al., 2015; Yushkevich et al., 2015a), there are substantial disagreements between various research groups as to where those boundaries ought to be placed (see Yushkevich et al., 2015a for protocol comparisons). For instance, our CA1/Sub boundary is more lateral than that of some other studies of subfield function (Bonnici et al., 2012; Copara et al., 2014; Eldridge et al., 2005; Stokes et al., 2015; Suthana et al., 2009, 2011; 2015; Zeineh et al., 2003). Furthermore, some studies included the presubiculum and parasubiculum within their Sub ROIs (e.g., Copara et al., 2014; Eldridge et al., 2005; Stokes et al., 2015; Suthana et al., 2009, 2011; 2015; Zeineh et al., 2003), while others (e.g., Bakker et al., 2008; Bonnici et al., 2012; Lacy et al., 2011; Tompary et al., 2016), including this study, excluded most of the presubiculum and parasubiculum from their Sub ROIs. As a result, it is best to exercise caution when relating results from various laboratories studying HC subfields since subfield ROIs, despite similar naming, might, in fact, represent different HC anatomy (Yushkevich et al., 2015a). Across 21 subfield segmentation protocols employed by various research groups, only the DG/CA4 region within the HC body showed a high degree of agreement. Fortunately, this is a well-known issue in the field and efforts at developing a harmonized subfield segmentation protocol are underway (Yushkevich et al., 2015a).

In the present study, we employed a manual classification procedure during our HRf model-building step. Manual classification and de-noising of fMRI signals following independent component analysis (ICA) decompositions is well-documented (Griffanti et al., 2017; Salimi-

Khorshidi et al., 2014), and although a number of automated component classifiers have been developed, visual inspection of each ICA component by an expert rater is still the gold standard in the field against which automated techniques are evaluated (Bhaganagarapu et al., 2013; Perlbarg et al., 2007; Rummel et al., 2013; Salimi-Khorshidi et al., 2014; Storti et al., 2013; Tohka et al., 2008). Similarly, future studies might benefit from developing a fully automated procedure for classifying estimated HRfs as activation, deactivation, or noise based on previously established criteria by expert raters. However, the development and validation of automated HRf classification procedures was not within the primary scope of the current work. Similar to ICA-based techniques, any future automated HRf classification would need to be validated/tested against manual classification prior to being applied in fMRI research.

Lastly, although the HC is crucial to memory processes, it is not the only brain structure needed for memory formation, maintenance, and retrieval. An extensive body of literature implicates the entorhinal, perirhinal, and parahippocampal cortices in memory (Kensinger, 2009; Moscovitch et al., 2016; Roy et al., 2017; Squire & Dede, 2015; Small, 2002; Spaniol et al., 2009; Tompary et al., 2016). Consequently, further work is needed to investigate the role that other brain regions perform in 'Designs'-like tests of visuospatial memory. Furthermore, even though our current study focused on memory formation and retrieval, the HC performs important functions in stress response, contextual fear conditioning, decision making, imagination, and even perceptual discrimination (Bannerman et al., 2003, 2004; 2014; Lee et al., 2005; Murray et al., 2007; O'Neil et al., 2015; Pentkowski et al., 2006; Suzuki & Baxter, 2009; Zeidman & Maguire, 2016). How the HC subfields within particular longitudinal segments relate to cognitive processes other than episodic memory is largely unexplored (but see, Hodgetts et al., 2017; Leal et al., 2017; Zeidman et al., 2015 for recent attempts).

4.5 Conclusion

We used anatomical landmarks to extract BOLD activity from the HC transverse subfields and longitudinal subregions and examined the role that both axes play in memory formation and memory retrieval. Our results showed that all subfields in the anterior and posterior segments of the HC formation were active during the encoding phase, whilst during memory retrieval, we observed an anterior to posterior gradient in HC activity. Our findings also confirmed presence of an anterior to posterior gradient in HC activity during spatial learning. The DG was more active than the

CA1-3 or Sub during both encoding and recall. Furthermore, our results suggest that metabolic demands on the HC subfields and subregions are similar for item, spatial, and relational memories, especially during the encoding phase. Lastly, our results provide insight into how the WMS-IV 'Designs' subtest relates to the HC function. Future high-field high-resolution fMRI studies of episodic memory will allow researchers to further understand the structure–function relationship of the human HC and its complex anatomy.

Acknowledgments

This project was supported by the Canadian Institutes of Health Research operating grant (MOP11501) and the Natural Sciences and Engineering Research Council of Canada operating grant (06186) to N.V.M. S.H. was supported by CIHR Doctoral Scholarship. C.R.M. was supported by a CIHR Postdoctoral Fellowship (FRN-146793). We thank Corey A. Baron for optimizing the 4.7 T EPI sequence and image reconstruction protocol for our high-resolution acquisition.

Chapter 5: Investigating Effecs of Healthy Cognitive Aging on Brain Functional Connectivity Using 4.7 T Resting-State fMRI

5.1. Introduction

Many cognitive functions decline with age (Buckner, 2004; Grady, 2008, 2012; Fabiani, 2012; Hedden & Gabrieli, 2004; Reuter-Lorenz & Cappell, 2008; Schneider-Garces et al., 2010; Spreng et al., 2010). Although the cognitive neuroscience literature tends to emphasize aging effects on high-level cognition, especially memory, task switching, and selective attention (Fabiani, 2012; Li et al., 2015; Spreng et al., 2010), laboratory tests of visual perception, facial processing, and motor function also revealed a drop in performance with age (Grady et al., 1994; Houx & Jolles, 1993; Kauranen & Vanharanta, 1996; Mattay et al., 2002). It has been hypothesized that brain physiology alterations are responsible for much of the age-related decline in cognitive capacity (Buckner, 2004; Grady, 2008, 2012; Reuter-Lorenz & Cappell, 2008; Sperling, 2007; Spreng et al., 2010).

The human brain can be conceptualized as a highly structured network, sometimes termed as the connectome of dynamically interacting neuronal communities (Buckner et al., 2013; Power et al., 2011; Rubinov & Sporns, 2010; Wig, 2017; Yeo et al., 2011, 2014). The brain's functional architecture is commonly estimated from spontaneous low-frequency blood-oxygen-level-dependent (BOLD) signal fluctuations, measured during resting-state functional Magnetic Resonance Imaging (RS-fMRI) scans (Buckner et al., 2013; Craddock et al., 2013; Smith et al., 2011; Wig, 2017; Wig et al., 2014). Functional connectivity (FC) studies report 7 to 20 major resting-state networks (RSNs) with network topography localized to visual, somatomotor, and cognitive regions of the brain (Allen et al., 2011; Christoff et al., 2016; Gordon et al., 2017; Laumann et al., 2015; Petersen & Posner, 2012; Power et al., 2011; Raichle & Snyder, 2007; Wig, 2017; Yeo et al., 2011). Because spatial profiles of many RSNs resemble activation patterns from task-based fMRI studies, it has been hypothesized that RSNs represent fundamental units of brain organization, which are recruited in various combinations to perform specific tasks (Buckner et al., 2013; Crossley et al., 2013; Deco & Corbetta, 2011; Smith et al., 2009; Spreng et al., 2010).

Much of the early work on the relationship between resting-state FC and age was focused on intra-network communication in select RSNs, especially the default mode system (e.g., Andrews-

Hanna et al., 2007; Damoiseaux et al., 2008; Grady et al., 2012; Hampson et al., 2012; Koch et al., 2010; Onoda et al., 2012; Persson et al., 2014; Sambataro et al., 2010). Those studies revealed an age-related loss of functional interaction between the medial frontal and the posterior cingulate/retrosplenial cortices (but see, Persson et al., 2014). More recent RS-fMRI studies showed that in addition to the default mode network (DMN), age-related reduction in within-system FC is also present in brain networks involved in attention, cognitive control, sensory processing, and motor function (Allen et al., 2011; Betzel et al., 2014; Grady et al., 2016; Ng et al., 2016; Song et al., 2014; Spreng et al., 2016; Zonneveld et al., 2019). In addition, studies that employed graphical models to quantify age effects on FC showed that network community structure becomes less efficient and less segregated in old age (Cao et al., 2014; Chan et al., 2014; Chong et al., 2019; Geerligs et al., 2015; Spreng et al., 2016), with long-range FC being particularly vulnerable (Tomasi & Volkow, 2012).

Despite these advances, the number of studies that examined age differences in functional architecture of the entire brain is still relatively small, with most relying on anatomical or functional atlases to define their networks (Betzel et al., 2014; Chan et al., 2014; Chong et al., 2019; Fjell et al., 2015; Geerligs et al., 2015; Meunier et al., 2009; Song et al., 2014; Wang et al., 2010). Unfortunately, it has been shown that connectivity estimates can vary substantially from one atlas to another, even when all image preprocessing and data analysis methods are controlled (Cao et al., 2014). Employing ROIs from a predefined atlas may also fail to capture inter-individual variability in brain organization since individual network architecture can deviate, sometimes substantially, from an average map (Gordon et al., 2017; Laumann et al., 2015; Mueller et al., 2013). Furthermore, most connectomic studies of brain aging used mass univariate correlation methods to quantify age effects on the brain's functional architecture (Andrews-Hanna et al., 2007; Betzel et al., 2014; Geerligs et al., 2015; Grady et al., 2016; Han et al., 2018; Meier et al., 2012; Rubinov & Sporns, 2010; Zonneveld et al., 2019). Although informative, correlation differences are challenging to interpret without additional information about the underlying BOLD signal properties (Duff et al., 2018). In addition to the time series coupling, two other factors are responsible for the correlation coefficient strength in all RS-fMRI connectivity comparisons: network amplitude and magnitude of background noise (Duff et al., 2018). For this reason, examining network amplitude adds another layer of valuable information about the underlying neurobiology of aging. It also provides insight into factors that may have caused the observed

increases/decreases in correlation-based FC. To date, research on the relationship between age and RSN amplitude has been limited. Most RS-fMRI studies of brain aging did not test for age differences in network amplitude (e.g., Betzel et al., 2014; Cao et al., 2014; Chan et al., 2014; Geerligs et al., 2015; Grady et al., 2016; Meunier et al., 2009; Spreng et al., 2016), while those that did focused either on early (up to middle adulthood) or late (50 years of age and older) aging only (Allen et al., 2011; Zonneveld et al., 2019).

Since conclusions from prior RS-fMRI studies of brain aging were limited by correlation-only methodology, our study's main goal was to investigate age effects on every primary measure of RS-fMRI signal – i.e., network amplitude, network topography, and inter-network communication. To adress these research questions, we combined a high-field RS-fMRI acquisition, data-driven network decomposition, sparse graphical model estimation, and a sample representing the entire adult lifespan. In task-based fMRI experiments, the most prominent activity differences between young and old adults are often found in the prefrontal and parietal association cortices (Cabeza et al., 2002, 2004; Davis et al., 2008; Grady et al., 1994; Gutchess et al., 2005; Li et al., 2015; Logan et al., 2002; Persson et al., 2014; Rypma & D'Esposito, 2000; Rajah & D'Esposito, 2005; Schneider-Garces et al., 2010; Spreng et al., 2010; Sugiura, 2016). Consequently, we were also interested in determining whether RSNs mapping onto frontal and parietal association areas are more affected by aging than visual, auditory, and somatomotor RSNs.

Because previous task-based and resting-state fMRI studies reported aging-related reductions of BOLD signal power in a variety of cortical areas (Allen et al., 2011; D'Esposito et al., 1999; Handwerker et al., 2007; Hesselmann et al., 2001; Mehagnoul-Schipper et al., 2002; Riecker et al., 2006; Taoka et al., 1998; West et al., 2019; Zonneveld et al., 2019), we predicted a widespread decline of BOLD signal amplitude with age across RSNs. According to recent boundary-based FC work (Han et al., 2018), network structure does not change drastically with age. Consequently, we expected a large degree of architectural stability throughout the adult lifespan. Lastly, since previous structural and functional imaging work showed frontal and parietal association cortices to be particularly vulnerable to aging processes (Grady et al., 2016; Damoiseaux, 2017; Fabiani, 2012; Raz et al., 2005; Sugiura, 2016; Wig, 2017), we expected frontal and parietal association networks to display the largest age differences in FC and BOLD signal amplitude.

5.2. Material and Methods

Participants

For this cross-sectional study, we recruited 105 healthy volunteers (45 men, 60 women) across the entire adult human lifespan (16 volunteers per decade of life, on average; age range: 18-85; Table 5.1) through online, newspaper, and poster advertisements. Of those, 78 participants were Caucasian (74%), 17 Asian (16%), 7 Latin American (7%), 2 (2%) Persian and 1 Arab (1%) Canadians. According to the 20-item Edinburgh Handedness Inventory (Oldfield, 1971), 12 of the participants were left-handed [individuals with laterality quotient ≥ +80 were determined as right-handed]. All participants had no lifetime psychiatric disorders and no reported psychosis or mood disorders in first-degree relatives, as assessed by the Anxiety Disorders Interview Schedule—IV (Brown et al., 2001; Di Nardo et al., 1994), which assesses for anxiety, affective, and substance use disorders. Medical exclusion criteria were defined as those active and inactive medical conditions

Table 5.1.
Age-specific demographic information of this study's participants. Volunteers ≤ 39 years of age were classified as young adults; volunteers who were ≥ 60 years were classified as old adults, and those between 40 and 59 years of age were classified as middle-aged adults. These age splits were consistent with our earlier volumetric work (Malykhin et al., 2017).

	AGE GROUP		
	Young (*N* = 43)	**Middle (*N* = 31)**	**Old (*N* = 31)**
Age (years)			
mean ± SD	27.1 ± 5.4	50.0 ± 5.6	70.3 ± 6.7
range [min/max]	18/39	41/59	61/85
Sex (males/females)	18/25	13/18	14/17
Handedness (left/right)	5/38	5/26	2/29
Smoking history (y/n)	2/41	1/30	1/30
Elevated blood pressure (y/n)	0/43	1/30	12/19
Family history of AD (y/n)	7/36	4/27	6/25
Education (years)			
mean ± SD	16.2 ± 1.8	16.0 ± 2.5	15.7 ± 3.0
range [min/max]	12/20	12/22	11/23
MOCA			
mean ± SD	28.1 ± 1.4	27.5 ± 1.1	27.4 ± 1.3
range [min/max]	26/30	26/30	26/30

that may interfere with normal cognitive function: cerebrovascular pathology, all tumors or congenital malformations of the nervous system, diabetes, multiple sclerosis, Parkinson's disease, epilepsy, organic psychosis (other than dementia), schizophrenia, and stroke. Furthermore, medications that directly affect cognition, including benzodiazepines, antipsychotics, anticholinergic drugs, and antidepressants were also exclusionary. The participants' demographic information is summarized in Table 5.1.

An in-person interview was conducted to assess each participant's cognitive abilities. Older subjects with mild cognitive impairment (MCI) and dementia were excluded from the study. MCI was defined by the presence of cognitive complaints (documented on the AD-8, Galvin et al., 2007) with documented impairment on the Montreal Cognitive Assessment (MOCA) test (Nasreddine et al., 2005). All of our participants attained MOCA scores between 26 and 30. Dementia was defined according to the DSM-IV criteria with Clinical Dementia Rating (CDR) as an additional screening tool in older (>50 years of age) participants (Hughes et al., 1982). CDR was used to assess functional performance in 6 key areas: memory, orientation, judgment and problem solving, community affairs, home and hobbies, and personal care. A composite score from 0 to 3 was calculated. All of our participants met the cutoff score of <0.5 for the total CDR score. To screen older volunteers for depression, the Geriatric Depression Scale was used (Yesavage et al., 1982). Designed to rate depression in the elderly, a score of >5 is suggestive of depression, and a score >10 is indicative of depression. All of our elderly (>50 years of age) participants had a cutoff score of 4 and below. Lastly, all older (>50 years of age) participants were assessed for vascular dementia with the Hachinski Ischemic Scale (HIS; Hachinski et al., 1975). A score above 7 out of 18 has 89% sensitivity. HIS scores of all elderly participants were 3 or lower. Written informed consent was obtained from each participant, and the study was approved by the University of Alberta Health Research Ethics Board.

Data acquisition

All images were acquired on a 4.7 T Varian Inova MRI scanner at the Peter S. Allen MR Research Centre (University of Alberta, Edmonton, AB) using a single-transmit volume head coil (XL Resonance) with a 4-channel receiver coil (Pulseteq). 200 functional volumes were collected axially (in parallel to the AC–PC line) using a custom-written T_2*-sensitive Gradient Echo Planar Imaging (EPI) pulse sequence sensitive to blood oxygenation level-dependent (BOLD) contrast

[repetition time (TR): 3000 ms; echo time (TE): 19 ms; flip angle: 90°; field of view (FOV): 216 × 204 mm^2; voxel size: 3 × 3 × 3 mm^3; 45 interleaved slices; phase encoding direction: anterior to posterior; GRAPPA parallel imaging with acceleration factor 2 (Griswold et al., 2002)]. For the resting-state portion of the scan, subjects were instructed to remain still, stay awake, and keep their eyes closed. To estimate B_0 inhomogeneity, two gradient echo images with different echo times were acquired with coverage and resolution matching those of the functional MRI data [TR: 500 ms; TE1: 4.52 ms; TE2: 6.53 ms; flip angle: 50°; FOV: 216 × 204 mm^2; voxel size: 3 × 3 × 3 mm^3; 45 interleaved slices]. A whole brain T_1-weighted 3D Magnetization Prepared Rapid Gradient-Echo (MPRAGE) sequence [TR: 8.5 ms; TE: 4.5 ms; inversion time: 300 ms; flip angle: 10°; FOV: 256 × 200 × 180 mm^3; voxel size: 1 × 1 × 1 mm^3] was used to acquire anatomical images for tissue segmentation and registration to standard space.

Image preprocessing

Functional images were processed using SPM12 (Wellcome Trust Centre for Neuroimaging, UCL, UK), FSL (Jenkinson et al., 2002; Smith et al., 2004), and ANTS (Avants & Gee, 2004; Avants et al., 2008) software packages. Prior to registration, MPRAGE images underwent correction for intensity non-uniformity using N3 software (Sled et al., 1998) and SPM12 bias correction algorithm. Subsequently, each participant's structural images were segmented into tissue probability maps using SPM12 unified segmentation.

Functional data were preprocessed with a series of steps commonly used in the field (Fig. 5.1a). The first four functional volumes of each dataset were discarded to ensure T_1-equilibrium. SPM12 FieldMap toolbox was used to estimate B_0 distortions and to generate voxel displacement maps caused by B_0 inhomogeneity. The unified '*realign & unwarp*' function in SPM12 was used to correct geometric distortions in fMRI data caused by B_0 inhomogeneity and to realign all fMRI volumes to the first functional volume (SPM12; Andersson et al., 2001). Following the realignment procedure, fMRI images underwent correction for slice acquisition-dependent time shifts. To ensure optimal tissue alignment between the anatomical and functional data, fMRI datasets were registered to matching T_1-weighted anatomical scans using boundary-based registration (FSL; Greve & Fischl, 2009). To register RS-fMRI data to the MNI template, the SyN algorithm (ANTS; Avants et al., 2008) was used to compute tissue deformation fields based on T_1-weighted structural data.

Normalized fMRI datasets were resampled to a 2 × 2 × 2 mm^3 voxel size and smoothed with a 6-mm FWHM Gaussian kernel (SPM12; Wellcome Trust Center for Neuroimaging, UCL, UK).

Manual labeling of subject-level independent components

We employed Probabilistic Independent Component Analysis with an automated estimation of the number of independent components (FSL; Beckmann & Smith, 2004) to remove motion-related, cardiovascular, and respiratory signals from our RS-fMRI data. ICA-based fMRI denoising strategies have two major advantages over scrubbing and spike regression approaches: (1) they preserve autocorrelation properties of the RS-fMRI signal, and (2) they are able to capture complex interactions between various noise sources (Pruim et al., 2015a). Since no other studies have performed noise component labeling on our 4.7 T Varian scanner, we performed manual identification of noise components in every subject. Building an automated classifier for ICA-based (e.g., FIX classifier; Salimi-Khorshidi et al., 2014) denoising using the current dataset was not feasible, as it would have necessitated removing subjects from our sample of 105 individuals to train a brand new classifier, reducing the study sample size.

Consequently, a single rater (SH) labeled all components as (1) potential resting-state network or (2) noise based on the criteria outlined in Griffanti et al. (2017). As advised by Pruim et al. (2017), only unambiguous noise components were labeled for removal. To this end, spatial maps, time-courses, and power spectra of every component were manually inspected. First, eye ghosting, scanner noise, cardiovascular, and respiratory components were identified by manual inspection. Components labeled as scanner noise were identified by two criteria: (1) majority of spatial activation outside the gray matter, and (2) distinct power spectrum pattern, dominated by high-frequency spikes – generally above 0.11 Hz – with little to no power represented by lower frequencies (i.e., < 0.10 Hz). Cardiovascular and respiratory noise sources were identified based on Griffanti et al. (2017) guidelines, while head motion artefacts were identified using Griffanti et al. (2017) criteria with the aide of a fully automated head motion component classifier ICA-AROMA (Pruim et al., 2015a).

Inter-rater and intra-rater reliabilities for component classification were performed on 100 components, chosen semi-randomly from 16 subjects. This reliability set consisted of 50 ‘noise’ and 50 ‘signal/unclear’ ICs, based on a prior (1 month earlier) classification by SH. The intra-rater reliability was assessed by SH, who classified those 100 ICs into ‘remove’/‘retain’ categories twice,

with a 2-week interval between each classification. The ‘remove’/‘retain’ inter-rater reliability was assessed by two independent analysts – SH and NVM. Intra-rater and inter-rater Dice Similarity Coefficients (DSCs) for ‘remove’/‘retain’ categories were 0.93/0.93 and 0.92/0.91, respectively. Thus, our manual component labelling showed a high degree of consistency, with more than 9 out of 10 ICs receiving identical labels in intra-observer and inter-observer evaluations.

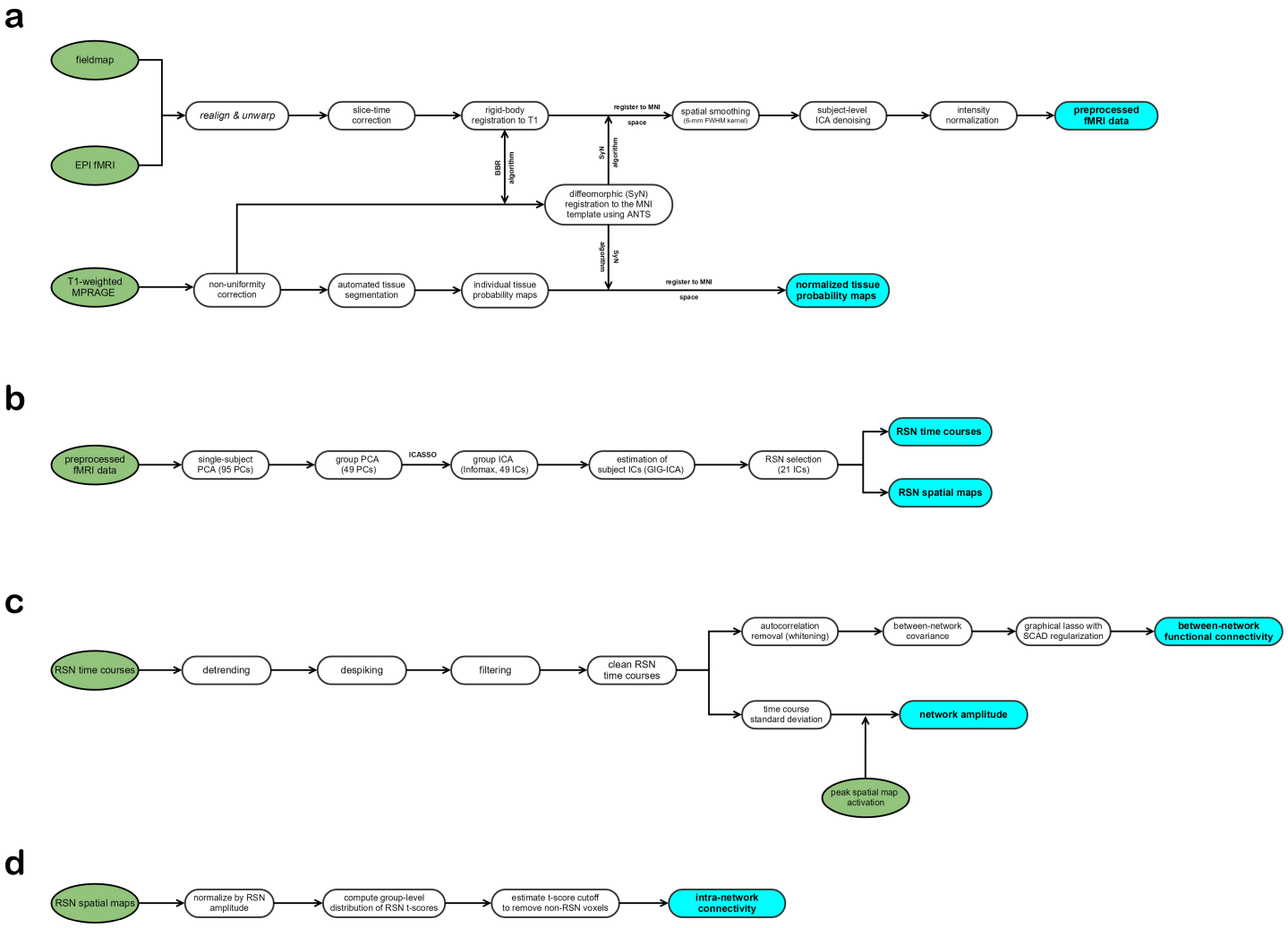

Fig. 5.1. Overview of image processing pipeline. (a) preprocessing of structural and functional data prior to group ICA decomposition; (b) fMRI decomposition into constituent signal sources using group ICA; (c) postprocessing of network time courses; (d) postprocessing of network spatial maps. Green, pipeline input; cyan, pipeline output. Outputs of panels (c) and (d) were used to study brain aging.

Eye ghosting and dominant head motion artefacts (e.g., global signal drifts with spatial maps localized exclusively to the skull) were removed using 'aggressive' option in *fsl_regfilt*, while all other artefacts were removed using 'soft' regression option in *fsl_regfilt* (Beckmann & Smith, 2004; Griffanti et al., 2014). Griffanti et al. (2014) demonstrated that 'soft' regression produces a good data cleanup without sacrificing network signals. Consequently, this was our primary approach for noise removal.

Lastly, prior to running the group ICA decomposition, each subject's denoised RS-fMRI dataset was intensity-normalized (Fig. 5.1a). Intensity normalization has been previously shown to improve the test-retest reliability of group-level ICA decompositions (Allen et al., 2010). It also ensures that resting-state BOLD signal fluctuations in every subject are scaled to % signal change units.

Group independent component analysis

Recent FC studies revealed that there are multiple regions in the human brain that participate in more than one RSN, primarily in the frontal and parietal association cortices (Liao et al., 2017; Mueller et al., 2013; Yeo et al., 2014). Group ICA (GICA; Calhoun et al., 2001) with a newer generation of subject-level reconstruction techniques can capture many of these FC complexities (Allen et al., 2012; Du et al., 2017; Yeo et al., 2014), while also foregoing the need to make somewhat arbitrary choices about which seeds/atlases one ought to use in connectivity comparisons. Here, we used the GIFT toolbox for MATLAB to perform group-level data-driven network decomposition (Calhoun et al., 2001; http://icatb.sourceforge.net/groupica.htm). Below we outline detailed choices of the parameters we used in our decompositions (see Fig. 5.1b for flow-chart form).

Because our data underwent substantial noise cleansing at the individual level, resulting in reduced source dimensionality, we chose not to set the ICA model order based on previously published literature. Instead, we estimated model order by running the Infomax ICA algorithm (Bell & Sejnowski, 1995) 200 times in ICASSO (http://www.cis.hut.fi/projects/ica/icasso). This approach renders Independent Component estimation insensitive to initial search parameters of the ICA algorithm, and directly estimates component reliability for each model order (Himberg et al., 2004). The ICASSO implementation in the GIFT toolbox provides quality estimates for all component clusters via the intra-cluster and extra-cluster similarity index, *Iq*. Our goal was to find the ICA

model order such that *Iq* for all component clusters was 0.80 or higher, which resulted in 49 components. The initial subject-specific principal component analysis (PCA) retained 95 principal components (PCs) using standard decomposition. On average, 95 PCs explained 92.3% (range: 87.7-99.7, SD = 1.99) of variance in each preprocessed subject-specific fMRI dataset, while providing some data compression to reduce the computational demands. We used group-information guided ICA (GIG-ICA; Du & Fan, 2013), which uses group-level ICs to guide subject-level ICA, for computing subject-level ICs and time courses (Fig. 5.1b). Inter-individual differences in network structure exist (Gordon et al., 2017; Laumann et al., 2015), and GIG-ICA is better positioned to capture those inter-individidual differences than back-reconstruction or dual regression (Du et al., 2016).

Group-level RSN ICs were identified by two viewers (SH and NVM) who manually inspected the aggregate spatial maps and power spectra. Specifically, when evaluating the average power spectra, two well-established metrics were used: (1) dynamic range, and (2) low frequency to high-frequency power ratio [for details see, Allen et al. (2011) and Robinson et al. (2009)]. We employed a relatively conservative labelling scheme, whereby only components resembling previously-identified networks (Allen et al., 2011; Power et al., 2011; Yeo et al., 2011) were classified as RSNs. Given our set of criteria, we successfully identified 21 RSN ICs [subsequently termed (network) components or simply RSNs].

Subject-specific network time courses were detrended (involving removal of the mean, slope, and period π and 2π sines and cosines over each time course) using the multi-taper approach (Mitra & Bokil, 2008) with the time-bandwidth product set to 3 and the number of tapers set to 5 (Fig. 5.1c). The RSN spatial maps were thresholded to ensure that our analyses were focused on the subset of voxels, which are most consistently associated with the network time courses across all subjects in our sample (Fig. 5.1d). Thresholding was based on the distribution of voxelwise *t*-scores using a model-based approach outlined in Allen et al. (2011). According to this model, the distribution of voxelwise *t*-statistic scores can be approximated by a linear combination of 1 normal and 2 gamma functions (Fig. 5.2). The normal distribution represents network-irrelevant voxels, while the two gamma functions represent positive and negative network sources (i.e., areas positively and negatively correlated with the network's time course). Mathematically, this relationship is explained by equation 5.1.

$$\mathbf{t} \approx p_{c1} N(\mathbf{t}_c | \mu_c, \sigma_c) + p_{c2} G(\mathbf{t}_c - \mu_c | \alpha_{c1}, \beta_{c1}) + (1 - p_{c1} - p_{c2}) G(-\mathbf{t}_c - \mu_c | \alpha_{c2}, \beta_{c2}) \qquad \textbf{(5.1)}$$

Values of the six parameters (μ_c, σ_c, α_{c1}, β_{c1}, α_{c2}, β_{c2}) were estimated by minimizing the root-mean-squared-deviation (RMSD) between the modeled and empirical **t**-statistic distributions using the SIMPLEX algorithm (Nelder & Mead, 1965). In order to ensure that the optimal global solution was obtained, the optimization algorithm was initiated 15,000 times, each time with a different set of randomly chosen values. The most relevant solutions for thresholding purposes are μ_c and σ_c parameters of the normal distribution, as the normal distribution represents network-irrelevant voxels. Here, we thresholded our spatial maps at $\mathbf{t} \geq \mu_c + 3\sigma_c$. We found this threshold to be a good compromise between sensitivity and specificity: in all networks, $\mathbf{t} \geq \mu_c + 3\sigma_c$ threshold was stricter than False Discovery Rate (FDR) $q < .05$ and stricter than FDR $q < .01$ in 8 RSNs, while, on average, 56% of RSN-related voxels were retained. All subsequent mentions of component topography and intra-network connectivity refer to thresholded ICs.

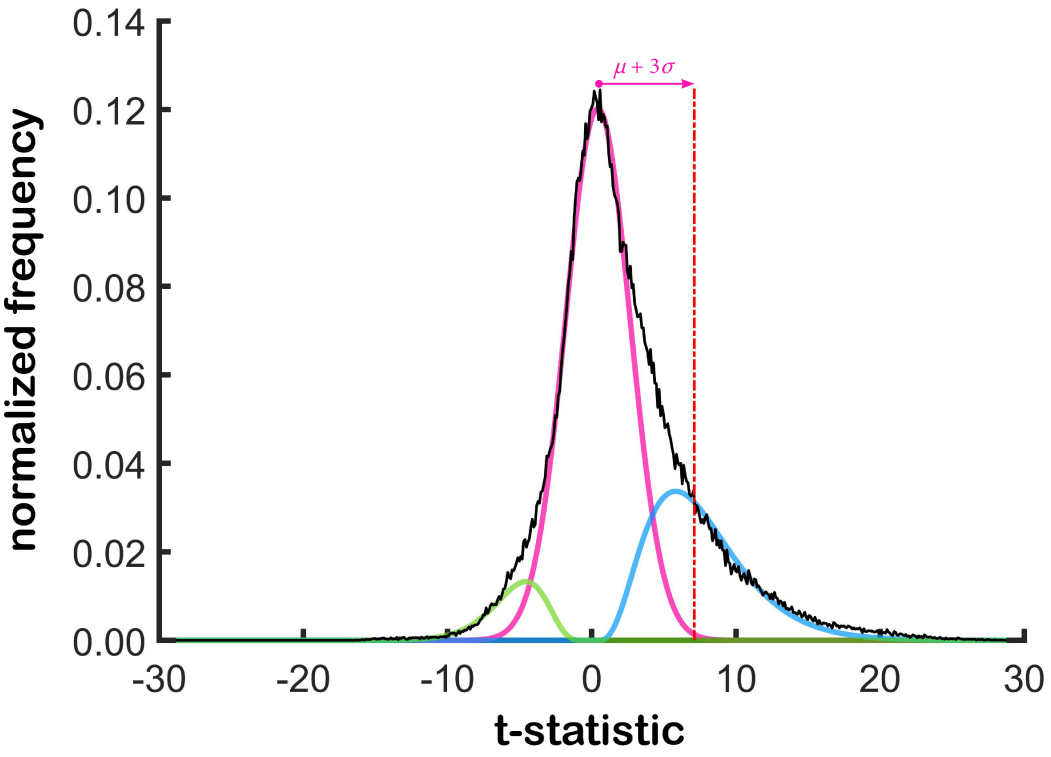

Fig. 5.2. Spatial map thresholding technique. The empirical *t*-statistic distribution (black) of a network component is relatively well described by a mixture of normal (magenta), positive gamma (cyan), and negative gamma (green) distributions. Cutoff score of $\mu + 3\sigma$ removes almost all of the noise voxels (represented by the normal component), while retaining a large number of positive network-related voxels (cyan gamma distribution). See equation 1 for mathematical details.

Since Allen et al. (2012) demonstrated that in the presence of spatial variability, network amplitude is best captured as a product of time course standard deviation and peak spatial map intensity (here, the average intensity value of the top 1% of IC's voxels), we used this measure as a proxy for RSN amplitude. Because of the pre-ICA intensity normalization, the resulting amplitude values were (approximately) in percent signal change units. To ensure that IC spatial maps represent only network topography, as opposed to topography + activation, we normalized all RSN spatial maps by network amplitude (Allen et al., 2011). Network components were visualized using open-source Visualization Toolkit software (VTK; Schroeder et al., 2006).

Modeling age relationships for network amplitude

To build models for each RSN's amplitude's relationship to age, we relied on the fractional polynomial [polynomial set: age^{-2}, age^{-1}, $age^{-0.5}$, ln(age), age^{1}, age^{2}, age^{3}] framework (Royston & Altman, 1994; Sauerbrei & Royston, 1999; Sauerbrei et al., 2006). The fractional polynomial (FP) technique controls for overfitting by restricting shape complexity if a model with $k + 1$ powers does not produce a statistically better fit than a model with k powers.

Since the residual normality and residual homoscedasticity assumptions of the OLS estimator were violated in our RSN amplitude data (see Table 5.2), we used L_1 (i.e., least absolute deviation), as opposed to L_2 (i.e., least squares), regressions to estimate the aging trajectories. Unlike L_2 models, which build trajectories to explain the population mean, L_1 regressions produce fits explaining the population median, and are more robust to heteroscedastic, highly skewed data with severe outliers (Dielman, 2005; Lawrence & Shier, 1981; Wimble et al., 2016). Custom-written MATLAB scripts employing the SIMPLEX algorithm (Nelder & Mead, 1965) were used to find optimal L_1 solutions for all the least absolute deviation regressions.

Statistical significance tests were performed sequentially: (1) best-fitting FP2 (i.e., fractional polynomial model with 2 age power terms) vs. best-fitting FP1, (2) best-fitting FP1 (i.e., fractional polynomial model with 1 non-linear age power term) vs. linear, (3) linear vs. constant. The test statistic (equation 5.2) that we used to evaluate all L_1 regressions was:

$$F_{LAD} = \frac{2(\mathrm{SAR}_{\mathrm{reduced}} - \mathrm{SAR}_{\mathrm{full}})}{\hat{\tau}} \qquad \textbf{(5.2)}$$

where $\mathrm{SAR}_{\mathrm{reduced}}$ and $\mathrm{SAR}_{\mathrm{full}}$ represent the sum of absolute values of the residuals for the reduced and full models, respectively. The denominator parameter τ is the L_1 estimate of residual variability for the full model (for more details on L_1 significance testing see Birkes & Dodge, 1993). To estimate F_{LAD} distributions under each null hypothesis, we performed Monte Carlo simulations (Fig. 5.3), using conceptual framework that is similar to Freedman & Lane's (1983) permutation tests for L_2 regressions. Consistent with the Freedman & Lane (1983) approach, we treated our sample's L_1 regression coefficients as proxies of the true population-level relationship. For each significance test, we first estimated L_1 residuals for the reduced model. However, rather than permuting those residuals (the assumption of residual exchangeability was severely violated in our data; see Table 5.2), we first split the L_1 residuals into 3 age groups: young adult [$N = 43$; age range: 18-39 years,

mean = 27.1 years], middle-aged [N = 31; age range: 41-59 years, mean = 50.0 years], and old adult [N = 31; age range: 61-85 years, mean = 70.3 years]. Each age group's residuals were then used to estimate (using MATLAB's *ksdensity* function) separate residual distributions for young, middle-aged, and old adults (see Fig. 5.3 for examples). Those distributions were subsequently bias-corrected to ensure that the average median of each distribution was centered at 0. In residual simulations, if an individual's age was under 27 years of age, all residuals were randomly sampled from the 'young' distribution exclusively. Similarly, for every individual above 70 years of age, residuals were randomly sampled from the 'old' distribution exclusively. For individuals between 27 and 70 years of age, sampling was performed probabilistically from the two distributions closest to a given subject's age with weights varying as a linear function of age (e.g., residuals for a 60-year-old had a 50/50 percent chance of being sampled from the 'middle-aged' or 'old' distribution; residuals for a 65-year-old had a 25/75 percent chance of being sampled from the 'middle-aged'/'old' distribution, respectively). Such probabilistic sampling smoothed out transitions between age groups by blending neighbouring residual distributions. Lastly, our simulated residuals were added to the previously-estimated null hypothesis (i.e., reduced) model, generating one null hypothesis dataset. Each of our F_{LAD} distributions was constructed from 25,000 such simulations (see Fig. 5.3 for a flow-chart example of linear vs. FP1 model comparison). System-level Holm–Bonferroni correction for multiple comparisons was applied for FP-selected vs. null (i.e., constant) model comparisons [3 comparisons for the somatomotor system, 4 comparisons for the visual system, 1 comparison for the auditory system, 6 comparisons for the default system, 1 comparison for the dorsal attention system, 2 comparisons for the executive control system, and 4 comparisons for the multi-system/mixed components].

Because of sampling-related uncertainty, model choice in data-driven model selection can vary from one dataset to the next. To minimize the effects of model selection uncertainty, we performed weighted model averaging for all of our non-linear fits. Model averaging was performed on a subset of all plausible regression shapes, up to the last statistically significant FP order. Since our RSN amplitude datasets did not satisfy the criteria of theory-driven model averaging, we used bootstrap model selection frequencies as proxies for model selection uncertainty (for an overview of model averaging see Burnham & Anderson, 2002). Bootstrap model averaging was done iteratively. First, a crude model-averaged fit was estimated using paired bootstrap sampling (100 samples). For each paired bootstrap sample, the model with the smallest sum of absolute error terms was selected

using a repeated (50 times) 20-fold cross-validation. Next, estimates of model selection uncertainty were refined by bootstrapping that average fit's residuals. In order to preserve age-specific residual properties (same issues as L_1 hypothesis testing), all bootstrap samples of the residuals were performed in an age-restricted manner (SD = 3 years, relative to each subject's age). During this refined estimation of model selection uncertainty, 500 bootstrap samples were taken, and the model with the smallest sum of absolute error terms was chosen as the best model for each bootstrap sample using a repeated (100 times) 20-fold cross-validation. These refined model selection frequencies were used to compute the final model averaged fits for all non-linear (i.e., FP1 and FP2) models.

To verify our L_1 regression results, we also performed amplitude comparisons among the three major age groups [young: under 40 years (mean age = 27.1 years); middle: 40-59 years (mean age = 50.0 years); old: 60 years and older (mean age = 70.3 years)]. A bias-corrected bootstrap test for statistical significance (50,000 samples) on the difference of age group medians was used for statistical inference. Significance was declared when the FWE 95% bias-corrected accelerated (BCa) confidence interval (CI) excluded zero. System-specific (as above) Holm–Bonferroni correction for multiple comparisons were carried out sequentially. Initially, we tested the significance of group comparisons with the largest amplitude differentials (typically young vs. old) among all RSNs of a brain system (e.g., visual, default, somatomotor, etc.). If statistically significant, follow-up Holm–Bonferroni-corrected comparisons [3 tests: (1) young vs. middle, (2) middle vs. old, and (3) young vs. old] were performed to determine whether network amplitude differed in the other age group comparisons.

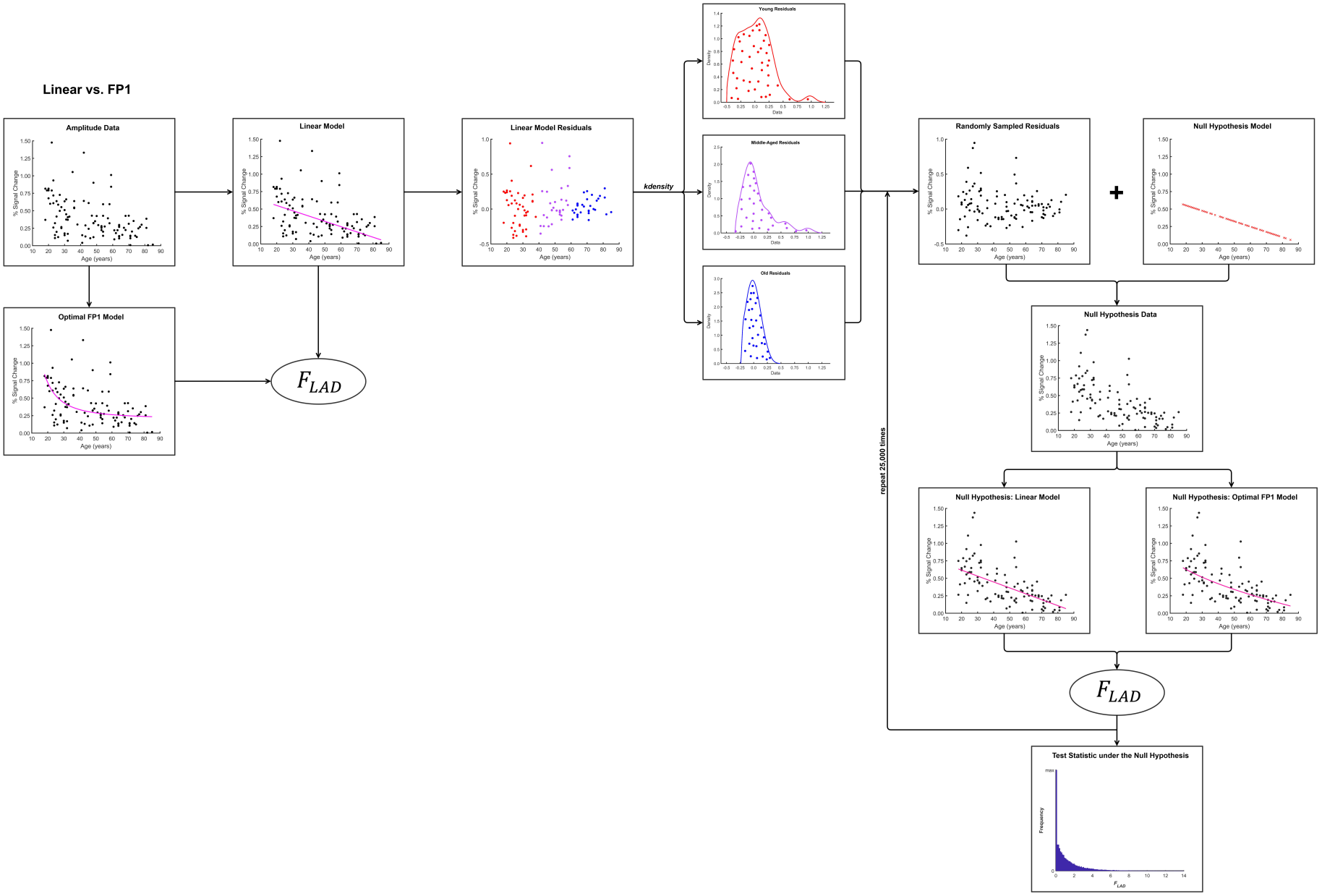

Fig. 5.3. Flow-chart of L_1 significance testing for fractional polynomial model comparisons [polynomial set: age^{-2}, age^{-1}, age$^{-0.5}$, ln(age), age^{1}, age^{2}, and age^{3}] that were used in age relationship analyses of network amplitude. An example linear vs. FP1 model comparison is presented; however, the same logic was applied in linear vs. constant and FP1 vs. FP2 comparisons. Abbreviations: FP1, fractional polynomial model with one age power term, except linear; FP2, fractional polynomial model with 2 age power terms. See the main text for additional details.

Modeling age relationships for spatial maps

Permutation-based *F*-tests (50,000 permutations using FSL's *randomize* function with threshold-free cluster enhancement option; Smith & Nichols, 2009) were used to test for the presence of linear or quadratic relationships to age in component topography. Clusters with statistically significant relationships to age were cleaned up by (1) removing all clusters with volume smaller than 80 mm^3, representing 1-3 native-space voxels, (2) removing all clusters dominated (i.e., 50% or more) by white matter (WM) or cerebrospinal fluid (CSF) signal, and (3) removing clusters, in which grey matter contribution to the cluster peak (top 30% of voxels with the strongest association to age) was less than 50%. All age clusters that survived this cleanup procedure were followed up with parametric fractional polynomial regression (RA2 model selection; Ambler & Royston, 2001). Similar to RSN amplitude methodology, if non-linearity tests were significant, bootstrapping was used to account for model selection uncertainty by building model-averaged fits.

Finally, because it is well established that cortical grey matter (GM) volume is negatively correlated with age (Good et al., 2001; Fjell et al., 2009a; Raz et al. 1997, 2004, 2005), we examined whether adding a cluster's GM volume would eliminate statistical association to age in spatial map regions showing age effects. To answer this question, we performed cluster-level regressions (i.e., RSN signal averaged across a cluster) with subject age and local GM density as the independent variables. Significant regression coefficients for age are indicative of age-related differences in network topography that cannot be fully accounted for by age-related changes in regional GM volume. Our GM density maps were estimated in native space using SPM12 automated tissue segmentation pipeline, and were subsequently registered to the MNI template using the same transformation matrices that we used for normalizing our fMRI data.

Between-system connectivity

The most common approach to building graphical models of brain organization is to use time course correlation coefficients as proxies for connectivity (Craddock et al., 2013; Smith et al., 2011). However, this approach suffers from two significant limitations: (1) a lack of control for communication via indirect paths, and (2) a reliance on somewhat arbitrary thresholding. To avoid these issues, we implemented a sparse precision matrix estimation procedure when reconstructing inter-IC connectivity graphs (Craddock et al., 2013; Epskamp & Fried, 2018; Rubinov & Sporns

2010; Smith et al., 2011; Zhu & Cribben, 2018). Instead of relying on arbitrary thresholds, sparse estimation methods shrink spurious or indirect connections to 0 by penalizing excessive model complexity (Smith et al., 2011; Zhu & Cribben, 2018).

Zhu & Cribben (2018) used simulations to show that sparse network structure is best recovered using the maximum likelihood estimation of the precision matrix with the smoothly clipped absolute deviation (SCAD) regularization term as a penalty for model complexity. This approach belongs to a family of graph estimation techniques building on the graphical lasso framework (Friedman et al., 2008). Similar to the graphical lasso, incorporating the SCAD regularization term during graph estimation allows for the optimal balance between network complexity and network likelihood; however, relative to the more common LASSO penalty term, using SCAD reduces bias without sacrificing model stability (Fan & Li, 2001; Zhu & Cribben, 2018). The SCAD penalty relies on two tuning parameters, a and ρ. To minimize the Bayes risk, Fan & Li (2001) recommend $a = 3.7$, which was used in the current study. The second tuning parameter, ρ, was selected using Bayesian Information Criterion (BIC) from a set of $\rho i = i \times 0.01$, with $i = 1, 2, 3 \ldots, 100$. The ρ with the lowest BIC value was used to build final graphs (Fan et al. 2009; Zhu & Cribben, 2018). Because temporal autocorrelation in the fMRI time series can produce biased FC estimates (Arbabshirani et al., 2014; Zhu & Cribben, 2018), each component's time course was whitened prior to graph estimation. Furthermore, since averaging across subjects improves the stability of edge detection when using sparse graphical methods, inter-component FC was estimated on group-averaged (i.e., young, middle-aged, and old adults) covariance matrices. For reasons detailed in Rubinov & Sporns (2010), edges representing anti-correlations were removed from the estimated graphs. All sparse graphs were estimated using custom-written *R* functions, and Gephi (v0.9.2; Bastian et al., 2009) was used for graph visualizations. Follow-up graph summary metrics were computed using freely available Brain Connectivity Toolbox for MATLAB (Rubinov & Sporns, 2010),

Since our inter-component FC was estimated at the group level, we relied on group comparisons [Young vs. Old, Young vs. Middle, Middle vs. Old], rather than on correlation-based methods, to study age differences in inter-component connectivity. Edge weight comparisons and weighted graph summary metrics were used to study age effects on FC strength, while unweighted graph summary metrics were used to study age differences in graph architecture, independent of FC

strength. Mathematical definitions of all weighted and unweighted graph summary metrics that were used in this study are provided in the *Appendix* (sections 5.5-5.6).

Statistical significance for each graph-based age comparison was assessed using permutation tests (10,000 permutations), and false discovery rate (FDR)-corrected results are reported, for q = .05 (Hochberg, 1988). Global graph summary metrics were corrected for 3 tests (i.e., Young vs. Old, Young vs. Middle, Middle vs. Old), node centrality metrics for 21 tests (i.e., 21 RSNs in each age comparison), and edge comparisons for 56-59 tests (depending on the number of non-zero edges in relevant age groups). Since this study was exploratory in nature, we also report edge weight differences that survived an uncorrected p <. 01 threshold.

5.3. Results

Resting-state brain networks and their functional connectivity profiles

Following group-level spatial ICA decomposition, we identified 21 ICs representing RSN sources: 3 somatomotor [SM1, SM3, SM3], 4 visual [Vis1, Vis2, Vis3, Vis4], 1 auditory [Au], 6 default mode [DM1, DM2, ..., DM6], 1 dorsal attention [DA], 2 executive control [EC1, EC2], and 4 ICs with spatial maps covering multiple brain systems, according to the Yeo et al. (2011) functional parcellation of the cerebral cortex. Here, we termed those multi-system ICs as mixed RSNs (Mix1-Mix4). Figures 5.4-5.7 demonstrate the spatial topography of each RSN in our study.

Consistent with the underlying physiology, our somatomotor RSNs map onto face, hand, and leg areas of the primary somatosensory and primary motor cortices. Similarly, our visual ICs approximate central/peripheral and primary/secondary visual processing pathways, while the default system was split into the dorsal medial (DM3, DM6), medial temporal (DM2), and core (DM1, DM4, DM5) subsystems. Although 3 default mode subsystems are typically emphasized in the previously published literature (Andrews-Hanna et al., 2010, 2014; Christoff et al., 2016), using 4.7 T data, we obtained a more refined splitting of the DMN into its sub-components. RSNs of other cognitive systems, namely the dorsal attention and executive control, were captured by relatively few ICs (Figs 5.4-5.7).

Our SCAD-regularized functional connectivity graph, representing direct inter-component FC for the entire (i.e., age-averaged) sample, revealed a high degree of functional specialization in the somatomotor and visual areas with few direct connections to other functional systems (Fig. 5.8).

This is in contrast to the default, dorsal attention, and executive control RSNs, which demonstrated a high degree of interconnectedness with network components from other functional systems: DA, DM1, DM5, and EC2 RSNs each had 2 or more direct connections with systems other than their own. Most multi-system (i.e., mixed) network components served as bridge nodes connecting functionally segregated systems to each other (Fig. 5.8).

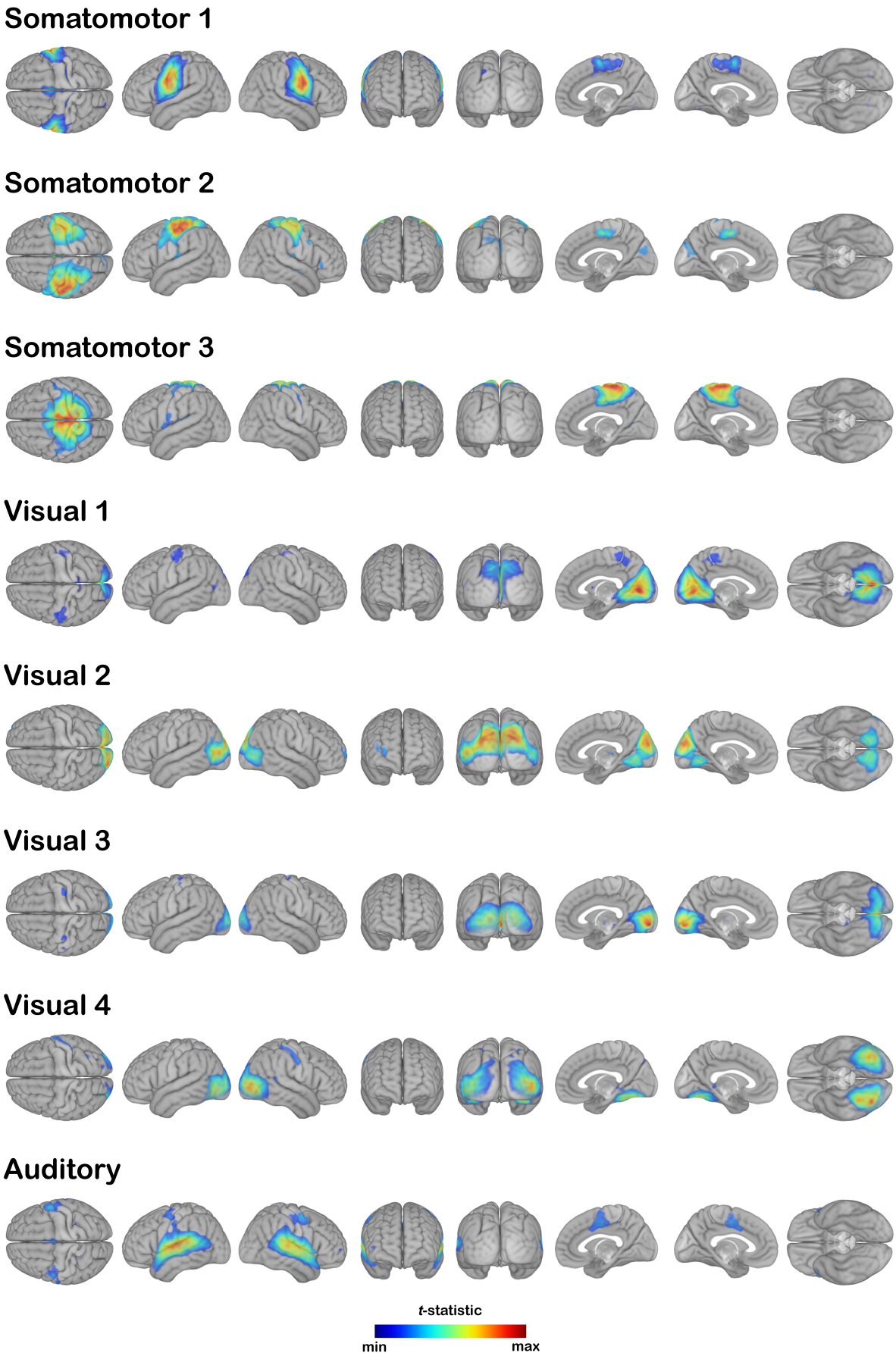

Fig. 5.4. Sensorimotor network components identified by group ICA.

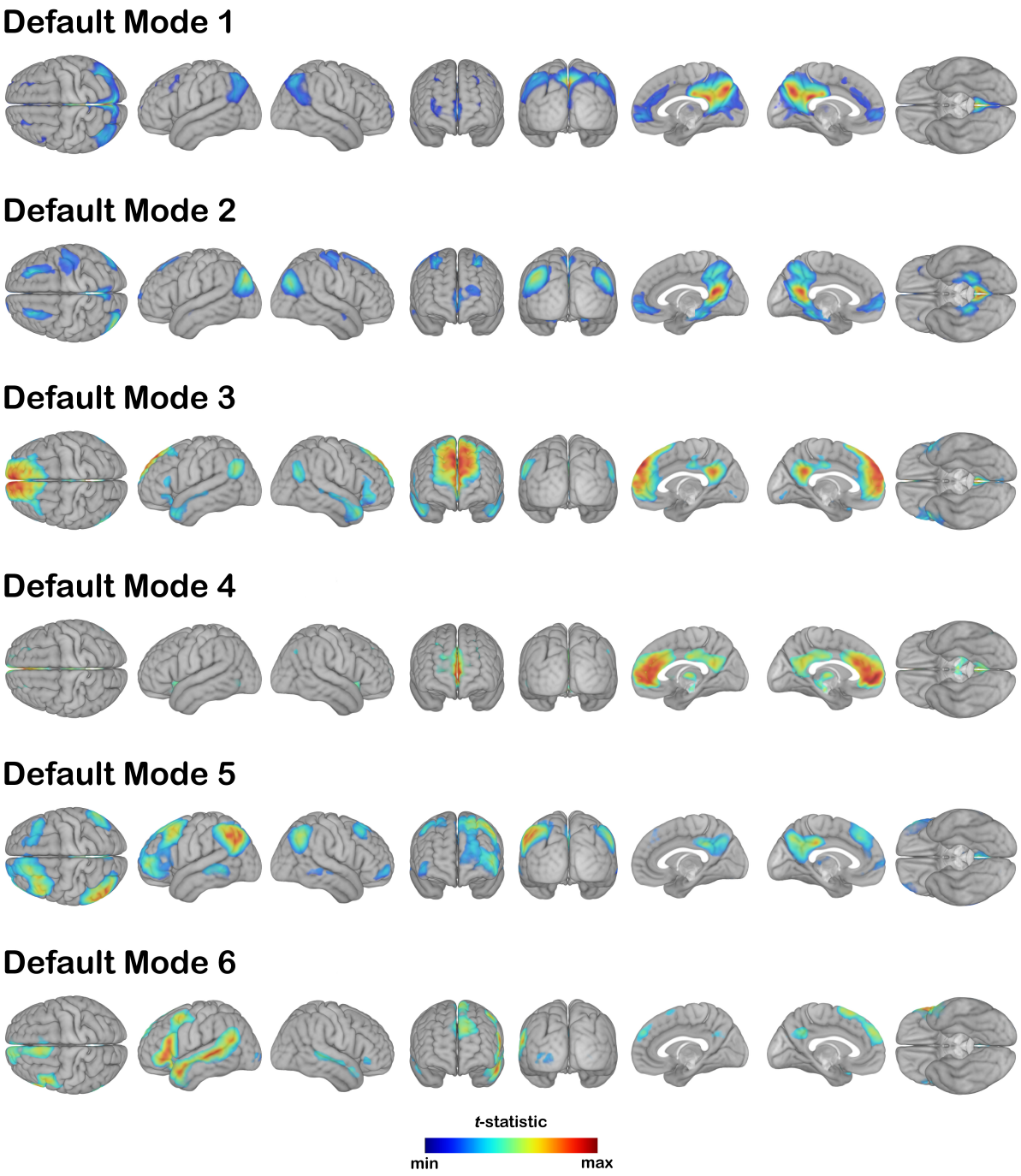

Fig. 5.5. Default mode network components identified by group ICA.

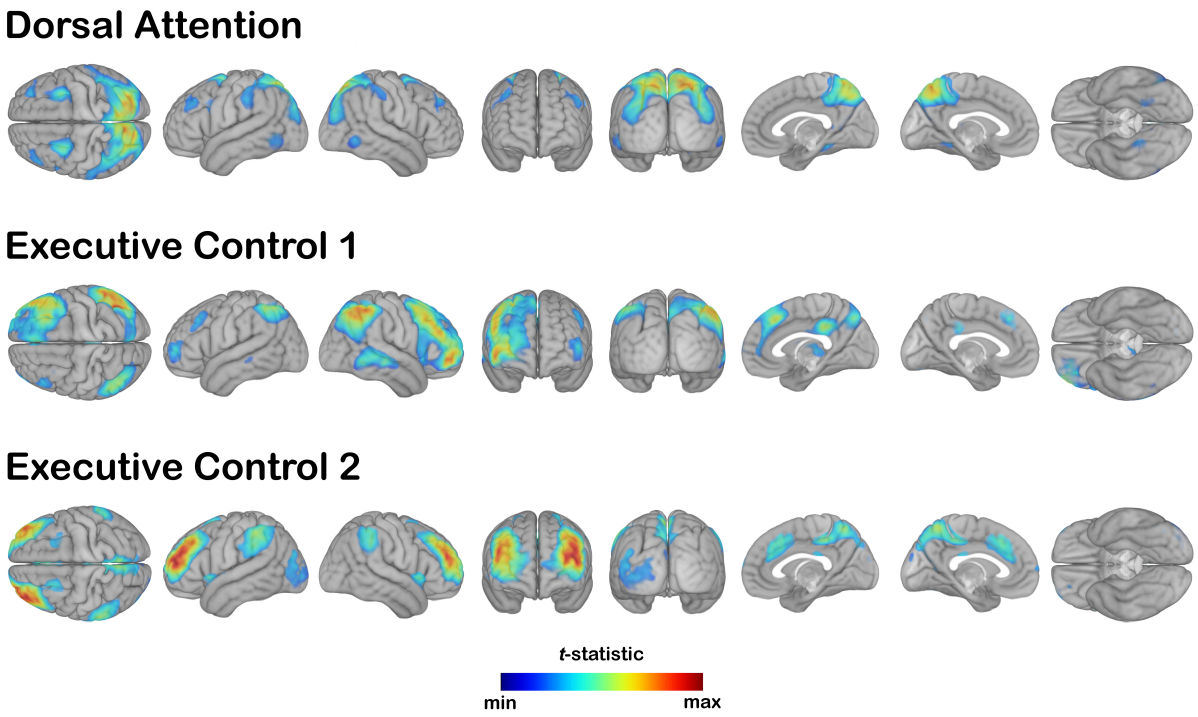

Fig. 5.6. Attention-related network components identified by group ICA.

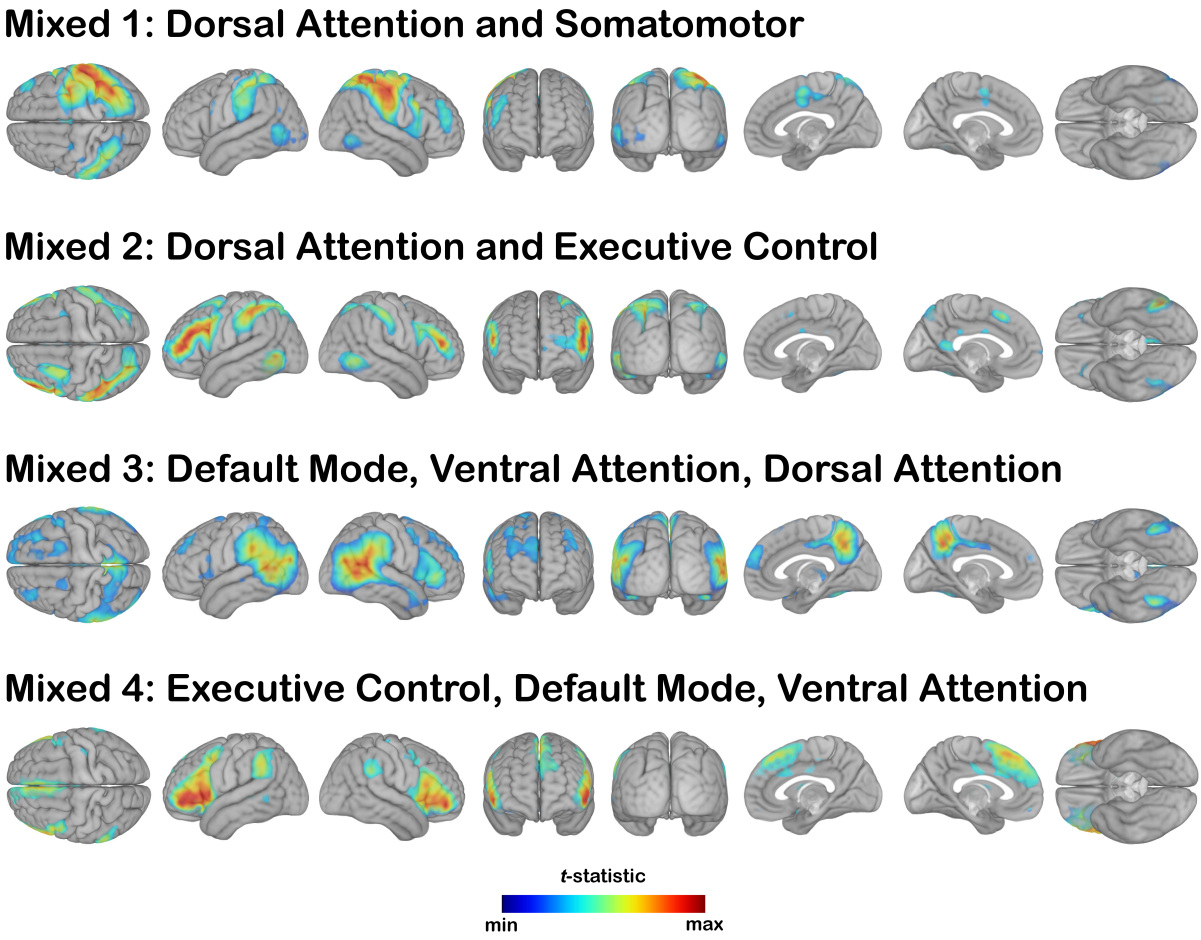

Fig. 5.7. Network components with multi-system or mixed topography.

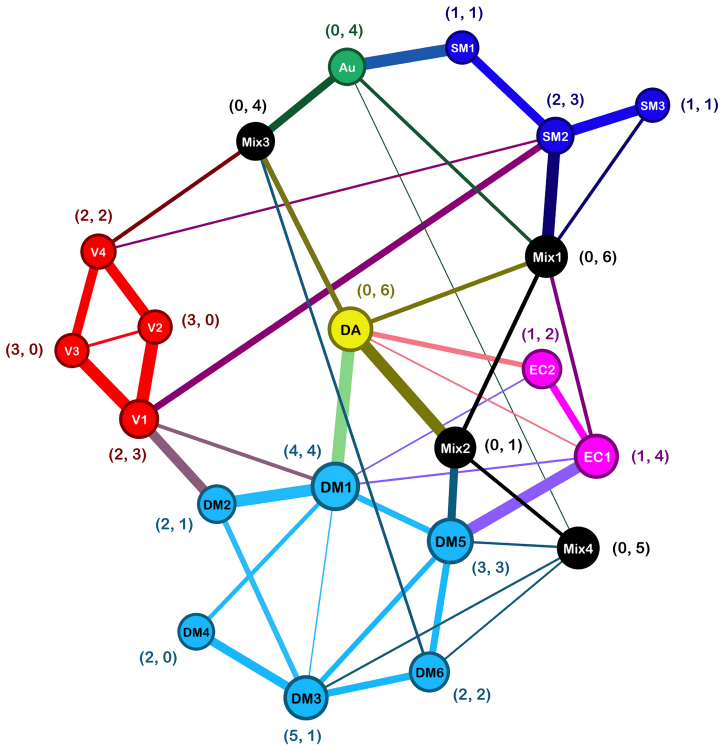

Fig. 5.8. Graphical representation of the intrinsic inter-component functional connectivity. Only positive correlations are shown. Edge thickness represents the magnitude of SCAD-regularized partial correlation for RSN pairs. Node size represents the magnitude of unweighted eigenvector centrality. Coordinates depict the number of within-system (left number) and between-system (right number) connections. Node colors represent functional systems to which each network component belongs: SM, somatomotor (blue); V, visual (red); Au, auditory (green); DM, default mode (cyan); DA, dorsal attention (yellow); EC, executive control (magenta); Mix, mixed (black). See Figs. 5.4-5.7 for spatial topography of each node.

Network amplitude and age

Our L_1 regression analyses showed that signal amplitude in every RSN was negatively associated with age (all corrected *p*s < .05; Figs. 5.9-5.11). Non-linearity tests were statistically significant in only 4 out of 21 RSNs — SM2, SM3, Vis3, and DA — indicating that linear models provide a reasonable explanation of the association between age and BOLD signal amplitude in most brain areas. In a typical 75-year-old, the system-averaged (i.e., averaged across 6 default mode components, 4 visual components, 3 somatomotor components, etc.) BOLD signal amplitude was reduced by 61% in the somatomotor system, 63% in the visual system, 41% in the auditory system, 37% in the default system, 53% in the dorsal attention system, and 38% in the executive control system, when compared to a typical 25-year-old (Figs. 5.9-5.11). The smallest (30% or less) age-associated decline of BOLD amplitude was observed in the default mode and Mix4 ICs (Figs. 5.10-5.11), while all of the somatomotor and visual ICs showed >50% BOLD amplitude reduction from young adulthood to old age (Fig. 5.9).

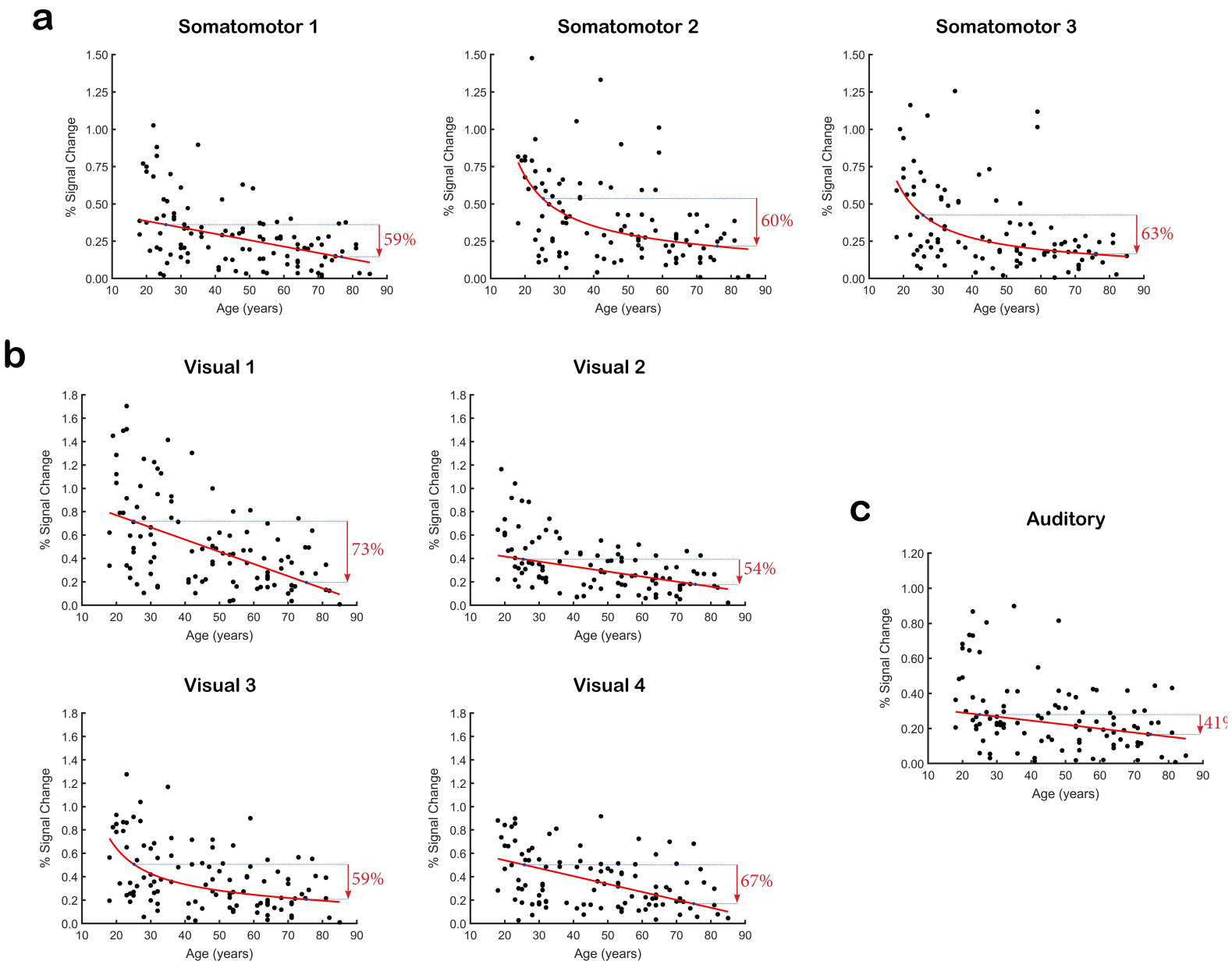

Fig. 5.9. L_1 fractional polynomial regression plots showing relationships between age and RS-fMRI amplitude in all (a) somatomotor, (b) visual, and (c) auditory networks. Red arrows represent relative differences in resting-state fluctuation amplitude between a median 25-year-old and a median 75-year-old.

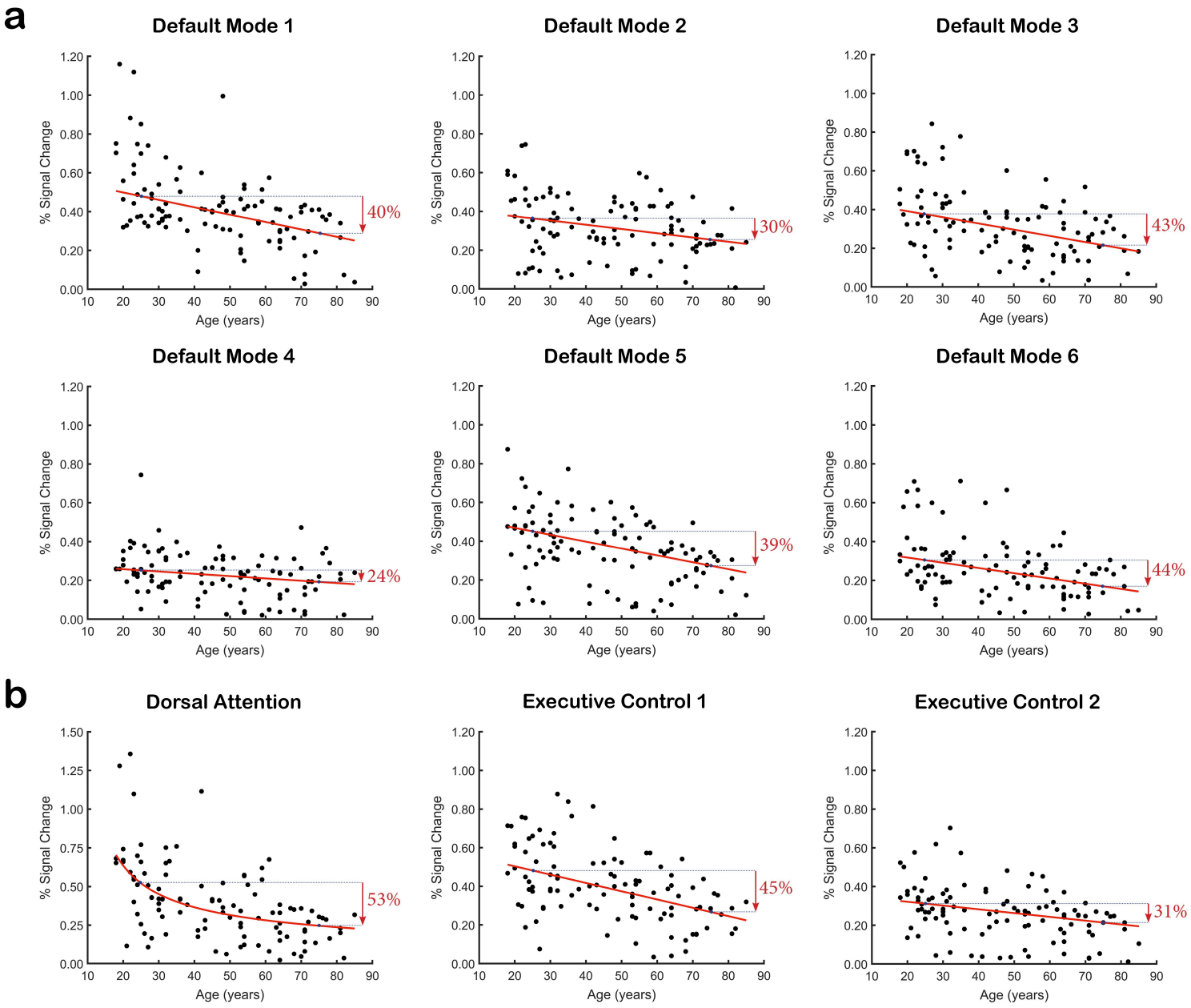

Fig. 5.10. L_1 fractional polynomial regression plots showing relationships between age and RS-fMRI amplitude in all (a) default mode and (b) attention-related networks. Red arrows represent relative differences in resting-state fluctuation amplitude between a median 25-year-old and a median 75-year-old.

To determine whether a common brain-wide process is responsible for the observed BOLD amplitude decline with age, we performed a principal component analysis (PCA) on the amplitude data from all network ICs. Only the first principal component, explaining 58% of the RSN amplitude variability, was statistically significant in this PCA decomposition. This principal component (Fig. 5.11b) was positively correlated with every RSN (correlation coefficients between .545 and .865) and negatively correlated with age (r = -.553, p < .001).

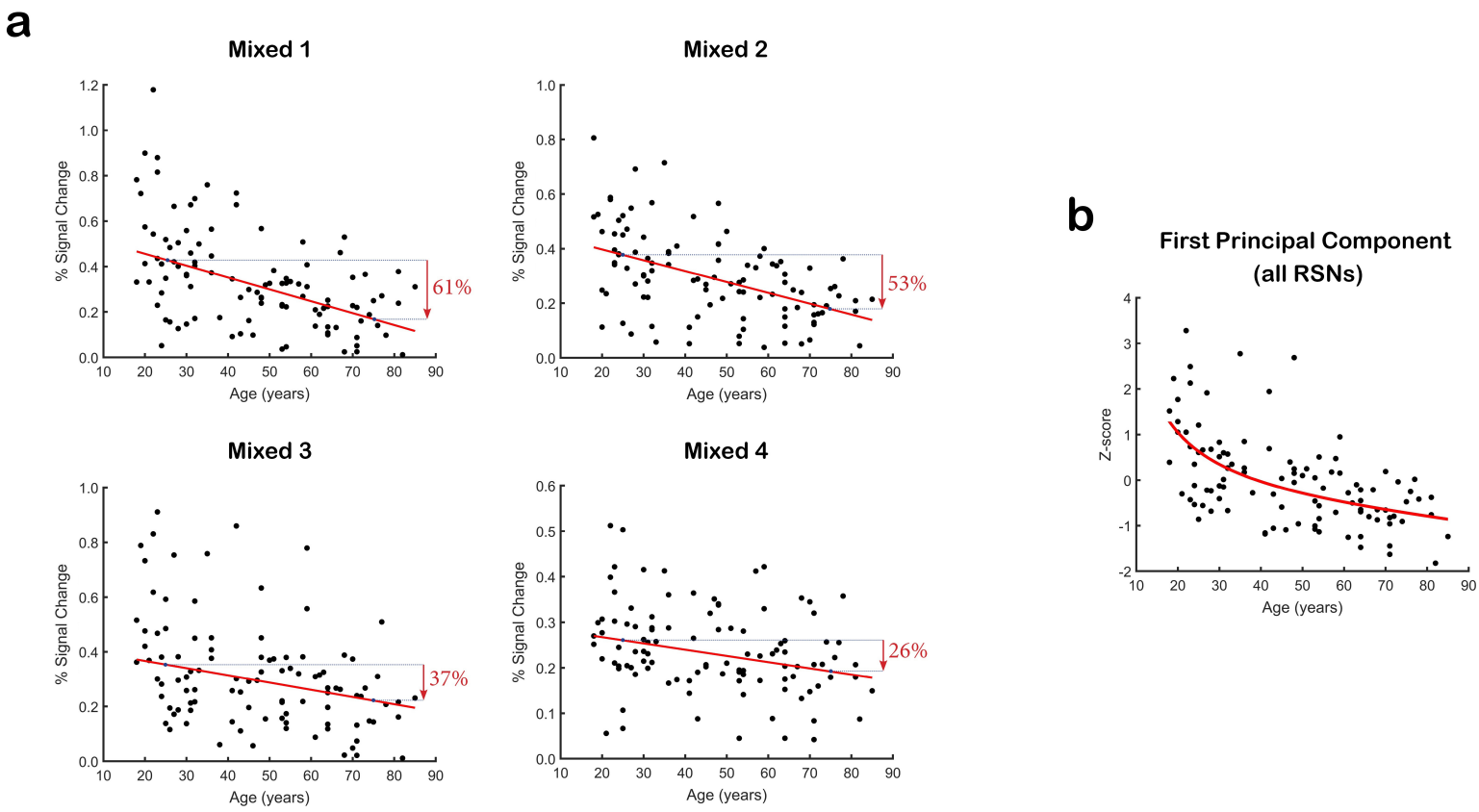

Fig. 5.11. L_1 fractional polynomial regression plots showing relationships between age RS-fMRI amplitude in (a) all mixed networks; (b) principal component explaining 58% of variability in network amplitude across all 21 networks. In panel (a) the relative difference in activity between an average 25-year old and an average 75-year old is shown in percentage units. Because aging trajectories for individuals RSNs were either linear or FP1 models, the age relationship trendline for the principal component in panel (b) represents a model-averaged fit of L_1 linear and FP1 models.

Age group comparisons of the RSN amplitude and amplitude variability were statistically significant in most young vs. old tests, with some networks also showing statistically significant differences in young vs. middle and/or middle vs. old comparisons (Figs. 5.12-5.14). However, unlike the continuous models, which showed age-associated decline of BOLD amplitude in every RSN, group amplitude comparisons did not detect any age differences in the DM2 and Mix4 network components. In all instances where young vs. old comparisons were statistically significant, median RSN amplitude was larger in young adults than in middle-aged and old adults, and larger in middle-aged adults than in old adults, suggesting a continuous and progressive reduction in RSN signal amplitude throughout life. Lastly, old adults had significantly lower inter-individual BOLD amplitude variability in all sensorimotor (SM1-3, Vis1-4, and Au) ICs, two default mode ICs (DM2 and DM3), two attention (DA and EC1) ICs, and three mixed (Mix1-3) ICs

Table 5.2

L_1 inter-individual variability of network amplitude for the young adult, middle age, and old adult groups. L_1 variability was calculated for each RSN separately as an average of absolute deviations from each age group's median amplitude. Measures are in % signal change units that represent relative magnitude of BOLD signal fluctuations around the intensity-normalized baseline.

	YOUNG	MIDDLE	OLD	STATISTICAL COHORT DIFFERENCES
Sensorimotor				
Somatomotor 1	0.191	0.121	0.088	Young > Old [$p < .001$]; Young > Middle [$p < .05$]
Somatomotor 2	0.226	0.199	0.092	Young > Old [$p < .001$]; Middle > Old [$p < .001$]
Somatomotor 3	0.245	0.316	0.059	Young > Old [$p < .001$]; Middle > Old [$p < .001$]
Visual 1	0.345	0.198	0.145	Young > Old [$p < .001$]; Young > Middle [$p < .01$]
Visual 2	0.201	0.123	0.089	Young > Middle > Old [all $ps < .05$]
Visual 3	0.258	0.179	0.121	Young > Middle > Old [all $ps < .05$]
Visual 4	0.215	0.165	0.127	Young > Old [$p < .05$]
Auditory	0.168	0.130	0.089	Young > Old [$p < .01$]
Default Mode				
Default Mode 1	0.154	0.105	0.105	None
Default Mode 2	0.141	0.115	0.084	Young > Old [$p < .05$]
Default Mode 3	0.148	0.105	0.091	Young > Old [$p < .05$]
Default Mode 4	0.081	0.077	0.086	None
Default Mode 5	0.128	0.140	0.087	None
Default Mode 6	0.118	0.095	0.080	None
Attention				
Dorsal Attention	0.198	0.201	0.102	Young > Old [$p < .001$]; Middle > Old [$p < .01$]
Executive Control 1	0.154	0.120	0.099	Young > Old [$p < .05$]
Executive Control 2	0.106	0.123	0.074	None
Multi-System				
Mix 1	0.179	0.110	0.095	Young > Old [$p < .01$]; Young > Middle [$p < .05$]
Mix 2	0.127	0.105	0.073	Young > Old [$p < .01$]
Mix 3	0.161	0.131	0.092	Young > Old [$p < .01$]
Mix 4	0.073	0.074	0.063	None

[all corrected *p*s < .05; Table 5.2]. Six network components – DM1, DM4-6, Mix4, and EC2 – showed no age differences in BOLD amplitude's inter-individual variability (all *p*s > .1).

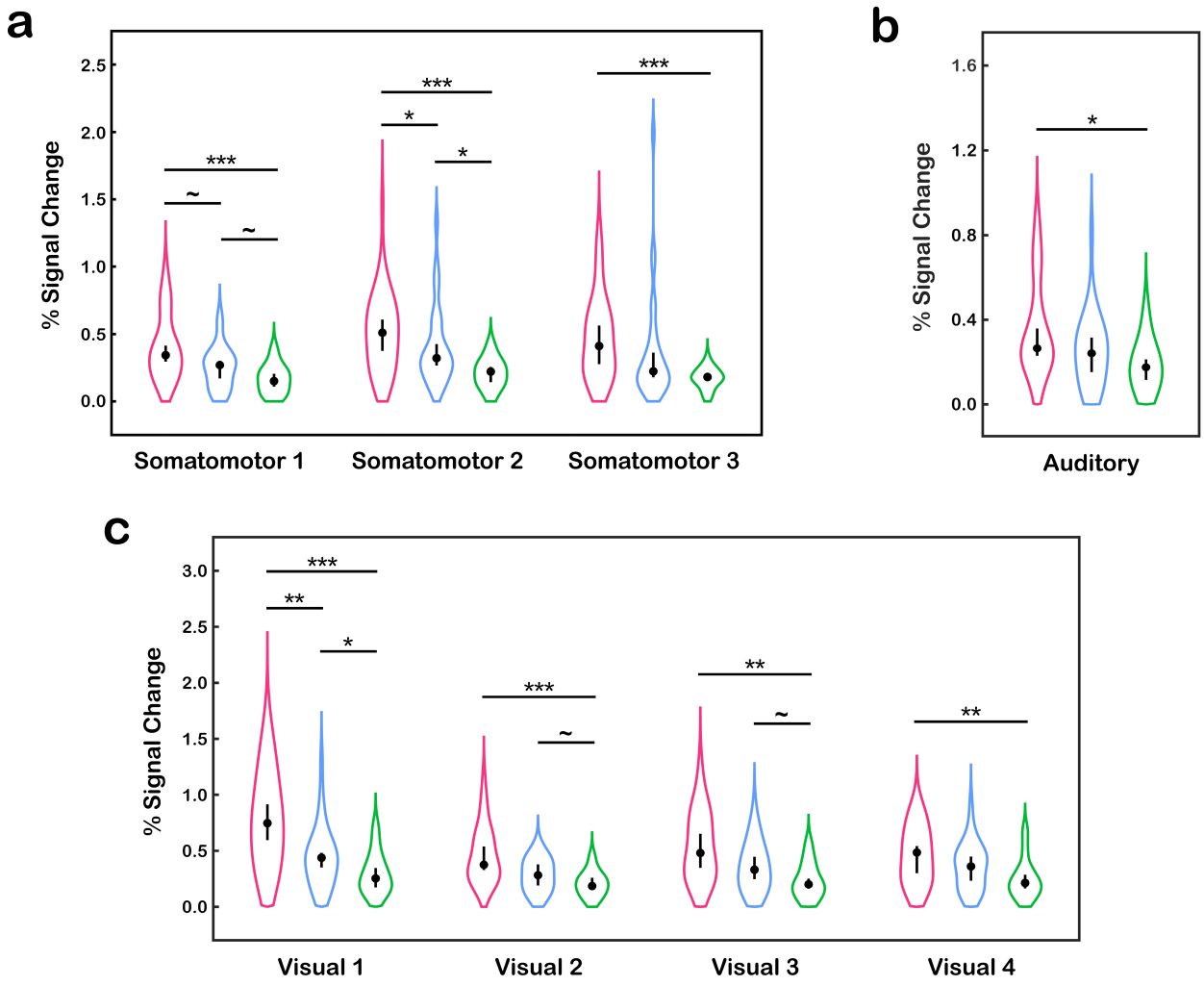

Fig. 5.12. Violin plots showing distribution of network amplitude for young (red), middle-aged (blue), and old (green) adults. All measures of network amplitude are in % signal change units, representing relative magnitude of BOLD signal fluctuations around the intensity-normalized baseline. (a) somatomotor networks; (b) auditory network; (c) visual networks. Group medians are represented by dots at the center of each violin plot with the uncertainty intervals representing the 95% BCa bootstrap confidence interval around the group median. Bootstrap technique was used to evaluate the statistical significance of the difference between age group medians. Pairwise comparisons were declared significant if the BCa bootstrap confidence intervals of the difference between two group medians did not cross 0 at tested thresholds:

~ 90%; * 95%; ** 99%; *** 99.9%.

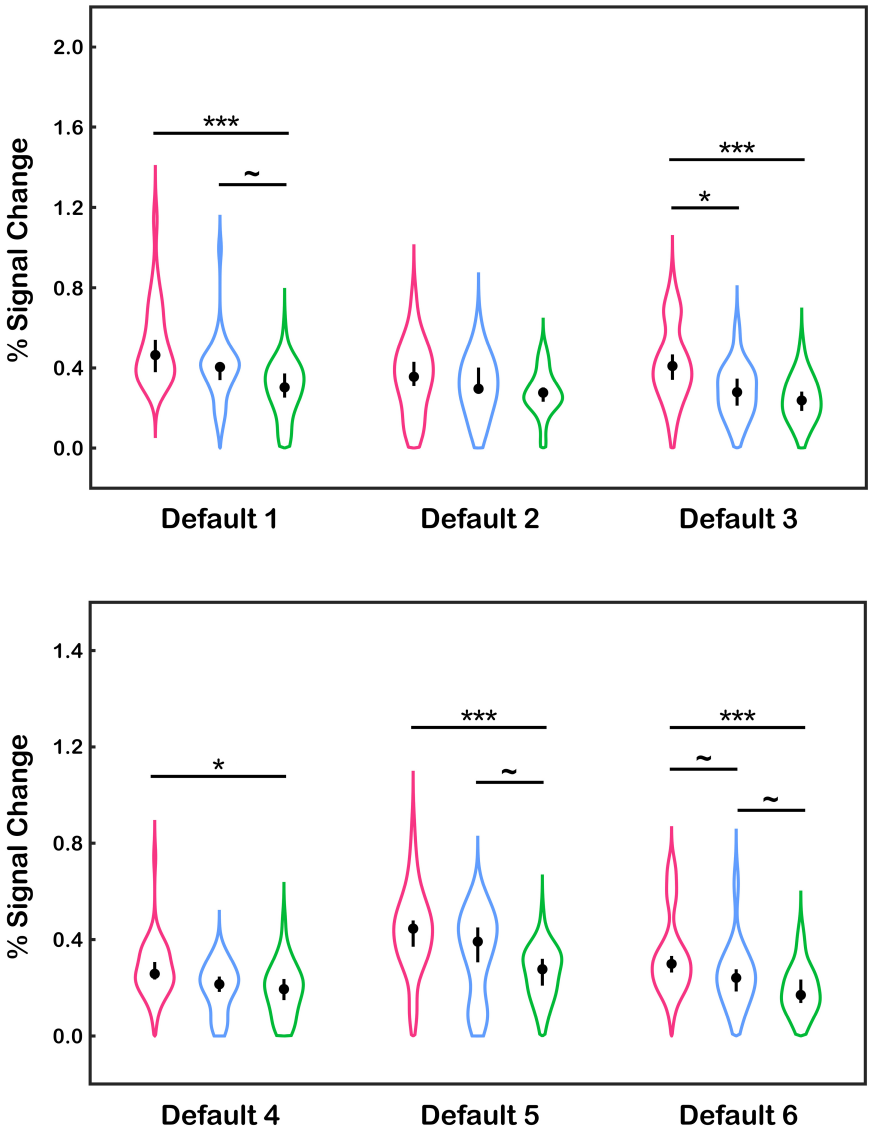

Fig. 5.13. Violin plots showing distribution of network amplitude for young (red), middle-aged (blue), and old (green) adults for each of the default mode networks. All measures of network amplitude are in % signal change units, representing relative magnitude of BOLD signal fluctuations around the intensity-normalized baseline. Group medians are represented by a dot at the center of each violin plot with the uncertainty interval representing the 95% BCa bootstrap confidence interval around the group median. Bootstrap technique was used to evaluate the statistical significance of the difference between age group medians. Pairwise comparisons were declared significant if the BCa bootstrap confidence intervals of the difference between two group medians did not cross 0 at tested thresholds:
~ 90%; * 95%; ** 99%; *** 99.9%.

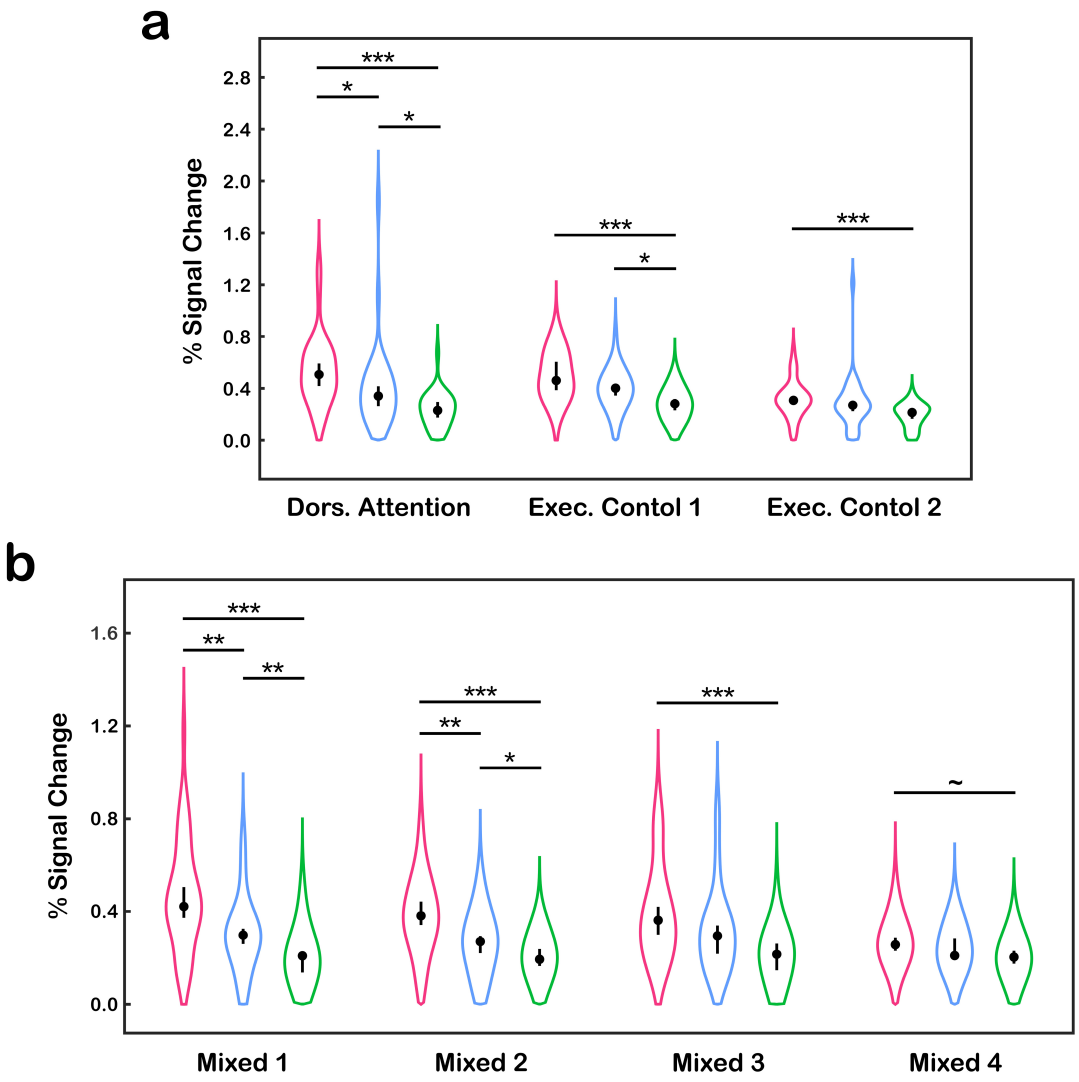

Fig. 5.14. Violin plots showing distribution of network amplitude for young (red), middle-aged (blue), and old (green) adults for each of the (a) attention, and (b) mixed networks. All measures of network amplitude are in % signal change units, representing relative magnitude of BOLD signal fluctuations around the intensity-normalized baseline. Group medians are represented by a dot at the center of each violin plot with the uncertainty interval representing the 95% BCa confidence interval around the group median. Bootstrap technique was used to evaluate the statistical significance of the difference between age group medians. Pairwise comparisons were declared significant if the BCa bootstrap confidence intervals of the difference between two group medians did not cross 0 at tested thresholds:
~ 90%; * 95%; ** 99%; *** 99.9%.

Network topography and age

Across all network components, we identified 23 clusters with either linear or non-linear statistical relationship to age (Table 5.3; Figs. 5.15-5.18). Age relationship clusters were present in 5 out of 8 sensorimotor ICs, 4 out of 6 default mode ICs, 2 out of 3 attention/control ICs, and 2 out of 4 mixed ICs, suggesting that age effect on RSNs' spatial map profiles is not limited to one particular functional system. Most of those age relationship clusters (19 out of 23) represented reduced intra-component connectivity among the elderly; however, a small number (4 out of 23), restricted to the DM1 and DA RSNs, showed areas with stronger intra-component connectivity in old age. With the exception of a few clusters, age relationships were linear.

The largest clusters, representing age differences in network topography, belonged to the Mix4 IC. Those two clusters (clusters V & W; Table 5.3) were located within the bilateral inferior frontal gyrus and bilateral orbitofrontal cortex [BA44-47], roughly corresponding to the Broca's area and nearby cortices. Participation of these brain areas in Mix4 RSN declined from moderate/high in young adults (normalized activation of 0.4 and higher) to weak (normalized activation < 0.4) in old adults, which is indicative of BA44-47 areas becoming increasingly disconnected from the rest of the network with age. Two other large clusters (1) cluster K, belonging to the DM4 RSN, and (2) cluster F, belonging to the Vis4 RSN, also showed a reduction in intra-component connectivity with age. Four clusters with the strongest association to age (i.e., largest absolute correlation with age) were clusters F, W, V, and C, belonging to the Vis1, Vis4, and Mix4 RSNs (Table 5.3). All 4 clusters showed negative linear relationships to age with correlation coefficients ranging between -.54 and -.58. Cluster C was localized within the left lingual, intracalcarine, and precuneus cortices, while cluster F's anatomy was restricted to the right fusiform gyrus (Table 5.3). Clusters V and W and their anatomical profiles were described above.

GM volume was negatively associated with age in 21 out of 23 clusters. However, adding regional GM volume as an extra variable to cluster-level age regressions did not eliminate age effects in 21 out of 23 clusters (Table 5.3), demonstrating that age differences in component structure were not driven solely by age effects on cortical GM. Despite these overall trends, it is important to note that adding local GM volume as a regressor of no-interest, eliminated age effects in clusters A and L (SM1 and DM4 RSNs, respectively). Together, these observations indicate that age differences in component topography are partially driven by age differences in regional GM. Furthermore, since cluster GM volume and intra-component connectivity were statistically

associated in 17 clusters (assessed using distance correlation with 50,000 permutation tests for significance), causal study designs are needed for an accurate estimation of the extent to which structural and functional changes in the aging brain produce age differences in network topography.

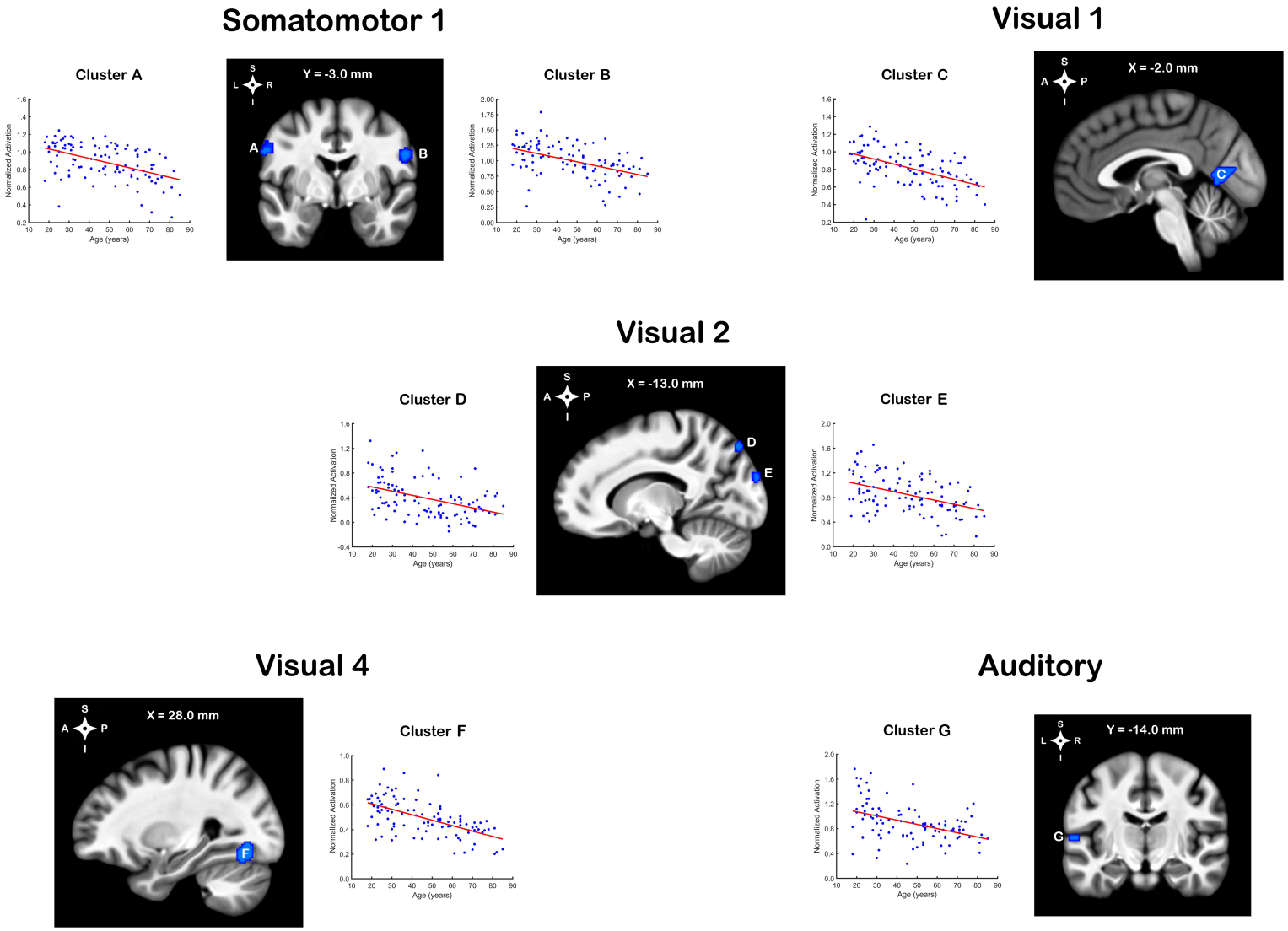

Fig. 5.15. Clusters with statistical relationships to age for sensorimotor ICs. Each cluster represents brain region(s) with age differences in network topography. Regression plots represent voxel-averaged fractional polynomial follow-ups. Because spatial maps were normalized by peak activation amplitude, values close to 1 represent network core, while those close to 0 represent network periphery.

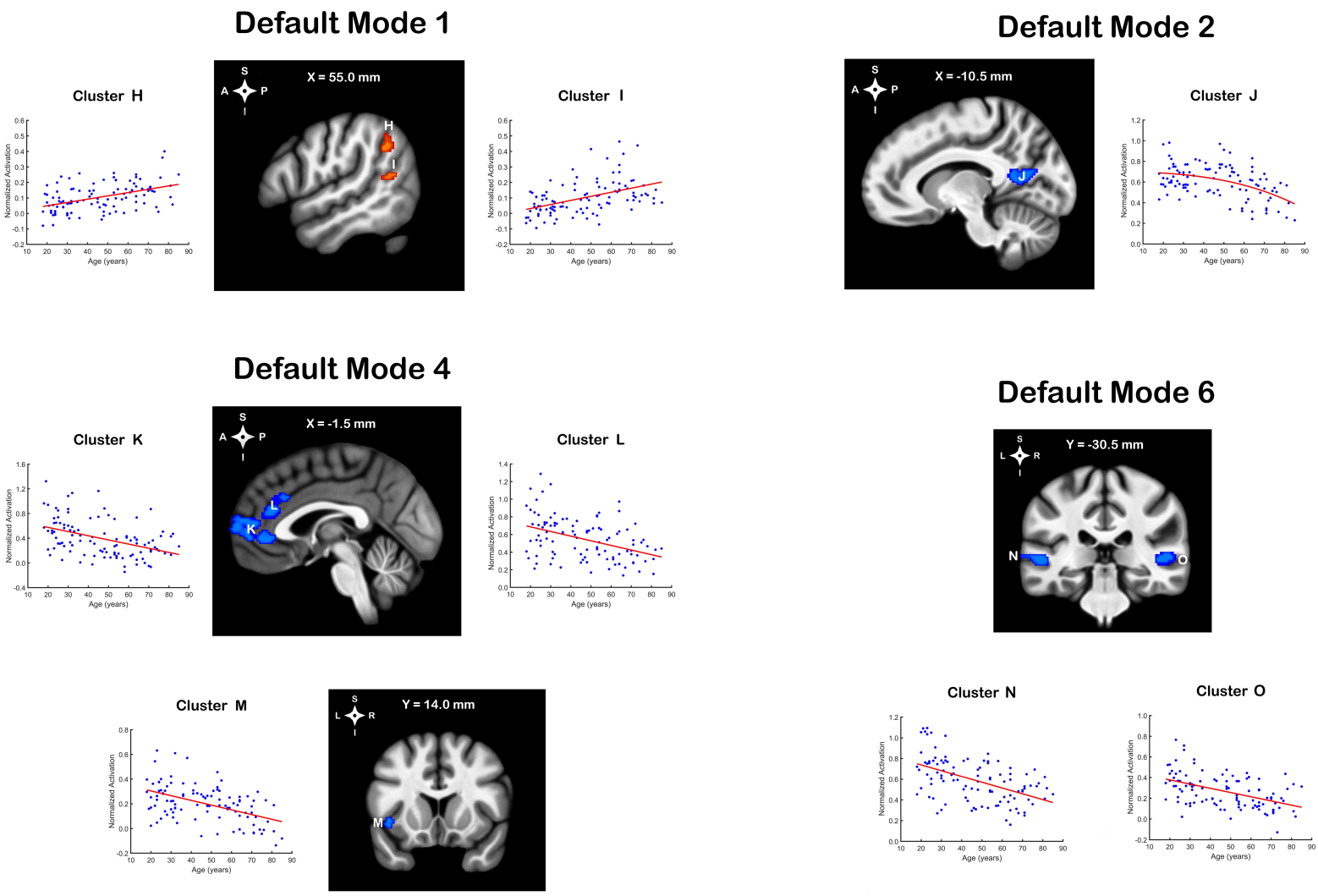

Fig. 5.16. Clusters with statistical relationships to age for the default mode ICs. Blue clusters represent negative association to age; red clusters represent positive association to age.

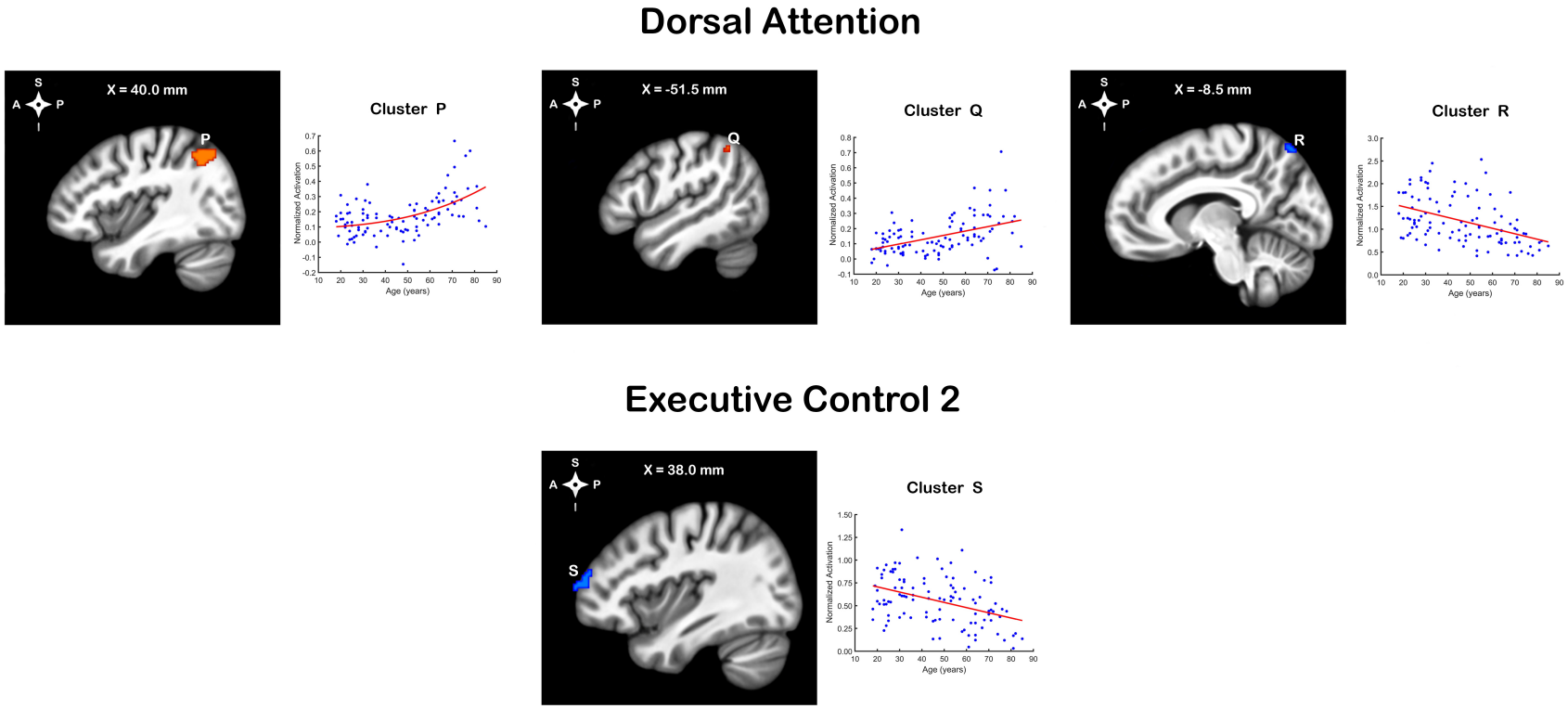

Fig. 5.17. Clusters with statistical relationships to age for the attention-related ICs. Blue clusters represent negative age relationships; red clusters represent positive age relationships.

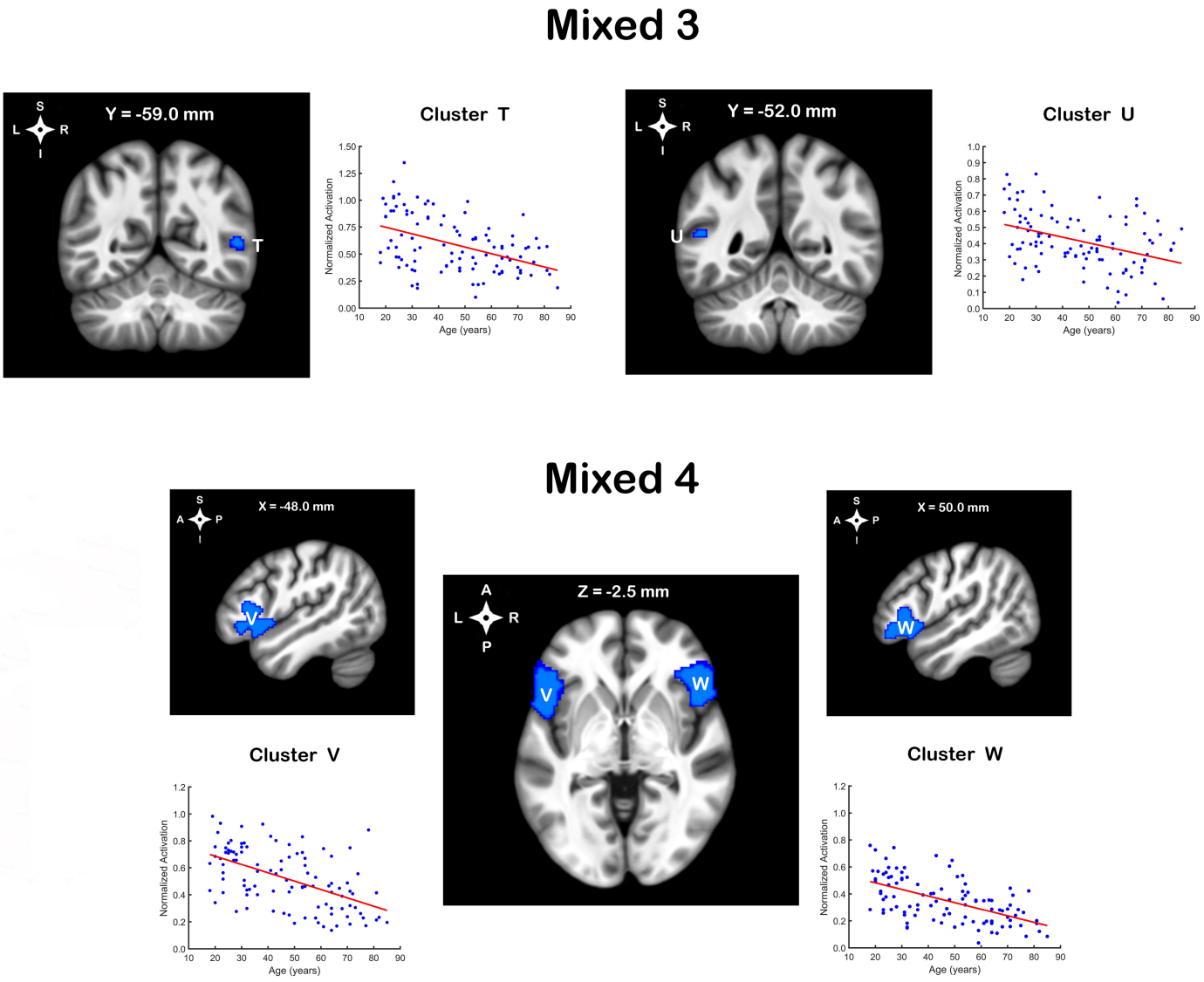

Fig. 5.18. Clusters with statistical relationships to age for multi-system (i.e., 'Mixed') ICs. All statistically significant clusters in 'Mixed' ICs showed negative associations to age.

Table 5.3.
Topographical age differences in network component structure. This table complements Figs. 5.15-5.18.

	cluster peak (MNI coordinate)	anatomy	cluster size (mm^3)	RSN cluster's relationship to age	cluster's grey matter relationship to age	semi-partial correlation between age and cluster, controlling the latter for grey matter volume
Somatomotor 1						
Cluster A	−56, −6, 34	left precentral gyrus, left postcentral gyrus [BA3, BA4, BA6, BA2]	952	linear ↓ [R^2 = .244]	linear ↓ [R^2 = .671]	n.s.
Cluster B	58, −2, 28	right precentral gyrus [BA6, BA4]	424	linear ↓ [R^2 = .222]	linear ↓ [R^2 = .577]	r = −.415 [p < .001]
Visual 1						
Cluster C	0, −66, 6	left lingual gyrus, left intracalcarine cortex, left precuneus cortex [BA30, BA18, BA19, BA23]	1,624	linear ↓ [R^2 = .293]	linear ↓ [R^2 = .559]	r = −.328 [p < .001]
Visual 2						
Cluster D	−12, −82, 50	left lateral occipital cortex [BA19, BA7]	280	linear ↓ [R^2 = .182]	linear ↓ [R^2 = .147]	r = −.320 [p < .001]
Cluster E	−14, −96, 24	left occipital pole [BA18]	280	linear ↓ [R^2 = .189]	linear ↓ [R^2 = .322]	r = −.233 [p = .008]
Visual 4						
Cluster F	38, −68, −16	right occipital fusiform gyrus [BA19, BA18, BA37]	2,816	linear ↓ [R^2 = .340]	linear ↓ [R^2 = .287]	r = −.544 [p < .001]
Auditory						
Cluster G	−60, −12, 6	left planum temporale, left Heschl's gyrus [BA41, BA42, BA22]	160	linear ↓ [R^2 = .189]	linear ↓ [R^2 = .470]	r = −.233 [p = .010]
Default Mode 1						
Cluster H	54, −52, 36	right angular gyrus [BA40, BA39]	312	linear ↑ [R^2 = .201]	linear ↓ [R^2 = .084]	r = .504 [p < .001]
Cluster I	56, −54, 12	right middle temporal gyrus, right angular gyrus [BA39, BA22]	176	linear ↑ [R^2 = .211]	linear ↓ [R^2 = .103]	r = .450 [p < .001]
Default Mode 2						
Cluster J	−8, −66, 16	left supracalcarine cortex, left precuneous cortex, left intracalcarine cortex [BA30, BA18, BA23, BA31]	1,328	nonlinear ↓ [R^2 = .231]	linear ↓ [R^2 = .436]	r = −.446 [p < .001]
Default Mode 4						
Cluster K	−4, 40, −2	left anterior cingulate gyrus, right anterior cingulate gyrus, left paracingulate gyrus, right paracingulate gyrus, left frontal pole [BA32, BA24, BA9, BA10]	3,392	linear ↓ [R^2 = .182]	linear ↓ [R^2 = .513]	r = −.208 [p = .018]
Cluster L	2, 34, 20	left anterior cingulate gyrus, right anterior cingulate gyrus, left paracingulate gyrus, right paracingulate gyrus [BA32, BA24]	1,400	linear ↓ [R^2 = .173]	linear ↓ [R^2 = .646]	n.s.
Cluster M	−42, 14, −6	left insular cortex [BA13]	224	linear ↓ [R^2 = .238]	linear ↓ [R^2 = .437]	r = −.420 [p < .001]
Default Mode 6						
Cluster N	−52, −32, 2	left superior temporal gyrus [BA22, BA21]	1,448	linear ↓ [R^2 = .253]	linear ↓ [R^2 = .257]	r = −.407 [p < .001]
Cluster O	52, −32, 2	right superior temporal gyrus [BA22, BA41]	840	linear ↓ [R^2 = .230]	linear ↓ [R^2 = .339]	r = −.341 [p < .001]
Dorsal Attention						
Cluster P	44, −60, 46	right lateral occipital cortex, right angular gyrus, right supramarginal gyrus [BA39, BA40, BA7, BA19]	1,488	nonlinear ↑ [R^2 = .278]	linear ↓ [R^2 = .422]	r = .536 [p < .001]
Cluster Q	−48, −52, 48	left angular gyrus, left supramarginal gyrus [BA40]	144	linear ↑ [R^2 = .207]	linear ↓ [R^2 = .090]	r = .447 [p < .001]

Cluster R	−8, −72, 60	left lateral occipital cortex [BA7]	112	linear ↓ [R^2 = .193]	n.s.	r = −.451 [p < .001]
Executive Control 2						
Cluster S	38, 58, 14	right frontal pole [BA10, BA9]	480	linear ↓ [R^2 = .169]	n.s.	r = −.408 [p < .001]
Mixed 3						
Cluster T	52, −58, 8	right middle temporal gyrus (temporooccipital part), right lateral occipital cortex (inferior division) [BA39, BA37]	352	linear ↓ [R^2 = .203]	linear ↓ [R^2 = .181]	r = −.356 [p < .001]
Cluster U	−50, −54, 12	left middle temporal gyrus (temporooccipital part), left angular gyrus [BA39]	104	linear ↓ [R^2 = .160]	nonlinear ↓ [R^2 = .077]	r = −.354 [p < .001]
Mixed 4						
Cluster V	−48, 16, −6	left inferior frontal gyrus (*pars triangularis* and *pars opercularis*), left orbitofrontal cortex, left frontal operculum [BA47, BA44, BA45, BA46, BA22, BA13]	7,192	linear ↓ [R^2 = .295]	linear ↓ [R^2 = .542]	r = −.280 [p < .001]
Cluster W	50, 24, −4	right inferior frontal gyrus (*pars triangularis* and *pars opercularis*), right orbitofrontal cortex, right frontal operculum, right frontal pole [BA45, BA47, BA44, BA46, BA9, BA13]	6,464	linear ↓ [R^2 = .322]	linear ↓ [R^2 = .483]	r = −.394 [p < .001]

Abbreviations: BA, Brodmann Area; n.s., statistically not significant.

Inter-component functional connectivity and age

Lastly, we examined the effects of age on inter-component FC. First, we built sparse graphical representations of inter-IC communication for the young, middle-aged, and old adult groups. Those graphs are visualized in Fig. 5.19.

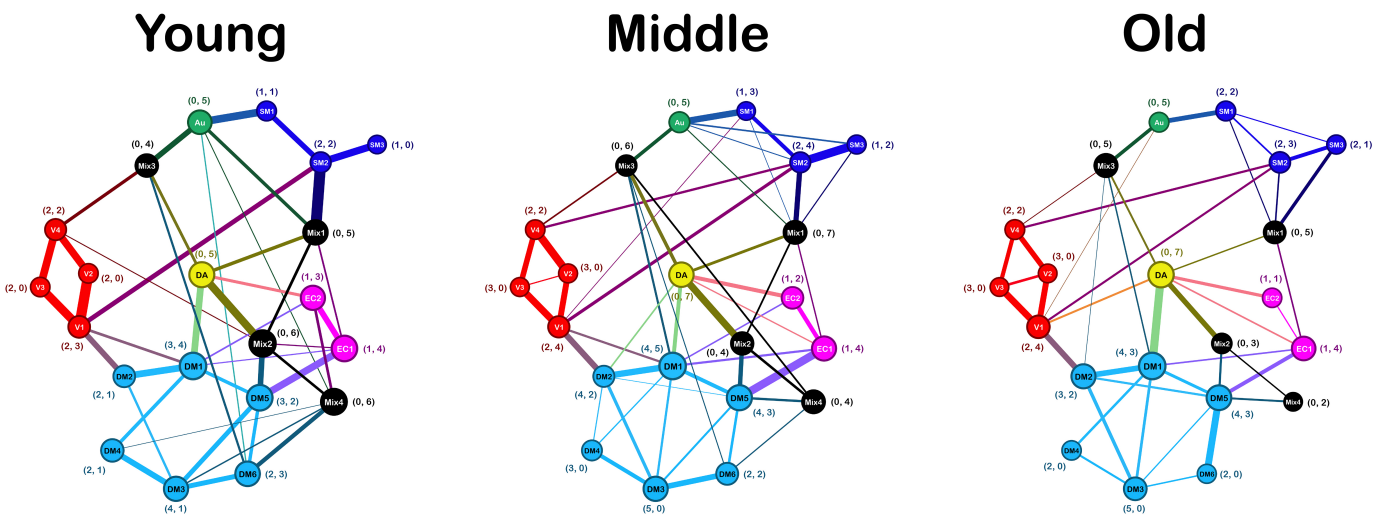

Fig. 5.19. Graphical representation of direct between-component connectivity, separated by age group. Only positive correlations are shown. Edge thickness represents functional connectivity strength (i.e., magnitude of SCAD-regularized partial correlations). Node size of each network component represents its unweighted eigenvector centrality. Coordinates depict the number of within-system (left number) and between-system (right number) connections. Node colors represent functional units (or systems) to which a given network component belongs. SM, somatomotor (blue); V, visual (red); Au, auditory (green); DM, default mode (cyan); DA, dorsal attention (yellow); EC, executive control (magenta); Mix, mixed (black). See Figs. 5.4-5.7 for anatomical profiles of each node/RSN.

Descriptively, a core set of 31 connections was identified in every age group, suggesting that the overall pattern of the brain's functional organization did not differ drastically among age groups (Fig. 5.20). Most unweighted graph summary metrics, computed from binarized graphs, support this conclusion: global efficiency, transitivity, density, radius, diameter, characteristic path length, and centralization did not show any age statistical differences [all *q*s > .10, see Table 5.4 for details; see *Appendix* in sections 5.5 for mathematical definitions]. The only unweighted summary metric that attained statistical significance in our age comparisons was the number of intra-system connections. Specifically, the young adult group had fewer intra-system connections (a total of 15 edges) than middle-aged or old adult groups (a total of 19 edges in each group) [both *q*s < .05]. Despite differences in the number of intra-system connections, age groups did not show any statistical differences in the number of inter-system connections [all uncorrected *p*s > .10, see Table 5.4 for details].

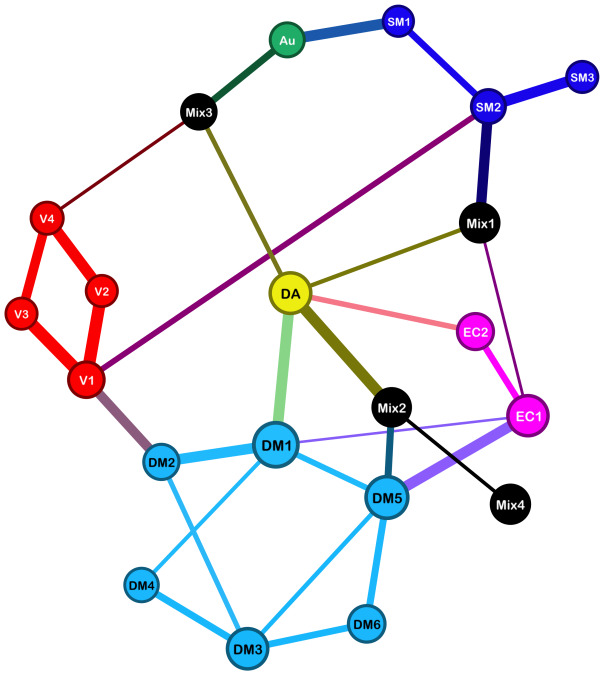

Fig. 5.20. A core set of inter-component connections that were present in every age group (i.e., young, middle-aged, old). Edge thickness represents connectivity strength, collapsed across age groups. SM, somatomotor (blue); V, visual (red); Au, auditory (green); DM, default mode (cyan); DA, dorsal attention (yellow); EC, executive control (magenta); Mix, mixed (black).

Contrary to results from binarized graphs, we observed substantial age differences if weighted graphs were used to compute graph summary metrics (Table 5.4; see *Appendix* section 5.5 for mathematical definitions of unweighted graph summary metrics and *Appendix* section 5.6 for mathematical definitions of weighted graph summary metrics). The average edge thickness of all non-zero positive edges was greater in the young adult group than in the old adult group [M_{diff} = 0.055, q < .010], and greater in the young adult group than in the middle-aged group [M_{diff} = 0.0424, q < .050]. However, the average edge thickness of the middle-aged group did not differ from that of the old adult group [uncorrected p > 0.10], suggesting that inter-IC partial correlation strength declines with age and that this decline is more pronounced in early aging. Furthermore, the aforementioned age differences in edge weight were driven by intra-system, not inter-system, connections (Table 5.4). Our age comparisons of weighted efficiency metrics – global efficiency, network radius, network diameter, and characteristic path length – revealed a gradual loss of connectivity efficiency with age [$\text{efficiency}_{\text{young}} > \text{efficiency}_{\text{middle}} > \text{efficiency}_{\text{old}}$; for details, see Table 5.4].

Table 5.4.
Global graph summary metrics, separated by age group, for binary and weighted graphs represnting inter-component functional connectivity.

	BINARIZED				WEIGHTED			
	young	**middle-aged**	**old**	**statistical differences**	**young**	**middle-aged**	**old**	**statistical differences**
density	0.2095	0.2476	0.2095	none	0.0443	0.0419	0.0328	young > old *** middle > old ***
efficiency	0.5413	0.5698	0.5290	none	0.1145	0.0975	0.0840	young > old *** young > middle *** middle > old *
transitivity	0.2195	0.3974	0.3373	none	0.0365	0.0611	0.0489	none
radius	3	2	3	none	12.7969	16.0334	18.3483	young < old ** young < middle *
diameter	4	4	4	none	21.5832	25.7084	32.4533	young < old *** young < middle * middle < old *
characteristic path length	2.0862	1.9864	2.1859	none	10.5684	12.3702	14.3148	young < old *** young < middle ** middle < old *
average edge weight	N/A	N/A	N/A	N/A	0.2117	0.1692	0.1565	young > old ** young > middle *
intra-system edge density	0.6000	0.7600	0.7600	young < old ** young < middle *	0.1589	0.1522	0.1318	young > old ** middle > old *
inter-system edge density	0.1568	0.1784	0.1351	none	0.0289	0.0270	0.0194	young > old ** middle > old **
average weight of intra-system connections	N/A	N/A	N/A	N/A	0.2648	0.2003	0.1734	young > old *** young > middle **
average weight of inter-system connections	N/A	N/A	N/A	N/A	0.1842	0.1513	0.1436	none
centralization								
degree	0.1553	0.2237	0.1553	none	N/A	N/A	N/A	N/A
closeness	0.1673	0.2977	0.3070	young > old $^{~}$ young > middle $^{~}$	N/A	N/A	N/A	N/A
betweeness	0.1249	0.1424	0.1566	none	N/A	N/A	N/A	N/A

*** FDR < .001; ** FDR < .010; * FDR < .050; $^{~}$ FDR < .100.

Next, we investigated node centrality measures to determine whether there were any age differences in component importance to the rest of the connectome. Similar to the unweighted global metrics, the unweighted degree, closeness, and betweenness centralities did not show any statistically significant age differences [all *q*s > .10]. For the unweighted eigenvector centrality, we observed one statistically significant age difference in our Mix2 node: lower centrality in old relative to young adults [$\text{EigenCentrality}_{\text{young}} = 0.9705$, $\text{EigenCentrality}_{\text{old}} = 0.405$, $q \approx .050$]. Weighted betweenness centrality also did not show any statistically significant age effects. However, unlike binary closeness centrality, weighted closeness centrality was reduced in old relative to young adults in all 21 RNS (Table 5.5). Age differences in weighted degree and/or eigenvector centrality were found in SM2, Vis1, Au, DM1, DM2, DM6, DA, EC2, Mix1, Mix2, and Mix4 RSNs (see Table 5.5 for details), further demonstrating that age effects are represented primarily by connectivity strength, not an outright presence or absence of functional connectivity.

Table 5.5.
Age differences in node centrality for weighted between-network functional connectivity graphs. Abbreviations: SM, somatomotor; Vis, visual; Au, auditory; DM, default mode; DA, dorsal attention; EC, executive control.

RSN	DEGREE		CLOSENESS		BETWEENNESS		EIGENVECTOR	
	Young/Middle/Old	Statistical Differences	Young/Middle/Old	Statistical Differences	Young/Middle/Old	Statistical Differences	Young/Middle/Old	Statistical Differences
SM1	0.584/0.633/0.514	none	1.752/1.415/1.086	**Y > O, *Y > M	0.042/0.021/0.026	none	0.115/0.113/0.056	none
SM2	1.248/1.196/0.667	**Y > O, *M > O	2.153/1.784/1.364	**Y > O, *Y > M	0.216/0.190/0.084	none	0.252/0.194/0.110	*Y > O
SM3	0.317/0.566/0.454	none	1.647/1.483/1.213	**Y > O	0.000/0.000/0.000	none	0.082/0.107/0.055	none
Vis1	1.429/1.227/1.155	**Y > O	2.135/1.912/1.796	*Y > O, *Y > M	0.205/0.258/0.305	none	0.311/0.273/0.336	none
Vis2	0.754/0.709/0.665	none	1.839/1.542/1.434	**Y > O, *Y > M	0.047/0.037/0.063	none	0.196/0.146/0.189	none
Vis3	0.701/0.662/0.652	none	1.802/1.566/1.457	**Y > O, *Y > M	0.000/0.000/0.000	none	0.177/0.144/0.193	none
Vis4	0.911/0.847/0.663	none	1.748/1.545/1.314	*Y > O	0.058/0.032/0.011	none	0.172/0.142/0.141	none
Au	0.940/0.749/0.475	**Y > O	1.808/1.444/1.198	**Y > O, *Y > M	0.053/0.042/0.047	none	0.147/0.115/0.083	none
DM1	1.307/1.390/1.267	none	2.251/2.069/1.971	*Y > O	0.163/0.195/0.195	none	0.300/0.372/0.461	**Y < O
DM2	0.693/0.993/0.894	*Y < M	2.154/2.026/1.857	*Y > O	0.037/0.232/0.190	none	0.198/0.298/0.370	**Y < O, *Y < M
DM3	0.956/0.876/0.649	none	1.852/1.614/1.444	*Y > O	0.037/0.068/0.000	none	0.165/0.205/0.238	none
DM4	0.514/0.385/0.265	none	1.617/1.221/1.224	*Y > O, *Y > M	0.005/0.000/0.000	none	0.110/0.111/0.115	none
DM5	1.143/1.228/1.130	none	2.025/1.755/1.586	*Y > O	0.079/0.084/0.195	none	0.255/0.305/0.321	none
DM6	0.837/0.580/0.409	*Y > O	1.771/1.490/1.301	**Y > O	0.058/0.011/0.000	none	0.145/0.130/0.150	none
DA	1.129/1.238/1.214	none	2.340/1.961/1.967	*Y > O, *Y > M	0.158/0.116/0.237	none	0.278/0.306/0.390	*Y < O
EC1	0.875/0.885/0.611	none	1.793/1.609/1.400	*Y > O	0.011/0.047/0.042	none	0.209/0.253/0.215	none
EC2	0.686/0.513/0.262	**Y > O	1.657/1.483/1.302	*Y > O	0.016/0.016/0.000	none	0.158/0.164/0.105	none
Mix1	1.076/0.864/0.579	**Y > O	2.230/1.720/1.361	**Y > O, *Y > M	0.153/0.084/0.068	none	0.262/0.184/0.109	*Y > O
Mix2	1.071/0.779/0.471	**Y > O	2.188/1.725/1.542	**Y > O, *Y > M	0.105/0.032/0.026	none	0.261/0.210/0.175	none
Mix3	0.705/0.793/0.550	none	2.000/1.807/1.379	**Y > O	0.079/0.126/0.090	none	0.132/0.173/0.178	none
Mix4	0.752/0.488/0.221	Y > O **	1.556/1.389/1.039	**Y > O	0.005/0.000/0.000	none	0.132/0.111/0.069	none

** FDR < .010; * FDR < .050.

To determine which edges were most responsible for the above age differences in weighted global summary metrics and weighted node centralities, we performed age comparisons of connectivity strength on each non-zero edge in our graphs. After correcting for multiple hypothesis testing (FDR < .05, 56-59 tests), age differences were found in young vs. old and young vs. middle-aged, but not in middle-aged vs. old comparisons (Fig. 5.21, Table 5.6). These age effects were represented by 5 connectivity differences in the young vs. old comparison [SM2 ↔ Mix1, DM6 ↔ Mix4, Au ↔ Mix1, EC1 ↔ EC2, EC2 ↔ Mix4], and 3 connectivity differences in the young vs. middle-aged comparison [SM2 ↔ Mix1, EC2 ↔ Mix4, DM1 ↔ Mix3]. All but one (i.e., DM1 ↔ Mix3) differences in edge weight displayed a reduction in FC with age, and all but one (EC1 ↔ EC2) involved one of the transition multi-system 'Mixed' ICs. Because this study employed a novel graph estimation methodology and was exploratory in nature, we are also presenting age group differences in weight strength that survived uncorrected $p < .01$ statistical comparisons. Lowering the statistical threshold resulted in 8 additional edges showing age differences (Fig. 5.21, Table 5.6). More than half of those additional edges were in the middle-aged vs. old adult comparison.

Table 5.6.
Age differences in edge connectivity strength for weighted between-IC functional connectivity graphs. Only edges that survived the uncorrected $p < .01$ threshold in at least one age comparison are shown. Abbreviations: SM, somatomotor; Vis, visual; Au, auditory; DM, default mode; DA, dorsal attention; EC, executive control. This table accompanies Fig. 5.21.

	young (*r*)	middle (*r*)	old (*r*)	young vs. middle (uncorrected *p*)	middle vs. old (uncorrected *p*)	young vs. old (uncorrected *p*)	FDR-corrected age differences
SM2 ↔ Mix1	0.460	0.243	0.107	$p < .001$	n.s.	$p < .001$	young > old young > middle
EC2 ↔ Mix4	0.147	0.000	0.000	$p < .002$	n.s.	$p < .001$	young > old young > middle
EC1 ↔ EC2	0.270	0.211	0.094	n.s.	$p < .040$	$p < .003$	young > old
Au ↔ Mix1	0.173	0.088	0.000	n.s.	n.s.	$p < .003$	young > old
DM6 ↔ Mix4	0.205	0.094	0.000	n.s.	n.s.	$p < .005$	young > old
DM1 ↔ Mix3	0.000	0.127	0.103	$p < .002$	n.s.	$p < .040$	young < middle
Vis1 ↔ Vis2	0.433	0.271	0.271	$p \approx .010$	n.s.	$p < .007$	none
DM1 ↔ DM3	0.000	0.131	0.150	$p < .006$	n.s.	$p < .020$	none
DM5 ↔ EC1	0.311	0.349	0.192	n.s.	$p < .002$	$p < .020$	none
DM3 ↔ DM6	0.233	0.257	0.103	n.s.	$p < .003$	$p < .030$	none
DM5 ↔ DM6	0.174	0.144	0.306	n.s.	$p < .005$	$p < .020$	none
SM2 ↔ SM3	0.317	0.366	0.192	n.s.	$p < .009$	n.s.	none
Mix3 ↔ Mix4	0.000	0.115	0.000	$p < .020$	$p < .010$	n.s.	none

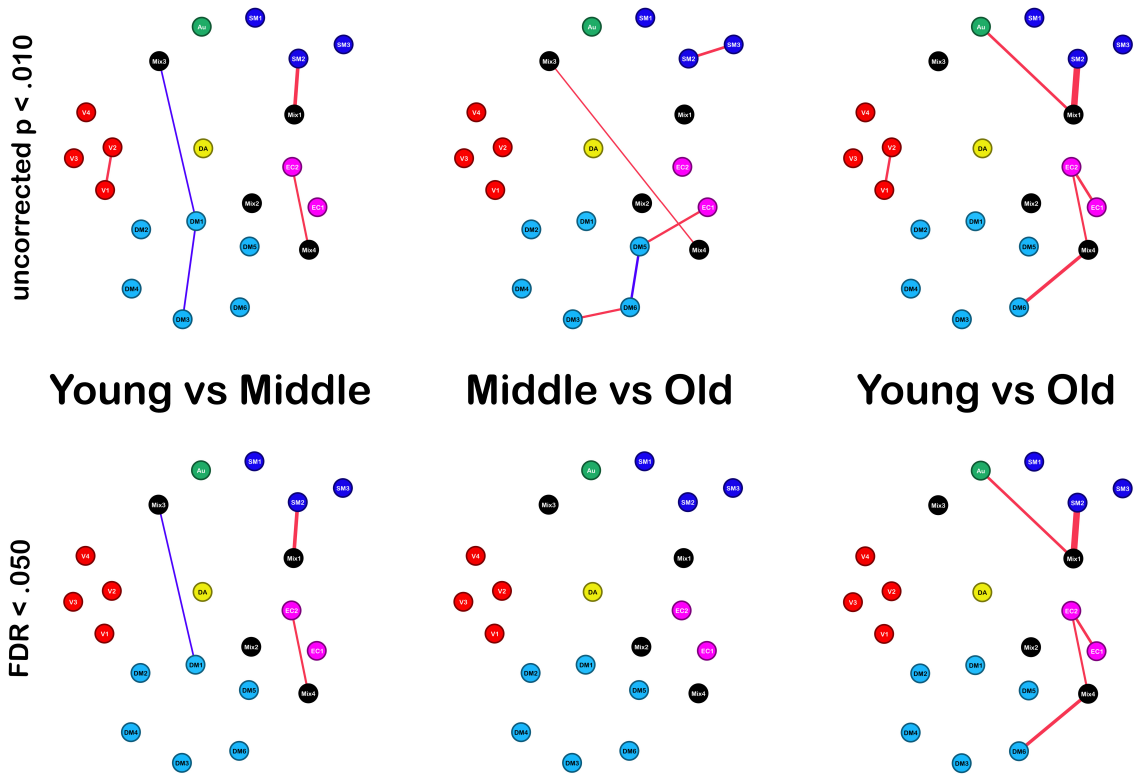

Fig. 5.21. Graphical representations of uncorrected (top) and FDR-corrected (bottom) age differences in inter-IC functional connectivity. Red edge color represents lower functional connectivity in the older group; blue edge color represents greater functional connectivity in the older group. Edge thickness represents the magnitude of functional connectivity differences in each age comparison. Abbreviations: SM, somatomotor; V, visual; Au, auditory; DM, default mode; DA, dorsal attention; EC, executive control.

5.4. Discussion

In the current study, we investigated age differences for three primary features in ICA-based RSN decompositions: network amplitude, spatial topography of network sources, and inter-component functional interactions. For RSN amplitude, our findings led to three main conclusions: (1) BOLD amplitude is negatively associated with age in all networks, and a single process might underly these global amplitude trends; (2) sensorimotor networks, and not frontal and parietal association networks, showed the steepest amplitude reduction with age; (3) compared to young adults, old adults showed reduced inter-individual variability in network amplitude. For RSN/component topography, age differences in network structure were modest, and except for a few clusters in the parietal association areas, represented reduced intra-network connectivity. Finally, our age comparisons of inter-component functional connectivity revealed a large degree of age invariance in inter-network interactions. Where present, age differences in inter-component FC were captured by weighted, as opposed to unweighted, graph summary metrics. Together, weighted graph summary metrics indicate weakened inter-system (e.g., visual ↔ default mode, somatomotor ↔ attention) communication in old age, driven by age differences in functional communication via 'Mixed' (or multi-system) network components. To our best knowledge, this is the first high-field RS-fMRI study to provide such a comprehensive overview of alterations in the human brain's functional architecture for the entire adult lifespan.

Network amplitude and age

Our results showed that healthy cognitive aging was associated with a reduction of BOLD signal amplitude in every brain system. These findings are consistent with two previous studies that also used ICA to study age effects on FC (Allen et al., 2011; Zonneveld et al., 2019). In the first study, Allen et al. (2011) showed that aging was associated with a widespread reduction in low-frequency BOLD signal power (< 0.15 Hz). However, Allen et al. (2011) focused predominantly on maturation and early aging, with 80% of their sample falling in the 13-30 age range, and only 7 (~1.2%) subjects older than 50 at the time of data collection. In the second study, Zonneveld et al. (2019) found that advanced age was associated with lower mean signal amplitude in most RSNs; however, the authors did not study the entire adulthood and sampled older adults exclusively.

In the current study, we demonstrated that the fMRI signal amplitude of most RSNs declines linearly throughout the entire adult lifespan. In networks with non-linear trajectories, we observed a

rapid reduction of BOLD amplitude in young adulthood, followed by a more gradual decline in middle and late adulthood. Furthermore, we demonstrated that a single source of variance could explain age differences in BOLD amplitude in most RSNs, suggesting that a common set of biological processes might be responsible for these BOLD amplitude effects. According to our results, the largest young vs. old amplitude differences were localized primarily within visual and somatomotor RSNs. Because previous structural imaging studies showed that GM in the primary sensorimotor regions is not as vulnerable to age-related atrophy as frontal GM (Fjell et al., 2009a, 2009b; Leong et al., 2017; McDonald et al., 2009; Raz et al., 1997, 2004, 2005, 2010; Resnick et al., 2003), it is unlikely that cortical atrophy is the only cause of declining RSN amplitude in old age. Finally, we would like to point out that RSN amplitude among old adults was not only smaller but also had lower inter-individual variability.

Most previous studies on the relationship between BOLD amplitude and age were task-based, and not resting-state (Cabeza et al., 2002, 2004; Grady et al., 1994; D'Esposito et al., 1999; Fabiani et al., 2014; Gutchess et al., 2005; Hesselmann et al., 2001; Hutchinson et al., 2002; Levine et al., 2000; Logan et al., 2002; Madden et al., 1996; Park et al., 2003, 2004; West et al., 2019). Experiments that employed motor paradigms to investigate age effects on the sensorimotor cortex reported: (1) smaller activation clusters in old adults (D'Esposito et al., 1999, 2003; Handwerker et al., 2007; Hesselmann et al., 2001; Mehagnoul-Schipper et al., 2002; Riecker et al., 2006); (2) age differences in BOLD response timing and BOLD response shape (Handwerker et al., 2007; Stefanova et al., 2013; Taoka et al., 1998; West et al., 2019); and (3) elevated noise levels among the elderly, relative to task-evoked activity (D'Esposito et al., 1999; Kannurpatti et al., 2011). In the visual system, a wide variety of task-based neuroimaging experiments revealed reduced BOLD activation (Grady et al., 1994; Fabiani et al., 2014; Ross et al., 1997; West et al., 2019; Wright & Wise, 2018). These age effects were detected not only in fMRI experiments, but also in Positron Emission Tomography (PET) and functional Near-Infrared Spectroscopy (fNIRS) studies, which employed a wide variety of visual paradigms, ranging from pure perception to face matching, working/episodic memory, and visual attention (Ances et al., 2009; Buckner et al., 2000; Cabeza et al., 2004; Fabiani et al., 2014; Grady et al., 1994; Handwerker et al., 2007; Hutchison et al., 2013; Levine et al., 2000; Li et al., 2015; Madden et al., 1996; Park et al., 2003; Rieck et al., 2015; Ross et al., 1997; Spreng et al., 2010; Ward et al., 2015; West et al., 2019). Age differences in activation amplitude were also identified in brain regions belonging to the default system (Grady et al. 2006;

Lustig et al. 2003; Miller et al. 2008; Persson et al. 2007; Sambataro et al., 2010). However, the DMN's activity differences during task-based studies were reported as reduced or failed deactivation in old adults since the default system is more active at rest than during cognitively demanding tasks (Park & Reuter-Lorenz, 2009; Persson et al., 2007, 2014; Raichle & Snyder, 2007). The same biological changes might be responsible for amplitude differences in both resting-state and task-based fMRI research. This idea is supported by evidence from Yan et al. (2011), who showed that – at least in the visual cortex – the magnitude of RS-fMRI fluctuations was predictive of task-induced activation.

Each brain region's BOLD signal time course represents a complex interplay of four dynamic factors: local blood volume, rate of local blood flow, local vascular reactivity, and local rate of cerebral metabolic oxygen utilization ($CMRO_2$) (Cohen et al., 2004; Kim, 2018; Kim & Ogawa, 2012; Uludağ & Blinder, 2018; Uludağ et al., 2009; Wright & Wise, 2018). Reduced BOLD amplitude in old adults can be driven by lower cerebral blood flow (CBF), lower cerebrovascular reactivity (CVR), or higher $CMRO_2$. It is well documented that aging causes substantial changes in the cerebral vasculature, including stiffening of the vessel walls, reduction of the capillary density, and thickening of the capillary basement membrane (for reviews see, D'Espotio et al., 2003; Farkas & Luiten, 2001; Wright & Wise, 2018). *In vivo* work using PET and Arterial Spin Labeling (ASL) methods showed that aging individuals display lower CBF and lower CVR, when compared to healthy young adults (Aanerud et al., 2012; Beason-Held et al., 2008; Bertsch et al., 2009; Chen et al., 2011; Galiano et al., 2019; Hutchison et al., 2013; Kety, 1956; Liu et al., 2013; Lu et al., 2011; Melamed et al., 1980; Peng et al., 2014; Wright & Wise, 2018; Yamaguchi et al., 1986). Consequently, age effects on RSN amplitude might be driven by cardiovascular risk factors (Aanerud et al., 2012; D'Esposito et al., 2003; Farkas & Luiten, 2001; Gagnon et al., 2015; Hillman, 2014; Kety et al., 1956; Liu, 2013; Melamed et al., 1980; Zonneveld et al., 2019). For instance, a recent whole-brain RS-fMRI study by Zonneveld et al. (2019) reported a positive relationship between RSN amplitude and systolic blood pressure. However, it is unlikely that age effects on RSN amplitude are driven exclusively by age differences in blood pressure. Only 1 volunteer in our middle-aged cohort had a history of elevated blood pressure, while the other 30 did not. Nonetheless, when compared to young adults, our middle-aged volunteers displayed lower group-level measures of RSN amplitude in multiple network components. Furthermore, a comparison of RSN amplitude between old adults with a history of high blood pressure to those

without did not reveal any amplitude differences in our RSN data (all uncorrected *p*s > .10). It is worth noting, however, that only individuals with no history of high blood pressure or those whose high blood pressure was *controlled* by medications or lifestyle adjustments were recruited for this study. To what extent our RSN amplitude results might generalize to a broader population with a more severe history of cardiovascular disease is a topic that merits further research.

In addition to vascular factors, it is plausible that the aging process affects $CMRO_2$, modulating the oxy-/deoxy-hemoglobin ratio in the regional cerebral vasculature, which in turn affects the fMRI-measured T_2^* contrast. Unlike CBF and CVR, $CMRO_2$ is a direct measure of neuronal metabolic demands (Cohen et al., 2004; D'Espotio et al., 2003; Kim, 2018; Kim & Ogawa, 2012; Uludağ & Blinder, 2018; Wright & Wise, 2018), and age differences in $CMRO_2$ likely represent differences in spiking rates and neurotransmitter trafficking (D'Espotio et al., 2003; Kim & Ogawa, 2012; Logothetis et al., 2001). Unfortunately, human imaging literature is inconclusive on the direction of $CMRO_2$ changes in healthy aging: some studies (e.g., Aanerud et al., 2012) reported lower $CMRO_2$ in old adults, while others reported the opposite pattern (e.g., Lu et al., 2011; Peng et al., 2014). Additional research, employing quantitative high-resolution (1.8-mm isotropic or less) fMRI techniques, is needed to determine the exact cause of brain-wide age differences in RSN amplitude that were observed in this study.

Functional connectivity and age

By combining GIG-ICA with sparse graphical methods we demonstrated a substantial degree of age-invariance in network architecture, a result that is in agreement with recent non-ICA-based RS-fMRI studies (e.g., Chan et al. 2017; Grady et al., 2016; Han et al., 2018). Specifically, almost half of our network components displayed no age differences in component structure, and among the ones that did, age effects were captured by small (2% of IC volume, on average) regional clusters. Similarly, age comparisons of various unweighted graph summary metrics in our inter-component FC analyses revealed a relatively age-invariant graph structure.

To our knowledge, only three other studies used GICA or similar techniques for investigating brain-wide age differences in network topography (Allen et al., 2011; Huang et al., 2015; Vij et al., 2018). In the first such study, Allen et al. (2011) employed IC scaling methods similar to the ones used in our current work, and reported declining intra-network connectivity in every network that could not be fully accounted for by age-related volumetric differences in cortical

GM volume. This is similar to our observations: except for a few clusters, age effects on network topography could not be fully accounted for by age differences in regional GM volume, indicating that functional connectivity provides information about brain aging beyond what can be explained using cortical thickness/volume alone. In the second study, Huang et al. (2018) computed average intra-network connectivity metrics for the entire IC by collapsing spatial map intensity values across all voxels in a network. The authors reported negative associations between age and intra-IC connectivity in 5 RSNs: auditory, ventral default mode, right executive control, sensorimotor, and visual medial. No positive associations between age and spatial map intensity were detected. However, because the authors estimated age relationships for connectivity measures collapsed across all of IC's voxels, it was not clear which of the IC's regions were responsible for the aggregate age effects, and whether any of their network ICs disaplyed age-associated restructuring (i.e., some regions positively associated with age, and others negatively associated with age). In the third study, Vij et al. (2018) reported negative associations between RSN volume and age in most functional systems with sensorimotor (i.e., visual, somatomotor, auditory) networks being especially vulnerable to age-related decline. However, those negative associations between RSN volume and age were not limited to sensorimotor regions: executive, salience, and basal ganglia networks also displayed lower component volumes in aging adults. In addition, 2 network components — posterior default mode and central executive control — showed positive associations with age, indicating that at least in some cognitive regions of the brain there is a pattern of intra-network reorganization occurring throughout life, as opposed to an outright loss of network structure. Despite these insights, it should be noted that Vij et al. (2018) defined network volume as the number of voxels in a subject's component map above a predifined *z*-statistic cut-off. Consequently, it was not clear whether age differences in RSN volumes were caused by age differences in network structure or age differences in network amplitude.

Rather than *z*-scoring our IC spatial maps, we normalized our IC spatial maps by BOLD amplitude, which more accurately captures true group differences in spatial features (Allen et al., 2011, 2012). We also performed voxel-based age comparisons, enabling us to detect both increases and decreases in intra-component FC. According to our age comparisons of IC topography, the three largest age-relationship clusters were localized within the frontal lobes, and all three showed negative linear relationships between the amplitude-normalized SM intensity and age. Two of those clusters belonged to the 'Mixed 4' network component and were located primarily within the

bilateral inferior frontal gyrus and bilateral orbitofrontal cortex. The third cluster represented bilateral anterior cingulate and bilateral paracingulate regions of the DMN's frontal subsystem. In addition to frontal lobes we identified age relationship clusters in the parietal, visual, and temporal regions of the brain. Of these, parietal networks deserve special attention since only the parietal association cortex contained clusters representing both positive and negative correlations to age, indicating age-related network restructuring in those regions. A number of recent studies, employing different network estimation techniques, reported similar age effects on functional organization of the parietal association cortex (Grady et al., 2016; Meunier et al., 2009; Onoda & Yamaguchi, 2013; Park et al., 2010).

Initial imaging evidence for altered network dynamics in old age was demonstrated in task-based fMRI and PET experiments, which showed an over-recruitment of frontal and parietal association cortices in older cohorts in a wide variety of cognitive tasks (Cabeza et al., 2002, 2004; Davis et al., 2008; Grady et al., 1994; Gutchess et al., 2005; Li et al., 2015; Logan et al., 2002; Rypma & D'Esposito, 2000; Rajah & D'Esposito, 2005; Schneider-Garces et al., 2010; Spreng et al., 2010; Sugiura, 2016). Age effects on network dynamics were reported even in simple motor experiments, during which older adults showed greater activity in the ipsilateral somatomotor cortex, supplementary motor and premotor areas, basal ganglia, as well as association regions in the parietal cortex (Kim et al., 2010; Riecker et al., 2006; Tsvetanov et al., 2015). This additional activity seems to be compensatory in nature and plays a vital role in maintaining cognitive performance in old age (Fera et al., 2005; Park & Reuter-Lorenz, 2009; Rossi et al., 2004; Solé-Padullés et al., 2006; Schneider-Garces et al., 2010).

Recently, interest has grown in graph theory and its ability to summarize age effects on the brain's functional architecture (Rubinov & Sporns, 2010; Damoiseaux, 2017; Wig, 2017). In general, brain aging studies that employed graphical models to study FC indicate functional dedifferentiation among old adults, typically manifesting as a less distinct or less stable grouping of certain brain areas into network communities (Chan et al., 2014; Chong et al., 2019; Geerligs et al., 2015; Grady et al., 2016; Keller et al., 2015; Onoda & Yamaguchi, 2013; Spreng et al., 2016; Vij et al., 2018). However, since almost all previous connectivity studies that relied on graphical methods, estimated their graphs using bivariate, not partial correlations, their results may have been confounded by indirect connections (Epskamp & Fried, 2018; Smith et al., 2011). To our best

knowledge, this is the first study to combine sparse graphical estimation methods with ICA-based network extraction to investigate age effects on inter-component FC.

Consistent with other graph-based FC studies of brain aging, our weighted efficiency-related graph summary metrics (i.e., global efficiency, characteristic path length, network diameter, network radius) suggest that functional communication in the human brain becomes increasingly inefficient with age [$Efficiency_{young} > Efficiency_{middle\text{-}aged} > Efficiency_{old}$]. Furthermore, as evidenced by weighted closeness and betweenness centralities, age differences were primarily characterized by a widespread reduction in network integration in old relative to young adults – and not by any particular IC's importance to the overall information flow in the brain. Despite this broad loss of network efficiency in old age, our unweighted graph summary metrics indicate that the fundamental network architecture is stable in young, middle, and late adulthood. We also want to point out that age differences in the overall edge weight were more pronounced in young vs. middle-aged comparisons than in middle-aged vs. old comparisons indicating relatively early aging effects on FC. In general, intra-system FC strength was more vulnerable to aging than inter-system FC strength; however, certain inter-system connections, especially those connected to the "Mixed" ICs, also showed age-associated FC decline that was evident by middle adulthood.

Contrary to some previous research (e.g., Betzel et al., 2014; Chan et al., 2014; Geerligs et al., 2015; Spreng et al., 2016), we did not find substantial evidence for greater inter-system integration in old age: almost all edges with age differences in our FDR-corrected age comparisons represented connections between one of the clearly defined RSNs and one of the 'Mixed' (i.e., multi-system) RSNs. Because those 'Mixed' RSNs act as hubs that interconnect multiple functional systems with each other, declining FC between these multi-system RSNs and other systems, is also indicative of less efficient network architecture. Of particular note here is the loss of connectivity between the DM6 and Mix4 components with age. Structurally, the Mix4 IC showed the largest topographical age differences, especially in the bilateral inferior frontal gyrus. As these regions become increasingly disconnected from the rest of the component with age, the entire IC loses its connectivity to the DM6 network. With a less strict statistical threshold (uncorrected $p < .010$), we identified additional age differences in inter-component connectivity, primarily among various default mode sub-systems (Andrews-Hanna et al., 2014; Christoff et al., 2016). Early FC experiments showed that communication between distant areas of the DMN, especially between the medial frontal and posterior cingulate/retrosplenial hubs, declines with age (Andrews-Hanna et al.,

2007; Damoiseaux et al. 2008; Wu et al., 2011). More recent work, employing not only cross-sectional but also longitudinal designs, produced mixed results with some groups supporting the early findings (e.g., Geerligs et al., 2015; Grady et al., 2016; Ng et al., 2016) and others finding no age effects (Hirsiger et al., 2016; Persson et al. 2014). Our inter-component connectivity results demonstrated a relatively complex pattern of age-related network reorganization within this system. Age-related shifts in the DMN's organization could represent age differences in spontaneous thought processes or changes in network architecture away from long-range communication to favour anatomically proximal short-range communication (as suggested by Tomasi & Volkow, 2012). Even though our data suggest age differences in the architecture of the default mode system, these findings should be interpreted with caution since they did not survive the FDR correction for multiple hypothesis testing.

Limitations

In light of our results on network amplitude, caution should be exercised when interpreting such measures without additional knowledge of how non-BOLD contribution to the fMRI time series is affected in healthy aging. For similar reasons, findings from other studies on functional dedifferentiation with age should also be interpreted with caution, since age effects on BOLD amplitude (and consequently temporal SNR) might be responsible for lower correlation strength in old adults, which in turn would result in less stable estimates of network community structure. Because of technical and computational limitations, we relied on linear and quadratic regression models in our initial screening for topographical differences in component topograhy. We do not consider this to be a major issue in our study as most linear, curved, and u-shaped patterns can be detected using quadratic and linear fits. To further mitigate the downsides of linear and quadratic fits (Aghamohammadi-Sereshki et al., 2019; Fjell et al., 2010), all clusters showing statistical age differences were followed-up with fractional polynomial modelling.

It is important to keep in mind that head motion has been shown to modulate FC in multiple RSNs (Mowinckel et al., 2012; Power et al., 2012; Van Dijk et al., 2012). As is typically reported in the field (e.g., Madan, 2018), our older participants were not as still inside the scanner as younger ones. Since we employed some of the most rigorous techniques for removing head motion artifacts in our customized preprocessing pipeline, we believe that our findings on age differences in RSN structure represent true age differences in neurovascular coupling and functional connectomics

(Mowinckel et al., 2012; Power et al., 2012; Van Dijk et al., 2012). Additional research, employing physical restrains (Power et al., 2019), as opposed to post-acquisition clean-up techniques, is needed to eliminate any residual concerns about the effects of head motion on FC studies of brain aging.

Lastly, we need to emphasize that our study was cross-sectional. A longitudinal sample is needed to confirm our results as true aging effects, rather than a byproduct of cohort differences. Future research would benefit from addressing the issue of sex differences in brain aging. Even though we did not attain sufficient statistical power to perform sex comparisons in our inter-network connectivity graphs (< 15 males in middle-aged and old adult groups), we were able to test for male vs. female differences in network topography and BOLD amplitude. Those analyses did not reveal any statistically significant sex effects or interactions. However, in those tests too, potential consequences of limited statistical power come to mind: it is plausible that sex differences in brain aging are subtle, necessitating a larger sample size for sex effect detection using statistical testing.

Acknowledgments

This project was supported by the Canadian Institutes of Health Research (CIHR) operating grant (MOP11501) and the Natural Sciences and Engineering Research Council of Canada (NSERC) operating grant (06186) to N.V.M. S.H. was supported by CIHR Doctoral Scholarship. The work of I.C. was partially supported by the NSERC operating grant (06638) and the Xerox Faculty Fellowship, Alberta School of Business.

5.5. Appendix A: Summary Metrics for Unweighted Graphs

$$\text{Density} = \frac{\sum_{i,j \in N} a_{ij}}{n(n-1)},$$

where $\sum_{i,j \in N} a_{ij}$ represents the sum of all edges in a graph, n is the number of nodes in a graph, and N is the set of all nodes in a network.

$$\text{Global efficiency} = \frac{1}{n} \sum_{i \in N} \frac{\sum_{j \in N} d_{ij}^{-1}}{n-1},$$

where d_{ij} represents shortest path length (distance) between nodes i and j, n is the number of nodes in a graph, and N is the set of all nodes in a network.

$$\text{Transitivity} = \frac{\sum_{i \in N} 2t_i}{\sum_{i \in N} k_i(k_i - 1)},$$

where t_i is the number of triangles around node i, k_i is the degree of node i, and N is the set of all nodes in a network.

$$\text{Characteristic path length} = \frac{1}{n} \sum_{i \in N} L_i,$$

where L_i is the average shortest path between node i and all other nodes, and N is the set of all nodes in a network.

$$\text{Radius} = \min_{i \in N} \max_{j \in N} d_{ij},$$

where d_{ij} represents shortest path length between nodes i and j – elements of the set N containing all nodes in a network.

$$\text{Diameter} = \max_{i \in N} \max_{j \in N} d_{ij},$$

where d_{ij} represents shortest path length between nodes i and j – elements of the set N containing all nodes in a network.

$$\text{Degree centrality}^{(i)} = \sum_{j \in N} a_{ij},$$

where a_{ij} is the connection status (i.e., 0 or 1) between nodes i and j, and N is the set of all nodes in a network.

$$\text{Closeness centrality}^{(i)} = \frac{n-1}{\sum_{j \in N, j \neq i} d_{ij}},$$

where d_{ij} represents the shortest path length between nodes i and j, n is the number of nodes in a graph, and N is the set of all nodes in a network.

$$\text{Betweenness centrality}^{(i)} = \frac{1}{(n-1)(n-2)} \sum_{\substack{h,j \in N \\ h \neq j, h \neq i, j \neq i}} \frac{\rho_{hj}^{(i)}}{\rho_{hj}},$$

where ρ_{hj} is the number of shortest paths between nodes h and j, and $\rho_{hj}^{(i)}$ is the number of shortest paths between h and j that pass through node i, n is the number of nodes in a graph, and N is the set of all nodes in a network.

$$\text{Degree centralization} = \frac{\sum_{i=1}^{n}(C_{max} - C_i)}{(n-2)(n-1)},$$

where C_{max} is the degree of the node with the largest degree centrality, C_i is the degree of node i, and n is the number of nodes in a graph.

$$\text{Closeness centralization} = \frac{\sum_{i=1}^{n}(C_{max} - C_i)}{[(n-2)(n-1)/(2n-3)]},$$

where C_{max} is the closeness centrality of the node with the largest closeness centrality values, C_i is the closeness centrality of node i, and n is the number of nodes in a graph.

$$\text{Betweenness centralization} = \frac{\sum_{i=1}^{n}(C_{max} - C_i)}{(n-1)},$$

where C_{max} is the betweenness centrality of the node with the largest betweenness centrality value, C_i is the betweenness centrality of node i, and n is the number of nodes in a graph.

5.6. Appendix B: Summary Metrics for Weighted Graphs

$$\text{Density} = \frac{\sum_{i,j \in N} w_{i,j}}{n(n-1)},$$

where $\sum_{i,j \in N} w_{ij}$ represents the sum of all edge weights (i.e., correlation strengths) between nodes in a graph, n is the number of nodes in a graph, and N is the set of all nodes in a network.

$$\text{Global efficiency} = \frac{1}{n} \sum_{i \in N} \frac{\sum_{j \in N} (d_{ij}^{w})^{-1}}{n-1},$$

where d_{ij}^{w}represents the shortest weighted path length between nodes i and j computed from length weights (i.e., inverse of correlation strength; length$^{(ij)}$ = $1/w_{ij}$ = $1/r_{ij}$), n is the number of nodes in a graph, and N is the set of all nodes in a network.

$$\text{Transitivity} = \frac{\sum_{i \in N} 2t_i^{w}}{\sum_{i \in N} k_i(k_i - 1)},$$

where t_i^{w} is the weighted geometric mean of triangles around node i, k_i is the unweighted degree of node i, and N is the set of all nodes in a network.

$$\text{Characteristic path length} = \frac{1}{n} \sum_{i \in N} L_i^{w},$$

where L_i^{w} is the average weighted shortest path between node i and all other nodes, computed using length-connectivity (i.e., inverse of correlation strength) weights, and N is the set of all nodes in a network.

$$\text{Radius} = \min_{i \in N} \max_{j \in N} d_{ij}^{w},$$

where d_{ij}^{w} is the shortest weighted path length between nodes *i* and *j,* computed from length (i.e., inverse of correlation strength) weights, and *N* is the set of all nodes in a network.

$$\text{Diameter} = \max_{i \in N} \max_{j \in N} d_{ij}^{w},$$

where d_{ij}^{w} is the shortest weighted path length between nodes *i* and *j,* computed from length (i.e., inverse of correlation strength) weights, and *N* is the set of all nodes in a network.

$$\text{Degree centrality}^{(i)} = \sum_{j \in N} w_{ij},$$

where w_{ij} is the connection weight (i.e., correlation r_{ij}) between nodes *i* and *j*, and *N* is the set of all nodes in a network.

$$\text{Closeness centrality}^{(i)} = \frac{n-1}{\sum_{j \in N, j \neq i} d_{ij}^{w}},$$

where d_{ij}^{w} is the shortest weighted path length between nodes *i* and *j,* computed from length (i.e., inverse of correlation strength) weights, and *N* is the set of all nodes in a network.

$$\text{Betweenness centrality}^{(i)} = \frac{1}{(n-1)(n-2)} \sum_{\substack{h,j \in N \\ h \neq j, h \neq i, j \neq i}} \frac{\rho_{hj}^{(i)}}{\rho_{hj}},$$

where ρ_{hj} is the number of shortest paths between nodes *h* and *j*, and $\rho_{hj}^{(i)}$ is the number of shortest paths between *h* and *j* that pass through node *i*, *n* is the number of nodes in a graph, and *N* is the set of all nodes in a network. This metric is identical to its unweighted counterpart, except that path lengths are computed on weighted (i.e., inverse of correlation strength) edges.

$$\text{Average edge weight} = \frac{\text{Density}_{\text{weighted}}}{\text{Density}_{\text{unweighted}}}$$

Chapter 6: General Discussion and Conclusions

This thesis's work demonstrates the feasibility and advantages of high-field fMRI imaging, especially for high-resolution experiments (1.5-mm isotropic) of small MTL structures. Reasonable estimates of the AG and HC functional properties are possible with 10-15 trials per condition, and a sample of 25 healthy young adults. Because structures the MTL are notoriously difficult to study using fMRI, mainly due to dropouts, geometric distortions, signal contamination from large drainage veins, and less dense vasculature (Andersson et al., 2001; Boubela et al., 2015; Ekstrom, 2010), the proposed high-resolution framework will be even more sensitive for cortical regions. Indeed, our own results from Chapter 5 indicate that BOLD signal power is the greatest in somatosensory, motor, and visual cortices, especially when studying brain activity in healthy young adults. However, the advantages of high-field data extend beyond high-resolution imaging. As demonstrated in Chapter 5, when working on the 3-mm isotropic 4.7 T data, our results attained a stable parcellation of the brain into 21 functional systems with 105 participants and 10-minute-long fMRI acquisitions.

Chapter 3 showed not only the feasibility of studying functional properties of the human amygdala subnuclei *in vivo* but the necessity of doing so. Since various amygdala subnuclei responded differently to visual stimuli: the LA nucleus was largely unresponsive to both neutral and negative pictures, the BA group was activated by all pictures, regardless of emotional content, while the CeM group showed preferential sensitivity to negative pictures. Critically, because of its size (Brabec et al., 2010; Garcia-Amado & Prensa, 2012), function of the CeM amygdala can only be studied using high-resolution fMRI with no spatial smoothing during image post-processing. Similarly, the anterior and posterior hippocampal subfields showed differential activity profiles during memory retrieval (i.e., Chapter 4). Because of the subfields' anatomical proximity (Adler et al., 2014; Duvernoy, 2005; Malykhin et al., 2010), any spatial smoothing with a kernel size > 2 mm FWHM would lead to signal averaging across the subfield boundaries, minimizing the advantages of high-resolution imaging. Functional MRI datasets with 2-mm isotropic (or larger) voxels would make it virtually impossible to study subfield activity *in vivo*.

A key advantage of the methodology in Chapters 3 and 4 was the manual segmentation of the amygdala subnuclei and hippocampal subfields and subregions in native space on T2-weighted structural MRI with a sub-millimeter spatial resolution (Aghamohammadi-Sereshki et al., 2018;

Malykhin et al., 2010). Such T2-weighted FSE images allow for direct visualization of the intra-hippocampal white matter, *stratum lacunosum-moleculare*, and provide additional contrast for segmenting the amygdala from nearby MTL structures (Aghamohammadi-Sereshki et al., 2018; Malykhin et al., 2010), ensuring the anatomical accuracy of all activity estimates. Registering each participant's scan to a template brain can introduce anatomical errors due to the deformations required (Yassa & Stark, 2009). Subject-specific segmentation by an expert rater is the gold standard in structural brain imaging since it bypasses most of the issues arising during such complex transformations. Furthermore, analyzing activity in native space reduces data interpolation, as the only preprocessing steps that must be performed prior to activation analyses are correction of inhomogeneity-induced geometric distortions, realignment, de-spiking, motion scrubbing, and physiological noise removal. Head movement can be a serious problem for high-resolution fMRI studies as relatively minor rotations of 1-2° or displacement of 1-2 mm can pose a serious challenge for precise activity localization. Future high-resolution fMRI experiments may benefit from customized head molds as a preventive measure to additionally reduce the confounding effects of head motion (Power et al., 2019), especially in populations prone to greater head movement during the scanning procedure (for example in pediatric or elderly volunteers).

Alternatively, as was done in Chapter 5, it is possible to use the ICA-based manual denoising technique with the guidance of an automated classifier of head motion signal sources (Griffanti et al., 2017; Pruim et al., 2015a). This approach worked well in a full-brain study with previously-described network/noise features (e.g., Griffanti et al., 2017), but would be less effective for high-resolution datasets with partial brain coverage since noise/signal sources of such acquisitions require further validation. Instead, physiological denoising derived from cardiac and respiratory waveforms (Chapter 4) is a more suitable method for high-resolution work (Glover et al., 2000; Birn et al., 2006, 2008; Chang et al., 2009). Alternatively, CompCor methodology (Behzadi et al., 2007) with strict CSF and WM masks can be used to account for some of the aliased physiological noise, as was done in Chapter 3.

The necessity of building customized HRf models was evidenced most strongly in Chapter 4 (i.e., *Experiment 2*). Even though we presented encoding grids for 10 seconds, the HC of our participants was not active for the entire duration that the stimulus was presented on the screen. Simply convolving the stimulus duration with the canonical HRf, as is frequently done in the field, would have resulted in a highly inaccurate model of regional BOLD activity. Poor BOLD models

not only weaken one's ability to detect activity in the first place but may also produce biased or even incorrect estimates, especially when a region's actual response deviates drastically from the expected model (Calhoun et al., 2004; Lindquist et al., 2009; Pernet et al., 2014). Even though it was not feasible to develop subfield/subnucleus-specific models at this time, mainly because there was a lack of prior knowledge about functional properties that individual subnuclei and anterior/posterior subfields play in our cognitive tasks, future high-resolution studies of the MTL would benefit from estimating HRfs not only for the total HC/AG, but also for their subfields/subnuclei. As the number of high-resolution fMRI studies grows, future studies will be able to administer cognitive tasks engaging specific subnuclei and subfields, which in turn will allow for even more accurate BOLD modeling within the MTL.

The remaining section of this chapter will consider the field-specific implications of my work on our understanding of the human brain. For each of the experimental chapters, I first provide a brief overview of what was previously known about each research area and how my results advance that specific field.

8.1 *In vivo* study of amygdala subnuclei function in humans

Background and knowledge gaps

Most previous studies of the human amygdala investigated its function either as a single unitary structure or investigated coarse and anatomically-unrepresentative dorsal/ventral (Kim et al., 2004; Morris et al., 2001; Whalen et al., 1998; Whalen et al., 2001), medial/lateral (Kim et al., 2003; Zald & Pardo, 2002), or anterior/posterior subdivisions (Gottfried et al., 2002; Morris et al., 2002; Wang et al., 2008). Where subnuclei were studied separately, studies sometimes used sub-optimal atlases with inaccurate subnuclei and amygdala boundaries (e.g., Ball et al., 2007, 2009; Frühholz & Grandjean, 2013; Grant et al., 2015; Roy et al., 2009; Styalidis et al., 2014). To my best knowledge, no earlier studies investigated intra-amygdala functional connectivity.

Contributions

This was the first study to combine ultra-high-resolution T_2-weighted structural MRI with high-resolution functional MRI to study the amygdala subnuclei function *in vivo* and demonstrated for the first time that subnuclei of the human AG respond differently to emotional stimuli. Research

presented in Chapter 3 is also the first demonstration of intra-AG functional connectivity in humans.

To perform the study, multiple innovative techniques were used. First, we employed histological references (Brabec et al., 2010; Mai et al., 2008) to subdivide the AG into 3 major subnuclei groups that closely approximate the subnuclei anatomy (Aghamohammadi-Sereshki et al., 2018). Furthermore, we developed a customized BOLD response model for the AG and used this methodology to study not only response amplitude but also time-to-peak. Our methodology was designed as a compromise between model flexibility and statistical sensitivity. More flexible approaches, like the Finite Impulse Response (FIR) technique, estimate activity for each invidividual time point separately (Glover, 1999). As can be expected, doing so comes at the expense of reduced statistical power, no baseline enforcement, and no shape constraints. Consequently, FIR-based techniques are prone to overfitting, especially with a limited number of trials and subjects. Our BOLD analysis technique was able to capture not just amplitude, but also temporal differences in CeM activity following stimulation by emotionally-salient stimuli.

8.2 *In vivo* study of the anterior and posterior hippocampal subfield function in humans

Background and knowledge gaps

The HC has been studied extensively in both human and animal literature (Cohen et al., 1999; Eichenbaum, 2001; Lisman et al., 2017; Moscovitch et al., 2005, 2016; Scoville & Milner, 1957; Squire & Dede, 2015, Squire & Wixted, 2011; Squire et al., 2015). Since the famous HM case (Scoville & Milner, 1957), those studies largely focused on the HC role in declarative, especially episodic, memory. However, most prior HC research focused either on its longitudinal or cross-sectional axis, but not both. This was partly due to methodological limitations of standard acquisition and analysis techniques. Thickness of the CA1-3 and Sub subfields is less than 2-mm on many coronal slices (Adler et al., 2014), requiring high-resolution imaging with customized analytical approches. Furthermore, many previous high-resolution fMRI studies of the HC subfield function were limited in their acquisitions or segmentation methodology and, as a result, did not study subfield function of the most anterior portions of the HC head (Chen et al., 2011; Copara et al., 2014; Eldridge et al., 2005; Nauer et al., 2015; Stokes et al., 2015; Suthana et al., 2009, 2011; Zeineh et al., 2003) or the most posterior HC segments, especially the HC tail (Berron et al., 2016; Chen et al., 2011; Eldridge et al., 2005; Zeineh et al., 2003). Consequently, one of the major

methodological goals in Chapter 4 was to come up with acquisition and analysis methodology that was capable of measuring activity in every part of the human HC without sacrificing 1.5-mm isotropic resolution. The second objective of my high-resolution HC study was to elucidate the relationship between different types of memory and the role that the HC plays in forming and retrieving them.

In the current literature, there is limited consensus as to whether the HC is responsible for processing of spatial vs. non-spatial memory (Eichenbaum, 2017; Eichenbaum & Cohen, 2014; Kumaran & Maguire, 2005; Lisman et al., 2017; Nadel et al., 2012), and whether the HC is involved in item, not just relational memory (Davachi et al., 2003; Gold et al., 2006; Konkel et al., 2008). Instead, a substantial segment of high-resolution fMRI literature on the role that the HC subfields play in episodic memory was attained using pattern separation/completion tasks (Bakker et al., 2008; Duncan et al., 2012; Lacy et al., 2011; Yassa & Stark, 2011). Whether the anterior or posterior HC subfields are specialized for one vs. another type of explicit memory has not been studied directly.

Contributions

To my best knowledge, Chapter 4 is the first study that investigated item, spatial, and associative memory during memory encoding and memory retrieval in each of the anterior and posterior hippocampal subfields. This chapter builds on high-resolution techniques that were introduced in Chapter 3. Because the HC is a much larger structure that the AG, and consequently more vulnerable to inhomogeneity-induced distortions, our preprocessing and activity detection methodology was optimized further. To deal with physiological noise sources, our research team recorded cardiac and respiratory waveforms during the fMRI scan (Glover et al., 2000; Birn et al., 2006, 2008; Chang et al., 2009). To improve the structural-functional image alignment, fieldmap-based correction for geometric distortions was added to the pipeline (Andersson et al., 2001), while correction for slice acquisition delay was removed to minimize data interpolation. Due to task complexity, two separate HC BOLD response models were created: one for the encoding phase and the other for the retrieval phase. The HRf-creation procedure incorporates a new HRf/noise classification scheme that takes into account subfield- and subregion-related differences in activity (e.g., activation/deactivation/noise). Similar to the AG study, *Experiment 2* relied on manual

segmentation of the hippocampal subregions and subfields on ultra-high-resolution structural MRI (Malykhin et al., 2010).

The results of this study filled a number of gaps in the field of human memory and HC function. First, *Experiment 2* showed that the entire HC (i.e., both anterior and posterior subfields) was active during memory encoding. Second, there was an anterior to posterior gradient in HC activity during memory retrieval. This gradient was characterized by above-baseline activity in the posterior HC (HC body and tail) and below-baseline activity in the anterior HC (HC head). Third, the DG was more active than in the CA1-3 or Sub during both encoding and retrieval. Fourth, the type of memory process (i.e., item, spatial, associative) had marginal effects on HC activity during memory encoding; however, there was a global right-hemisphere preference for spatial trials during memory retrieval. Lastly, the results from Chapter 4 demonstrate the necessity of studying functional aspects of the anterior and posterior HC subfields separately, since our data showed differential functional responses of the anterior and posterior HC subfields during some types of memory processing.

8.3 *In vivo* study of healthy brain aging using high-field resting-state fMRI

Background and knowledge gaps

Multiple fMRI studies of brain aging reported reduced BOLD activity during simple non-cognitive tasks, like visual stimulation and finger tapping (D'Esposito et al., 1999, 2003; Handwerker et al., 2007; Hesselmann et al., 2001; Mehagnoul-Schipper et al., 2002; Riecker et al., 2006; Ross et al., 1997; West et al., 2019). In tasks that place substantial loads on working memory and selective attention, fMRI experiments revealed more extensive frontal and parietal activation among old adults (Cabeza et al., 2002, 2004; Davis et al., 2008; Gutchess et al., 2005; Logan et al., 2002; Rypma & D'Esposito, 2000; Rajah & D'Esposito, 2005; Spreng et al., 2010), suggesting either age effects on the underlying network architecture or additional engagement of brain reserves to compensate for declining information processing via conventional streams (Buckner, 2004; Cabeza, 2002; Fabiani, 2012; Grady, 2008). Old adults also show reduced deactivation of the default mode system during cognitive tasks (Park & Reuter-Lorenz, 2009; Persson et al., 2007, 2014; Raichle & Snyder, 2007), suggesting either a reduction in fMRI signal power or a failure to disengage task un-related thoughts.

Resting-state functional connectivity studies, on the other hand, indicate functional de-differentiation with age and a loss of long-range functional connectivity, especially in the default mode system (Andrews-Hanna et al., 2007; Damoiseaux, 2017; Tomasi & Volkow, 2012; Wu et al., 2011; Wig, 2017). However, few resting-state fMRI experiments investigated how network amplitude is affected in aging (but see, Allen et al., 2011). Furthermore, most prior work on the relationship between age and functional connectivity used simple bivariate correlations as a proxy for age effects on functional coupling (e.g., Andrews-Hanna et al., 2007; Betzel et al., 2014; Geerligs et al., 2015; Grady et al., 2016; Zonneveld et al., 2019). Unfortunately, correlation is an ambiguous measure, and without broader understanding of how fMRI signal is affected by the aging processes, since correlation differences among age groups can be due to age differences in BOLD amplitude, background noise, or coupling (Duff et al., 2018). Furthermore, bivariate correlations require somewhat arbitrary thresholding and can detect false connections due to indirect network coupling (i.e., if A ↔ B, and B ↔ C connectivity exists, there is a high probability that A ↔ C will also be statistically associated under a typical bivariate correlation approach; Smith et al., 2011).

Contributions

To my best knowledge, Chapter 5 is the first example of a high-field resting-state fMRI study into neurobiological processes occurring as a part of healthy cognitive aging. It is also the first application of a SCAD-regularized sparse graphical methodology for studying age effects on the brain's functional architecture.

Chapter 5 showed that BOLD signal amplitude declines in every resting-state network with age, suggesting that a reduction in the BOLD signal itself might be responsible for the previously reported age effect on BOLD activity during task-based fMRI. Despite the regional variation, biological causes of these amplitude trends likely share a common origin, and could represent global vascular or neurobiological changes, and carry wide-ranging implications for most correlation-based functional connectivity studies of brain aging. Specifically, previously reported de-differentiation trends, typically measured as a reduction in network modularity, might represent a weakened BOLD contrast-to-noise ratio and not altered coupling *per se*. Binarized bivariate correlations with arbitrary cutoffs may introduce further confusion, as noise sources might appear as

true ‘connectivity’ if the correlation-based cutoffs for edge detection are set low enough (Power et al., 2012).

Consistent with the hypothesis that many of the age differences in prior resting-state functional connectivity studies may have been driven by a reduction in network amplitude as opposed to direct differences in the functional coupling, the overall network architecture was similar in young, middle-aged, and old adults. Nonetheless, modest differences (mainly reduction) in intra-network connectivity were detected in most functional systems. Because age effects on network amplitude were removed from network maps, these small differences likely represent true functional rewiring, especially in brain regions where age-related GM atrophy cannot fully account for statistical associations between network maps and age. The 4.7 T MRI system enabled me to separate the default mode system into 6 main sub-systems, the relationship between which was evaluated using sparse graphical methods. Unlike previously studies by others (Andrews-Hanna et al., 2007; Damoiseaux et al. 2008; Wu et al., 2011), which reported a loss of functional connectivity between the medial frontal and medial parietal hubs in ageing individuals, the results of my work suggest an age-related functional reorganization within the default mode system, and not an outright breakdown in network structure in old age. Lastly, our graphical methods also suggest weakened inter-system (i.e., somatomotor ↔ attention, attention ↔ default, etc.) communication in old adults. In summary, because of improved sensitivity to BOLD contrast at 4.7 T, Chapter 5 provides a comprehensive overview of the relationship between age effects and resting-state fMRI with significant implications for previous task-based and functional connectivity literature.

References

Aanerud, J., Borghammer, P., Chakravarty, M. M., Vang, K., Rodell, A. B., Jónsdottir, K. Y., Møller, A., Ashkanian, M., Vafaee, M. S., Iversen, P., Johannsen, P., & Gjedde, A. (2012). Brain energy metabolism and blood flow differences in healthy aging. *Journal of Cerebral Blood Flow and Metabolism*, *32*, 1177–1187.

Adler, D. H., Pluta, J., Kadivar, S., Craige, C., Gee, J. C., Avants, B. B., & Yushkevich, P. A. (2014). Histology-derived volumetric annotation of the human hippocampal subfields in postmortem MRI. *NeuroImage*, *84*, 505–523.

Adolphs, R., Tranel, D., Damasio, H., & Damasio, A. R. (1994). Impaired recognition of emotion in facial expressions following bilateral damage to the human amygdala. *Nature*, *372*, 669–672.

Adolphs, R., Tranel, D., Damasio, H., & Damasio, A. R. (1995). Fear and the human amygdala. *Journal of Neuroscience*, *15*(9), 5879–5891.

Adolphs, R., Gosselin, F., Buchanan, T. W., Tranel, D., Schyns, P., & Damasio, A. R. (2005). A mechanism for impaired fear recognition after amygdala damage. *Nature*, *433*, 68–72.

Aghamohammadi-Sereshki, A., Hrybouski, S., Travis, S., Huang, Y., Olsen, F., Carter, R., Camicioli, R., & Malykhin, N. V. (2019). Amygdala subnuclei and healthy cognitive aging. *Human Brain Mapping*, *40*, 34–52.

Allen, E. A., Erhardt, E. B., Damaraju, E., Gruner, W., Segall, J. M., Silva, R. F., Havlicek, M., Rachakonda, S., Fries, J., Kalyanam, R., Michael, A. M., Caprihan, A., Turner, J. A., Eichele, T., Adelsheim, S., Bryan, A. D., Bustillo, J., Clark, V. P., Feldstein Ewing, S. W., Filbey, F., Ford, C. C., Hutchison, K., Jung, R. E., Kiehl, K. A., Kodituwakku, P., Komesu, Y. M., Mayer, A. R., Pearlson, G. D., Phillips, J. P., Sadek, J. R., Stevens, M., Teuscher, U., Thoma, R. J., & Calhoun, V. D. (2011). A baseline for the multivariate comparison of resting-state networks. *Frontiers in Systems Neuroscience*, *5*, 2.

Allen, E. A., Erhardt, E. B., Eichele, T., Mayer, A. R., and Calhoun, V. D. (2010). "Comparison of pre-normalization methods on the accuracy of group ICA results", in *16th Annual Meeting of the Organization for Human Brain Mapping*, 6–10 June, Barcelona, Spain.

Allen, E. A., Erhardt, E. B., Wei, Y., Eichele, T., & Calhoun, V. D. (2012). Capturing inter- subject variability with group independent component analysis of fMRI data: a simulation study. *NeuroImage*, *59*, 4141–4159.

Allen, J. S., Joel, B., Brown, K. C., & Damasio, H. (2005). Normal neuroanatomical variation due to age: the major lobes and a parcellation of the temporal region. *Neurobiology of Aging, 26*, 1245–1260.

Allen, R. J., Vargha-Khadem, F., & Baddeley, A. D. (2014). Item-location binding in working memory: is it hippocampus-dependent? *Neuropsychologia*, *59*, 74–84.

Aly, M., & Turk-Browne, N. B. (2016). Attention stabilizes representations in the human Hippocampus. *Cerebral Cortex*, *26*, 783–796.

Amaro, E., & Barker, G. J. (2006). Study design in fMRI: basic principles. *Brain and Cognition*, *60*, 220–232.

Ambler, G., & Royston, P. (2001). Fractional polynomial model selection procedures: investigation of type I error rate. *Journal of Statistical Computation and Simulation*, *69*, 89–108.

Amunts, K., Kedo, O., Kindler, M., Pieperhoff, P., Mohlberg, H., Shah, N. J., Habel, U., Schneider, F., & Zilles, K. (2005). Cytoarchitectonic mapping of the human amygdala, hippocampal region and entorhinal cortex: intersubject variability and probability maps. *Anatomy and Embryology*, *210*, 343–352.

Ances, B. M., Liang, C. L., Leontiev, O., Perthen, J. E., Fleisher, A. S., Lansing, A. E., & Buxton, R. B. (2009). Effects of aging on cerebral blood flow, oxygen metabolism, and blood oxygenation level dependent responses to visual stimulation. *Human Brain Mapping*, *30*, 1120–1132.

Andersson, J. L., Hutton, C., Ashburner, J., Turner, R., & Friston, K. (2001). Modeling geometric deformations in EPI time series. *NeuroImage*, *13*, 903–919.

Andrews-Hanna, J. R. (2012). The brain's default network and its adaptive role in internal mentation. *Neuroscientist*, *18*, 251–270.

Andrews-Hanna, J. R., Reidler, J. S., Sepulcre, J., Poulin, R., & Buckner, R. L. (2010). Functional-anatomic fractionation of the brain's default network. *Neuron*, *65*, 550–562.

Andrews-Hanna, J. R., Smallwood, J., & Spreng, R. N. (2014). The default network and self-generated thought: component processes, dynamic control, and clinical relevance. *Annals of the New York Academy of Sciences*, *1316*, 29–52.

Andrews-Hanna, J. R., Snyder, A. Z., Vincent, J. L., Lustig, C., Head, D., Raichle, M. E., & Buckner, R. L. (2007). Disruption of large-scale brain systems in advanced aging. *Neuron*, *56*, 924–935.

Arbabshirani, M. R., Damaraju, E., Phlypo, R., Plis, S., Allen, E., Ma, S., Mathalon, D., Preda, A., Vaidya, J. G., Adali, T., & Calhoun, V. D. (2014). Impact of autocorrelation on functional connectivity. *NeuroImage*, *102 Pt 2*, 294–308.

Attwell, D., Buchan, A. M., Charpak, S., Lauritzen, M., MacVicar, B. A., & Newman, E. A. (2010). Glial and neuronal control of brain blood flow. *Nature*, *468*, 232–243.

Attwell, D., & Laughlin, S. B. (2001). An energy budget for signaling in the grey matter of the brain. *Journal of Cerebral Blood Flow and Metabolism*, *21*, 1133–1145.

Avants, B. B., Epstein, C. L., Grossman, M., & Gee, J. C. (2008). Symmetric diffeomorphic image registration with cross-correlation: evaluating automated labeling of elderly and neurodegenerative brain. *Medical Image Analysis*, *12*, 26–41.

Avants, B., & Gee, J. C. (2004). Geodesic estimation for large deformation anatomical shape averaging and interpolation. *NeuroImage*, *23 Suppl 1*, S139–50.

Azab, M., Stark, S. M., & Stark, C. E. L. (2014). Contributions of human hippocampal subfields to spatial and temporal pattern separation. *Hippocampus*, *24*, 293–302.

Bach, D. R., Weiskopf, N., & Dolan, R. J. (2011). A stable sparse fear memory trace in human amygdala. *Journal of Neuroscience*, *31*, 9383–9389.

Bainbridge, W. A., & Oliva, A. (2015). Interaction envelope: local spatial representations of objects at all scales in scene-selective regions. *NeuroImage*, *122*, 408–416.

Baker, S., Vieweg, P., Gao, F., Gilboa, A., Wolbers, T., Black, S. E., & Rosenbaum, R. S. (2016). The human dentate gyrus plays a necessary role in discriminating new memories. *Current Biology*, *26*, 2629–2634.

Bakker, A., Kirwan, C. B., Miller, M., & Stark, C. E. (2008). Pattern separation in the human hippocampal CA3 and dentate gyrus. *Science*, *319*, 1640–1642.

Ball, T., Rahm, B., Eickhoff, S. B., Schulze-Bonhage, A., Speck, O., & Mutschler, I. (2007). Response properties of human amygdala subregions: evidence based on functional MRI combined with probabilistic anatomical maps. *PLoS One*, *2*, e307.

Ball, T., Derix, J., Wentlandt, J., Wieckhorst, B., Speck, O., Schulze-Bonhage, A., & Mutschler, I. (2009). Anatomical specificity of functional amygdala imaging of responses to stimuli with positive and negative emotional valence. *Journal of Neuroscience Methods*, *180*, 57–70.

Balleine, B. W., & Killcross, S. (2006). Parallel incentive processing: an integrated view of amygdala function. *Trends in Neurosciences*, *29*, 272–279.

Banks, S. J., Sziklas, V., Sodums, D. J., & Jones-Gotman, M. (2012). fMRI of verbal and nonverbal memory processes in healthy and epileptogenic medial temporal lobes. *Epilepsy & Behavior*, *25*, 42–49.

Bannerman, D. M., Grubb, M., Deacon, R. M. J., Yee, B. K., Feldon, J., & Rawlins, J. N. P. (2003). Ventral hippocampal lesions affect anxiety but not spatial learning. *Behavioural Brain Research*, *139*, 197–213.

Bannerman, D. M., Rawlins, J. N. P., McHugh, S. B., Deacon, R. M. J., Yee, B. K., Bast, T., Zhang, W. N., Pothuize, H. H., & Feldon, J. (2004). Regional dissociations within the hippocampus–memory and anxiety. *Neuroscience and Biobehavioral Reviews*, *28*, 273–283.

Bannerman, D. M., Sprengel, R., Sanderson, D. J., McHugh, S. B., Rawlins, J. N. P., Monyer, H., & Seeburg, P. H. (2014). Hippocampal synaptic plasticity, spatial memory and anxiety. *Nature Reviews. Neuroscience*, *15*, 181–192.

Barret, L. F. (2006). Valence is a basic building block of emotional life. *Journal of Research in Personality*, *40*, 35–55.

Bastian, M., Heymann, S., & Jacomy, M. (2009). Gephi: an open source software for exploring and manipulating networks. In: Third International AAAI Conference on Weblogs and Social Media, pp. 361e362. Available at: http://aaai.org/ocs/ index.php/ICWSM/09/paper/view/154.

Beason-Held, L. L., Kraut, M. A., & Resnick, S. M. (2008). I. Longitudinal changes in aging brain function. *Neurobiology of Aging*, *29*, 483–496.

Beckmann, C. F., DeLuca, M., Devlin, J. T., & Smith, S. M. (2005). Investigations into resting-state connectivity using independent component analysis. *Philosophical Transactions of the Royal Society B: Biological Sciences*, *360*, 1001–1013.

Beckmann, C. F., & Smith, S. M. (2004). Probabilistic independent component analysis for functional magnetic resonance imaging. *IEEE Transactions on Medical Imaging*, *23*, 137–152.

Behzadi, Y., Restom, K., Liau, J., & Liu, T. T. (2007). A component based noise correction method (CompCor) for BOLD and perfusion based fMRI. *NeuroImage*, *37*, 90–101.

Bell, A. J., & Sejnowski, T. (1995). An information-maximization approach to blind separation and blind deconvolution. *Neural Computation*, *7*, 1129–1159.

Berron, D., Schütze, H., Maass, A., Cardenas-Blanco, A., Kuijf, H. J., Kumaran, D., & Düzel, E. (2016). Strong evidence for pattern separation in human dentate gyrus. *Journal of Neuroscience*, *36*, 7569–7579.

Bertsch, K., Hagemann, D., Hermes, M., Walter, C., Khan, R., & Naumann, E. (2009). Resting cerebral blood flow, attention, and aging. *Brain Research*, *1267*, 77–88.

Betzel, R. F., Byrge, L., He, Y., Goñi, J., Zuo, X.-N., & Sporns, O. (2014). Changes in structural and functional connectivity among resting-state networks across the human lifespan. *NeuroImage*, *102 Pt 2*, 345–357.

Bhaganagarapu, K., Jackson, G. D., & Abbott, D. F. (2013). An automated method for identifying artifact in independent component analysis of resting-state fMRI. *Frontiers in Human Neuroscience*, *7*.

Birkes, D., & Dodge, Y. (1993). *Alternative methods of regression*. Hoboken, NJ, USA: John Wiley & Sons, Inc.

Birn, R. M., Diamond, J. B., Smith, M. A., & Bandettini, P. A. (2006). Separating respiratory-variation-related fluctuations from neuronal-activity-related fluctuations in fMRI. *NeuroImage*, *31*, 1536–1548.

Birn, R. M., Smith, M. A., Jones, T. B., & Bandettini, P. A. (2008). The respiration response function: the temporal dynamics of fMRI signal fluctuations related to changes in respiration. *NeuroImage*, *40*, 644–654.

Boccardi, M., Bocchetta, M., Ganzola, R., Robitaille, N., Redolfi, A., Duchesne, S., Jack, C. R., & Frisoni, G. B. (2015). Operationalizing protocol differences for EADC-ADNI manual hippocampal segmentation. *Alzheimer's Dementia*, *11*, 184–194.

Boll, S., Gamer, M., Kalisch, R., & Büchel, C. (2011). Processing of facial expressions and their significance for the observer in subregions of the human amygdala. *NeuroImage*, *56*, 299–306.

Boll, S., Gamer, M., Gluth, S., Finsterbusch, J., & Büchel, C. (2013). Separate amygdala subregions signal surprise and predictiveness during associative fear learning in humans. *European Journal of Neuroscience*, *37*, 758–767.

Bonne, O., Vythilingam, M., Inagaki, M., Wood, S., Neumeister, A., Nugent, A. C., Snow, J., Luckenbaugh, D. A., Bain, E. E., Drevets, W. C., & Charney, D. S. (2008). Reduced posterior hippocampal volume in posttraumatic stress disorder. *Journal of Clinical Psychiatry*, *69*, 1087–1091.

Bonnici, H. M., Chadwick, M. J., Kumaran, D., Hassabis, D., Weiskopf, N., & Maguire, E. A. (2012). Multi-voxel pattern analysis in human hippocampal subfields. *Frontiers in Human Neuroscience*, *6*, 290.

Boubela, R. N., Kalcher, K., Huf, W., Seidel, E. M., Derntl, B., Pezawas, L., Našel, C., & Moser, E. (2015). fMRI measurements of amygdala activation are confounded by stimulus correlated signal fluctuation in nearby veins draining distant brain regions. *Scientific Reports*, *5*, 10499.

Bouchard, T. P., Malykhin, N., Martin, W. R. W., Hanstock, C. C., Emery, D. J., Fisher, N. J., & Camicioli, R. M. (2008). Age and dementia-associated atrophy predominates in the hippocampal head and amygdala in Parkinson's disease. *Neurobiology of Aging*, *29*, 1027–1039.

Brabec, J., Rulseh, A., Hoyt, B., Vizek, M., Horinek, D., Hort, J., & Petrovicky, P. (2010). Volumetry of the amygdala — an anatomical study. *Psychiatry Research*, *182*, 67–72.

Bradley, M. M., & Lang, P. J. (1994). Measuring emotion: the self-assessment manikin and the semantic differential. *Journal of Behavior Therapy and Experimental Psychiatry*, *25*, 49–59.

Broks, P., Young, A. W., Maratos, E. J., Coffey, P. J., Calder, A. J., Isaac, C. L., Mayes, A. R., Hodges, J. R., Montaldi, D., Cezayirli, E., Roberts, N., & Hadley, D. (1998). Face processing impairments after encephalitis: amygdala damage and recognition of fear. *Neuropsychologia*, *36*, 59–70.

Brooks, B. L., Strauss, E., Sherman, E. M. S., Iverson, G. L., & Slick, D. J. (2009). Developments in neuropsychological assessment: refining psychometric and clinical interpretive methods. *Canadian Psychology*, *50*, 196–209.

Brooks, B. L., Sherman, E. M. S., & Strauss, E. (2010). Test Review: NEPSY-II: a developmental neuropsychological assessment, Second edition. *Child Neuropsychology*, *16*, 80–101.

Brown, T. A., Di Nardo, P. A., Lehman, C. L., & Campbell, L. A. (2001). Reliability of DSM-IV anxiety and mood disorders: implications for the classification of emotional disorders. *Journal of Abnormal Psychology*, *110*, 49–58.

Brown, T. I., Hasselmo, M. E., & Stern, C. E. (2014). A high-resolution study of hippocampal and medial temporal lobe correlates of spatial context and prospective overlapping route memory. *Hippocampus*, *24*, 819–839.

Büchel, C., Morris, J., Dolan, R. J., & Friston, K. J. (1998). Brain systems mediating aversive conditioning: an event-related fMRI study. *Neuron*, *20*, 947–957.

Buckner, R. L. (2004). Memory and executive function in aging and AD: multiple factors that cause decline and reserve factors that compensate. *Neuron*, *44*, 195–208.

Buckner, R. L., Krienen, F. M., & Yeo, B. T. T. (2013). Opportunities and limitations of intrinsic functional connectivity MRI. *Nature Neuroscience*, *16*, 832–837.

Buckner, R. L., Snyder, A. Z., Sanders, A. L., Raichle, M. E., & Morris, J. C. (2000). Functional brain imaging of young, nondemented, and demented older adults. *Journal of Cognitive Neuroscience*, *12 Suppl 2*, 24–34.

Bullmore, E., & Sporns, O. (2009). Complex brain networks: graph theoretical analysis of structural and functional systems. *Nature Reviews. Neuroscience*, *10*, 186–198.

Burnham, K. P., & Anderson, D. R. (2002). *Model selection and multimodel inference: A practical information-theoretic approach* (2nd ed.). New York: Springer-Verlag.

Button, K. S., Ioannidis, J. P. A., Mokrysz, C., Nosek, B. A., Flint, J., Robinson, E. S. J., & Munafò, M. R. (2013). Power failure: why small sample size undermines the reliability of neuroscience. *Nature Reviews. Neuroscience*, *14*, 365–376.

Cabeza, R., Anderson, N. D., Locantore, J. K., & McIntosh, A. R. (2002). Aging gracefully: compensatory brain activity in high-performing older adults. *NeuroImage*, *17*, 1394–1402.

Cabeza, R., Daselaar, S. M., Dolcos, F., Prince, S. E., Budde, M., & Nyberg, L. (2004). Task-independent and task-specific age effects on brain activity during working memory, visual attention and episodic retrieval. *Cerebral Cortex*, *14*, 364–375.

Calhoun, V. D., Adali, T., Pearlson, G. D., & Pekar, J. J. (2001). A method for making group inferences from functional MRI data using independent component analysis. *Human Brain Mapping*, *14*, 140–151.

Calhoun, V. D., Stevens, M. C., Pearlson, G. D., & Kiehl, K. A. (2004). fMRI analysis with the general linear model: removal of latency-induced amplitude bias by incorporation of hemodynamic derivative terms. *NeuroImage*, *22*, 252–257.

Cao, M., Wang, J.-H., Dai, Z.-J., Cao, X.-Y., Jiang, L.-L., Fan, F.-M., Song, X.-W., Xia, M.-R., Shu, N., Dong, Q., Milham, M. P., Castellanos, F. X., Zuo, X.-N., & He, Y. (2014). Topological organization of the human brain functional connectome across the lifespan. *Developmental Cognitive Neuroscience*, *7*, 76–93.

Caplan, J. B., & Madan, C. R. (2016). Word imageability enhances association-memory by increasing hippocampal engagement. *Journal of Cognitive Neuroscience*, *28*, 1522–1538.

Cardinal, R. N., Parkinson, J. A., Hall, J., & Everitt, B. J. (2002). Emotion and motivation: the role of the amygdala, ventral striatum, and prefrontal cortex. *Neuroscience and Biobehavioral Reviews*, *26*, 321–352.

Chan, M. Y., Alhazmi, F. H., Park, D. C., Savalia, N. K., & Wig, G. S. (2017). Resting-state network topology differentiates task signals across the adult life span. *Journal of Neuroscience*, *37*, 2734–2745.

Chan, M. Y., Park, D. C., Savalia, N. K., Petersen, S. E., & Wig, G. S. (2014). Decreased segregation of brain systems across the healthy adult lifespan. *Proceedings of the National Academy of Sciences of the United States of America*, *111*, E4997–E5006.

Chang, C., Cunningham, J. P., & Glover, G. H. (2009). Influence of heart rate on the BOLD signal: the cardiac response function. *NeuroImage*, *44*, 857–869.

Chareyron, L. J., Banta Lavenex, P., Amaral, D. G., & Lavenex, P. (2011). Stereological analysis of the rat and monkey amygdala. *Journal of Comparative Neurology*, *519*, 3218–3239.

Chen, K. H. M., Chuah, L. Y. M., Sim, S. K. Y., & Chee, M. W. L. (2010). Hippocampal region-specific contributions to memory performance in normal elderly. *Brain and Cognition*, *72*, 400–407.

Chen, J., Olsen, R. K., Preston, A. R., Glover, G. H., & Wagner, A. D. (2011). Associative retrieval processes in the human medial temporal lobe: hippocampal retrieval success and CA1 mismatch detection. *Learning & Memory*, *18*, 523–528.

Chen, J. J., Rosas, H. D., & Salat, D. H. (2011). Age-associated reductions in cerebral blood flow are independent from regional atrophy. *NeuroImage*, *55*, 468–478.

Chong, J. S. X., Ng, K. K., Tandi, J., Wang, C., Poh, J.-H., Lo, J. C., Chee, M. W. L., & Zhou, J. H. (2019). Longitudinal changes in the cerebral cortex functional organization of healthy elderly. *Journal of Neuroscience*, *39*, 5534–5550.

Christoff, K., Irving, Z. C., Fox, K. C. R., Spreng, R. N., & Andrews-Hanna, J. R. (2016). Mind-wandering as spontaneous thought: a dynamic framework. *Nature Reviews. Neuroscience*, *17*, 718–731.

Chua, E. F., Schacter, D. L., Rand-Giovannetti, E., & Sperling, R. A. (2007). Evidence for a specific role of the anterior hippocampal region in successful associative encoding. *Hippocampus*, *17*, 1071–1080.

Cohen, N. J., & Eichenbaum, H. (1993). Memory, Amnesia, and the Hippocampal System. The MIT Press, Cambridge, MA, US.

Cohen, E. R., Rostrup, E., Sidaros, K., Lund, T. E., Paulson, O. B., Ugurbil, K., & Kim, S.-G. (2004). Hypercapnic normalization of BOLD fMRI: comparison across field strengths and pulse sequences. *NeuroImage*, *23*, 613–624.

Cohen, N. J., Ryan, J., Hunt, C., Romine, L., Wszalek, T., Nash, C. (1999). Hippocampal system and declarative (relational) memory: summarizing the data from functional neuroimaging studies. *Hippocampus*, *9*, 83–98.

Colombo, M., Fernandez, T., Nakamura, K., & Gross, C.G. (1998). Functional differentiation along the anterior-posterior axis of the hippocampus in monkeys. *Journal of Neurophysiology*, *80*, 1002–1005.

Copara, M. S., Hassan, A. S., Kyle, C. T., Libby, L. A., Ranganath, C., & Ekstrom, A. D. (2014). Complementary roles of human hippocampal subregions during retrieval of spatiotemporal context. *Journal of Neuroscience*, *34*, 6834–6842.

Costantini, G., Epskamp, S., Borsboom, D., Perugini, M., Mõttus, R., Waldorp, L. J., & Cramer, A. O. J. (2015). State of the aRt personality research: A tutorial on network analysis of personality data in R. *Journal of Research in Personality*, *54*, 13–29.

Craddock, R. C., Jbabdi, S., Yan, C.-G., Vogelstein, J. T., Castellanos, F. X., Di Martino, A., Kelly, C., Heberlein, K., Colcombe, S., & Milham, M. P. (2013). Imaging human connectomes at the macroscale. *Nature Methods*, *10*, 524–539.

Crossley, N. A., Mechelli, A., Vértes, P. E., Winton-Brown, T. T., Patel, A. X., Ginestet, C. E., McGuire, P., & Bullmore, E. T. (2013). Cognitive relevance of the community structure of the human brain functional coactivation network. *Proceedings of the National Academy of Sciences of the United States of America*, *110*, 11583–11588.

Damoiseaux, J. S. (2017). Effects of aging on functional and structural brain connectivity. *NeuroImage*, *160*, 32–40.

Damoiseaux, J. S., Beckmann, C. F., Arigita, E. J. S., Barkhof, F., Scheltens, P., Stam, C. J., Smith, S. M., & Rombouts, S. A. R. B. (2008). Reduced resting-state brain activity in the "default network" in normal aging. *Cerebral Cortex*, *18*, 1856–1864.

Das, S. R., Mechanic-Hamilton, D., Pluta, J., Korczykowski, M., Detre, J. A., & Yushkevich, P. A. (2011). Heterogeneity of functional activation during memory encoding across hippocampal subfields in temporal lobe epilepsy. *NeuroImage*, *58*, 1121–1130.

Davis, M. (1992). The role of the amygdala in conditioned fear. In: Aggleton, J. (Ed.), The Amygdala: Neurobiological Aspects of Emotion, Memory, and Mental Dysfunction. New York, NY, Wiley, pp. 255–305.

Davis, S. W., Dennis, N. A., Daselaar, S. M., Fleck, M. S., & Cabeza, R. (2008). Que PASA? The posterior-anterior shift in aging. *Cerebral Cortex*, *18*, 1201–1209.

Davis, M., & Whalen, P. J. (2001). The amygdala: vigilance and emotion. *Molecular Psychiatry*, *6*, 13–34.

Davis, C. F., Johnstone, T., Mazzulla, E. C., Oler, J. A., & Whalen, P. J. (2010). Regional response differences across the human amygdaloid complex during social conditioning. *Cerebral Cortex*, *20*, 612–621.

Daugherty, A. M., Yu, Q., Flinn, R., & Ofen, N. (2015). A reliable and valid method for manual demarcation of hippocampal head, body, and tail. *International Journal of Developmental Neuroscience*, *41*, 115–122.

Davachi, L., Mitchell, J. P., & Wagner, A. D. (2003). Multiple routes to memory: distinct medial temporal lobe processes build item and source memories. *Proceedings of the National Academy of Sciences of the United States of America*, *100*, 2157–2162.

De Martino, F., Yacoub, E., Kemper, V., Moerel, M., Uludağ, K., De Weerd, P., Ugurbil, K., Goebel, R., & Formisano, E. (2018). The impact of ultra-high field MRI on cognitive and computational neuroimaging. *NeuroImage*, *168*, 366–382.

de Vanssay-Maigne, A., Noulhiane, M., Devauchelle, A. D., Rodrigo, S., Baudoin-Chial, S., Meder, J. F., Oppenheim, C., Chiron, C., & Chassoux, F. (2011). Modulation of encoding and retrieval by recollection and familiarity: mapping the medial temporal lobe networks. *NeuroImage*, *58*, 1131–1138.

Deco, G., & Corbetta, M. (2011). The dynamical balance of the brain at rest. *Neuroscientist*, *17*, 107–123.

DeMaster, D., Pathman, T., Lee, J. K., & Ghetti, S. (2014). Structural development of the hippocampus and episodic memory: developmental differences along the anterior/posterior axis. *Cerebral Cortex*, *24*, 3036–3045.

D'Esposito, M., Zarahn, E., Aguirre, G. K., & Rypma, B. (1999). The effect of normal aging on the coupling of neural activity to the bold hemodynamic response. *NeuroImage*, *10*, 6–14.

D'Esposito, M., Deouell, L. Y., & Gazzaley, A. (2003). Alterations in the BOLD fMRI signal with ageing and disease: a challenge for neuroimaging. *Nature Reviews. Neuroscience*, *4*, 863–872.

Devonshire, I. M., Papadakis, N. G., Port, M., Berwick, J., Kennerly, A. J., Mayhew, J. E. W., & Overton, P. G. (2012). Neurovascular coupling is brain region-dependent. *NeuroImage*, *59*, 1997–2006.

Di Nardo, P. A., Brown, T. A., & Barlow, D. H. (1994). Anxiety Disorders Interview Schedule for DSM-IV—Lifetime Version (ADIS-IV-L). Psychological Corporation, San Antonio, TX.

Dielman, T. E. (2005). Least absolute value regression: recent contributions. *Journal of Statistical Computation and Simulation*, *75*, 263–286.

Ding, S.-L., & Van Hoesen, G. W. (2015). Organization and detailed parcellation of human hippocampal head and body regions based on a combined analysis of cyto- and chemoarchitecture. *Journal of Comparative Neurology*, *523*, 2233–2253.

Dolcos, F., LaBar, K. S., & Cabeza, R. (2004). Interaction between the amygdala and the medial temporal lobe memory system predicts better memory for emotional events. *Neuron*, *42*, 855–863.

Doty, R. L. (2012). Olfaction in Parkinson's disease and related disorders. *Neurobiology of Disease*, *46*, 527–552.

Drton, M., & Perlman, M. D. (2004). Model selection for Gaussian concentration graphs. *Biometrika*, *91*, 591–602.

Du, Y., Allen, E. A., He, H., Sui, J., Wu, L., & Calhoun, V. D. (2016). Artifact removal in the context of group ICA: A comparison of single-subject and group approaches. *Human Brain Mapping*, *37*, 1005–1025.

Du, Y., & Fan, Y. (2013). Group information guided ICA for fMRI data analysis. *NeuroImage*, *69*, 157–197.

Du, Y., Lin, D., Yu, Q., Sui, J., Chen, J., Rachakonda, S., Adali, T., & Calhoun, V. D. (2017). Comparison of IVA and GIG-ICA in brain functional network estimation using fMRI data. *Frontiers in Neuroscience*, *11*, 267.

Duan, H., Wearne, S. L., Rocher, A. B., Macedo, A., Morrison, J. H., & Hof, P. R. (2003). Age-related dendritic and spine changes in corticocortically projecting neurons in macaque monkeys. *Cerebral Cortex, 13*, 950–961.

Duff, E. P., Makin, T., Cottaar, M., Smith, S. M., & Woolrich, M. W. (2018). Disambiguating brain functional connectivity. *NeuroImage*, *173*, 540–550.

Duncan, K., Ketz, N., Inati, S. J., & Davachi, L. (2012). Evidence for area CA1 as a match/ mismatch detector: a high-resolution fMRI study of the human hippocampus. *Hippocampus*, *22*, 389–398.

Duvarci, S., & Paré, D. (2014). Amygdala microcircuits controlling learned fear. *Neuron*, *82*, 966–980.

Duvernoy, H. M. (2005). The Human hippocampus: Functional Anatomy, Vascularization, and Serial Sections with MRI, third ed. Springer-Verlag, Berlin; New York, p. 232.

Eichenbaum, H. (2001). The hippocampus and declarative memory: cognitive mechanisms and neural codes. *Behavioural Brain Research*, *127*, 199–207.

Eichenbaum, H. (2017). On the integration of space, time, and memory. *Neuron*, *95*, 1007–1018.

Eichenbaum, H., & Cohen, N. J. (2014). Can we reconcile the declarative memory and spatial navigation views on hippocampal function? *Neuron*, *83*, 764–770.

Ekstrom, A. (2010). How and when the fMRI BOLD signal relates to underlying neural activity: the danger in dissociation. *Brain Research Reviews*, *62*, 233–244.

Ekstrom, A. D., Copara, M. S., Isham, E. A., Wang, W.-C., Yonelinas, A. P. (2011). Dissociable networks involved in spatial and temporal order source retrieval. *NeuroImage*, *56*, 1803–1813.

Eldridge, L. L., Engel, S. A., Zeineh, M. M., Bookheimer, S. Y., & Knowlton, B. J. (2005). A dissociation of encoding and retrieval processes in the human hippocampus. *Journal of Neuroscience*, *25*, 3280–3286.

Elliott, C. A., Gross, D. W., Wheatley, B. M., Beaulieu, C., & Sankar, T. (2016). Progressive contralateral hippocampal atrophy following surgery for medically refractory temporal lobe epilepsy. *Epilepsy Research*, *125*, 62–71.

Entis, J. J., Doerga, P., Barrett, L. F., & Dickerson, B. C. (2012). A reliable protocol for the manual segmentation of the human amygdala and its subregions using ultra-high resolution MRI. *Neuroimage*, *60*, 1226–1235.

Epskamp, S., & Fried, E. I. (2018). A tutorial on regularized partial correlation networks. *Psychological Methods*, *23*, 617–634.

Evensmoen, H. R., Lehn, H., Xu, J., Witter, M. P., Nadel, L., & Håberg, A. K. (2013). The anterior hippocampus supports a coarse, global environmental representation and the posterior hippocampus supports fine-grained, local environmental representations. *Journal of Cognitive Neuroscience*, 25, 1908–1925.

Fabiani, M. (2012). It was the best of times, it was the worst of times: a psychophysiologist's view of cognitive aging. *Psychophysiology*, *49*, 283–304.

Fabiani, M., Gordon, B. A., Maclin, E. L., Pearson, M. A., Brumback-Peltz, C. R., Low, K. A., McAuley, E., Sutton, B. P., Kramer, A. F., & Gratton, G. (2014). Neurovascular coupling in normal aging: a combined optical, ERP and fMRI study. *NeuroImage*, *85 Pt 1*, 592–607.

Fan, J., & Li, R. (2001). Variable Selection via Nonconcave Penalized Likelihood and its Oracle Properties. *Journal of the American Statistical Association*, *96*, 1348–1360.

Farkas, E., & Luiten, P. G. M. (2001). Cerebral microvascular pathology in aging and Alzheimer's disease. *Progress in Neurobiology*, *64*, 575–611.

Fera, F., Weickert, T. W., Goldberg, T. E., Tessitore, A., Hariri, A., Das, S., Lee, S., Zoltick, B., Meeter, M., Myers, C. E., Gluck, M. A., Weinberger, D. R., & Mattay, V. S. (2005). Neural mechanisms underlying probabilistic category learning in normal aging. *Journal of Neuroscience*, *25*, 11340–11348.

Fisher, R. A. (1921). On the 'probable error' of a coefficient of correlation deduced from a small sample. *Metron*, *1*, 3–32.

Fjell, A. M., Sneve, M. H., Grydeland, H., Storsve, A. B., de Lange, A.-M. G., Amlien, I. K., Røgeberg, O. J., & Walhovd, K. B. (2015). Functional connectivity change across multiple cortical networks relates to episodic memory changes in aging. *Neurobiology of Aging*, *36*, 3255–3268.

Fjell, A. M., Walhovd, K. B., Fennema-Notestine, C., McEvoy, L. K., Hagler, D. J., Holland, D., Brewer, J. B., & Dale, A. M. (2009a). One-year brain atrophy evident in healthy aging. *Journal of Neuroscience*, *29*, 15223–15231.

Fjell, A. M., Westlye, L. T., Amlien, I., Espeseth, T., Reinvang, I., Raz, N., Agartz, I., Salat, D. H., Greve, D. N., Fischl, B., Dale, A. M., & Walhovd, K. B. (2009b). High consistency of regional cortical thinning in aging across multiple samples. *Cerebral Cortex*, *19*, 2001–2012.

Formisano, E., & Goebel, R. (2003). Tracking cognitive processes with functional MRI mental chronometry. *Current Opinion in Neurobiology*, *13*, 174–181.

Freedman, D., & Lane, D. (1983). A Nonstochastic Interpretation of Reported Significance Levels. *Journal of Business & Economic Statistics*, *1*, 292.

Freese, J. L., & Amaral, D. G. (2009). Neuroanatomy of the primate amygdala. In: Whalen, P. J., Phelps, E. A. (Eds.), The Human Amygdala. New York, NY, Guilford Press, pp. 3–42.

Friedman, J., Hastie, T., & Tibshirani, R. (2008). Sparse inverse covariance estimation with the graphical lasso. *Biostatistics*, *9*, 432–441.

Frisoni, G. B., Ganzola, R., Canu, E., Rüb, U., Pizzini, F. B., Alessandrini, F., Zoccatelli, G., Beltramello, A., Caltagirone, C., & Thompson, P. M. (2008). Mapping local hippocampal changes in Alzheimer's disease and normal ageing with MRI at 3 Tesla. *Brain*, *131*, 3266–3276.

Friston, K. J., Fletcher, P., Josephs, O., Holmes, A., Rugg, M. D., & Turner, R. (1998). Event-related fMRI: characterizing differential responses. *NeuroImage*, *7*, 30–40.

Fröhlich, F. (2016). Network Neuroscience. Academic Press, London, San Diego, Cambridge, Oxford.

Frühholz, S., & Grandjean, D. (2013). Amygdala subregions differentially respond and rapidly adapt to threatening voices. *Cortex*, *49*, 1394–1403.

Galiano, A., Mengual, E., García de Eulate, R., Galdeano, I., Vidorreta, M., Recio, M., Riverol, M., Zubieta, J. L., & Fernández-Seara, M. A. (2019). Coupling of cerebral blood flow and functional connectivity is decreased in healthy aging. *Brain Imaging and Behavior*. http://doi.org/10.1007/s11682-019-00157-w

Gamer, M., Zurowski, B., & Büchel, C. (2010). Different amygdala subregions mediate valence-related and attentional effects of oxytocin in humans. *Proceedings of the National Academy of Sciences of the United States of America*, *107*, 9400–9405.

Gagnon, L., Sakadžić, S., Lesage, F., Musacchia, J. J., Lefebvre, J., Fang, Q., Yücel, M. A., Evans, K. C., Mandeville, E. T., Cohen-Adad, J., Polimeni, J. R., Yaseen, M. A., Lo, E. H., Greve, D. N., Buxton, R. B., Dale, A. M., Devor, A., & Boas, D. A. (2015). Quantifying the microvascular origin of BOLD-fMRI from first principles with two-photon microscopy and an oxygen-sensitive nanoprobe. *Journal of Neuroscience*, *35*, 3663–3675.

Galvin, J. E., Roe, C. M., Coats, M. A., & Morris, J. C. (2007). Patient's rating of cognitive ability: Using the AD8, a brief informant interview, as a self-rating tool to detect dementia. *Archives of Neurology*, *64*, 725–730.

Garcia-Amado, M., & Prensa, L. (2012). Stereological analysis of neuron, glial, and endothelial cell numbers in the human amygdaloid complex. *PLoS One*, *7*, e38692.

Geerligs, L., Renken, R. J., Saliasi, E., Maurits, N. M., & Lorist, M. M. (2015). A brain-wide study of age-related changes in functional connectivity. *Cerebral Cortex*, *25*, 1987–1999.

Glover, G.H. (1999). Deconvolution of impulse response in event-related BOLD fMRI. *NeuroImage*, *9*, 416–429.

Glover, G. H., Li, T. Q., & Ress, D. (2000). Image-based method for retrospective correction of physiological motion effects in fMRI: RETROICOR. *Magnetic Resonance in Medicine*, *44*, 162–167.

Good, C. D., Johnsrude, I. S., Ashburner, J., Henson, R. N., Friston, K. J., & Frackowiak, R. S. (2001). A voxel-based morphometric study of ageing in 465 normal adult human brains. *NeuroImage*, *14 Pt 1*, 21–36.

Gottfried, J. A., O'Doherty, J., & Dolan, R. J. (2002). Appetitive and aversive olfactory learning in humans studied using event-related functional magnetic resonance imaging. *Journal of Neuroscience*, *22*, 10829–10837.

Gold, J. J., Smith, C. N., Bayley, P. J., Shrager, Y., Brewer, J. B., Stark, C. E. L., Hopkins, R. O., & Squire, L. R. (2006). Item memory, source memory, and the medial temporal lobe: concordant findings from fMRI and memory-impaired patients. *Proceedings of the National Academy of Sciences of the United States of America*, 103, 9351–9356.

Gordon, E. M., Laumann, T. O., Adeyemo, B., & Petersen, S. E. (2017). Individual variability of the system-level organization of the human brain. *Cerebral Cortex*, *27*, 386–399.

Goubran, M., Rudko, D. A., Santyr, B., Gati, J., Szekeres, T., Peters, T. M., & Khan, A. R. (2013). In vivo normative atlas of the hippocampal subfields using multi-echo susceptibility imaging at 7 Tesla. *Human Brain Mapping*, *35*, 3588–3601.

Goutte, C., Nielsen, F. A., & Hansen, L. K. (2000). Modeling the haemodynamic response in fMRI using smooth FIR filters. *IEEE Transactions on Medical Imaging*, *19*, 1188–1201.

Grady, C. L. (2008). Cognitive neuroscience of aging. *Annals of the New York Academy of Sciences*, *1124*, 127–144.

Grady, C. L., Springer, M. V., Hongwanishkul, D., McIntosh, A. R., & Winocur, G. (2006). Age-related changes in brain activity across the adult lifespan. *Journal of Cognitive Neuroscience*, *18*, 227–241.

Grady, C. L. (2012). The cognitive neuroscience of ageing. *Nature Reviews. Neuroscience*, *13*, 491–505.

Grady, C. L., Sarraf, S., Saverino, C., & Campbell, K. (2016). Age differences in the functional interactions among the default, frontoparietal control, and dorsal attention networks. *Neurobiology of Aging*, *41*, 159–172.

Grady, C. L., Maisog, J. M., Horwitz, B., Ungerleider, L. G., Mentis, M. J., Salerno, J. A., Pietrini, P., Wagner, E., & Haxby, J. V. (1994). Age-related changes in cortical blood flow activation during visual processing of faces and location. *Journal of Neuroscience*, *14 Pt 2*, 1450–1462.

Grant, M. M., Wood, K., Sreenivasan, K., Wheelock, M., White, D., Thomas, J., Knight, D. C., & Deshpande, G. (2015). Influence of early life stress on intra- and extra-amygdaloid causal connectivity. *Neuropsychopharmacology*, *40*, 1782–1793.

Greicius, M. D., Krasnow, B., Boyett-Anderson, J. M., Eliez, S., Schatzberg, A. F., Reiss, A. L., & Menon, V. (2003). Regional analysis of hippocampal activation during memory encoding and retrieval: fMRI study. *Hippocampus*, *13*, 164–174.

Greve, D. N., & Fischl, B. (2009). Accurate and robust brain image alignment using boundary-based registration. *NeuroImage*, *48*, 63–72.

Griffanti, L., Douaud, G., Bijsterbosch, J., Evangelisti, S., Alfaro-Almagro, F., Glasser, M. F., Fuff, E. P., Fitzgibbon, S., Westphal, R., Carone, D., Beckmann, C. F., & Smith, S. M. (2017). Hand classification of fMRI ICA noise components. *NeuroImage*, *154*, 188–205.

Griffanti, L., Salimi-Khorshidi, G., Beckmann, C. F., Auerbach, E. J., Douaud, G., Sexton, C. E., Zsoldos, E., Ebmeier, K. P., Filippini, N., Mackay, C. E., Moeller, S., Xu, J., Yacoub, E., Baselli, G., Ugurbil, K., Miller, K. L., & Smith, S. M. (2014). ICA-based artefact removal and accelerated fMRI acquisition for improved resting state network imaging. *NeuroImage*, *95*(C), 232–247.

Griswold, M. A., Jakob, P. M., Heidemann, R. M., Nittka, M., Jellus, V., Wang, J., Kiefer, B., & Haase, A. (2002). Generalized autocalibrating partially parallel acquisitions (GRAPPA). *Magnetic Resonance in Medicine*, *47*, 1202–1210.

Gutchess, A. H., Welsh, R. C., Hedden, T., Bangert, A., Minear, M., Liu, L. L., & Park, D. C. (2005). Aging and the neural correlates of successful picture encoding: frontal activations compensate for decreased medial-temporal activity. *Journal of Cognitive Neuroscience*, *17*, 84–96.

Hachinski, V. C., Iliff, L. D., Zilhka, E., Du Boulay, G. H., McAllister, V. L., Marshall, J., Russel, R. W., & Symon, L. (1975). Cerebral blood flow in dementia. *Archives of Neurology*, *32*, 632–637.

Hafkemeijer, A., van der Grond, J., & Rombouts, S. A. (2012). Imaging the default mode network in aging and dementia. *Biochimica et Biophysica Acta, 1822*, 431–441.

Hampson, M., Tokoglu, F., Shen, X., Scheinost, D., Papademetris, X., & Constable, R. T. (2012). Intrinsic brain connectivity related to age in young and middle aged adults. *PloS One*, *7*, e44067.

Han, L., Savalia, N. K., Chan, M. Y., Agres, P. F., Nair, A. S., & Wig, G. S. (2018). Functional parcellation of the cerebral cortex across the human adult lifespan. *Cerebral Cortex*, *28*, 4403–4423.

Handwerker, D. A., Gazzaley, A., Inglis, B. A., & D'Esposito, M. (2007). Reducing vascular variability of fMRI data across aging populations using a breathholding task. *Human Brain Mapping*, *28*, 846–859.

Handwerker, D. A., Ollinger, J. M., & D'Esposito, M. (2004). Variation of BOLD hemodynamic responses across subjects and brain regions and their effects on statistical analyses. *NeuroImage*, *21*, 1639–1651.

Hanna-Pladdy, B., & Gajewski, B. (2012). Recent and past musical activity predicts cognitive aging variability: direct comparison with general lifestyle activities. *Frontiers in Human Neuroscience, 6*, 198.

Harmon-Jones, E., Gable, P. A., & Price, T. F. (2013). Does negative affect always narrow and positive affect always broaden the mind? Considering the influence of motivational intensity on cognitive scope. *Current Directions in Psychological Science*, *22*, 301–307.

Hasselmo, M. E., Schnell, E., & Barkai, E. (1995). Dynamics of learning and recall at excitatory recurrent synapses and cholinergic modulation in rat hippocampal region CA3. *Journal of Neuroscience*, *15*, 5249–5262.

Hayes, J. P., LaBar, K. S., McCarthy, G., Selgrade, E., Nasser, J., Dolcos, F., VISN 6 Mid-Atlantic MIRECC workgroup, & Morey, R. A. (2011). Reduced hippocampal and amygdala activity predicts memory distortions for trauma reminders in combat-related PTSD. *Journal of Psychiatric Research*, *45*, 660–669.

Hedden, T., & Gabrieli, J. D. E. (2004). Insights into the ageing mind: a view from cognitive neuroscience. *Nature Reviews. Neuroscience*, *5*, 87–96.

Heeger, D. J., & Ress, D. (2002). What does fMRI tell us about neuronal activity? *Nature Reviews. Neuroscience*, *3*, 142–151.

Henson, R. N. A., Price, C. J., Rugg, M. D., Turner, R., & Friston, K. J. (2002). Detecting latency differences in event-related BOLD responses: application to words versus nonwords and initial versus repeated face presentations. *NeuroImage*, *15*, 83–97.

Hesselmann, V., Zaro Weber, O., Wedekind, C., Krings, T., Schulte, O., Kugel, H., Krug, B., Klug, N., & Lackner, K. J. (2001). Age related signal decrease in functional magnetic resonance imaging during motor stimulation in humans. *Neuroscience Letters*, *308*, 141–144.

Hillman, E. M. C. (2014). Coupling mechanism and significance of the BOLD signal: a status report. *Annual Review of Neuroscience*, *37*, 161–181.

Himberg, J., Hyvärinen, A., & Esposito, F. (2004). Validating the independent components of neuroimaging time series via clustering and visualization. *NeuroImage*, *22*, 1214–1222.

Hirano, Y., Stefanovic, B., & Silva, A. C. (2011). Spatiotemporal evolution of the functional magnetic resonance imaging response to ultrashort stimuli. *Journal of Neuroscience*, *31*, 1440–1447.

Hirsiger, S., Koppelmans, V., Mérillat, S., Liem, F., Erdeniz, B., Seidler, R. D., & Jäncke, L. (2016). Structural and functional connectivity in healthy aging: Associations for cognition and motor behavior. *Human Brain Mapping*, *37*, 855–867.

Hodgetts, C. J., Voets, N. L., Thomas, A. G., Clare, S., Lawrence, A. D., & Graham, K. S. (2017). Ultra-high-field fMRI reveals a role for the subiculum in scene perceptual discrimination. *Journal of Neuroscience*, *37*, 3150–3159.

Hoelzle, J. B., Nelson, N. W., & Smith, C. A. (2011). Comparison of Wechsler Memory Scale-Fourth Edition (WMS-IV) and Third Edition (WMS-III) dimensional structures: improved ability to evaluate auditory and visual constructs. *Journal of Clinical and Experimental Neuropsychology*, *33*, 283–291.

Holdnack, J. A., Zhou, X., Larrabee, G. J., Millis, S. R., & Salthouse, T. A. (2011). Confirmatory factor analysis of the WAIS-IV/WMS-IV. *Assessment*, *18*, 178–191.

Horecka, K. M., Dulas, M. R., Schwarb, H., Lucas, H. D., Duff, M., & Cohen, N. J. (2018). Reconstructing relational information. *Hippocampus*, *28*, 164–177.

Hoscheidt, S. M., Nadel, L., Payne, J., & Ryan, L. (2010). Hippocampal activation during retrieval of spatial context from episodic and semantic memory. *Behavioural Brain Research*, *212*, 121–132.

Houx, P. J., & Jolles, J. (1993). Age-related decline of psychomotor speed: effects of age, brain health, sex, and education. *Perceptual and Motor Skills*, *76*, 195–211.

Hrybouski, S., Aghamohammadi-Sereshki, A., Madan, C. R., Shafer, A. T., Baron, C. A., Seres, P., Beaulieu, C., Olsen, F., & Malykhin, N. V. (2016). Amygdala subnuclei response and connectivity during emotional processing. *NeuroImage*, *133*, 98–110.

Hrybouski, S., MacGillivray, M., Huang, Y., Madan, C. R., Carter, R., Seres, P., & Malykhin, N. V. (2019). Involvement of hippocampal subfields and anterior-posterior subregions in encoding and retrieval of item, spatial, and associative memories: Longitudinal versus transverse axis. *NeuroImage*, *191*, 568–586.

Huang, Y., Coupland, N. J., Lebel, R. M., Carter, R., Seres, P., Wilman, A. H., & Malykhin, N. V. (2013). Structural changes in hippocampal subfields in major depressive disorder: a high-field magnetic resonance imaging study. *Biological Psychiatry*, *74*, 62–68.

Huang, C.-C., Hsieh, W.-J., Lee, P.-L., Peng, L.-N., Liu, L.-K., Lee, W.-J., Huang, J.-K., Chen, L.-K., & Lin, C.-P. (2015). Age-related changes in resting-state networks of a large sample size of healthy elderly. *CNS Neuroscience & Therapeutics*, *21*, 817–825.

Hughes, C. P., Berg, L., Danziger, W. L., Coben, L. A., & Martin, R. L. (1982). A new clinical scale for the staging of dementia. *British Journal of Psychiatry*, *140*, 566–572.

Hutchinson, S., Kobayashi, M., Horkan, C. M., Pascual-Leone, A., Alexander, M. P., & Schlaug, G. (2002). Age-related differences in movement representation. *NeuroImage*, *17*, 1720– 1728.

Hutchison, J. L., Lu, H., & Rypma, B. (2013). Neural mechanisms of age-related slowing: the $\Delta CBF/\Delta CMRO_2$ ratio mediates age-differences in BOLD signal and human performance. *Cerebral Cortex*, *23*, 2337–2346.

Hutton, C., Josephs, O., Stadler, J., Featherstone, E., Reid, A., Speck, O., Bernarding, J., & Weiskopf, N. (2011). The impact of physiological noise correction on fMRI at 7 T. *NeuroImage*, *57*, 101–112.

Iglesias, J. E., Augustinack, J. C., Nguyen, K., Player, C. M., Player, A., Wright, M., Roy, N., Frosch, M. P., McKee, A. C., Wald, L. L., Fischl, B., & Leemput, K. V. (2015). A computational atlas of the hippocampal formation using ex vivo, ultra-high resolution MRI: application to adaptive segmentation of in vivo MRI. *NeuroImage*, *115*, 117–137.

Janak, P. H., & Tye, K. M. (2015). From circuits to behaviour in the amygdala. *Nature*, *517*, 284–292.

Jenkinson, M., Bannister, P., Brady, M., & Smith, S. (2002). Improved optimization for the robust and accurate linear registration and motion correction of brain images. *NeuroImage*, *17*, 825–841.

Jeon, T., Mishra, V., Uh, J., Weiner, M., Hatanpaa, K. J., White III, C. L., Zhao, Y. D., Lu, H, Diaz-Arrastia, R., & Huang, H. (2012). Regional changes of cortical mean diffusivities with aging after correction of partial volume effects. *NeuroImage, 62*, 1705-1716.

Johnston, J. B. (1923). Further contributions to the study of the evolution of the fore-brain. *Journal of Comparative Neurology*, *35*, 271–482.

Jones, M. W., & McHugh, T. J. (2011). Updating hippocampal representations: CA2 joins the circuit. *Trends in Neurosciences*, *34*, 526–535.

Kalin, N. H., Shelton, S. E., & Davidson, R. J. (2004). The role of the central nucleus of the amygdala in mediating fear and anxiety in the primate. *Journal of Neuroscience*, *24*, 5506–5515.

Kannurpatti, S. S., Motes, M. A., Rypma, B., & Biswal, B. B. (2011). Increasing measurement accuracy of age-related BOLD signal change: minimizing vascular contributions by resting-state-fluctuation-of-amplitude scaling. *Human Brain Mapping*, *32*, 1125–1140.

Kapp, B. S., Supple, W. F., & Whalen, P. J. (1994). Effects of electrical stimulation of the amygdaloid central nucleus on neocortical arousal in the rabbit. *Behavioral Neuroscience*, *108*, 81–93.

Kauranen, K., & Vanharanta, H. (1996). Influences of aging, gender, and handedness on motor performance of upper and lower extremities. *Perceptual and Motor Skills*, *82*, 515–525.

Keller, J. B., Hedden, T., Thompson, T. W., Anteraper, S. A., Gabrieli, J. D. E., & Whitfield-Gabrieli, S. (2015). Resting-state anticorrelations between medial and lateral prefrontal cortex: association with working memory, aging, and individual differences. *Cortex*, *64*, 271– 280.

Kensinger, E. A. (2009). Remembering the details: effects of emotion. *Emotion Review*, *1*, 99–113.

Kensinger, E. A., & Corkin, S. (2004). Two routes to emotional memory: distinct neural processes for valence and arousal. *Proceedings of the National Academy of Sciences of the United States of America*, *101*, 3310–3315.

Kessels, R. P. C., Jaap Kappelle, L., de Haan, E. H. F., & Postma, A. (2002). Lateralization of spatial-memory processes: evidence on spatial span, maze learning, and memory for object locations. *Neuropsychologia*, *40*, 1465–1473.

Kety, S. S. (1956). Human cerebral blood flow and oxygen consumption as related to aging. *Journal of Chronic Diseases*, *3*, 478–486.

Kim, H. (2015). Encoding and retrieval along the long axis of the hippocampus and their relationships with dorsal attention and default mode networks: the HERNET model. *Hippocampus*, *25*, 500–510.

Kim, S.-G. (2018). Biophysics of BOLD fMRI investigated with animal models. *Journal of Magnetic Resonance*, *292*, 82–89.

Kim, J.-H., Lee, Y.-S., Lee, J.-J., Song, H.-J., Yoo, D.-S., Lee, H. J., Kim, H.-J., & Chang, Y. (2010). Functional magnetic resonance imaging reveals age-related alterations to motor networks in weighted elbow flexion-extension movement. *Neurological Research*, *32*, 995–1001.

Kim, S. G., & Ogawa, S. (2012). Biophysical and physiological origins of blood oxygenation level-dependent fMRI signals. *Journal of Cerebral Blood Flow and Metabolism*, *32*, 1188–1206.

Kim, H., Somerville, L. H., Johnstone, T., Alexander, A. L., & Whalen, P. J. (2003). Inverse amygdala and medial prefrontal cortex responses to surprised faces. *Neuroreport*, *14*, 2317–2322.

Kim, H., Somerville, L. H., Johnstone, T., Polis, S., Alexander, A. L., Shin, L. M., & Whalen, P. J. (2004). Contextual modulation of amygdala responsivity to surprised faces. *Journal of Cognitive Neuroscience*, *16*, 1730–1745.

Klein, A., Andersson, J., Ardekani, B. A., Ashburner, J., Avants, B., Chiang, M.-C., Christensen, G. E., Collins, D. L., Gee, J., Hellier, P., Song, J. H., Jenkinson, M., Lepage, C., Rueckert, D., Thompson, P., Vercauteren, T., Woods, R. P., Mann, J. J., & Parsey, R. V. (2009). Evaluation of 14 nonlinear deformation algorithms applied to human brain MRI registration. *NeuroImage*, *46*, 786–802.

Klumpers, F., Morgan, B., Terburg, D., Stein, D. J., & van Honk, J. (2014). Impaired acquisition of classically conditioned fear-potentiated startle reflexes in humans with focal bilateral basolateral amygdala damage. *Social Cognitive and Affective Neuroscience*, *10*, 1161–1168.

Koch, W., Teipel, S., Mueller, S., Buerger, K., Bokde, A. L. W., Hampel, H., Coates, U., Reiser, M., & Meindl, T. (2010). Effects of aging on default mode network activity in resting state fMRI: does the method of analysis matter? *NeuroImage*, *51*, 280–287.

Konkel, A., Warren, D. E., Duff, M. C., Tranel, D. N., & Cohen, N. J. (2008). Hippocampal amnesia impairs all manner of relational memory. *Frontiers in Human Neuroscience*, *2*, 15.

Kumaran, D., & Maguire, E. A. (2005). The human hippocampus: cognitive maps or relational memory? *Journal of Neuroscience*, *25*, 7254–7259.

Kyle, C. T., Smuda, D. N., Hassan, A. S., & Ekstrom, A. D. (2015). Roles of human hippocampal subfields in retrieval of spatial and temporal context. *Behavioural Brain Research*, *278*, 549–558.

La Joie, R., Fouquet, M., Mézenge, F., Landeau, B., Villain, N., Mevel, K., Pélerin, A., Eustache, F., Desgranges, B., & Chételat, G. (2010). Differential effect of age on hippocampal subfields assessed using a new high-resolution 3T MR sequence. *NeuroImage*, *53*, 506–514.

LaBar, K. S., Gatenby, J. C., Gore, J. C., LeDoux, J. E., & Phelps, E. A. (1998). Human amygdala activation during conditioned fear acquisition and extinction: a mixed-trial fMRI study. *Neuron*, *20*, 937–945.

Lacy, J. W., Yassa, M. A., Stark, S. M., Muftuler, L. T., & Stark, C. E. L. (2011). Distinct pattern separation related transfer functions in human CA3/dentate and CA1 revealed using high-resolution fMRI and variable mnemonic similarity. *Learning & Memory*, *18*, 15–18.

Lang, P. J., Bradley, M. M., & Cuthbert, B. N. (1998). Emotion, motivation, and anxiety: brain mechanisms and psychophysiology. *Biological Psychiatry*, *44*, 1248–1263.

Lang, P. J., Bradley, M. M., & Cuthbert, B. N. (2008). International Affective Picture System (IAPS): affective ratings of pictures and instruction manual. Technical Report A-8. Center for the Study of Emotion and Attention at the University of Florida, Gainsville, FL.

Laumann, T. O., Gordon, E. M., Adeyemo, B., Snyder, A. Z., Joo, S. J., Chen, M.-Y., Gilmore, A. W., McDermott, K. B., Nelson, S. M., Dosenbach, N. U. F., Schlaggar, B. L., Mumford, J. A., Poldrack, R. A., & Petersen, S. E. (2015). Functional system and areal organization of a highly sampled individual human brain. *Neuron*, *87*, 657–670.

Lawrence, K. D., & Shier, D. R. (1981). A comparison of least squares and least absolute deviation regression models for estimating Weibull parameters. *Communications in Statistics - Simulation and Computation*, *10*, 315–326.

Leal, S. L., Noche, J. A., Murray, E. A., & Yassa, M. A. (2017). Disruption of amygdala-entorhinal-hippocampal network in late-life depression. *Hippocampus*, *27*, 464–476.

Lebel, C., Gee, M., Camiciolo, R., Wieler, M., Martin, W., & Beaulieu, C. (2012). Diffusion tensor imaging of white matter tract evolution over the lifespan. *NeuroImage, 60*, 340-352.

LeDoux, J. E. (2000). Emotion circuits in the brain. *Annual Review of Neuroscience*, *23*, 155–184.

LeDoux, J. E. (2012). Rethinking the emotional brain. *Neuron*, *73*, 653–676.

LeDoux, J. E. (2014). Coming to terms with fear. *Proceedings of the National Academy of Sciences of the United States of America*, *111*, 2871–2878.

LeDoux, J. E. (2007). The amygdala. *Current Biology*, *17*, R868–R874.

LeDoux, J. E., & Schiller, D. (2009). The human amygdala: insights from other animals. In: Whalen, P. J., Phelps, E. A. (Eds.), The Human Amygdala. New York, NY, Guilford Press, pp. 43–60.

Lee, A. C. H., Barense, M. D., & Graham, K. S. (2005). The contribution of the human medial temporal lobe to perception: bridging the gap between animal and human studies. *Quaterly Journal of Experimental Psychology. B, Comparative and Physiological Psychology*, *58*, 300–325.

Leong, R. L. F., Lo, J. C., Sim, S. K. Y., Zheng, H., Tandi, J., Zhou, J., & Chee, M. W. L. (2017). Longitudinal brain structure and cognitive changes over 8 years in an East Asian cohort. *NeuroImage*, *147*, 852–860.

Lepage, M., Habib, R., & Tulving, E. (1998). Hippocampal PET activations of memory encoding and retrieval: the HIPER model. *Hippocampus*, *8*, 313–322.

Levine, B. K., Beason-Held, L. L., Purpura, K. P., Aronchick, D. M., Optican, L. M., Alexander, G. E., Horwitz, B., Rapoport, S. I., & Schapiro, M. B. (2000). Age-related differences in visual perception: a PET study. *Neurobiology of Aging*, *21*, 577–584.

Li, H.-J., Hou, X.-H., Liu, H.-H., Yue, C.-L., Lu, G.-M., & Zuo, X.-N. (2015). Putting age-related task activation into large-scale brain networks: a meta-analysis of 114 fMRI studies on healthy aging. *Neuroscience and Biobehavioral Reviews*, *57*, 156–174.

Liao, X., Cao, M., Xia, M., & He, Y. (2017). Individual differences and time-varying features of modular brain architecture. *NeuroImage*, *152*, 94–107.

Lin, A.-L., Fox, P. T., Hardies, J., Duong, T. Q., & Gao, J.-H. (2010). Nonlinear coupling between cerebral blood flow, oxygen consumption, and ATP production in human visual cortex. *Proceedings of the National Academy of Sciences of the United States of America*, *107*, 8446–8451.

Lindberg, O., Walterfang, M., Looi, J. C. L., Malykhin, N., Östberg, P., Zandbelt, B., Styner, M., Paniagua, B., Velakoulis, D., Örndahl, E., & Wahlund, L.-O. (2012). Hippocampal shape analysis in Alzheimer's disease and frontotemporal lobar degeneration subtypes. *Journal of Alzheimer's Disease*, *30*, 355–365.

Lindquist, M. A., Meng Loh, J., Atlas, L. Y., & Wager, T. D. (2009). Modeling the hemodynamic response function in fMRI: efficiency, bias and mis-modeling. *NeuroImage*, *45*, S187–S198.

Lindquist, M. A., & Wager, T. D. (2007). Validity and power in hemodynamic response modeling: a comparison study and a new approach. *Human Brain Mapping*, *28*, 764–784.

Lisman, J. E., & Grace, A. A. (2005). The hippocampal-VTA loop: controlling the entry of information into long-term memory. *Neuron, 46*, 703–713.

Lisman, J., Buzsáki, G., Eichenbaum, H., Nadel, L., Ranganath, C., & Redish, A. D. (2017). Viewpoints: how the hippocampus contributes to memory, navigation and cognition. *Nature Neuroscience*, *20*, 1434–1447.

Liu, P., Hebrank, A. C., Rodrigue, K. M., Kennedy, K. M., Section, J., Park, D. C., & Lu, H. (2013). Age-related differences in memory-encoding fMRI responses after accounting for decline in vascular reactivity. *NeuroImage*, *78*, 415–425.

Logan, J. M., Sanders, A. L., Snyder, A. Z., Morris, J. C., & Buckner, R. L. (2002). Under-recruitment and nonselective recruitment: dissociable neural mechanisms associated with aging. *Neuron*, *33*, 827–840.

Logothetis, N. K. (2008). What we can do and what we cannot do with fMRI. *Nature*, *453*, 869–878.

Logothetis, N. K., & Wandell, B. A. (2004). Interpreting the BOLD signal. *Annual Review of Physiology*, *66*, 735–769.

Logothetis, N. K., Pauls, J., Augath, M., Trinath, T., & Oeltermann, A. (2001). Neurophysiological investigation of the basis of the fMRI signal. *Nature*, *412*, 150–157.

Lu, H., Xu, F., Rodrigue, K. M., Kennedy, K. M., Cheng, Y., Flicker, B., Hebrank, A. C., Uh, J., & Park, D. C. (2011). Alterations in cerebral metabolic rate and blood supply across the adult lifespan. *Cerebral Cortex*, *21*, 1426–1434.

Lustig, C., Snyder, A. Z., Bhakta, M., O'Brien, K. C., McAvoy, M., Raichle, M. E., Morris, J. C., & Buckner, R. L. (2003). Functional deactivations: change with age and dementia of the Alzheimer type. *Proceedings of the National Academy of Sciences*, *100*, 14504–14509.

Macedo, C. E., Martinez, R. C. R., Albrechet-Souza, L., Molina, V. A., & Brandão, M. L. (2007). 5-HT_2- and D_1-mechanisms of the basolateral nucleus of the amygdala enhance conditioned fear and impair unconditioned fear. *Behavioural Brain Research*, *177*, 100–108.

Madan, C. R. (2013). Toward a common theory for learning from reward, affect, and motivation: the SIMON framework. *Frontiers in Systems Neuroscience*, *7*, 59.

Madan, C. R. (2018). Age differences in head motion and estimates of cortical morphology. *PeerJ*, *6*, e5176.

Madan, C. R., Fujiwara, E., Caplan, J. B., & Sommer, T. (2017). Emotional arousal impairs association-memory: roles of amygdala and hippocampus. *NeuroImage*, *156*, 14–28.

Madden, D. J., Turkington, T. G., Coleman, R. E., Provenzale, J. M., DeGrado, T. R., & Hoffman, J. M. (1996). Adult age differences in regional cerebral blood flow during visual world identification: evidence from $H_2{}^{15}O$ PET. *NeuroImage*, *3*, 127–142.

Maguire, E. A., Gadian, D. G., Johnsrude, I. S., Good, C. D., Ashburner, J., Frackowiak, R. S., & Frith, C. D. (2000). Navigation-related structural change in the hippocampi of taxi drivers. *Proceedings of the National Academy of Sciences of the United States of America*, *97*, 4398–4403.

Maguire, E. A., Spiers, H. J., Good, C. D., Hartley, T., Frackowiak, R. S. J., & Burgess, N. (2003). Navigation expertise and the human hippocampus: a structural brain imaging analysis. *Hippocampus*, *13*, 250–259.

Mai, J. K., Assheuer, J., & Paxinos, G. (1997). Atlas of the Human Brain. Academic Press, San Diego, CA.

Mai, J. K., Paxinos, G., & Voss, T. (2008). Atlas of the Human Brain. Third edition. Academic Press, New York, London.

Maller, J. J., Daskalakis, Z. J., & Fitzgerald, P. B. (2007). Hippocampal volumetrics in depression: the importance of the posterior tail. *Hippocampus*, *17*, 1023–1027.

Maller, J. J., Daskalakis, Z. J., Thomson, R. H. S., Daigle, M., Barr, M. S., & Fitzgerald, P. B. (2012). Hippocampal volumetrics in treatment-resistant depression and schizophrenia: the devil's in de-tail. *Hippocampus*, 22, 9–16.

Malykhin, N. V., Bouchard, T. P., Ogilvie, C. J., Coupland, N. J., Seres, P., & Camicioli, R. (2007). Three-dimensional volumetric analysis and reconstruction of amygdala and hippocampal head, body and tail. *Psychiatry Research*, *155*, 155–165.

Malykhin, N. V., Lebel, R. M., Coupland, N. J., Wilman, A. H., & Carter, R. (2010). In vivo quantification of hippocampal subfields using 4.7 T fast spin echo imaging. *NeuroImage*, *49*, 1224–1230.

Malykhin, N. V., Huang, Y., Hrybouski, S., & Olsen, F. (2017). Differential vulnerability of hippocampal subfields and anteroposterior hippocampal subregions in healthy cognitive aging. *Neurobiology of Aging*, *59*, 121–134.

Martin, C., Martindale, J., Berwick, J., & Mayhew, J. (2006). Investigating neural-hemodynamic coupling and the hemodynamic response function in the awake rat. *NeuroImage*, *32*, 33–48.

Martin, P. K., & Schroeder, R. W. (2014). Chance performance and floor effects: threats to the validity of the Wechsler Memory Scale–fourth edition designs subtest. *Archives of Clinical Neuropsychology*, *29*, 385–390.

Mattay, V. S., Fera, F., Tessitore, A., Hariri, A. R., Das, S., Callicott, J. H., & Weinberger, D. R. (2002). Neurophysiological correlates of age-related changes in human motor function. *Neurology*, *58*, 630–635.

McDonald, C. R., McEvoy, L. K., Gharapetian, L., Fennema-Notestine, C., Hagler, D. J., Holland, D., Koyama, A., Brewer, J. B., & Dale, A. M. (2009). Regional rates of neocortical atrophy from normal aging to early Alzheimer disease. *Neurology*, *73*, 457–465.

Meeter, M., Murre, J. M. J., & Talamini, L. M. (2004). Mode shifting between storage and recall based on novelty detection in oscillating hippocampal circuits. *Hippocampus*, *14*, 722–741.

Mehagnoul-Schipper, D. J., van der Kallen, B. F. W., Colier, W. N. J. M., van der Sluijs, M. C., van Erning, L. J. T. O., Thijssen, H. O. M., Oeseburg, B., Hoefnagels, W. H. L., & Jansen, R. W. M. M. (2002). Simultaneous measurements of cerebral oxygenation changes during brain activation by near-infrared spectroscopy and functional magnetic resonance imaging in healthy young and elderly subjects. *Human Brain Mapping*, *16*, 14–23.

Meier, T. B., Desphande, A. S., Vergun, S., Nair, V. A., Song, J., Biswal, B. B., Meyerand, M. E., Birn, R. M., & Prabhakaran, V. (2012). Support vector machine classification and characterization of age-related reorganization of functional brain networks. *NeuroImage*, *60*, 601–613.

Melamed, E., Lavy, S., Bentin, S., Cooper, G., & Rinot, Y. (1980). Reduction in regional cerebral blood flow during normal aging in man. *Stroke*, *11*, 31–35.

Meunier, D., Achard, S., Morcom, A., & Bullmore, E. (2009). Age-related changes in modular organization of human brain functional networks. *NeuroImage*, *44*, 715–723.

Michielse, S., Coupland, N., Camicioli, R., Carter, R., Seres, P., Sabino, J., & Malykhin, N. V.. (2010). Selective effects of aging on brain white matter microstructure: a diffusion tensor imaging tractography study. *NeuroImage*, 1190–1201.

Miller, S. L., Celone, K., DePeau, K., Diamond, E., Dickerson, B. C., Rentz, D., Pihlajamäki, M., & Sperling, R. A. (2008). Age-related memory impairment associated with loss of parietal deactivation but preserved hippocampal activation. *Proceedings of the National Academy of Sciences of the United States of America*, *105*, 2181–2186.

Mitra, P., & Bokil, H. (2008). *Observed Brain Dynamics*. New York: Oxford University Press.

Morris, J. S., Büchel, C., & Dolan, R. J. (2001). Parallel neural responses in amygdala subregions and sensory cortex during implicit fear conditioning. *NeuroImage*, *13*, 1044–1052.

Morris, J. S., deBois, M., & Dolan, R. J. (2002). Human amygdala responses to fearful eyes. *NeuroImage*, *17*, 214–222.

Morrison, J. H., & Baxter, M. G. (2012). The ageing cortical synapse: hallmarks and implications for cognitive decline. *Nature Reviews. Neuroscience*, *13*, 240–250.

Morrison, J. H., & Hof, P. R. (2007). Life and death of neurons in the aging cerebral cortex. *International Review of Neurobiology, 81*, 41-57.

Moscovitch, M., Rosenbaum, R. S., Gilboa, A., Addis, D. R., Westmacott, R., Grady, C., McAndrews, M. P., Levine, B., Black, S., Winocur, G., & Nadel, L. (2005). Functional neuroanatomy of remote episodic, semantic and spatial memory: a unified account based on multiple trace theory. *Journal of Anatomy*, *207*, 35–66.

Moscovitch, M., Cabeza, R., Winocur, G., & Nadel, L. (2016). Episodic memory and beyond: the hippocampus and neocortex in transformation. *Annual Review of Psychology*, *67*, 105–134.

Mowinckel, A. M., Espeseth, T., & Westlye, L. T. (2012). Network-specific effects of age and in-scanner subject motion: a resting-state fMRI study of 238 healthy adults. *NeuroImage*, *63*, 1364–1373.

Mueller, S., Wang, D., Fox, M. D., Yeo, B. T. T., Sepulcre, J., Sabuncu, M. R., Shafee, R., Lu, J., & Liu, H. (2013). Individual variability in functional connectivity architecture of the human brain. *Neuron*, *77*, 586–595.

Murray, E. A., Bussey, T. J., & Saksida, L. M. (2007). Visual perception and memory: a new view of medial temporal lobe function in primates and rodents. *Annual Review of Neuroscience*, *30*, 99–122.

Murty, V. P., Ritchey, M., Adcock, R. A., & LaBar, K. S. (2010). fMRI studies of successful emotional memory encoding: a quantitative meta-analysis. *Neuropsychologia*, *48*, 3459–3469.

Namburi, P., Beyeler, A., Yorozu, S., Calhoon, G. G., Halbert, S. A., Wichmann, R., Holden, S. S., Mertens, K. L., Felix-Ortiz, A. C., Wickersham, I. R., Gray, J. M., & Tye, K. M. (2015). A circuit mechanism for differentiating positive and negative associations. *Nature*, *520*, 675–678.

Nadel, L., Hupbach, A., Gomez, R., & Newman-Smith, K. (2012). Memory formation, consolidation and transformation. *Neuroscience and Biobehavioral Reviews*, *36*, 1640–1645.

Nasreddine, Z. S., Phillips, N. A., Bédirian, V., Charbonneau, S., Whitehead, V., Collin, I., Cummings, J. L., & Chertkow, H. (2005). The Montreal cognitive assessment, MoCA: A brief screening tool for mild cognitive impairment. *Journal of the American Geriatrics Society*, *53*, 695–699.

Nauer, R. K., Whiteman, A. S., Dunne, M. F., Stern, C. E., & Schon, K. (2015). Hippocampal subfield and medial temporal cortical persistent activity during working memory reflects ongoing encoding. *Frontiers in Systems Neuroscience*, *9*, 30.

Nelder, J. A., & Mead, R. (1965). A simplex method for function minimization. *The Computer Journal*, *7*, 308–313.

Ng, K. K., Lo, J. C., Lim, J. K. W., Chee, M. W. L., & Zhou, J. (2016). Reduced functional segregation between the default mode network and the executive control network in healthy older adults: a longitudinal study. *NeuroImage*, *133*, 321–330.

Nishimoto, S., & Gallant, J. L. (2011). A three-dimensional spatiotemporal receptive field model explains responses of area MT neurons to naturalistic movies. *Journal of Neuroscience*, *31*, 14551–14564.

Norman, K. A., & O'Reilly, R. C. (2003). Modeling hippocampal and neocortical contributions to recognition memory: a complementary-learning-systems approach. *Psychological Review*, *110*, 611–646.

Ogawa, S., Lee, T. M., Kay, A. R., & Tank, D. W. (1990). Brain magnetic resonance imaging with contrast dependent on blood oxygenation. *Proceedings of the National Academy of Sciences of the United States of America*, *87*, 9868–9872.

Ogawa, S., Tank, D. W., Menon, R., Ellermann, J. M., Kim, S. G., Merkle, H., & Ugurbil, K. (1992). Intrinsic signal changes accompanying sensory stimulation: functional brain mapping with magnetic resonance imaging. *Proceedings of the National Academy of Sciences*, *89*, 5951–5955.

O'Keefe, J., & Nadel, L. (1978). The hippocampus as a Cognitive Map. Clarendon Press, Oxford.

Oldfield, R. C. (1971). The assessment and analysis of handedness: The Edinburgh inventory. *Neuropsychologia*, *9*, 97–113.

O'Mara, S. (2006). Controlling hippocampal output: the central role of subiculum in hippocampal information processing. *Behavioural Brain Research*, *174*, 304–312.

O'Neil, E. B., Newsome, R. N., Li, I. H. N., Thavabalasingam, S., Ito, R., & Lee, A. C. H. (2015). Examining the role of the human Hippocampus in approach-avoidance decision making using a novel conflict paradigm and multivariate functional magnetic resonance imaging. *Journal of Neuroscience*, 35, 15039–15049.

Onoda, K., Ishihara, M., & Yamaguchi, S. (2012). Decreased functional connectivity by aging is associated with cognitive decline. *Journal of Cognitive Neuroscience*, *24*, 2186–2198.

Onoda, K., & Yamaguchi, S. (2013). Small-worldness and modularity of the resting-state functional brain network decrease with aging. *Neuroscience Letters*, *556*, 104–108.

Olman, C. A., Davachi, L., & Inati, S. (2009). Distortion and signal loss in medial temporal lobe. *PLoS One*, *4*, e8160.

Otte, C., Gold, S. M., Penninx, B. W., Pariante, C. M., Etkin, A., Fava, M., Mohr, D. C., & Schatzberg, A. F. (2016). Major depressive disorder. *Nature Reviews. Disease Primers*, *2*, 16065.

Owen, A. M., Milner, B., Petrides, M., & Evans, A. C. (1996). A specific role for the right parahippocampal gyrus in the retrieval of object-location: a positron emission tomography study. *Journal of Cognitive Neuroscience*, *8*, 588–602.

Page, T. L., Einstein, M., Duan, H., He, Y., Flores, T., Rolshud, D., Erwin, J. M., Wearne, S. L., Morrison, J. H., & Hof, P. R. (2002). Morphological alterations in neurons forming corticortical projection in the neocortex of aged Patas monkeys. *Neuroscience Letters, 317*, 37–41.

Park, D. C., Polk, T. A., Hebrank, A. C., & Jenkins, L. J. (2010). Age differences in default mode activity on easy and difficult spatial judgment tasks. *Frontiers in Human Neuroscience*, *3*, 7

Park, D. C., Polk, T. A., Park, R., Minear, M., Savage, A., & Smith, M. R. (2004). Aging reduces neural specialization in ventral visual cortex. *Proceedings of the National Academy of Sciences*, *101*, 13091–13095.

Park, D. C., & Reuter-Lorenz, P. (2009). The adaptive brain: aging and neurocognitive scaffolding. *Annual Review of Psychology*, *60*, 173–196.

Park, D. C., Welsh, R. C., Marshuetz, C., Gutchess, A. H., Mikels, J., Polk, T. A., Noll, D. C., & Taylor S. F. (2003). Working memory for complex scenes: age differences in frontal and hippocampal activations. *Journal of Cognitive Neuroscience*, *15*, 1122–1134.

Peirce, J. W. (2007). PsychoPy–psychophysics software in Python. *Journal of Neuroscience Methods*, *162*, 8–13.

Peirce, J. W. (2009). Generating stimuli for neuroscience using PsychoPy. *Frontiers in Neuroinformatics*, *2*, 10.

Peng, S.-L., Dumas, J. A., Park, D. C., Liu, P., Filbey, F. M., McAdams, C. J., Pinkham, A. E., Adinoff, B., Zhang, R., & Lu, H. (2014). Age-related increase of resting metabolic rate in the human brain. *NeuroImage*, *98*, 176–183.

Pentkowski, N. S., Blanchard, D. C., Lever, C., Litvin, Y., Blanchard, R. J. (2006). Effects of lesions to the dorsal and ventral hippocampus on defensive behaviors in rats. *Eurorepan Journal of Neuroscience*, *23*, 2185–2196.

Perlbarg, V., Bellec, P., Anton, J.-L., Péléegrini-Issac, M., Doyon, J., & Benali, H. (2007). CORSICA: correction of structured noise in fMRI by automatic identification of ICA components. *Magnetic Resonance Imaging*, *25*, 35–46.

Pernet, C. R. (2014). Misconceptions in the use of the General Linear Model applied to functional MRI: a tutorial for junior neuro-imagers. *Frontiers in Neuroscience*, *8*, 1.

Pernet, C., Franceries, X., Basan, S., Cassol, E., Démonet, J. F., & Celsis, P. (2004). Anatomy and time course of discrimination and categorization process in vision: an fMRI study. *NeuroImage*, *22*, 1563–1577.

Persson, J., Lustig, C., Nelson, J. K., & Reuter-Lorenz, P. A. (2007). Age differences in deactivation - a link to cognitive control? *Journal of Cognitive Neuroscience*, *19*, 1021–1032.

Persson, J., Pudas, S., Nilsson, L.-G., & Nyberg, L. (2014). Longitudinal assessment of default-mode brain function in aging. *Neurobiology of Aging*, *35*, 2107–2117.

Peters, A., Morrison, J. H., Rosene, D. L., & Hyman, B. T. (1998). Are neurons lost from the primate cerebral cortex during normal aging? *Cerebral Cortex, 8*, 295–300.

Petersen, S. E., & Posner, M. I. (2012). The attention system of the human brain: 20 years after. *Neuroscience*, *35*, 73–89.

Power, J. D., Barnes, K. A., Snyder, A. Z., Schlaggar, B. L., & Petersen, S. E. (2012). Spurious but systematic correlations in functional connectivity MRI networks arise from subject motion. *NeuroImage*, *59*, 2142–2154.

Power, J. D., Cohen, A. L., Nelson, S. M., Wig, G. S., Barnes, K. A., Church, J. A., Vogel, A. C., Laumann, T. O., Miezin, F. M., Schlaggar, B. L., & Petersen, S. E. (2011). Functional network organization of the human brain. *Neuron*, *72*, 665–678.

Power, J. D., Silver, B. M., Silverman, M. R., Ajodan, E. L., Bos, D. J., & Jones, R. M. (2019). Customized head molds reduce motion during resting state fMRI scans. *NeuroImage*, *189*, 141–149.

Phelps, E. A., & LeDoux, J. E. (2005). Contributions of the amygdala to emotion processing: from animal models to human behavior. *Neuron*, *48*, 175–187.

Phelps, E. A., Delgado, M. R., Nearing, K. I., & LeDoux, J. E. (2004). Extinction learning in humans: the role of the amygdala and vmPFC. *Neuron*, *43*, 897–905.

Pitkänen, A., Savander, V., & LeDoux, J. E. (1997). Organization of intra-amygdaloid circuitries in the rat: an emerging framework for understanding functions of the amygdala. *Trends in Neurosciences*, *20*, 517–523.

Pitkänen, A., Pikkarainen, M., Nurminen, N., & Ylinen, A. (2000). Reciprocal connections between the amygdala and the hippocampal formation, perirhinal cortex, and postrhinal cortex in rat. A review. *Annals of the New York Academy of Sciences*, *911*, 369–391.

Pohmann, R., Speck, O., & Scheffler, K. (2016). Signal-to-noise ratio and MR tissue parameters in human brain imaging at 3, 7, and 9.4 tesla using current receive coil arrays. *Magnetic Resonance in Medicine*, *75*, 801–809.

Poppenk, J., & Moscovitch, M. (2011). A hippocampal marker of recollection memory ability among healthy young adults: contributions of posterior and anterior segments. *Neuron*, *72*, 931–937.

Poppenk, J., Walia, G., McIntosh, A. R., Joanisse, M. F., Klein, D., & Köhler, S. (2008). Why is the meaning of a sentence better remembered than its form? An fMRI study on the role of novelty-encoding processes. *Hippocampus*, *18*, 909–918.

Poppenk, J., Evensmoen, H. R., Moscovitch, M., & Nadel, L. (2013). Long-axis specialization of the human hippocampus. *Trends in Cognitive Sciences*, *17*, 230–240.

Postma, A., Kessels, R. P. C., & van Asselen, M. (2008). How the brain remembers and forgets where things are: the neurocognition of object-location memory. *Neuroscience and Biobehavioral Reviews*, *32*, 1339–1345.

Preston, A. R., Bornstein, A. M., Hutchinson, J. B., Gaare, M. E., Glover, G. H., & Wagner, A. D. (2010). High-resolution fMRI of content-sensitive subsequent memory responses in human medial temporal lobe. *Journal of Cognitive Neuroscience*, *22*, 156–173.

Prévost, C., McCabe, J. A., Jessup, R. K., Bossaerts, P., & O'Doherty, J. P. (2011). Differentiable contributions of human amygdalar subregions in the computations underlying reward and avoidance learning. *European Journal of Neuroscience*, *34*, 134–145.

Prévost, C., Liljeholm, M., Tyszka, J. M., & O'Doherty, J. P. (2012). Neural correlates of specific and general Pavlovian-to-instrumental transfer within human amygdalar subregions: a high-resolution fMRI study. *Journal of Neuroscience*, *32*, 8383–8390.

Prévost, C., McNamee, D., Jessup, R. K., Bossaerts, P., & O'Doherty, J. P. (2013). Evidence for model-based computations in the human amygdala during Pavlovian conditioning. *PLoS Computational Biology*, *9*, e1002918.

Pruessner, J. C., Li, L. M., Serles, W., Pruessner, M., Collins, D. L., Kabani, N., Lupien, S., & Evans, A. C. (2000). Volumetry of hippocampus and amygdala with high-resolution MRI and three-dimensional analysis software: minimizing the discrepancies between laboratories. *Cerebral Cortex*, *10*, 433–442.

Pruim, R. H. R., Mennes, M., van Rooij, D., Llera, A., Buitelaar, J. K., & Beckmann, C. F. (2015a). ICA-AROMA: A robust ICA-based strategy for removing motion artifacts from fMRI data. *NeuroImage*, *112*, 267–277.

Pruim, R. H. R., Mennes, M., Buitelaar, J. K., & Beckmann, C. F. (2015b). Evaluation of ICA-AROMA and alternative strategies for motion artifact removal in resting state fMRI. *NeuroImage*, *112*, 278–287.

Raichle, M. E. (2015). The brain's default mode network. *Neuroscience*, *38*, 433–447.

Raichle, M. E., MacLeod, A. M., Snyder, A. Z., Powers, W. J., Gusnard, D. A., & Shulman, G. L. (2001). A default mode of brain function. *Proceedings of the National Academy of Sciences*, *98*, 676–682.

Raichle, M. E., & Mintun, M. A. (2006). Brain work and brain imaging. *Neuroscience*, *29*, 449–476.

Raichle, M. E., & Snyder, A. Z. (2007). A default mode of brain function: a brief history of an evolving idea. *NeuroImage*, *37*, 1083–1090.

Rajah, M. N., & D'Esposito, M. (2005). Region-specific changes in prefrontal function with age: a review of PET and fMRI studies on working and episodic memory. *Brain*, *128*(Pt 9), 1964–1983.

Rajah, M. N., Kromas, M., Han, J. E., & Pruessner, J. C. (2010). Group differences in anterior hippocampal volume and in the retrieval of spatial and temporal context memory in healthy young versus older adults. *Neuropsychologia*, *48*, 4020–4030.

Ranganath, C., & Ritchey, M. (2012). Two cortical systems for memory-guided behaviour. *Nature Reviews. Neuroscience*, *13*, 713–726.

Ranganath, C., Yonelinas, A. P., Cohen, M. X., Dy, C. J., Tom, S. M., & D'Esposito, M. (2004). Dissociable correlates of recollection and familiarity within the medial temporal lobes. Neuropsychologia 42 (1), 2–13.

Ranganath, C., Yonelinas, A. P., Cohen, M. X., Dy, C. J., Tom, S. M., D'Esposito, M. (2004). Dissociable correlates of recollection and familiarity within the medial temporal lobes. Neuropsychologia, *42*, 2–13.

Raz, N., Ghisletta, P., Rodrigue, K. M., Kennedy, K. M., & Lindenberger, U. (2010). Trajectories of brain aging in middle-aged and older adults: regional and individual differences. *NeuroImage*, *51*, 501–511.

Raz, N., Gunning, F. M., Head, D., Dupuis, J. H., McQuain, J., Briggs, S. D., Loken, W. J., Thornton, A. E., & Acker, J. D. (1997). Selective aging of the human cerebral cortex observed in vivo: differential vulnerability of the prefrontal gray matter. *Cerebral Cortex*, *7*, 268– 282.

Raz, N., Gunning-Dixon, F., Head, D., Rodrigue, K. M., Williamson, A., & Acker, J. D. (2004). Aging, sexual dimorphism, and hemispheric asymmetry of the cerebral cortex: replicability of regional differences in volume. *Neurobiology of Aging*, *25*, 377–396.

Raz, N., Lindenberger, U., Rodrigue, K. M., Kennedy, K. M., Head, D., Williamson, A., Dahle, C., Gerstorf, D., & Acker, J. D. (2005). Regional brain changes in aging healthy adults: general trends, individual differences and modifiers. *Cerebral Cortex*, *15*, 1676–1689.

Raz, N., & Rodrigue, K. M. (2006). Differential aging of the brain: Patterns, cognitive correlates and modifiers. *Neuroscience & Biobehavioral Reviews, 30*, 730-748.

Reagh, Z. M., Watabe, J., Ly, M., Murray, E., & Yassa, M. A. (2014). Dissociated signals in human dentate gyrus and CA3 predict different facets of recognition memory. *Journal of Neuroscience*, *34*, 13301–13313.

Resnick, S. M., Pham, D. L., Kraut, M. A., Zonderman, A. B., & Davatzikos, C. (2003). Longitudinal magnetic resonance imaging studies of older adults: a shrinking brain. *Journal of Neuroscience*, *23*, 3295–3301.

Reuter-Lorenz, P. A., & Cappell, K. A. (2008). Neurocognitive Aging and the Compensation Hypothesis. *Current Directions in Psychological Science*, *17*, 177–182.

Rieck, J. R., Rodrigue, K. M., Kennedy, K. M., Devous, M. D., & Park, D. C. (2015). The effect of beta-amyloid on face processing in young and old adults: A multivariate analysis of the BOLD signal. *Human Brain Mapping*, *36*, 2514–2526.

Riecker, A., Gröschel, K., Ackermann, H., Steinbrink, C., Witte, O., & Kastrup, A. (2006). Functional significance of age-related differences in motor activation patterns. *NeuroImage*, *32*, 1345–1354.

Robinson, S., Basso, G., Soldati, N., Sailer, U., Jovicich, J., Bruzzone, L., Kryspin-Exner, I., Bauer, H., & Moser, E. (2009). A resting state network in the motor control circuit of the basal ganglia. *BMC Neuroscience*, *10*, 137.

Rolfe, D. F., & Brown, G. C. (1997). Cellular energy utilization and molecular origin of standard metabolic rate in mammals. *Physiological Reviews*, *77*, 731–758.

Ross, M. H., Yurgelun-Todd, D. A., Renshaw, P. F., Maas, L. C., Mendelson, J. H., Mello, N. K., Cohen, B. M., & Levin, J. M. (1997). Age-related reduction in functional MRI response to photic stimulation. *Neurology*, *48*, 173–176.

Rossi, S., Miniussi, C., Pasqualetti, P., Babiloni, C., Rossini, P. M., & Cappa, S. F. (2004). Age-related functional changes of prefrontal cortex in long-term memory: a repetitive transcranial magnetic stimulation study. *Journal of Neuroscience*, *24*, 7939–7944.

Rössler, M., Zarski, R., Bohl, J., & Ohm, T.G. (2002). Stage-dependent and sector-specific neuronal loss in hippocampus during Alzheimer's disease. *Acta Neuropathologica*, *103*, 363–369.

Roy, D. S., Kitamura, T., Okuyama, T., Ogawa, S. K., Sun, C., Obata, Y., Yoshiki A., & Tonegawa, S. (2017). Distinct neural circuits for the formation and retrieval of episodic memories. *Cell*, *170*, 1000–1012.e19.

Roy, K. A., Shehzad, Z., Margulies, D. S., Clare Kelly, A. M., Uddin, L. Q., Gotimer, K., Biswal, B. B., Castellanos, F. X., & Milham, M. P. (2009). Functional connectivity of the human amygdala using resting state fMRI. *NeuroImage*, *45*, 614–626.

Royston, P., & Altman, D. G. (1994). Regression Using Fractional Polynomials of Continuous Covariates: Parsimonious Parametric Modelling. *Applied Statistics*, *43*, 429.

Rubinov, M., & Sporns, O. (2010). Complex network measures of brain connectivity: uses and interpretations. *NeuroImage*, *52*, 1059–1069.

Rummel, C., Verma, R. K., Schoepf, V., Abela, E., Hauf, M., Zapata Berruecos, J. F., & Wiest, R. (2013). Time course based artifact identification for independent components of resting-state fMRI. *Frontiers in Human Neuroscience*, *7*.

Russell, J. A. (1980). A circumplex model of affect. *Journal of Personality and Social Psychology*, *39*, 1161–1178.

Russell, J. A. (2003). Core affect and the psychological construction of emotion. *Psychological Review*, *110*, 145–172.

Ryan, L., Lin, C.-Y., Ketcham, K., & Nadel, L. (2010). The role of medial temporal lobe in retrieving spatial and nonspatial relations from episodic and semantic memory. *Hippocampus*, 20, 11–18.

Rypma, B., & D'Esposito, M. (2000). Isolating the neural mechanisms of age-related changes in human working memory. *Nature Neuroscience*, *3*, 509–515.

Sah, P., Faber, E. S., Lopez de Armentia, M., & Power, J. (2003). The amygdaloid complex: anatomy and physiology. *Physiological Reviews*, *83*, 803–834.

Sala-Llonch, R., Bartrés-Faz, D., & Junqué, C. (2015). Reorganization of brain networks in aging: a review of functional connectivity studies. *Frontiers in Psychology*, *6*, 663.

Salimi-Khorshidi, G., Douaud, G., Beckmann, C. F., Glasser, M. F., Griffanti, L., & Smith, S. M. (2014). Automatic denoising of functional MRI data: combining independent component analysis and hierarchical fusion of classifiers. *NeuroImage*, *90*, 449–468.

Salthouse, T. A. (2012). Does the direction and magnitude of cognitive change depend on initial level of ability? *Intelligence, 40*, 352–361.

Sambataro, F., Murty, V. P., Callicott, J. H., Tan, H.-Y., Das, S., Weinberger, D. R., & Mattay, V. S. (2010). Age-related alterations in default mode network: impact on working memory performance. *Neurobiology of Aging*, *31*, 839–852.

Sauerbrei, W., Meier-Hirmer, C., Benner, A., & Royston, P. (2006). Multivariable regression model building by using fractional polynomials: Description of SAS, STATA and R programs. *Computational Statistics & Data Analysis*, *50*, 3464–3485.

Sauerbrei, W., & Royston, P. (1999). Building multivariable prognostic and diagnostic models: transformation of the predictors by using fractional polynomials. *Journal of the Royal Statistical Society. Series A (Statistics in Society), 162*, 71-94.

Schacter, D. L., & Wagner, A. D. (1999). Medial temporal lobe activations in fMRI and PET studies of episodic encoding and retrieval. *Hippocampus*, *9*, 7–24.

Schacter, D. L., Curran, T., Reiman, E. M., Chen, K., Bandy, D. J., & Frost, J. T. (1999). Medial temporal lobe activation during episodic encoding and retrieval: a PET study. *Hippocampus*, *9*, 575–581.

Schneider-Garces, N. J., Gordon, B. A., Brumback-Peltz, C. R., Shin, E., Lee, Y., Sutton, B. P., Maclin, E. L., Gratton, G., & Fabiani, M. (2010). Span, CRUNCH, and beyond: working memory capacity and the aging brain. *Journal of Cognitive Neuroscience*, *22*, 655–669.

Schroeder, W., Martin, K., & Lorensen, B. (2006). Visualization Toolkit: An Object-Oriented Approach to 3D Graphics, 4th Edition. Kitware, ISBN 978-1-930934-19-1.

Scoville, W. B., & Milner, B. (1957). Loss of recent memory after bilateral hippocampal lesions. J. Neurol. Neurosurg. Psychiatr. 20 (1), 11–21.

Sergerie, K., Chochol, C., & Armony, J. L. (2008). The role of the amygdala in emotional processing: a quantitative meta-analysis of functional neuroimaging studies. *Neuroscience and Biobehavioral Reviews*, *32*, 811–830.

Shafer, A. T., & Dolcos, F. (2012). Neural correlates of opposing effects of emotional distraction on perception and episodic memory: an event-related fMRI investigation. *Frontiers in Integrative Neuroscience*, *6*, 70.

Shafer, A. T., Matveychuck, D., Penney, T., O'Hare, A. J., Stokes, J., & Dolcols, F. (2012). Processing of emotional distraction is both automatic and modulated by attention: evidence from an event-related fMRI investigation. *Journal of Cognitive Neuroscience*, *24*, 1233–1252.

Shmuel, A., Augath, M., Oeltermann, A., & Logothetis, N. K. (2006). Negative functional MRI response correlates with decreases in neuronal activity in monkey visual area V1. *Nature Neuroscience*, *9*, 569–577.

Shmuel, A., Yacoub, E., Chaimow, D., Logothetis, N. K., & Ugurbil, K. (2007). Spatio-temporal point-spread function of fMRI signal in human gray matter at 7 Tesla. *NeuroImage*, *35*, 539–552.

Simić, G., Kostović, I., Winblad, B., & Bogdanović, N. (1997). Volume and number of neurons of the human hippocampal formation in normal aging and Alzheimer's disease. *Journal of Comparative Neurology*, *379*, 482–494.

Singhal, A., Shafer, A. T., Russell, M., Gibson, B., Wang, L., Vohra, S., & Dolcos, F. (2012). Electrophysiological correlates of fearful and sad distraction on target processing in adolescents with attention deficit-hyperactivity symptoms and affective disorders. *Frontiers in Integrative Neuroscience*, *6*, 119.

Sladky, R., Baldinger, P., Kranz, G. S., Tröstl, J., Höflich, A., Lanzenberger, R., Moser, E., & Windischberger, C. (2013). High-resolution functional MRI of the human amygdala at 7 T. *European Journal of Radiology*, *82*, 728–733.

Sled, J. G., Zijdenbos, A. P., & Evans, A. C. (1998). A nonparametric method for automatic correction of intensity nonuniformity in MRI data. *IEEE Transactions on Medical Imaging*, *17*, 87–97.

Small, S. A. (2002). The longitudinal axis of the hippocampal formation: its anatomy, circuitry, and role in cognitive function. *Reviews in the Neurosciences*, *13*, 183–194.

Smith, S. M., Fox, P. T., Miller, K. L., Glahn, D. C., Fox, P. M., Mackay, C. E., Filippini, N., Watkins, K. E., Toro, R., Laird, A. R., & Beckmann, C. F. (2009). Correspondence of the brain's functional architecture during activation and rest. *Proceedings of the National Academy of Sciences of the United States of America*, *106*, 13040–13045.

Smith, S. M., Jenkinson, M., Woolrich, M. W., Beckmann, C. F., Behrens, T. E. J., Johansen- Berg, H., Bannister, P. R., De Luca, M., Drobnjak, I., Flitney, D. E., Niazy, R. K., Saunders, J., Vickers, J., Zhang, Y., De Stefano, N., Brady, J. M., & Matthews, P. M. (2004). Advances in functional and structural MR image analysis and implementation as FSL. *NeuroImage*, *23 Suppl 1*, S208–19.

Smith, M. L., & Milner, B. (1981). The role of the right hippocampus in the recall of spatial location. *Neuropsychologia*, *19*, 781–793.

Smith, S. M., Miller, K. L., Salimi-Khorshidi, G., Webster, M., Beckmann, C. F., Nichols, T. E., Ramsey, J. D., & Woolrich, M. W. (2011). Network modelling methods for FMRI. *NeuroImage*, *54*(2), 875–891.

Smith, S. M., & Nichols, T. E. (2009). Threshold-free cluster enhancement: addressing problems of smoothing, threshold dependence and localisation in cluster inference. *NeuroImage*, *44*, 83–98.

Solé-Padullés, C., Bartrés-Faz, D., Junqué, C., Clemente, I. C., Molinuevo, J. L., Bargalló, N., Sánchez-Aldeguer, J., Bosch, B., Falcón, C., & Valls-Solé, J. (2006). Repetitive transcranial magnetic stimulation effects on brain function and cognition among elders with memory dysfunction. A randomized sham-controlled study. *Cerebral Cortex*, *16*, 1487–1493.

Song, J., Birn, R. M., Boly, M., Meier, T. B., Nair, V. A., Meyerand, M. E., & Prabhakaran, V. (2014). Age-related reorganizational changes in modularity and functional connectivity of human brain networks. *Brain Connectivity*, *4*, 662–676.

Spaniol, J., Davidson, P. S. R., Kim, A. S. N., Han, H., Moscovitch, M., & Grady, C. L. (2009). Event-related fMRI studies of episodic encoding and retrieval: meta-analyses using activation likelihood estimation. *Neuropsychologia*, *47*(8-9), 1765–1779.

Strange, B. A., Witter, M. P., Lein, E. S., & Moser, E. I. (2014). Functional organization of the hippocampal longitudinal axis. *Nature Reviews. Neuroscience*, *15*(10), 655–669.

Styalidis, C., Ioannides, A. A., Bamidis, P. D., & Papadelis, C. (2014). Amygdala responses to valence and its interaction by arousal revealed by MEG. *International Journal of Psychophysiology*, *93*, 121–133.

Spalletta, G., Cravello, L., Gianni, W., Piras, F., Iorio, M., Cacciari, C., Casini, A. R., Chiapponi, C., Sancesario, G., Fratangeli, C., Orfei, M. D., Caltagirone, C., & Piras, F. (2016). Homotaurine effects on hippocampal volume loss and episodic memory in amnestic mild cognitive impairment. *Journal of Alzheimer's Disease*, *50*, 807–816.

Sperling, R. (2007). Functional MRI studies of associative encoding in normal aging, mild cognitive impairment, and Alzheimer's disease. *Annals of the New York Academy of Sciences*, *1097*, 146–155.

Spreng, R. N., Stevens, W. D., Viviano, J. D., & Schacter, D. L. (2016). Attenuated anticorrelation between the default and dorsal attention networks with aging: evidence from task and rest. *Neurobiology of Aging*, *45*, 149–160.

Spreng, R. N., Wojtowicz, M., & Grady, C. L. (2010). Reliable differences in brain activity between young and old adults: a quantitative meta-analysis across multiple cognitive domains. *Neuroscience and Biobehavioral Reviews*, *34*, 1178–1194.

Squire, L. R., & Dede, A. J. O. (2015). Conscious and unconscious memory systems. *Cold Spring Harbor Perspectives in Biology*, *7*, a021667.

Squire, L. R., & Wixted, J. T. (2011). The cognitive neuroscience of human memory since H.M. *Annual Review of Neuroscience*, *34*, 259–288.

Squire, L. R., Genzel, L., Wixted, J. T., & Morris, R. G. (2015). Memory consolidation. *Cold Spring Harbor Perspectives in Biology*, *7*, a021766.

Stark, C. E., & Squire, L. R. (2001). When zero is not zero: the problem of ambiguous baseline conditions in fMRI. *Proceedings of the National Academy of Sciences of the United States of America*, *98*, 12760–12766.

Stefanova, I., Stephan, T., Becker-Bense, S., Dera, T., Brandt, T., & Dieterich, M. (2013). Age-related changes of blood-oxygen-level-dependent signal dynamics during optokinetic stimulation. *Neurobiology of Aging*, *34*, 2277–2286.

Stokes, J., Kyle, & C., Ekstrom, A. D. (2015). Complementary roles of human hippocampal subfields in differentiation and integration of spatial context. *Journal of Cognitive Neuroscience*, *27*, 546–559.

Storti, S. F., Formaggio, E., Nordio, R., Manganotti, P., Fiaschi, A., Bertoldo, A., & Toffolo, G. M. (2013). Automatic selection of resting-state networks with functional magnetic resonance imaging. *Frontiers in Neuroscience*, *7*, 72.

Strange, B. A., Witter, M. P., Lein, E. S., & Moser, E. I. (2014). Functional organization of the hippocampal longitudinal axis. *Nature Reviews. Neuroscience*, *15*, 655–669.

Sugiura, M. (2016). Functional neuroimaging of normal aging: Declining brain, adapting brain. *Ageing Research Reviews*, *30*, 61–72.

Suthana, N. A., Ekstrom, A. D., Moshirvaziri, S., Knowlton, B., & Bookheimer, S. Y. (2009). Human hippocampal CA1 involvement during allocentric encoding of spatial information. *Journal of Neuroscience*, *29*, 10512–10519.

Suthana, N. A., Ekstrom, A. D., Moshirvaziri, S., Knowlton, B., Bookheimer, S. Y. (2011). Dissociations within human hippocampal subregions during encoding and retrieval of spatial information. *Hippocampus*, *21*, 694–701.

Suthana, N. A., Donix, M., Wozny, D. R., Bazih, A., Jones, M., Heidemann, R. M., Trampel, R., Ekstrom, A. D., Scharf, M., Knowlton, B., Turner, R., & Bookheimer, S. Y. (2015). High-resolution 7T fMRI of human hippocampal subfields during associative learning. *Journal of Cognitive Neuroscience*, *27*, 1194–1206.

Suzuki, A., & Akiyama, H. (2012). Cognitive aging explains age-related differences in face-based recognition of basic emotions except for anger and disgust. *Aging, Neuropsychology, and Cognition. Section B, Aging, Neuropsychology, and Cognition*, *20*, 253–270.

Suzuki, W. A., & Baxter, M. G. (2009). Memory, perception, and the medial temporal lobe: a synthesis of opinions. *Neuron*, *61*, 678–679.

Tao, H., Guo, S., Ge, T., Kendrick, K. M., Xue, Z., Liu, Z., & Feng, J. (2013). Depression uncouples brain hate circuit. *Molecular Psychiatry*, *18*, 101–111.

Taoka, T., Iwasaki, S., Uchida, H., Fukusumi, A., Nakagawa, H., Kichikawa, K., Takayama, K., Yoshioka, T., Takewa, M., & Ohishi, H. (1998). Age correlation of the time lag in signal change on EPI-fMRI. *Journal of Computer Assisted Tomography, 22*, 514-517.

Terburg, D., Morgan, B. E., Montoya, E. R., Hooge, I. T., Thornton, H. B., Hariri, A. R., Panksepp, J., Stein, D. J., & van Honk, J. (2012). Hypervigilance for fear after basolateral amygdala damage in humans. *Translational Psychiatry*, *2*, e115.

Tohka, J., Foerde, K., Aron, A. R., Tom, S. M., Toga, A. W., & Poldrack, R. A. (2008). Automatic independent component labeling for artifact removal in fMRI. *NeuroImage*, *39*, 1227–1245.

Tomasi, D., & Volkow, N. D. (2012). Aging and functional brain networks. *Molecular Psychiatry*, *17*(5), 549-558.

Tompary, A., Duncan, K., & Davachi, L. (2016). High-resolution investigation of memory-specific reinstatement in the hippocampus and perirhinal cortex. *Hippocampus*, *26*, 995–1007.

Torralba, A., & Oliva, A. (2003). Statistics of natural image categories. *Network*, *14*, 391–412.

Travis, S. G., Huang, Y., Fujiwara, E., Radomski, A., Olsen, F., Carter, R., Seres, P., & Malykhin, N. V. (2014). High field structural MRI reveals specific episodic memory correlates in the subfields of the hippocampus. *Neuropsychologia*, *53*, 233–245.

Triantafyllou, C., Hoge, R. D., Krueger, G., Wiggins, C. J., Potthast, A., Wiggins, G. C., & Wald, L. L. (2005). Comparison of physiological noise at 1.5 T, 3 T and 7 T and optimization of fMRI acquisition parameters. *NeuroImage*, *26*, 243–250.

Tsvetanov, K. A., Henson, R. N. A., Tyler, L. K., Davis, S. W., Shafto, M. A., Taylor, J. R., Williams, N., Cam-CAN, & Rowe, J. B. (2015). The effect of ageing on fMRI: Correction for the confounding effects of vascular reactivity evaluated by joint fMRI and MEG in 335 adults. *Human Brain Mapping*, *36*, 2248–2269.

Ugurbil, K. (2016). What is feasible with imaging human brain function and connectivity using functional magnetic resonance imaging. *Philosophical Transactions of the Royal Society B: Biological Sciences*, *371*.

Uludağ, K., & Blinder, P. (2018). Linking brain vascular physiology to hemodynamic response in ultra-high field MRI. *NeuroImage*, *168*, 279–295.

Uludağ, K., Müller-Bierl, B., & Ugurbil, K. (2009). An integrative model for neuronal activity-induced signal changes for gradient and spin echo functional imaging. *NeuroImage*, *48*, 150–165.

van Asselen, M., Kessels, R. P. C., Kappelle, L. J., Postma, A. (2008). Categorical and coordinate spatial representations within object-location memory. *Cortex*, *44*, 249–256.

van Dijk, K. R. A., Sabuncu, M. R., & Buckner, R. L. (2012). The influence of head motion on intrinsic functional connectivity MRI. *NeuroImage*, *59*, 431–438.

van den Heuvel, M. P., & Hulshoff Pol, H. E. (2010). Exploring the brain network: a review on resting-state fMRI functional connectivity. *European Neuropsychopharmacology*, *20*, 519–534.

van der Zwaag, W., Francis, S., Head, K., Peters, A., Gowland, P., Morris, P., & Bowtell, R. (2009). fMRI at 1.5, 3 and 7 T: characterising BOLD signal changes. *NeuroImage*, *47*, 1425–1434.

van Honk, J., Eisenegger, C., Terburg, D., Stein, D. J., & Morgan, B. (2013). Generous economic investments after basolateral amygdala damage. *Proceedings of the National Academy of Sciences of the United States of America*, *110*, 2506–2510.

Vassilopoulou, K., Papathanasiou, M., Michopoulos, I., Boufidou, F., Oulis, P., Kelekis, N., Rizos, E., Nikolaou, C., Pantelis, C., Velakoulis, D., & Lykouras, L. (2013). A magnetic resonance imaging study of hippocampal, amygdala and subgenual prefrontal cortex volumes in major depression subtypes: melancholic versus psychotic depression. *Journal of Affective Disorders*, *146*, 197–204.

Vaughan, J. T., Garwood, M., Collins, C. M., Liu, W., DelaBarre, L., Adriany, G., Andersen, P., Merkle, H., Goebel, R., Smith, M. B., & Ugurbil, K. (2001). 7T vs. 4T: RF power, homogeneity, and signal-to-noise comparison in head images. *Magnetic Resonance in Medicine*, *46*, 24–30.

Vij, S. G., Nomi, J. S., Dajani, D. R., & Uddin, L. Q. (2018). Evolution of spatial and temporal features of functional brain networks across the lifespan. *NeuroImage*, *173*, 498–508.

Vinogradova, O. S. (2001). Hippocampus as comparator: role of the two input and two output systems of the hippocampus in selection and registration of information. *Hippocampus*, *11*, 578–598.

Wang, M., Gamo, N. J., Yang, Y., Jin, L. E., Wang, X.-J., Laubach, M., Mazer, J. A., Lee, D., & Arnsten, A. F. T. (2011). Neuronal basis of age-related working memory decline. *Nature*, *476*, 210–213.

Wang, L., LaBar, K. S., Smoski, M., Rosenthal, M. Z., Dolcos, F., Lynch, T. R., Krishnan, R. R., & McCarthy, G. (2008). Prefrontal mechanisms for executive control over emotional distraction are altered in major depression. *Psychiatry Research*, *163*, 143–155.

Wang, L., Li, Y., Metzak, P., He, Y., & Woodward, T. S. (2010). Age-related changes in topological patterns of large-scale brain functional networks during memory encoding and recognition. *NeuroImage*, *50*, 862–872.

Wang, L., McCarthy, G., Song, A. W., & LaBar, K. S. (2005). Amygdala activation to sad pictures during high-field (4 Tesla) functional magnetic resonance imaging. *Emotion*, *5*, 12–22.

Ward, L. M., Aitchison, R. T., Tawse, M., Simmers, A. J., & Shahani, U. (2015). Reduced haemodynamic response in the ageing visual cortex measured by absolute fNIRS. *PloS One*, *10*, e0125012.

Watson, P. D., Voss, J. L., Warren, D. E., Tranel, D., & Cohen, N. J. (2013). Spatial reconstruction by patients with hippocampal damage is dominated by relational memory errors. *Hippocampus*, *23*, 570–580.

Wechsler, D. (2009). Wechsler Memory Scale-IV Administration and Scoring Manual. Pearson, San Antonio, TX.

Weiskrantz, L. (1956). Behavioral changes associated with ablation of the amygdaloid complex in monkeys. *Journal of Comparative and Physiological Psychology*, *49*, 381–391.

West, K. L., Zuppichini, M. D., Turner, M. P., Sivakolundu, D. K., Zhao, Y., Abdelkarim, D., Spence, J. S., & Rypma, B. (2019). BOLD hemodynamic response function changes significantly with healthy aging. *NeuroImage*, *188*, 198–207.

Whalen, P. J., Rauch, S. L., Etcoff, N. L., McInerney, S. C., Lee, M. B., Jenike, M. A. (1998). Masked presentations of emotional facial expressions modulate amygdala activity without explicit knowledge. *Journal of Neuroscience*, *18*, 411–418.

Whalen, P. J., Shin, L. M., McInerney, S. C., Fischer, H., Wright, C. I., & Rauch, S. L. (2001). A functional MRI study of human amygdala responses to facial expressions of fear versus anger. *Emotion*, *1*, 70–83.

Whalen, P. J., Davis, F. C., Oler, J. A., Kim, H., Kim, M. J., & Neta, M. (2009). Human amygdala responses to facial expressions of emotion. In: Whalen, P. J., Phelps, E. A. (Eds.), The Human Amygdala. New York, NY, Guilford Press, pp. 265–288.

Whitfield-Gabrieli, S., & Nieto-Castanon, A. (2012). Conn: a functional connectivity toolbox for correlated and anticorrelated brain networks. *Brain Connectivity*, *2*, 125–141.

Wig, G. S. (2017). Segregated Systems of Human Brain Networks. *Trends in Cognitive Sciences*, *21*, 981–996.

Wig, G. S., Laumann, T. O., & Petersen, S. E. (2014). An approach for parcellating human cortical areas using resting-state correlations. *NeuroImage*, *93 Pt 2*, 276–291.

Wimble, M., Yoder, M., & Ro, Y. K. (2016). Understanding least absolute value in regression-based data mining. *International Journal of Data Mining & Knowledge Management Process*, *6*, 1–10.

Winterburn, J. L., Pruessner, J. C., Chavez, S., Schira, M. M., Lobaugh, N. J., Voineskos, A. N., & Chakravarty, M. M. (2013). A novel in vivo atlas of human hippocampal subfields using high-resolution 3 T magnetic resonance imaging. *NeuroImage*, *74*, 254–265.

Wisse, L. E. M., Gerritsen, L., Zwanenburg, J. J. M., Kuijf, H. J., Luijten, P. R., Biessels, G. J., & Geerlings, M. I. (2012). Subfields of the hippocampal formation at 7 T MRI: in vivo volumetric assessment. *NeuroImage*, *61*, 1043–1049.

Woollett, K., & Maguire, E. A. (2009). Navigational expertise may compromise anterograde associative memory. *Neuropsychologia*, *47*, 1088–1095.

Woollett, K., & Maguire, E. A. (2011). Acquiring “the Knowledge” of London's layout drives structural brain changes. *Current Biology*, *21*, 2109–2114.

Woollett, K., & Maguire, E. A. (2012). Exploring anterograde associative memory in London taxi drivers. *Neuroreport*, *23*, 885–888.

Woollett, K., Spiers, H. J., & Maguire, E. A. (2009). Talent in the taxi: a model system for exploring expertise. *Philosophical Transactions of the Royal Society of London. Series B, Biological Sciences*, *364*, 1407–1416.

Worsley, K. J., & Friston, K. (1995). Analysis of fMRI time-series revised – again. *NeuroImage*, *2*, 173–181.

Wright, M. E., & Wise, R. G. (2018). Can blood oxygenation level dependent functional magnetic resonance imaging be used accurately to compare older and younger populations? A mini literature review. *Frontiers in Aging Neuroscience*, *10*, 371.

Wu, J.-T., Wu, H.-Z., Yan, C.-G., Chen, W.-X., Zhang, H.-Y., He, Y., & Yang, H.-S. (2011). Aging-related changes in the default mode network and its anti-correlated networks: a resting- state fMRI study. *Neuroscience Letters*, *504*, 62–67.

Yamaguchi, T., Kanno, I., Uemura, K., Shishido, F., Inugami, A., Ogawa, T., et al. (1986). Reduction in regional cerebral metabolic rate of oxygen during human aging. *Stroke*, *17*(6), 1220–1228.

Yan, L., Zhuo, Y., Wang, B., & Wang, D. J. J. (2011). Loss of coherence of low frequency fluctuations of BOLD FMRI in visual cortex of healthy aged subjects. *Open Neuroimaging Journal*, *5*(Suppl 1), 105–111.

Yassa, M. A., & Stark, C. E. L. (2009). A quantitative evaluation of cross-participant registration techniques for MRI studies of the medial temporal lobe. *NeuroImage*, *44*, 319–327.

Yassa, M. A., & Stark, C. E. L. (2011). Pattern separation in the hippocampus. *Trends in Neurosciences*, *34*, 515–525.

Yassa, M. A., Mattfeld, A. T., Stark, S. M., & Stark, C. E. L. (2011). Age-related memory deficits linked to circuit-specific disruptions in the hippocampus. *Proceedings of the National Academy of Sciences of the United States of America*, *108*, 8873–8878.

Yeo, B. T. T., Krienen, F. M., Chee, M. W. L., & Buckner, R. L. (2014). Estimates of segregation and overlap of functional connectivity networks in the human cerebral cortex. *NeuroImage*, *88*, 212–227.

Yeo, B. T. T., Krienen, F. M., Sepulcre, J., Sabuncu, M. R., Lashkari, D., Hollinshead, M., Roffman, J. L., Smoller, J. W., Zöllei, L., Polimeni, J. R., Fischl, B., Liu, H., & Buckner, R. L. (2011). The organization of the human cerebral cortex estimated by intrinsic functional connectivity. *Journal of Neurophysiology*, *106*, 1125–1165.

Yesavage, J. A., Brink, T. L., Rose, T. L., Lum, O., Huang, V., Adey, M., & Leirer, V. O. (1982). Development and validation of a geriatric depression screening scale: A preliminary report. *Journal of Psychiatric Research*, *17*, 37–49.

Yeşilyurt, B., Ugurbil, K., & Uludağ, K. (2008). Dynamics and nonlinearities of the BOLD response at very short stimulus durations. *Magnetic Resonance Imaging*, *26*, 853–862.

Yilmazer-Hanke, D. M. (2012). Amygdala. In: Mai, J. K., Paxinos, G. (Eds.), The Human Nervous System, 3rd edition. Academic Press, London, UK, pp. 759-834.

Yoder, K. J., Porges, E. C., & Decety, J. (2015). Amygdala subnuclei connectivity in response to violence reveals unique influences of individual differences in psychopathic traits in a nonforensic sample. *Human Brain Mapping*, *36*, 1417–1428.

Yushkevich, P. A., Piven, J., Hazlett, H. C., Smith, R. G., Ho, S., Gee, J. C., & Gerig, G. (2006). User-guided 3D active contour segmentation of anatomical structures: significantly improved efficiency and reliability. *NeuroImage*, *31*, 1116–1128.

Yushkevich, P. A., Amaral, R. S., Augustinack, J. C., Bender, A. R., Bernstein, J. D., Boccardi, M., Bocchetta, M., Burggren, A. C., Carr, V. A., Chakravarty, M. M., Chételat, G., Daugherty, A. M., Davachi, L., Ding, S. L., Ekstrom, A., Geerlings, M. I., Hassan, A., Huang, Y., Iglesias, J. E., La Joie, R., Kerchner, G. A., LaRocque, K. F., Libby, L. A., Malykhin, N. V., Mueller, S. G., Olsen, R. K., Palombo, D. J., Parekh, M. B., Pluta, J. B., Preston, A. R., Pruessner, J. C., Ranganath, C., Raz, N., Schlichting, M. L., Schoemaker, D., Singh, S., Stark, C. E., Suthana, N., Tompary, A., Turowski, M. M., Van Leemput, K., Wagner, A. D., Wang, L., Winterburn, J. L., Wisse, L. E., Yassa, M. A., & Zeineh, M. M. (2015a). Quantitative comparison of 21 protocols for labeling hippocampal subfields and parahippocampal subregions in in vivo MRI: towards a harmonized segmentation protocol. *NeuroImage*, *111*, 526–541.

Yushkevich, P. A., Pluta, J. B., Wang, H., Xie, L., Ding, S.-L., Gertje, E. C., Mancuso, L., Kliot, D., Das, S. R., & Wolk, D. A. (2015b). Automated volumetry and regional thickness analysis of hippocampal subfields and medial temporal cortical structures in mild cognitive impairment. *Human Brain Mapping*, *36*, 258–287.

Zald, D. H., & Pardo, J. V. (2002). The neural correlates of aversive auditory stimulation. *NeuroImage*, *16*, 746–753.

Zalesky, A., Fornito, A., & Bullmore, E. (2012). On the use of correlation as a measure of network connectivity. *NeuroImage*, *60*, 2096–2106.

Zeidman, P., & Maguire, E.A. (2016). Anterior hippocampus: the anatomy of perception, imagination and episodic memory. *Nature Reviews. Neuroscience*, *17*, 173–182.

Zeidman, P., Lutti, A., & Maguire, E. A. (2015). Investigating the functions of subregions within anterior hippocampus. *Cortex*, *73*, 240–256.

Zeineh, M. M., Engel, S. A., Thompson, P. M., & Bookheimer, S. Y. (2003). Dynamics of the hippocampus during encoding and retrieval of face-name pairs. *Science*, *299*, 577–580.

Zhang, N., Yacoub, E., Zhu, X.-H., Ugurbil, K., & Chen, W. (2009). Linearity of blood-oxygenation-level dependent signal at microvasculature. *NeuroImage*, *48*, 313–318.

Zhu, Y., & Cribben, I. (2018). Sparse graphical models for functional connectivity networks: best methods and the autocorrelation issue. *Brain Connectivity*, *8*, 139–165.

Zonneveld, H. I., Pruim, R. H., Bos, D., Vrooman, H. A., Muetzel, R. L., Hofman, A., Rombouts, S. A. R. B., van der Lugt, A., Niessen, W. J., Ikram, M. A., & Vernooij, M. W. (2019). Patterns of functional connectivity in an aging population: The Rotterdam Study. *NeuroImage*, *189*, 432–444.